Gait Modulation of Undulatory Microswimmers through the Lens of Optimality

Lukas Deutz

School of Computing

The University of Leeds

Submitted in accordance with the requirements for the degree of

Doctor of Philosophy

February 2024

Intellectual Property

The candidate confirms that the work submitted is his own and that appropriate credit has been given where reference has been made to the work of others.

To
Wolfgang, Birgit and Sarah

In the midst of winter, I found there was, within me, an invincible summer. And that makes me happy. For it says that no matter how hard the world pushes against me, within me, there's something stronger — something better, pushing right back.

— Albert Camus

Acknowledgements

I would like to express my heartfelt gratitude to my supervisors, Thomas Ranner and Netta Cohen. Throughout this journey, they have been incredibly supportive, encouraging, and instrumental in keeping me on track. I want to express my profound gratitude to Netta for welcoming me into her group and making me feel like a truly valuable member of her team. Her broad knowledge and interest, seemingly endless energy and passion have been inspiring. A special thanks to Thomas, whose support was indispensable in rebuilding my confidence during a challenging point of my PhD journey.

The foundation of my research is the result of tireless efforts from Netta and the WormLab group members, past and present. In particular, I wish to acknowledge Thomas, Tom Ilett and Yongxing Wang who laid the theoretical groundwork, provided the initial design, and implemented the simulator this work builds upon. Their dedication and expertise have been crucial in enabling the accurate and insightful simulations of microswimmers presented in this work. And lastly, of course, Netta, for providing the inspiration and driving force to keep the project going through a changing cast of members. I am very grateful for the numerous discussions with my colleagues, as they have significantly contributed to improving my understanding and skill set in conducting better research. I want to thank Felix Salfelder, with whom I spent many evenings in front of a whiteboard discussing my work. Felix always showed a genuine interest and made a real effort to provide valuable feedback. I also want to express my gratitude to Yongxing Wang and Petar Bollada for their contributions and camaraderie throughout this research journey. From engaging walks to shared lunches and coffees, they created a supportive, creative and humorous atmosphere which made the PhD that much more enjoyable. I am very grateful to Carolin for meticulously proofreading my thesis, from the title to the final page of the appendix.

Finally, I am extremely grateful to my family and friends for their love and support who encouraged me throughout. I'm grateful to my sister Sarah for always welcoming me into her family whenever I go home. Her love and care mean the world to me. I want to thank my father, Wolfgang, who nourished my love for philosophy and science from a young age and taught me the importance of kindness. I want to thank my mother, Birgit, for reading to me and my sister most nights when we were young and for her unconditional love.

Abstract

To navigate its habitat, an organism must be able to adapt its locomotory gait to its physical surroundings and behavioral objectives. We analyze the gait performance of lateral undulatory slender limbless microswimmers immersed in a Newtonian fluid environment. Our goal is to investigate the optimality of gait selection and adaptation, considering variables such as speed and energy efficiency. Specifically, we focus on the 1 mm long roundworm *Caenorhabditis elegans* (*C. elegans*), which adapts its swimming gait to the external load imposed by its surrounding environment. So far, it has not been understood if this gait adaptation can be considered optimal.

Here, we hypothesize that *C. elegans* selects an undulation frequency and waveform that optimizes energy efficiency. Using a viscoelastic Cosserat rod model to describe the worm's biomechanics, we simulate its undulatory locomotion in fluid environments spanning four orders of magnitude in viscosity. We demonstrate that *C. elegans*' undulation frequency minimizes its cost of transport and is significantly slower than the predicted fastest frequency. Furthermore, *C. elegans* frequency adaptation can be understood as an attempt to match its actuation time scale to the response time of its body in a given environment. We show that this adaption is crucial to facilitate efficient undulatory locomotion in more viscous environments and can, therefore, be observed in other microswimmers such as sperm. In low fluid viscosities, we find that the worm's energy cost is dominated by internal friction, favoring long wavelengths and small amplitudes, whereas in high viscosities, external friction takes precedence, favoring shorter wavelengths and larger amplitudes. This trend aligns with experimental observation, which suggests that *C. elegans* gait adaptation is driven by energy efficiency. Through a quantitative comparison between experimental data and model prediction, we estimate an optimal value for the internal damping coefficient (viscosity) of *C. elegans*' body material.

Our results show how the interplay between the different friction forces within the model shapes gait optimality. We believe that this interplay could be a more general driver behind gait adaptation in organisms that need to navigate environments with varying levels of external load.

Contents

List of Figures

List of Tables

Chapter 1

Introduction

The beauty, efficiency, and diversity of animal locomotion inspire human curiosity and ingenuity to this day. Animals move for many reasons, such as foraging food, mating, or escaping predators. The ability to move is essential for the survival of most animals, and natural selection has, therefore, shaped their locomotion strategies. Yet, the study of animal locomotion not only offers insight into the mechanics of movement and evolutionary adaptation of different species but also inspires technological innovations in fields such as biomechanics and robotics [110].

Organisms live on land, in water, and in the air, and to a large extent, the physical properties and forces imposed by these media have shaped their locomotion mechanisms. As a result, distinct locomotion modes such as walking, running, crawling, swimming, and flying have evolved, each uniquely adapted to the constraints posed by their specific environments. However, beneath this remarkable diversity lie core principles of biological organization and key evolutionary objectives that underpin most locomotory systems. The study of animal locomotion seeks to identify and understand these core principles and objectives [1, 19]. To examine these principles, microorganisms offer an ideal starting point due to the simplicity of their anatomy, locomotory patterns, and behavioral objectives [83].

Therefore, this thesis explores the undulatory locomotion of microswimmers. Undulatory locomotion, characterized by a wave-like body motion, can be observed in many species across all length scales of the animal kingdom; prominent examples include sperm, the larvae of insects such as caterpillars, worms, anguilliform fish and snakes [24, 39, 49, 58, 132]. The basis for thrust generation during lateral undulatory locomotion rests on the anisotropy of the friction force created by the relative movement between the organism's body surface and its environment. This anisotropy enables the organism to produce a propulsion force in the longitudinal body direction through lateral body movement.

In the context of microswimmers, the local hydrodynamic stresses created by such a movement were first modeled by the seminal work of Taylor [127], Lighthill [86], and Gray & Hancock [55, 60] in the 1950s. Gray & Hancock demonstrated how the propagating flagellar wave of sea urchin sperm produces a propulsive thrust that is balanced by the drag on the cell head, enabling steady forward motion. Since then, the field has evolved significantly, allowing for more accurate descriptions of the fluid-body interaction observed in actively deforming microswimmers, typically based on numerical methods.

However, there are still many unresolved questions. Different species of microswimmers exhibit unique locomotion patterns under similar environmental conditions. For instance, the undulation frequency of singular cellular microswimmers and multicellular organisms such as larvae and worms differs by orders of magnitude [25, 45, 113]. Thus far, it remains unclear how this discrepancy in undulation frequencies relates to the differences in the biomechanical properties of the propulsion appendages of singular cellular and the bodies of multicellular organisms, respectively. Furthermore, it is unclear how the details of the internal actuation mechanism in these organisms influence the range of undulation frequencies available to an organism.

Single cellular (eukaryotic) microswimmers such as sperm and euglena generate propulsion by actively deforming their slender, flexible propulsion appendages called flagella. The flagellum's internal structure is called axoneme and consists of long polymeric filaments called microtubules doubles. Within the axoneme, ATP-driven molecular motor proteins called dyan generate forces that slide microtubules past each other. This sliding motion generates shear forces that induce local bending in the flexible flagellum [92]. Thus, through the coordinated action of these motor proteins, flagellated microswimmers can induce a bending wave that travels across the entire length of the flagellum, resulting in the flagellum's "sinusoidal" waveform observed during undulatory locomotion [83].

In contrast, multicellular animals such as *C. elegans* bend their bodies by contracting their muscles. Muscles comprise many muscle fibers (cells) composed of repeating units called sarcomeres. The sarcomere forms the basic contractile units of muscle tissues. Within the sarcomere, contraction is generated by myosin motor proteins that interact with actin filaments to generate movement. Actin filaments are thin, flexible fibers that form the structural network of the sarcomere. Myosin proteins are organized into thick filaments that run parallel to the actin filaments and whose heads provide binding sites for the actin filaments. Under the provision of ATP, myosin heads bind on adjacent actin filaments, pulling them towards the center of the sarcomere, a process referred to as a power stroke. The repeated cycle of power strokes and detachment causes the actin filaments to slide past the myosin filaments, shortening the sarcomere and, thereby, the muscle fiber. Hence, muscle contraction is achieved by simultaneously shortening the muscle fibers within it [76].

In undulating animals such as *C. elegans*, muscles are tethered to their outer body shell, enabling them to bend their body locally by contracting their muscles [6]. Thus, similar to the coordinated action of dyan motor proteins in the flagellum of single cellular (eukaryotic) microswimmers, undulating animals such as *C. elegans* use coordinated muscle activation to induce a bending wave that travels along their body and gives rise to the characteristic "sinusoidal" body wave observed during undulatory locomotion. We will discuss the anatomy and muscular system of *C. elegans* in more detail in Chapter 2.

Note that regardless of the details underlying the actuation mechanism in different undulating organisms, the spatiotemporal pattern of the actuation along their propulsion appendages or body determines the frequency and waveform of the undulation. Many undulatory organisms modulate their undulation gait, adjusting both undulation frequency and body waveform in response to changing environmental conditions and external cues [18, 23, 45, 114, 126, 135, 144]. This prompts the question: what are the evolutionary and behavioral objectives that drive these selections and adaptations? In this thesis, we exclusively focus on global objectives such as speed or energy efficiency.

To estimate the swimming energy and speed of a microswimmer, a detailed biomechanical model of the swimmer's body coupled with a hydrodynamic model of its surrounding fluid environment is required. The energy injected into such a system, often associated with the organism's propulsion mechanism, must equal the total energy lost due to internal and external friction. The external losses due to friction between the body surface and surrounding fluid can, in principle, be estimated with high accuracy by solving the fluid-structure interaction problem. The flow regime of microswimmers is defined by low Reynolds numbers, where viscous fluid forces are significantly larger than inertia forces [83]. In this regime, the flow in the vicinity of the swimmer can be approximated by the Stokes equation, which has a unique solution for specified velocity boundary conditions. [77]. Conversely, the internal losses depend on the details of the biomechanical model of the swimmer's body, which can include arbitrary levels of complexity. Typical sources of internal friction are the relaxation and contraction processes of body muscles and the viscoelastic properties of the passive body material.

Early work by Lighthill [87] and others only considered the energy loss due to external friction. Lighthill maximized the hydrodynamic efficiency for periodic waves traveling down the length of an infinitely long flagellum, proposing a non-smooth triangle wave as the optimal waveform. More recently, internal losses have been included to estimate the energy cost associated with undulatory locomotion [45, 58, 122, 141]. Building upon these results, we employ a viscoelastic Cosserat rod to model the undulatory locomotion of a microswimmer immersed in a Newtonian fluid. Using this model, we aim to understand the influence of gait modulation on the performance of undulating microswimmers. Our study explores how the interplay of the physical model parameters, such as body stiffness, internal damping, and fluid viscosity, shapes gait optimality.

We apply our model to describe the undulatory locomotion of the one-millimeter-long nematode *Caenorhabditis elegans* (*C. elegans*). This tiny worm has been extensively studied, dating back to pioneering work by Sydney Brenner [26] in the 1960s, leading to crucial insights across different research areas, including genetics, developmental biology, and neurology. Within the field of biomechanics, the worm's rather simple neural system and body anatomy make it an ideal model organism to study the interplay between neural circuitry, muscles, surrounding fluid environment, and sensorimotor feedback [23, 40, 42]. In the context of this work, *C. elegans* serves as an ideal study object as it adapts its undulatory gait in response to changing environmental conditions [18, 22, 45, 126]. Until now, it remains unclear if this adaptive behavior can be considered optimal.

1.1 Thesis outline

This thesis aims to provide insights into the underlying reasons that govern gait selection and modulation in microswimmers. Therefore, we develop a biomechanical model of a limbless slender microswimmer immersed in a Newtonian fluid environment. Using this model, we simulate the undulatory locomotion of a generic microswimmer, varying model and undulation parameters. By comparing the performance for different undulation parameters, we seek to identify which gait can be considered optimal with respect to speed and energy efficiency in a given scenario. This analysis enables us to infer whether the undulation gait of a particular microswimmer prioritizes speed or energy efficiency. Specifically, we focus on *C. elegans*, which exhibit a continuous gait transition from low to high-viscosity fluids. Our aim is to assess whether this gait transition can be considered optimal. With this overarching goal in mind, the upcoming chapters of this thesis will be organized as follows:

Chapter 2 provides the necessary background for the thesis. It starts with an introduction to the fluid dynamics relevant for microswimmers and concludes with a brief description of the model organism *C. elegans*.

Chapter 3 formulates our microswimmer model. It includes a brief introduction to Cosserat rod theory, used to represent the biomechanical properties and deformation kinematics of the swimmer's body. We then formulate equations for an active viscoelastic Cosserat rod immersed in Newtonian Stokes flow to simulate microswimmer locomotion. The chapter concludes by introducing a numerical scheme for solving the model equations and validating its numerical accuracy and stability.

With our model established, Chapter 4 explores its dynamical properties. This involves analyzing the model's dynamic response to actuation. The goal is to uncover distinct dynamical regimes, each characterized by its unique response properties, which determine the relationship between the desired body wave (encoded in the spatiotemporal pattern of the actuation) and the emergent body wave. By comparing the performance of the different regimes in terms of speed and energy efficiency, we gain insight into how the interplay of physical model parameters affects the performance of undulatory locomotion in different fluid environments.

Building upon the results from 4, Chapter 5 analyzes the gait selection and modulation of a generic microswimmer. Our goal is to identify optimal gaits in terms of the swimmer's speed and energy efficiency in fixed and varying environmental conditions characterized by the fluid's viscosity. Furthermore, it aims to determine how the plausible range of the gait parameters (undulation frequency and waveform) in a given environment depends on the biomechanical parameters of the swimmer's body. To simplify our analysis, Chapter 5 is divided into two parts: the first part discusses gait modulation in a static environment, while the second part focuses on gait adaptation in response to varying fluid viscosities.

In Chapter 6, we apply our model to simulate the undulatory locomotion of the model organism *C. elegans*. Our aim is to infer whether *C. elegans* gait selection and transition can be considered optimal. Therefore, we evaluate gait performance under conditions that resemble those explored in the experimental literature. Within these conditions, we predict optimal gaits of *C. elegans* in relation to both speed and energy efficiency and compare them to gaits documented through experimental observation.

Finally, Chapter 7 concludes the thesis with a critical discussion of the results, outlining the limitations of our model and suggesting directions for future research.

1.2 Contributions

The theoretical framework and code base of the microswimmer model are built upon the model developed by Ranner [111] and Wang *et al.* [136]. The main contributions of the presented work are:

1. Formulation, implementation, and numerical validation of slender limbless microswimmer model based on Cosserat theory. The model includes a dimensionless formulation of the rod's equations of motion and the identification of key dimensionless model parameters.
2. Exploration of the model's dynamic response properties with respect to undulatory

actuation, including:

   (a) Identification of distinct dynamical regimes, each characterized by unique response properties.
   (b) Analysis of the microswimmer's performance across these regimes, focusing on speed and energy efficiency.
   (c) Discussion on how the microswimmer's operating point within these regimes is determined by the physical model parameters and the consequences thereof.

3. Simulating and analyzing the gait modulation of a generic slender microswimmer across a wide range of scenarios, including:
   (a) Establishing the limits for undulation frequency and waveform for optimal efficiency and speed, respectively.
   (b) Discussion on how these limits depend on the physical model parameters and the consequences thereof.
   (c) Offering a unique interpretation of microswimmer's gait adaptation in response to changing fluid viscosity

4. Simulation of the undulatory locomotion of the model organism *C. elegans* and comparison with experimental data. This includes:
   (a) Evaluating the performance of *C. elegans*' swimming gait in water. Proposing the hypothesis that *C. elegans* swimming gait is optimized for energy efficiency.
   (b) Providing a quantitative prediction for the internal damping coefficient (viscosity) of *C. elegans*' body material.
   (c) Proposing the hypothesis that the *C. elegans* gait transition from low to high fluid viscosities demonstrates optimal energy efficiency.

Chapter 2

Background

This chapter establishes the necessary context and introduces key concepts for the remainder of this thesis. We begin with a general description of the swimming problem, defined as the locomotion of an actively deforming body immersed in a viscous Newtonian fluid. Following this, we discuss the characteristics of low Reynolds number flow, highlighting its significance for the locomotion of microswimmers. This discussion leads us to resistive-force theory, which provides an explanation for the basic principle behind the propulsion mechanism of slender microswimmers. The chapter concludes with a brief introduction to the model organism *C. elegans*, including an overview of its existing biomechanical models and their relevance for the study of undulatory locomotion.

2.1 Swimming Problem

To set the scene, this section introduces the mathematical framework necessary to describe the swimming motion of an active swimmer. It closely follows the presentation in the recently published book on the fluid dynamics of cell motility by Eric Lauga [83].

The canonical swimming problem can be described as follows: An active swimmer immersed in a viscous fluid deforms its body, which sets the surrounding fluid into motion. The resulting fluid flow imparts hydrodynamic stresses onto the swimmer's body, propelling it forward. Consequently, solving the swimming problem requires us to model the deformation kinematics of the swimmer's active body and the fluid-structure interaction problem between the swimmer's body surface and its fluid environment.

The body's deformation kinematics and hydrodynamics can both be described using the framework of continuum mechanics [16, 117]. Consider a deformable body composed of an infinite number of material points labeled by their position $\boldsymbol{X}$ within a reference configuration shown in Fig. 2.1. Each material point $\boldsymbol{X}$ represents an infinitesimally small portion of the body that carries mass, has a position and velocity, and can be acted upon by forces. Collectively, the infinite set of material points $\boldsymbol{X} \in V_0$ forms a continuous representation of the swimmer's body, where V_0 is the volume occupied by this body in its reference configuration. Since all material points can be uniquely identified by their position $\boldsymbol{X}$ in the reference configuration, the current configuration of the swimmer's body at time t can be defined in terms of the instantaneous position $\boldsymbol{x}(t;\boldsymbol{X})$ of these material points. Together, these points make up the current body volume $V(t)$ of the swimmer, as illustrated in Fig. 2.1.

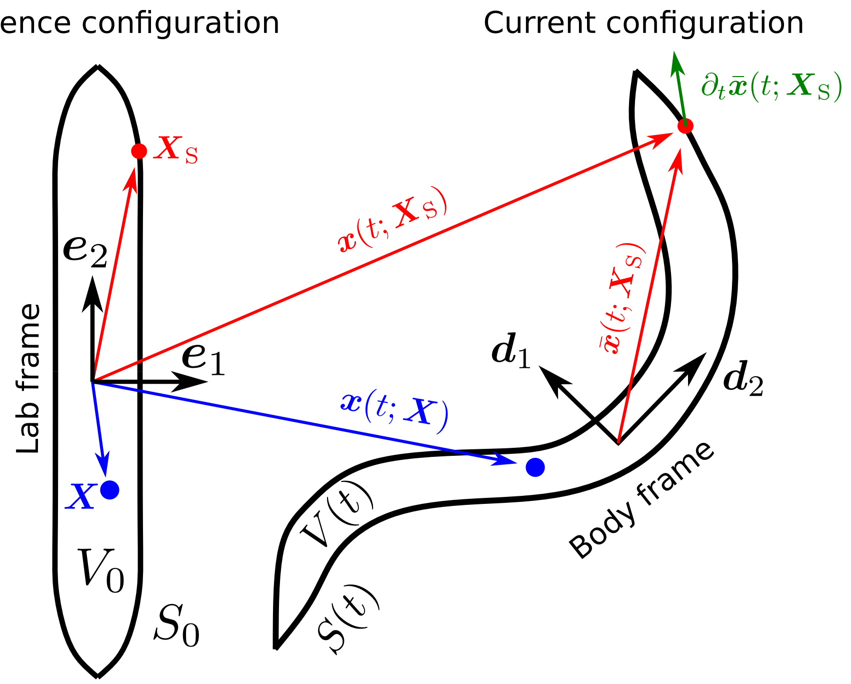

Figure 2.1: Schematic of a continuous deformable body represented by material points. Reference configuration with volume V_0 and surface S_0 on the left. Instantaneous configuration with volume $V(t)$ and surface $S(t)$ on the right. Lab-frame basis vectors ($\boldsymbol{e}_1$, $\boldsymbol{e}_2$) are placed within and aligned with the reference configuration, while fixed-body frame vectors ($\boldsymbol{d}_1$, $\boldsymbol{d}_2$) align with the current configuration. Exemplary material points within the interior (blue dot) and on the surface (red dot) of the reference configuration are marked. The blue vectors $\boldsymbol{X}$ and $\boldsymbol{x}(t;\boldsymbol{X})$ represent the position of the interior point in the reference and current configurations, respectively. The red vectors $\boldsymbol{X}_\mathrm{S}$, $\boldsymbol{x}_\mathrm{S}(t;\boldsymbol{X}_\mathrm{S})$, and $\bar{\boldsymbol{x}}_\mathrm{S}(t;\boldsymbol{X}_\mathrm{S})$ represent the position of the surface point in the reference configuration and the current configuration (lab and body frame), respectively. The green vector $\partial_t \bar{\boldsymbol{x}}_\mathrm{S}(t;\boldsymbol{X}_\mathrm{S})$ represents the surface point's velocity in the body frame.

To describe the interaction of the swimmer's outer body surface with the surrounding fluid environment, it is convenient to define the set of material points $\boldsymbol{X}_S = \{\boldsymbol{X} : \boldsymbol{X} \in S_0\}$, which constitute the body surface S_0 in the reference configuration. The swimmer's body surface $S(t)$ in its current configuration can then be defined by the instantaneous position $\boldsymbol{x}_S = \boldsymbol{x}(t; \boldsymbol{X}_S)$ of all the surface points. Here, we assume that the swimmer's body does not undergo deformations that change the topology of its surface.

In this work, we assume the swimmer's fluid environment to be incompressible and Newtonian. As state variables, we consider the fluid's pressure field $p(\boldsymbol{x}, t)$ and the fluid's velocity field $\boldsymbol{u}(\boldsymbol{x}, t)$ commonly referred to as the flow field. In the Eulerian picture, both p and $\boldsymbol{u}$ are defined with respect to a fixed reference frame and their time evolution is governed by the incompressible Navier-Stokes equations

$$\rho \frac{\mathrm{D}\boldsymbol{u}}{\mathrm{D}t} = \nabla \cdot \boldsymbol{\sigma}, \quad \nabla \cdot \boldsymbol{u} = 0, \tag{2.1}$$

where $\rho(\boldsymbol{x}, t)$ is the fluid's mass density, $\mathrm{D}\boldsymbol{u}(\boldsymbol{x}, t)/\mathrm{D}t$ is the material derivative, and $\boldsymbol{\sigma}(\boldsymbol{x}, t)$ the fluid stress tensor. For a thorough derivation and discussion of the Navier-Stokes equation, we refer to the classical textbook by Batchelor [16]. The first of the two equations in Eq. (2.1) represents the conservation of linear momentum within the fluid, whereas the second equation expresses the conservation of mass. The material derivative $\mathrm{D}\boldsymbol{u}/\mathrm{D}t$ is defined as

$$\frac{\mathrm{D}\boldsymbol{u}}{\mathrm{D}t} = \frac{\partial \boldsymbol{u}}{\partial t} + \boldsymbol{u} \cdot \nabla \boldsymbol{u}. \tag{2.2}$$

It describes the acceleration of a fluid material, taking into account both local changes and changes due to the transport of the material within the macroscopic flow field. The fluid stress tensor $\boldsymbol{\sigma}$ describes the distribution of stresses within a fluid. The element σ_{ij} represents the stress in i-th direction on a surface normal to the j-th direction of the fixed reference frame. For an incompressible Newtonian fluid, the stress tensor $\boldsymbol{\sigma}$ is given by

$$\boldsymbol{\sigma} = -p\mathbf{1} + \frac{\mu}{2}\left(\nabla \otimes \boldsymbol{u} + \nabla \otimes \boldsymbol{u}^T\right) \tag{2.3}$$

where $\mathbf{1}$ is the identity matrix, μ the fluid's viscosity and $\otimes$ the outer vector product defined as

$$[\nabla \otimes u]_{ij} = \frac{\partial u_i}{\partial x_j}. \tag{2.4}$$

To model the fluid-structure interaction between the swimmer's body surrounding fluid environment, we impose a nonslip boundary condition. The nonslip boundary condition assumes that at the body-fluid interface, the fluid velocity must be zero relative to the velocity of the body's surface. In other words, the fluid "sticks" to the swimmer's outer body surface. Consequently, the viscous friction between adjacent fluid layers causes the fluid near the swimmer to be dragged along with its motion.

Using the continuous representation of the swimmer's body, the nonslip boundary condition implies that the fluid velocity $\boldsymbol{u}$ at the surface point $\boldsymbol{x}_S$ must be equal to its velocity $\boldsymbol{v}_S = \partial_t \boldsymbol{x}_S$. It is common practice to express $\boldsymbol{v}_S$ in terms of the surface velocity $\bar{\boldsymbol{v}}_S = \partial_t \bar{\boldsymbol{x}}_S$ in the body-fixed frame [83]. The body-fixed for a deformable body is typically defined using a set of reference axes attached to the body itself, illustrated in Fig. 2.1. Hence, it translates and rotates with linear velocity $\boldsymbol{U}(t)$ and angular velocity $\boldsymbol{\Omega}(t)$, respectively. Consequently, the nonslip boundary condition in the lab frame can be expressed as

$$\boldsymbol{u} = \boldsymbol{Q} \cdot \bar{\boldsymbol{v}}_S + \boldsymbol{U} + \boldsymbol{\Omega} \times \bar{\boldsymbol{x}}_S, \tag{2.5}$$

where $\boldsymbol{Q}(t)$ is a time-dependent rotation matrix that transforms vectors from the body-fixed frame to the reference frame and $\bar{\boldsymbol{x}}_S$ is the surface points position in the body-fixed frame. For the remainder, we assume that the origin of the body-fixed frame coincides with the swimmer's center of mass.

As $\bar{\boldsymbol{v}}_S$ characterizes the active surface deformation of the swimmer's body within the body-fixed frame, it is commonly referred to as the swimming gait. To model a cyclic gait characterized by a repetitive locomotion pattern, $\bar{\boldsymbol{v}}_S$ must be a time-periodic function. In forward modeling, our goal is to determine the linear velocity $\boldsymbol{U}$ and angular velocity $\boldsymbol{\Omega}$ of the swimmer's center of mass for a given gait $\bar{\boldsymbol{v}}_S$. To achieve this, we must solve the equations of motion for of a deformable body, expressed as

$$M \frac{d}{dt} \boldsymbol{U}(t) = \boldsymbol{F}(t), \quad \frac{d}{dt} \left[\boldsymbol{I}(t) \cdot \boldsymbol{\Omega}(t) \right] = \boldsymbol{L}(t). \tag{2.6}$$

Here, M is the swimmer's mass, which we assume to be constant, and $\boldsymbol{F}$ and $\boldsymbol{L}$ are the net force and net torque acting onto the swimmer's body. The instantaneous inertia tensor $\boldsymbol{I}$ of the swimmer's body is defined as

$$\boldsymbol{I} = \int_{V(t)} \varrho \left[(\bar{\boldsymbol{x}} \cdot \bar{\boldsymbol{x}}) \, \boldsymbol{1} - \bar{\boldsymbol{x}} \otimes \bar{\boldsymbol{x}} \right] dV, \tag{2.7}$$

where $\varrho(\bar{\boldsymbol{x}}(t; \boldsymbol{X}))$ is the body's mass density associated with the material point $\boldsymbol{X}$ at position $\bar{\boldsymbol{x}}$. In the absence of other external forces and torques, $\boldsymbol{F}$ and $\boldsymbol{L}$ are fully determined by the hydrodynamic stress the fluid exerts onto the swimmer's body surface. To obtain $\boldsymbol{F}$ and $\boldsymbol{L}$, we integrate the fluid stress tensor over the body surface

$$\boldsymbol{F} = \int_{S(t)} \boldsymbol{\sigma} \cdot \boldsymbol{n} \, dS, \quad \boldsymbol{L} = \int_{S(t)} \bar{\boldsymbol{x}} \times (\boldsymbol{\sigma} \cdot \boldsymbol{n}) \, dS, \tag{2.8}$$

where $\boldsymbol{n}$ denotes the unit surface normal of the swimmer's current surface $S(t)$, oriented to point into the fluid. Hence, $\boldsymbol{\sigma} \cdot \boldsymbol{n}$ represents the local stress vector that acts on the swimmer's body surface that is normal to $\boldsymbol{n}$.

Note that the swimmer's equations of motion Eq. (2.6), and the Navier-Stokes equation Eq. (2.1) are fully coupled, as $\boldsymbol{U}$ and $\boldsymbol{\Omega}$ appear in the nonslip boundary condition Eq. (2.5) of the flow problem, and $\boldsymbol{\sigma}$ is required to determine the net force and torque in Eq. (2.6). This coupling makes the swimming problem very difficult to solve. Luckily, for very small organisms, such as microswimmers, the problem can be greatly simplified by approximating the Navier-Stokes equations by the Stokes equations, as we will discuss in the following.

2.2 Low Reynolds Numbers Dynamics

Microswimmers generate fluid flows characterized by low Reynolds numbers, which has significant consequences for their swimming kinematics. The Reynolds number is a dimensionless quantity that compares the relative importance of inertial to viscous forces in a fluid flow. For illustration, consider a generic swimmer with gait frequency f, characteristic length L_0, and swimming speed U. To determine the swimmer's flow regime, we choose f^{-1} as the characteristic time scale, L_0 as the characteristic length scale, and U as the characteristic velocity scale of the flow field and derive a nondimensional form of the Navier Stokes equation Eq. (2.8) given by

$$\mathrm{Re}_f \frac{\partial \boldsymbol{u}^*}{\partial t^*} + \mathrm{Re}\left(\boldsymbol{u}^* \cdot \nabla^*\right) \boldsymbol{u}^* = -\nabla^* p^* + \nabla^{*2} \boldsymbol{u}^*, \tag{2.9}$$

where we defined the dimensionless time $t^* = tf$, fluid velocity $\boldsymbol{u}^* = u/U$, gradient $\nabla^* = \nabla/L_0$, and pressure field $p^* = L_0\, p/\mu\, U$. The dimensionless parameters Re and Re_f are referred to as the steady and the oscillatory Reynolds number, respectively, and are defined as [16, 83]

$$\mathrm{Re} = \frac{\rho L_0 U}{\mu}, \quad \mathrm{Re}_f = \frac{\rho L_0^2 f}{\mu}. \tag{2.10}$$

The steady Reynolds number Re is proportional to U, the velocity scale of the fluid flow generated by the swimmer's steady swimming motion, whereas Re_f is proportional to $L_0\, f$, the velocity scale of the fluid flow generated by the oscillatory motion of its body shape.

The swimming speed of microswimmers is typically of the order of one body length per gait period or smaller [83]. Consequently, we establish the upper bound $U \sim f L_0$ from which follows that $\mathrm{Re} \sim \mathrm{Re}_f$. However, we note that Re and Re_f are not always equivalent. For example, an insect that hovers on the spot would have a small Re but a large Re_f due to the high-frequency flapping of its wings. As an example, we consider the nematode *C. elegans*, which has a length of approximately $L_0 = 1\,\mathrm{mm}$, undulation frequency of the order of $f = 1\,\mathrm{Hz}$ and swimming speed $U < L_0 f$. In water which has a viscosity of $\mu = 10^{-3}\,\mathrm{Pa\,s}$ and density of $\rho = 10^3\,\mathrm{kgm}^3$ under standard temperature and pressure, this yields a Reynolds number $\mathrm{Re} < 1.0$. This is just below the limit for which hydrodynamic forces and torques are approximately proportional to velocity [11, 22]. Consequently, in water, *C. elegans* are at the limit of what would be considered low Reynolds number locomotion. However, in fluids more viscous than water, Re decreases and the assumption becomes increasingly accurate.

In low Reynolds flow characterized by $(\mathrm{Re}, \mathrm{Re}_f) \ll 1$, the inertia terms on the left-hand side of the dimensionless Navier-Stokes equation Eq. (2.9) can be neglected. Under these conditions, the Navier-Stokes equation can be approximated by the incompressible Stokes equation, defined as

$$0 = -\nabla p + \nabla^2 \boldsymbol{u}, \quad \nabla \cdot \boldsymbol{u} = 0. \tag{2.11}$$

The Stokes equation has many important mathematical properties. Firstly, it is linear, i.e. solutions to the Stokes equation can be superimposed to create new solutions. However, this does not guarantee that the new solution fulfills the boundary conditions of the original solutions. Nonetheless, solutions that impose linear boundary conditions on a shared boundary can be superimposed to create a solution that fulfills the linear superposition of the individual boundary conditions. Moreover, it can be demonstrated that solutions to the Stokes equation that prescribe velocity boundary conditions are unique [77]. In other words, if a solution to a specific boundary problem is found through any method, then it is the only unique solution to that particular problem.

The fact that microswimmers swim at low Reynolds numbers has many implications for their swimming kinematics. From the swimmer's linear equation of motion Eq. (2.6), the following scaling relation can be derived

$$\frac{MU}{\tau} \sim \mu U L_0, \tag{2.12}$$

where we defined τ as the swimmer's characteristic response time to hydrodynamic stresses (see Appendix A.1.1 for details). To compare τ to relevant locomotion time scales, such as the gait (deformation) time scale $T = 1/f$ and the swimming time scale $\tau_\mathrm{s} = U/L_0$ (the time required for the swimmer to move a distance equal to its own length), we calculate the timescale ratios

$$\frac{\tau}{\tau_\mathrm{s}} = \frac{\rho_\mathrm{s}}{\rho}\mathrm{Re}, \quad \frac{\tau}{T} = \frac{\rho_\mathrm{s}}{\rho}\mathrm{Re}_f. \tag{2.13}$$

Here, ρ_s is the mass density of the swimmer's body, which is typically of the same order as the density of water. Consequently, if $(\mathrm{Re}, \ \mathrm{Re}_f) \ll 1$, then the swimmer's response time to hydrodynamic stresses is much faster compared to its deformation rate or swimming time scale. As a result, the swimmer's body responds effectively instantaneously to variations in hydrodynamic stresses, which means that the swimmer's equations of motion Eq. (2.6) can be approximated as quasi-steady

$$\boldsymbol{F}(t) = 0, \quad \boldsymbol{L}(t) = 0. \tag{2.14}$$

This implies that the hydrodynamic net force and torque that act on the swimmer's body are zero at all times, which is commonly referred to as force and torque-free swimming. Note this does not mean that the swimmer is not moving; instead, it means that the thrust that the swimmer generates by actively deforming its body balances the drag created by the translation and rotation of its body. At large Reynolds numbers, thrust and drag can not be decoupled because the Navier-Stokes equation is not linear. The Stokes equation, however, is linear, i.e. each term in the noslip boundary condition defined by Eq. (2.5) may be tackled separately. Thus, we split the boundary condition into two terms

$$\boldsymbol{u} = \boldsymbol{Q} \cdot \bar{\boldsymbol{v}}_{\mathrm{S}}, \quad \boldsymbol{u} = \boldsymbol{U} + \boldsymbol{\Omega} \times \bar{\boldsymbol{x}}_{\mathrm{S}} \tag{2.15}$$

describing two distinct scenarios.

In the first scenario, the swimmer is fixed at the spot actively deforming its body, resulting in the surface velocity $\bar{\boldsymbol{v}}_{\mathrm{S}}$. Since it is not allowed to swim, the surface deformation generates a flow that will exert a net force and torque on its body, denoted as the thrust force $\boldsymbol{F}_{\mathrm{Th}}$ and the thrust torque $\boldsymbol{L}_{\mathrm{Th}}$. Both can be, in principle, determined by solving the surface integrals in Eq. (2.8), which requires us to solve the Stokes flow around to determine the hydrodynamic stress tensor $\boldsymbol{\sigma}$ at swimmer's body surface. This can only be done analytically for very simple body shapes and gaits, i.e. numerical methods are required in most practical cases.

In the second scenario, the swimmer's instantaneous shape is frozen. Hence, it can be described as a rigid body that translates and rotates with $\boldsymbol{U}$ and $\boldsymbol{\Omega}$, respectively. This rigid body motion creates a flow that exerts the hydrodynamic drag force $\boldsymbol{F}_{\mathrm{D}}$ and drag torque $\boldsymbol{L}_{\mathrm{D}}$ on the swimmer's body. Since the Stokes equation is linear, drag and swimming kinematics must be related linearly

$$\begin{pmatrix} \boldsymbol{F}_{\mathrm{D}} \\ \boldsymbol{L}_{\mathrm{D}} \end{pmatrix} = -\boldsymbol{R} \begin{pmatrix} \boldsymbol{U} \\ \boldsymbol{\Omega} \end{pmatrix}, \tag{2.16}$$

where $\boldsymbol{R}$ is commonly referred to as the instantaneous resistance matrix. It depends on the instantaneous body shape of the swimmer and can only be solved analytically for very simple body shapes [63].

During swimming, we expect the drag and thrust balance, which implies that

$$\boldsymbol{F}_{\mathrm{TH}} + \boldsymbol{F}_{\mathrm{D}} = 0, \quad \boldsymbol{L}_{\mathrm{TH}} + \boldsymbol{L}_{\mathrm{D}} = 0. \tag{2.17}$$

It can be shown that the resistance matrix is symmetric and positive definite [63], i.e. it can be inverted, and Eq. (2.17) can, therefore, be written as

$$\begin{pmatrix} \boldsymbol{U} \\ \boldsymbol{\Omega} \end{pmatrix} = \boldsymbol{R}^{-1} \begin{pmatrix} \boldsymbol{F}_{\mathrm{Th}} \\ \boldsymbol{L}_{\mathrm{Th}} \end{pmatrix} \tag{2.18}$$

Thus, to predict the swimmer's kinematics $\boldsymbol{U}$ and $\boldsymbol{\Omega}$ for a prescribed swimming gait $\bar{\boldsymbol{v}}_{\mathrm{S}}$ involves the following steps: First, determine the resistance matrix $\boldsymbol{R}$ from the swimmer's instantaneous body shape. Second, solve the Stokes flow generated by the swimmer's surface velocity to determine the thrust $\boldsymbol{F}_{\mathrm{TH}}$ and $\boldsymbol{L}_{\mathrm{Th}}$. For nontrivial body shapes and gaits, this can only be done numerically. However, in the case of slender bodies whose breadth is much smaller than their length, it is possible to approximate the local fluid drag independently for each body segment. This approach is referred to as resistive-force theory [17, 38, 55, 60] and will be discussed in the next section.

2.3 Resistice-Force Theory

Resistive-force theory (RFT) characterizes the fluid drag force on a slender body undergoing active deformation in Stokes flow. RFT was first employed in the pioneering work by Gray & Hancock [55, 60] in the 1950s, who explained the basis for the hydrodynamic propulsion mechanism of sea urchin sperm during undulatory locomotion. Their study demonstrated that the sperm's undulating flagellum produces a thrust that balances the drag force onto the cell body, enabling steady forward motion. The analytic expression derived for the sperm's swimming speed showed good agreement with experimental observations, demonstrating the validity of RFT.

Batchelor [17] and Cox [38] attempted a rigorous derivation of RFT using flow singularities (Stokeslet) to approximate the Stokes flow around a deforming slender body representing the flagellum of single cellular microswimmers. The approach by Batchelor and Cox can be used to show that in the limit of slender and weakly bent bodies, RFT serves as a good approximation for the local hydrodynamic forces acting on the swimmer's body [83]. Weakly bent implies that the amplitude of the swimmer's body wave is much smaller than the length of its body, a justified assumption for the undulatory locomotion of *C. elegans* [18, 45, 126].

To motivate the use of RFT in the context of undulating microswimmers, consider a slender swimmer whose body is composed of small cylindrical body segments of constant radius and length Δl, as shown in Fig. 2.2. Each segment is characterized by its centreline position $\boldsymbol{r}(s)$ and its linear and angular velocity $\boldsymbol{u}(s)$ and $\boldsymbol{\omega}(s)$, where s is the arc-length parameter. To simplify, we treat each body segment as an isolated rigid cylinder, i.e. the drag force and torque acting segment can calculated from Eq. (2.16). Due to the rotational symmetry of the cylinder, it follows that

$$\boldsymbol{F}_{\mathrm{D}} = -\mu\Delta l\left[c_{||}\boldsymbol{u}_{||} + lc_{\perp}\boldsymbol{u}_{\perp}\right] \tag{2.19}$$

$$\boldsymbol{L}_{\mathrm{D}} = -\mu\Delta l\left[\gamma_{||}\boldsymbol{\omega}_{||} + l\gamma_{\perp}\boldsymbol{\omega}_{\perp}\right] \tag{2.20}$$

where $\boldsymbol{u}_{||}$ and $\boldsymbol{\omega}_{||}$ is the cylinder's linear and angular velocity in the longitudinal and $\boldsymbol{u}_{\perp}$ and $\boldsymbol{\omega}_{\perp}$ in the transversal direction. If we assume that the cylinder's longitudinal body axis is aligned with the centreline's tangent defined as $\boldsymbol{t} = \partial_s \boldsymbol{r}$, then it follows that

$$\boldsymbol{u}_{||} = \boldsymbol{t}\otimes\boldsymbol{t}\cdot\boldsymbol{u}, \quad \boldsymbol{u}_{\perp} = (\mathbf{1} - \boldsymbol{t}\otimes\boldsymbol{t})\cdot\boldsymbol{u}, \tag{2.21}$$

$$\boldsymbol{\omega}_{||} = \boldsymbol{t}\otimes\boldsymbol{t}\cdot\boldsymbol{\omega}, \quad \boldsymbol{\omega}_{\perp} = (\mathbf{1} - \boldsymbol{t}\otimes\boldsymbol{t})\cdot\boldsymbol{\omega}. \tag{2.22}$$

Hence, Eq. (2.19) can be written as

$$\boldsymbol{F}_{\mathrm{D}} = -\mu\Delta l\left[c_{||}\boldsymbol{t}\otimes\boldsymbol{t} + c_{\perp}\,(\mathbf{1} - \boldsymbol{t}\otimes\boldsymbol{t})\right]\cdot\boldsymbol{u} \tag{2.23}$$

$$\boldsymbol{L}_{\mathrm{D}} = -\mu\Delta l\left[\gamma_{||}\boldsymbol{t}\otimes\boldsymbol{t} + l\gamma_{\perp}\,(\mathbf{1} - \boldsymbol{t}\otimes\boldsymbol{t})\right]\cdot\boldsymbol{\omega} \tag{2.24}$$

Taking the limit $\Delta l \to 0$, we derive the drag force line distribution $\boldsymbol{f}_{\mathrm{D}} \approx \boldsymbol{F}_D/\Delta_l$ and torque line distribution $\boldsymbol{l}_{\mathrm{D}} \approx \boldsymbol{L}_{\mathrm{D}}/\Delta l$ experienced by a infinitesimally short cylindrical body segment

$$\boldsymbol{f}_{\mathrm{D}} = -\mu\left[c_{||}\boldsymbol{t}\otimes\boldsymbol{t} + c_{\perp}\,(\mathbf{1} - \boldsymbol{t}\otimes\boldsymbol{t})\right]\cdot\boldsymbol{u}, \tag{2.25}$$

$$\boldsymbol{l}_{\mathrm{D}} = -\mu\left[\gamma_{||}\boldsymbol{t}\otimes\boldsymbol{t} + l\gamma_{\perp}\,(\mathbf{1} - \boldsymbol{t}\otimes\boldsymbol{t})\right]\cdot\boldsymbol{\omega}. \tag{2.26}$$

We conclude that the drag force and torque experienced by an infinitesimally cylindrical body segment are proportional to its linear and angular velocity, respectively. The proportionality factors are referred to as drag coefficients. We distinguish for different coefficients:

1. Linear longitudinal drag coefficient $c_{||}$: This coefficient determines the drag force experienced by the body segment when it moves longitudinally

2. Linear transverse drag coefficient $c_{\perp}$: This coefficient determines the drag force experienced by the body segment when it moves transversely (laterally)

3. Angular longitudinal drag coefficient $\gamma_{||}$: This coefficient determines the drag torque experienced by the body segment when it rotates around its longitudinal axis.

4. Angular transverse drag coefficient $\gamma_\perp$: This coefficient determines the drag torque experienced by the body segment when it rotates around its transverse axis

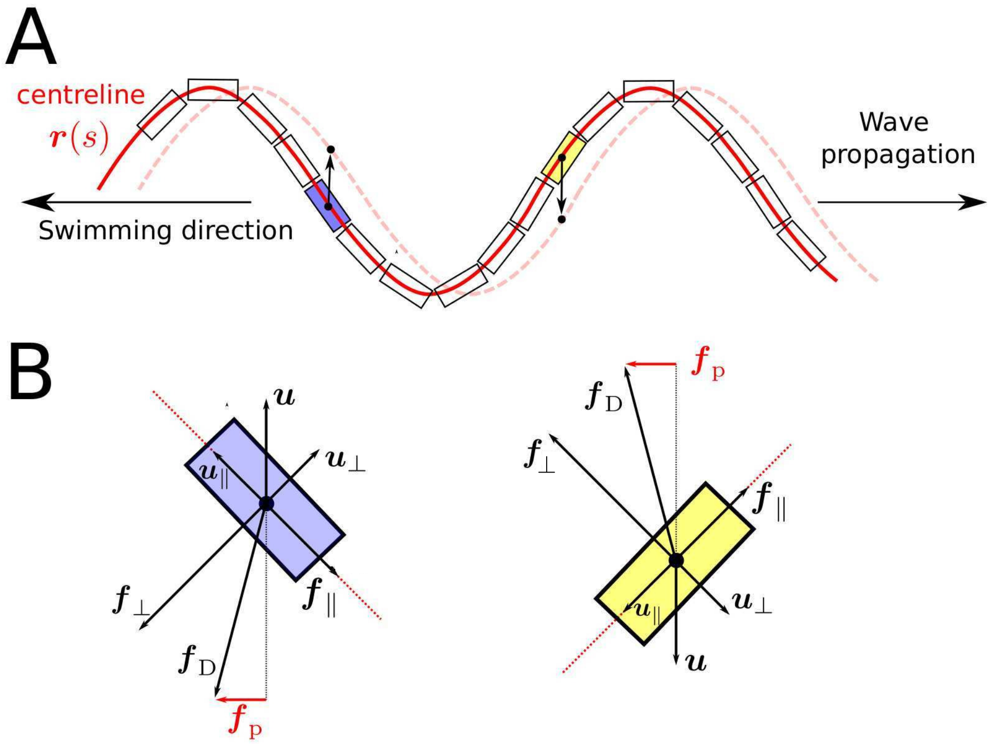

Figure 2.2: Schematic representation of propulsion mechanism in undulating microswimmers. (**A**): The swimmer's body is depicted by a series of cylindrical body segments centered on the centreline (red). Wave propagation to the left induces swimming in the opposite direction. (**B**): Illustration of the velocity $\boldsymbol{u}$, resulting drag force $\boldsymbol{f}_\mathrm{D}$, and propulsion force $\boldsymbol{f}_\mathrm{p}$ (red) for the two exemplary cylindrical body segments (blue and yellow) highlighted in panel A. Both $\boldsymbol{u}$ and $\boldsymbol{f}_\mathrm{D}$ can be decomposed into longitudinal $||$ and transversal $\perp$ (lateral) components defined as $\boldsymbol{u}_\mathrm{D} = \boldsymbol{u}_{||} + \boldsymbol{u}_\perp$ and $\boldsymbol{f}_\mathrm{D} = \boldsymbol{f}_{||} + \boldsymbol{f}_\perp$.

Various estimates for the drag coefficients exist. Garg & Kumar [51] employed the boundary integral method [142] to expand the solution of the Stokes flow around a tapered Cosserat rod in orders of the rod's slenderness parameter $\varepsilon = R_\mathrm{max}/L_0$, where R_max is the rod's maximum cross-sectional radius, and L_0 is its natural length in the stress-free configuration. A formal definition of a Cosserat will be provided in Chapter 3, where we discuss our model formulation in detail. Given that we will use a Cosserat rod to represent the swimmer's body, we use the results from Garg & Kumar to derive the following expressions for the linear and angular drag coefficients:

$$c_{\|} = \frac{2\pi}{\ln(1/\varepsilon) - \frac{1}{2}}, \quad c_{\perp} = \frac{4\pi}{\ln(1/\varepsilon) + \frac{1}{2}}, \quad \gamma_{\|} = \pi\varphi^2 R_{\max}^2, \quad \gamma_{\perp} = 4\pi\varphi^2 R_{\max}^2. \tag{2.27}$$

Here, $\varphi(s) \leq 1$ is the radius shape function, which determines the cross-sectional radius $R(s) = \varphi(s)R_{\max}$ along the rod's length. Note that the linear drag coefficients $c_{\|}$ and $c_{\perp}$ were derived for the specific case of a Cosserat rod with a prolate spheroidal shape. In the case of *C. elegans*, whose body is thickest at the center and tapers towards the ends, a prolate spheroidal shape serves as a sufficiently accurate representation. This is supported by the fact that local changes of the cross-sectional radius only contribute logarithmically to the drag coefficients [51]. Additionally, the expressions for the drag coefficients are applicable only if the Cosserat rod does not undergo large shear deformations, which is a valid assumption in the context of the undulatory locomotion of slender microswimmers, as we will discuss in Chapter 3.

We define the linear and angular drag coefficient ratios K_c and K_γ as

$$K_c = \frac{c_{\perp}}{c_{\|}}, \quad K_\gamma = \frac{\gamma_{\perp}}{\gamma_{\|}}. \tag{2.28}$$

From Eq. (2.27), it follows that in the limit of slender bodies $\epsilon \ll 1$, the linear drag coefficient ratio is of the order $K_c \sim 2$, whereas $K_\gamma = 4$ independent of ε. Consequently, body segments exhibit a stronger drag force when moving in the lateral compared to the longitudinal direction. Microswimmers exploit this drag anisotropy of the propulsion appendages or bodies to generate propulsion. To illustrate, Fig. 2.2 shows how the waving motion of a slender swimmer generates propulsion forces opposite to the propagation direction of the body wave. This shows that microswimmers actuate their body so that the propulsive forces generated along the body add constructively and align with the swimming direction.

However, while RFT is sufficient to explain the basic mechanism of how microswimmers generate propulsion, it neglects the long-range hydrodynamic interactions between the swimmer's individual body segments, which results in an inaccurate description in many scenarios. For example, it has been shown that the RFT by Lighthill [87] and Gray & Hancock [55, 60] inadequately capture the hydrodynamic forces generated by the rotation of the helical flagella of prokaryotic single cellular microswimmers such as bacteria [73, 115]. Other studies have attempted to address this limitation by calibrating the drag coefficients predicted by RFT to match experimental observations [46] or the solution obtained by numerically solving the Stokes equation [143]. Nevertheless, the need for calibration underscores the inaccuracy of RFT outside the calibration range.

For the case of undulating microswimmers, the main focus of this work, Rorai *et al.*

[116] compared the accuracy of RFT against benchmark solutions obtained using regularized Stokeslet [36] and solving the Stokes equations with a standard finite element method. Focusing on the undulatory locomotion of sperm, [116] showed that RFT performs reasonably well for waveforms closely resembling experimental observations, with predicted swimming speeds exhibiting a 5-15% error compared to the benchmark solutions. However, RFT becomes unreliable in the case of waveforms with short wavelengths of about 1/4 and 1/2 of the total flagellum length consistent with the results for helical flagella [73, 97, 115]. Furthermore, [116] showed that the hydrodynamic interactions between the sperm's head and flagellum are important for an accurate description of the fluid dynamics, as they introduce a front-rear symmetry breaking of the flow around the ellipsoidal head due to the presence of the flagellum. RFT neglects those interactions as it assumes that the hydrodynamics of the sperm's head and flagellum can be treated separately. Additionally, sperm's flagella typically exhibit an asymmetric waveform with a larger amplitude in the flagellum's tail compared to the anterior part close to the cell body. This asymmetry arises because the base of the flagellum, which connects to the cell body, acts as a fixed point while the rest of the flagellum undergoes active bending. The asymmetric waveform of the sperm's flagellum results in an asymmetric flow profile along the length of the flagellum. Consequently, the relationship between the drag force and the velocity of each segment along the flagellum will depend on its location relative to the cell body. RFT does not capture this asymmetry as it assumes the relationship between the drag force and velocity to be identical for all segments along the flagellum.

Unlike sperms, which possess a head and a tail, *C. elegans* feature a slender body with an approximate front-back symmetry, as will be illustrated in Section 2.4. Moreover, in contrast to the asymmetric waveform of sperm, *C. elegans* waveform during undulatory locomotion has an approximately constant amplitude only showing a small linear decrease from head to tail [18, 22, 45, 106]. Due to this symmetry in body shape and waveform, we expect RFT, which treats all body segments as identical, to provide a more accurate description of the fluid dynamics of *C. elegans* compared to sperm. However, we acknowledge that a rigorous comparison with more sophisticated solution methods, as presented in [116], is required to quantify the accuracy of RFT in the context of the undulatory locomotion of *C. elegans*. However, this task exceeds the scope of the present thesis. Nevertheless, we are confident that the qualitative results presented in this thesis remain robust with respect to the details of the fluid dynamics model, as will be discussed in more detail in Chapter 5 and 6.

We emphasize that for now, we have treated the swimmer as a purely geometric object whose body shape and surface velocity are prescribed and known at all times. However, we have not addressed the question of how the swimmer actively changes its body shape. Many biological swimmers use muscles and molecular motors to generate internal contractile forces to deform their shape in a synchronized manner [1, 19, 83]. Thus, modeling the active deformation necessitates a biomechanical model of the swimmer's body. Since microswimmers such as bacteria, sperm, and *C. elegans* are characterized by long, slender, and round propulsion appendages (flagella) or bodies, it is common practice to model their bodies as deformable rods [45, 52, 111, 112, 125]. In such a framework, the local hydrodynamic stresses acting on the swimmer's body must balance both the local actuation force and torque generated by its internal actuation mechanism, as well as the internal stresses that arise due to the elastic and viscous properties of the material constituting the rod [9]. In this thesis, we employ a Cosserat rod to represent a generic limbless slender microswimmer. However, before we do so, we provide a brief introduction to the model organism *C. elegans*, which will serve as a practical application to test our proposed model in Chapter 6.

2.4 *C. elegans* as a Model Organism

C. elegans, a microscopic nematode, is one of the most prominent model organisms in biology. It has been subject to intense study in genetics, cell biology, developmental biology, neuroscience, biomechanics, behavioral biology, and drug discovery. Originally chosen by Sydney Brenner as a model for whole-organism study [26] in the 1960s, by now *C. elegans* has become one of the most extensively characterized animals on Earth [5].

Despite its simple size and rather simple anatomy, *C. elegans* displays diverse locomotion patterns in both 2D and 3D. These include forward and backward undulation [39, 56], a variety of turn maneuvers that enable steering [27, 106, 134], roll maneuvers to re-orientated in 3D [20], and coiling behavior whose purpose remains unclear [70, 105].

Contrary to other singular cell microswimmers such as sperm, bacteria, and Euglena, *C. elegans* stand apart as a fully-fledged animal with a neuromuscular, digestive, and mating system [5]. This makes them an ideal model organism for behavioral biology, as they display a rich repertoire of behaviors, including mating and egg laying [34, 137], avoidance and escape [74], and exploration strategies that combine locomotion gaits and complex maneuvers [70]. Furthermore, several studies have shown that *C. elegans* exhibit a range of sensitivities to external stimuli, helping them to navigate toward food and away from danger. Those sensitivities are enabled by olfaction and thermosensation receptors in the anterior body region [99, 107], which allow the worm to move along thermal gradients [65] and chemical gradients [15], as well as oxygen gradients [31].

In a biomechanical context, *C. elegans* provide an ideal model organism to study how the interplay between neural circuitry, muscles, proprioceptive motor feedback, material body properties, and the environment collectively generates the various locomotion patterns and behaviors detailed earlier [42, 45, 101, 102, 111, 126]. As this thesis exclusively focuses on planar undulatory locomotion, we discuss *C. elegans* undulation gait in more detail in the following after giving a brief introduction of its anatomy. After that, we conclude this section by providing an overview of the biomechanical models used to study *C. elegans*.

2.4.1 Anatomy

C. elegans is a species of nematode (roundworm), characterized by its slender, non-segmented cylindrical body that tapers towards the head and tail. In adulthood, the worm reaches a length of 1-1.2 mm, with a maximum cross-sectional radius of 35 µm [13]. Similar to other nematodes, its body is divided into an outer and inner tube separated by the pseudocelemic space, as shown in Fig. 2.3. The outer tube (body wall) consists of a cuticle, hypodermis, and neuromuscular system, while the inner tube contains the digestive and reproductive systems [5].

The cuticle, a 0.5 µm thick shell, surrounds the worm on the outside. Mainly composed of collagen, a protein that forms a strong, fibrous, and flexible structure, the cuticle serves as a physical barrier that shields the worm from its external environment, preserves its body shape, and facilitates movement by acting as a deformable viscoelastic exoskeleton. The inner surface of the cuticle is covered by the hypodermis, a layer of cells responsible for its secretion and structural integrity. Within the hypodermis lie four major openings to the exterior, the anus, vulva (genitalia), and pharynx (‘mouth‘) [89].

Beneath the hypodermis, 95 rhomboid-shaped, striated body wall muscles are organized in pairs along the dorsal-ventral sides of the body. These muscles align in rows that run parallel to the longitudinal body axis alongside the dorsal and ventral nerve cords, respectively, resulting in the following distribution across four quadrants: dorsal left (24), dorsal right (24), ventral left (24), and ventral right (23). Muscles are tethered to the hypodermis across their entire surface area via specialized structures known as dense bodies and M-lines (analogs). When activated, the muscles contract along the longitudinal axis, generating contractile forces that bend the worm's body in either the dorsal or ventral direction [6]. The ability to bend locally gives *C. elegans* body a high degree of freedom, allowing for a large spectrum of body postures, which can be represented as a superposition of eigenworm postures in 2D [124] as well as 3D [70].

The muscles are activated by excitatory motor neurons, part of larger neural circuitry. The composition and connectivity of this circuitry have been extensively described in the seminar work by White *et al.* [138, 139]. Using electron micrography, the authors imaged progressive cross-sections of several hermaphrodite worms and demonstrated that their neural circuitry consists of 302 neurons interconnected through chemical synapses, gap

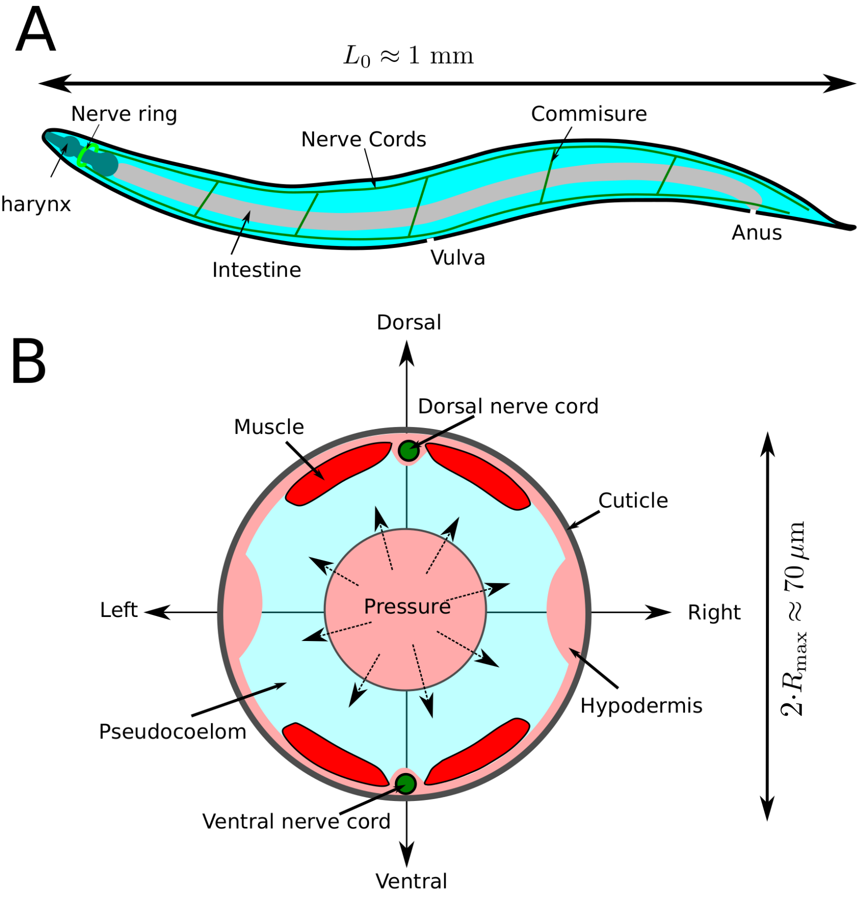

Figure 2.3: Schematic of *C. elegans* basic anatomy, adapted from Denham [41]. (**A**): Longitudinal section detailing the nervous and digestive system. (**B**): Lateral cross-section shows the body wall components, including the cuticle, hypodermis, muscles, and nerve cords, separated by the pseudocoelom from the pressurized inner tube containing the intestines.

junctions, and neuromuscular junctions. The neural circuitry can be separated into the pharyngeal nervous system, which contains 20 almost entirely isolated neurons that regulate the pumping of the pharynx ("mouth"), and the other 282 neurons of the somatic nervous system, which occupy the rest of the body [7, 138]. Within the somatic nervous system, a significant proportion of neurons are located in the nerve ring. They are part of an annulus structure of densely packed neural processes and soma surrounding the posterior section of the pharynx. Thus, the nerve ring is the closest thing that *C. elegans* has to a brain. Of all the 113 motor neurons, 75 are located within the ventral cord and innervate the body wall muscles on either side [7, 138, 139]. The ventral chord plays a key role in transmitting signals from the nerve ring ("brain") to the muscles.

2.4.2 Undulatory Locomotion

Nematodes such as *C. elegans* generate propulsion through transversal undulations. These undulations are typically defined by a sinusoidal body curvature [106] that propagates from one end of the worm's body to the other, which generates propulsion in the opposite direction to the propagation. The body curvature can be described as a traveling wave characterized by its amplitude, wavelength, and propagation speed. The latter can be expressed as the product of undulation frequency and wavelength. Together, these wave parameters are referred to as the undulation parameters.

To produce the curvature wave observed during forward and backward undulation, motor neurons along the ventral cord innervate dorsal and ventral body wall muscles alternating between the dorsal to ventral side along the body and in time [30, 64, 138]. Since the body wall muscles are arranged on the dorsal-ventral sides of the body, undulation primarily occurs in the dorsal-ventral body plane [32]. This can be confirmed by studying the behavior of worms on a flat surface, where they lie on their left or right side to undulate to be able to bend in the dorsal-ventral direction.

It has been shown that the details of *C. elegans*' undulatory locomotion are contingent on their environment. In water, *C. elegans* undulation gait is characterized by a fast frequency, long wavelength, and small curvature amplitude, resulting in a C-shape commonly referred to as the swimming gait. On agar surfaces, the frequency is lower, the wavelength is shorter, and the amplitude is higher, resulting in a W-shape commonly referred to as the crawling gait. The clear difference between waveform and frequency in these two media established the hypothesis that *C. elegans* employs two distinct gaits. However, more recently, Berri *et al.* [18] showed that *C. elegans* undulation parameters undergo a continuous transition with the viscosity of the medium. This led to the hypothesis that swimming and crawling gait are both generated by the modulation of a single undulation gait. This was confirmed in Newtonian fluids [45, 126] and non-Newtonian media [84], and the single gait hypothesis is now broadly accepted.

Two questions arise: Firstly, how do *C. elegans* modulate their undulation gait? This question has been addressed in multiple studies that used computational models, which included neurons, mechanosensory and proprioceptive feedback, muscles, body mechanics, and environmental stresses to reproduce the experimentally observed gait modulation [42]. Secondly, why do *C. elegans* modulate their undulation gait? This question will be addressed in Chapter 6, where we investigate whether gait modulation in *C. elegans* can be regarded optimal.

2.4.3 Computational Models

Over the past three decades, many computational biomechanical models of *C. elegans* have been developed. This discussion specifically focuses on two model types relevant to our work: mass-spring models and rod models.

So far, mass-spring models [23, 101, 102] have been limited to a 2D description of the worm's longitudinal section. Within this section, the body wall outline is modeled by a discrete set of mass points coupled with springs. At any time point, the worm's body shape is characterized by the positions of these mass points. The springs represent the forces generated by the viscoelastic properties of the cuticle, internal hydrostatic pressure, and contractile muscle forces. Drag forces from the surrounding environment have been modeled by resistive force theory and are assumed to be proportional to the mass-point's velocity. Spring models are difficult to generalize to 3D, as this would require the placement of spring-coupled mass points across the entire body surface, which made researchers explore alternative approaches.

Rod models [42, 45, 111, 126] represent the worm's body as a continuum of infinitesimal rigid cylindrical segments whose radius changes continuously along the body. The configuration of such a rod can be characterized by its centreline and the orientation of its circular cross-sections, as will be discussed in Chapter 3. Typically, the rod is assumed to be made of a homogeneous worm material, whose viscoelastic properties are characterized by constitutive laws that detail the rod's stress-strain relationship. The dorsal-ventral bending generated by contractile muscle forces is modeled as an effective actuation torque line distribution applied along the worm's body. Similar to mass-spring models, drag forces with the external medium have been modeled by resistive-force theory. However, since rods are a representation of a 3D body, the flow can be solved around them by, for example, using regularized Stokeslets [104]. The first computational model of *C. elegans* that integrated biomechanics, neuromuscular system, and interaction with the external environment was pioneered by Niebur and Erdös [101, 102] in the early 90s. Their mechanical representation featured coupled rectangular units of mass points connected by longitudinal springs on the dorsal-ventral sides to represent the elastic properties of the cuticle. Contractile muscle forces are controlled by the excitation status of the motor neurons and applied along the connection line of neighboring mass points. Internal hydrostatic pressure is calculated from the body volume, and pressure force acts perpendicular to the body wall. Drag forces to the external medium were modeled by resistive-force theory. A very large drag coefficient was chosen to represent an agar surface. The authors established a working example of a minimal neuron circuit that achieves sustained forward motion. The circuitry incorporated local proprioceptive feedback, where neurons are stimulated based on the body bend in their local vicinity. This challenged alternative notations, suggesting that upstream inter-neurons exert global control over muscle activation or that the body simply follows the groove that is carved into the agar surface by the undulatory movement of the head.

Building upon this work, Boyle *et al.* [23] developed a more detailed mass-spring model, incorporating 48 units to represent each of the muscle pairs situated at the dorsal-ventral sides of the body. In each unit, the worm's cross-sectional radius is fixed by lateral beams of fixed length, which connect opposite mass points on the dorsal and ventral sides. The length of these beams decreases towards the ends of the body to create a tapered body shape. The viscoelastic properties of the cuticle are represented by longitudinal parallel springs-damper systems connecting neighboring points on either side of the body. Contrary to Niebur and Erdös, the hydrostatic pressure is modeled by diagonal springs that connect neighboring mass points on opposite sites and is independent of the body volume. To mimic the tethering of the muscles to the cuticle, contractile muscle forces act on longitudinal spring-damper elements that represent the cuticle. Muscles are driven by repeated units of the core circuitry introduced by Niebur and Erdös [102]. The proprioceptive input to the motor neurons is modulated by the normalized difference between the rest and instantaneous length of the longitudinal elements that represent the local cuticle and muscle stretch. The passive mechanical parameters of the model were fitted by reproducing the relaxation experiments of Sauvage [118], who performed deformation relaxation experiments with anesthetized worms measuring timescales systematically varying the environment's viscosity.

Most relevant for our work, the model by Boyle *et al.* [23] was able to quantitatively reproduce the gait transition observed between agar and water without fitting any model parameters except for the drag coefficients, which account for the changing environmental conditions. However, it failed to produce coordinated locomotion for intermediate values of drag coefficients, indicating that further refinement is necessary. In general, the material properties of the spring models depend upon spring constants and damping coefficients. It is not a straightforward task to translate these spring parameters to measurable quantities, such as the bending rigidity and internal viscosity of the worm's body [13].

Conversely, rod models represent 3D deformable bodies, i.e. their model parameters can be directly compared to those obtained from experimental measures. Both Fang Yen [45] and Sznitman *et al.* [125, 126] used simple viscoelastic rod models to simulate the planar undulatory locomotion of *C. elegans*. These models did not include a neuromuscular system; instead, actuation is achieved by applying an actuation torque distribution along the body that mimics the torque generated by the contractile muscle forces. Fang Yen *et al.* [45] employed their rod model to reproduce the time scales obtained from deformation relaxation experiments with live worms in different fluid viscosities. This allowed them to estimate values for the bending rigidity and internal damping coefficient of the worm's body material, showing good agreement with direct experimental measures obtained by

Backholm *et al.* [13]. Fang Yen *et al.* then incorporated these measures in their rod model to simulate *C. elegans*' undulatory locomotion in Newtonian fluids with varying viscosity. Those simulations showed that *C. elegans* gait transition in more viscous environments coincides with a transition from a regime where internal friction dominates the worm's energy cost to a regime where external (fluid) friction takes precedence. This finding will become relevant in Chapter 6 when we analyze *C. elegans*' gait transition from the viewpoint of optimality.

Both Sznitman and Fang Yen employed a linearized rod equation assuming small body wave amplitudes. Yet, studies have shown that *C. elegans* exhibit significant curvature amplitudes and short wavelength during undulatory locomotion [106], leading to a considerable body wave amplitude. To address this limitation, Cohen & Ranner [33] developed a Kirchhoff rod model similar to that introduced by Guo & Mahadevan [58], which allows for an accurate description across the entire range of observed curvature amplitudes. Denham *et al.* [42] combined this Kirchhoff rod model with a model of the worm's neuromuscular system. The proprioceptive neuromechanical model was simplified relative to Boyle *et al.*'s [22] model, hence allowing more rigorous characterization, leading to two key results: first, a reinterpretation of *C. elegans* gait modulation in terms of the sperm number [43, 93], and second, a prediction that modulation of the control parameters in a fixed environment results in a distinct gait modulation compared to modulation of the mechanical or fluid parameters. The sperm number measures the relative strength between the hydrodynamic forces and the bending torque that is generated by the stiffness of the swimmer's body material. The sperm number appears as an important dimensionless parameter in our model equations and will be defined and discussed in more detail in Chapter 4.

So far, all discussed models were limited to planar locomotion. Thus, Ranner [111] extended his previous Kirchhoff rod model to facilitate 3D locomotion, allowing for bending in the left-right plane as well as twisting. This extension opens the avenue for studying the extensive dataset curated by Illet [70], which contains six hours of 3D reconstructed trajectories and body postures.

In this thesis, we employ a purely mechanical rod model, which extends the work by Ranner [111] and Wang *et al.* [136]. Contrary to the studies by Denham *et al.* [42] and Boyle *et al.* [22], our thesis does not address how *C. elegans* modulates its undulation gait, as this would require the inclusion of a neuromuscular model coupled proprioceptive feedback. Instead, our aim is to understand why microswimmers modulate their gait, viewing it through the lens of optimality. This necessitates estimating the worm's energy expenditure using our model, as we will discuss in the next chapter.

Chapter 3

Model Formulation

In this chapter, we develop a biomechanical model to describe the undulatory locomotion of a slender limbless microswimmer immersed in a Newtonian fluid environment. Readers not interested in the technical details of the model formulation are referred to Chapter 4, where we provide a brief nontechnical model description.

In our model, the swimmer's body is represented by a viscoelastic Cosserat rod. A rod is a mathematical model that describes the behavior of a slender flexible structure, conceptualized as a series of interconnected cross-sections along its length. Rods provide a one-dimensional spatial representation of a three-dimensional object, which makes them computationally very efficient. Our goal is to derive and implement the rod's equations of motion, integrating all relevant forces and torques acting on the swimmer's body. These encompass fluid drag, the internal resistance opposing body deformation, and actuation for driving undulatory locomotion.

With this goal in mind, the chapter is structured as follows: Section 3.1 provides a brief introduction to Cosserat rod theory, defining the rod's state and strain variables and deriving its equations of motion and introduces alongside all relevant energetic terms for estimating the swimmer's energy expenditure. In Section 3.2, we define the actuation torque for driving undulatory locomotion. Having established the model, Section 3.3 derives a dimensionless form of the rod's equations of motion and defines the key dimensionless variables that govern its dynamical behavior. Section 3.4 formulates the weak form of the dimensionless equations of motion and introduces a numerical scheme for solving them. We conclude this chapter by testing its numerical accuracy and stability in Section 3.5.

3.1 Cosserat Theory

The aim of this section is to formulate the equations of motion for an active Cosserat rod immersed in a low Reynolds number Newtonian fluid environment. For an excellent discussion of Cosserat rod theory, we refer to the seminal work by Simo [121], the classic book by Antman [9] and the more recent review by Chada *et al.* [29]. A Cosserat rod takes into account both translational and rotational degrees of freedom of its cross-sections, enabling local bending, twisting, shearing, and stretching. It is an extension of the inextensible, unshearable Kirchhoff rod, which only allows for local bending and twisting. To model planar undulatory locomotion, which primarily involves local bending, a Kirchhoff rod would be sufficient. However, Kirchhoff rods require the use of Lagrange multipliers to enforce inextensibility and unshearability [111]. Alternatively, the inextensibility and unshearability constraint of the Kirchhoff can be relaxed by postulating an energy penalty that maintains both conditions approximately [104]. Thus, although a Cosserat rod has more degrees of freedom, it is actually easier to implement from a numerical point of view.

The state of a Cosserat rod at time t is fully determined by its centreline coordinates $\boldsymbol{r}(s,t) \in \mathbb{R}^3$ and its Euler angles $\boldsymbol{\theta}(s,t) = (\alpha(s,t),\, \beta(s,t),\, \gamma(s,t))$ which are referred to as the rod's state variables. The reference arc-length parameter $s \in [0, L_0]$ determines the position along the rod's centreline, where $s = 0$ corresponds to the tip of the swimmer's head and $s = L_0$ to the end of its tail. Here, L_0 is the swimmer's length in its stress-free reference configuration. Derivatives with respect to s and t will be written as ∂_s and ∂_t, respectively. The centreline $\boldsymbol{r}$ aligns with the centroid of the rod's circular cross-sections along its length as illustrated in Fig. 3.1. Within each cross-section, we assume the mass to be distributed homogeneously, i.e. the cross-section's centroid is identical to its centre of mass. The Euler angles α, β, $\gamma \in [0, 2\pi]$ determine the orientation of the rod's cross-sections with respect to a fixed reference frame, as will be discussed in Section 3.1.1.

We distinguish between two reference frames depicted in Fig. 3.1:

1. The global lab frame with constant basis vectors $\boldsymbol{e}_i$ and vector representation $\boldsymbol{v} = v_1\boldsymbol{e}_1 + v_2\boldsymbol{e}_2 + v_3\boldsymbol{e}_3$
2. The local body frame with time and reference arc-length dependent basis vectors $\boldsymbol{d}_i(s,t)$ and vector representation $\boldsymbol{v} = \bar{v}_1\boldsymbol{d}_1 + \bar{v}_2\boldsymbol{d}_2 + \bar{v}_3\boldsymbol{d}_3$

The body frame vectors $\boldsymbol{d}_i(s,t)$, commonly referred to as directors, determine the orientation of the local cross-sections and can be expressed in terms of the Euler angles $\boldsymbol{\theta}$. Specifically, $\boldsymbol{d}_1$ and $\boldsymbol{d}_2$ align with the cross-section's lateral principal basis vectors while $\boldsymbol{d}_3$ is parallel to its unit normal. For biological swimmers, it is advantageous to align the in-plane body frame vectors $\boldsymbol{d}_1$ and $\boldsymbol{d}_2$ with their anatomy. For *C. elegans*, we choose $\boldsymbol{d}_1$ to be parallel to the left-right body axis, and $\boldsymbol{d}_2$ to be parallel to the dorsal-ventral axis.

The rod's equation of motion can be defined within the lab or the body frame. We opt for a formulation within the lab frame because it leads to more concise expressions. However, it is important to note that most of the rod's dynamical variables, such as the internal force and torque resultants, are defined in the body frame. Consequently, those variables must be transformed into the lab frame to arrive at a consistent formulation of the equations of motion. To achieve this transformation, we must establish a relationship between the lab frame and the local body frame, which will be derived in the next section.

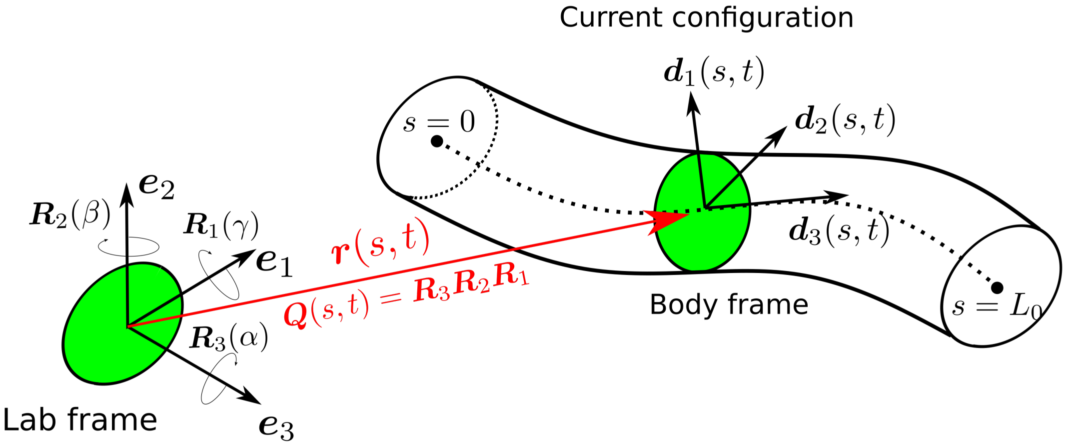

Figure 3.1: Schematic of a Cosserat rod in its current deformed configuration adapted from Arora *et al.* [10]. Centreline $\boldsymbol{r}(s,t)$ determines the position of the cross-section's centroid at body position s with respect to the reference frame. Rotation matrix $\boldsymbol{Q}(s,t) = R_3R_2R_1$ rotates the lab frame onto the local body frame of the cross-section.

3.1.1 Defining the Body Frame

For a given time t and body position s, we obtain the body frame from the Euler angles $\boldsymbol{\theta}(s) = (\alpha(s,t),\, \beta(s,t),\, \gamma(s,t))$ by performing three subsequent elementary extrinsic rotations. For a comprehensive description of this procedure, we refer to the classical textbook by Goldstein [54]. Each of the Euler angles $\alpha(s,t)$, $\beta(s,t)$ and $\gamma(s,t)$ defines a rotation $\boldsymbol{R}_i$ around one of the lab frame's coordinate axes $\boldsymbol{e}_i$, as depicted in Fig. 3.1. To reach any target frame, there exist twelve equally valid rotation sequences. However, for each of these sequences, the values of the Euler angles will be different. Here, we opt for a sequence that involves rotations around three distinct lab frame axes:

$$\boldsymbol{Q}(s,t) = \boldsymbol{R}_3(\alpha)\boldsymbol{R}_2(\beta)\boldsymbol{R}_1(\gamma). \tag{3.1}$$

For this specific sequence, the Euler angles α, β and γ are commonly referred to as the roll, pitch and yaw angles, respectively. The elementary rotations $\boldsymbol{R}_i$ are defined as:

$$\boldsymbol{R}_1(\gamma) = \begin{bmatrix} 1 & 0 & 0 \\ 0 & \cos\gamma & -\sin\gamma \\ 0 & \sin\gamma & \cos\gamma \end{bmatrix}, \boldsymbol{R}_2(\beta) = \begin{bmatrix} \cos\beta & 0 & \sin\beta \\ 0 & 1 & 0 \\ -\sin\beta & 0 & \cos\beta \end{bmatrix}, \boldsymbol{R}_3(\alpha) = \begin{bmatrix} \cos\alpha & -\sin\alpha & 0 \\ \sin\alpha & \cos\alpha & 0 \\ 0 & 0 & 1 \end{bmatrix}. \tag{3.2}$$

Substituting Eq. (3.2) into Eq. (3.1), we derive the following expression

$$\boldsymbol{Q} = \begin{bmatrix} c_\alpha c_\beta & c_\alpha s_\beta s_\gamma - c_\gamma s_\alpha & s_\alpha s_\gamma + c_\alpha c_\gamma s_\beta \\ c_\beta s_\alpha & c_\alpha c_\gamma + s_\alpha s_\beta s_\gamma & c_\gamma s_\alpha s_\beta - c_\alpha s_\gamma \\ -s_\beta & c_\beta s_\gamma & c_\beta c_\gamma \end{bmatrix}, \tag{3.3}$$

where we used the shorthand notation $c_x = \cos(x)$ and $s_x = \sin(x)$. The rotation matrix $\boldsymbol{Q}$ transforms the lab frame into the local body frame, which can be expressed as

$$\boldsymbol{d}_i = \boldsymbol{Q}^T \boldsymbol{e}_i, \quad \boldsymbol{e}_i = \boldsymbol{Q}\boldsymbol{d}_i, \quad i = 1,\, 2,\, 3, \tag{3.4}$$

where we used that $\boldsymbol{Q}$ is orthogonal, i.e. $\boldsymbol{Q}^T\boldsymbol{Q} = \boldsymbol{1}$. From Eq. (3.4) it follows that the columns of $\boldsymbol{Q}^T$ are the body frame vectors, i.e.

$$\boldsymbol{Q}^T = (\boldsymbol{d}_1,\, \boldsymbol{d}_2,\, \boldsymbol{d}_1). \tag{3.5}$$

The lab frame representation of any vector $\boldsymbol{v}$ can either be expressed in terms of lab or the body frame basis vectors, i.e.

$$\boldsymbol{v} = v_1\boldsymbol{e}_1 + v_2\boldsymbol{e}_2 + v_3\boldsymbol{e}_3 = \bar{v}_1\boldsymbol{d}_1 + \bar{v}_2\boldsymbol{d}_2 + \bar{v}_3\boldsymbol{d}_3. \tag{3.6}$$

For the remainder, we use the overbar to denote the components $\bar{v}_i$ of a vector $\boldsymbol{v}$ in the body frame. Multiplying Eq. (3.6) with $\boldsymbol{Q}$ from the left yields

$$\boldsymbol{Q}\boldsymbol{v} = \bar{v}_1\boldsymbol{e}_1 + \bar{v}_2\boldsymbol{e}_2 + \bar{v}_3\boldsymbol{e}_3 = \bar{\boldsymbol{v}}, \tag{3.7}$$

where we used Eq. (3.4) to transform the body frame vectors into the lab frame vectors. Thus, we find that one can transform between the lab frame and body frame representation of a vector via the equations:

$$\bar{\boldsymbol{v}} = \boldsymbol{Q}\boldsymbol{v}, \quad \boldsymbol{v} = \boldsymbol{Q}^T\bar{\boldsymbol{v}}. \tag{3.8}$$

To summarize, the Euler angles $\boldsymbol{\theta}(s)$ determine the orientation of the local body frame along the rod's centreline. To obtain the body frame at s, we calculate the rotation matrix $\boldsymbol{Q}$ from Eq. (3.3), which rotates the lab frame onto the local body frame.

3.1.2 Strain and Curvature Measures

This section introduces the rod's strain and curvature measures, which are crucial to describe its internal deformation dynamics. To capture the Cosserat rod's local deformation, we employ the strain vector $\boldsymbol{\sigma}(s,t)$ and the generalized curvature vector $\boldsymbol{\kappa}(s,t)$ [9, 121]. It is noteworthy that both $\boldsymbol{\kappa}$ and $\boldsymbol{\sigma}$ remain invariant with respect to rigid body transformations. In other words, if a rod undergoes a global translation and rotation, then the rod's strain vector $\boldsymbol{\sigma}$ and curvature vector $\boldsymbol{\kappa}$ do not change, as illustrated in Fig. 3.2A. Thus, together $\boldsymbol{\sigma}$ and $\boldsymbol{\kappa}$ determine the rod's shape.

In the lab frame, the strain vector $\boldsymbol{\sigma}$ is defined as:

$$\boldsymbol{\sigma} = \partial_s \boldsymbol{r} - \boldsymbol{d}_3. \tag{3.9}$$

Hence, it measures the local misalignment between the centreline's tangent vector $\partial_s \boldsymbol{r}$ and the cross-section's normal vector $\boldsymbol{d}_3$, as illustrated in Fig. 3.2B. To transform $\boldsymbol{\sigma}$ into the body frame, we multiply Eq. (3.9) with rotation matrix $\boldsymbol{Q}$ from the left, which yields:

$$\bar{\boldsymbol{\sigma}} = \boldsymbol{Q}\partial_s \boldsymbol{r} - \boldsymbol{e}_3. \tag{3.10}$$

The first two strain vector components $\bar{\sigma}_1$ and $\bar{\sigma}_2$ measure shear, i.e. the relative sliding of adjacent cross-sections with respect to the $\boldsymbol{d}_1$ and the $\boldsymbol{d}_2$ direction. The third component $\bar{\sigma}_3$ measures extensional strain, i.e. the stretching and contracting of the rod segments with respect to the cross-section's normal direction. Thus, if $\bar{\sigma}_3 > 0$ then the rod is locally stretched, whereas if $\bar{\sigma}_3 < 0$ then it is locally contracted. Notably, we use a slightly different definition for the extensional strain compared to the one initially proposed by Simo [121]; see Lang *et al.* [81] for a detailed discussion on the matter.

The generalized curvature vector $\boldsymbol{\kappa}(s,t)$ and the cross-section's angular velocity $\boldsymbol{\omega}(s,t)$ are defined in terms of Frenet-Serret type equations [9, 121]

$$\partial_s \boldsymbol{d}_i = \boldsymbol{\kappa} \times \boldsymbol{d}_i. \tag{3.11}$$

$$\partial_t \boldsymbol{d}_i = \boldsymbol{\omega} \times \boldsymbol{d}_i, \tag{3.12}$$

which govern the dynamics of the body frame. The generalized curvature vector $\boldsymbol{\kappa}$ specifies both the direction and the rate of the body frame's rotation as we move along the centreline

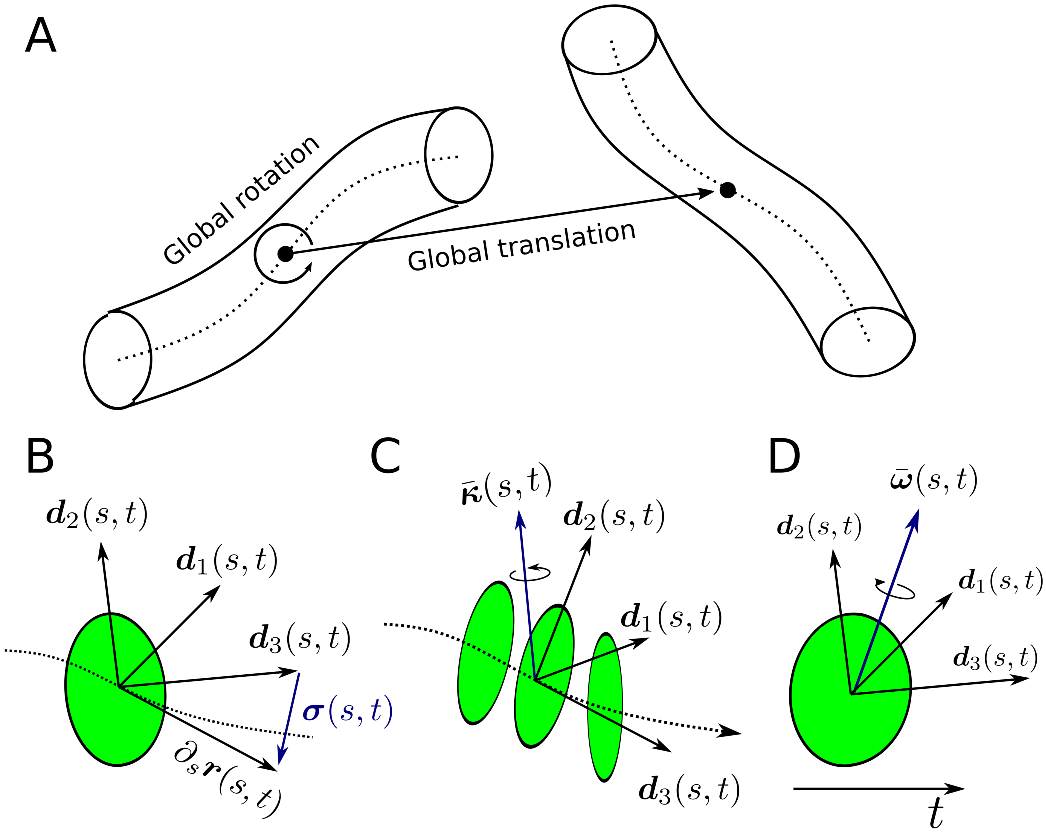

Figure 3.2: (**A**): Schematic depiction of a rigid body transformation, strain measures, and angular velocity of a Cosserat rod. (**B**): Illustration of the strain vector $\bar{\boldsymbol{\sigma}}$, which measures the misalignment between the cross-section normal $\boldsymbol{d}_3$ and the centreline's tangent $\partial_s \boldsymbol{r}$. (**C**): Illustration of the curvature vector $\bar{\boldsymbol{\kappa}}$, describing the rotation of the rod's cross-sections while moving along the rod's centreline. (**D**): Illustration of the angular velocity vector $\bar{\boldsymbol{\omega}}$, describing the rotation of a fixed cross-section over time.

at a fixed time t, as depicted in Fig. 3.2C. On the other hand, the angular velocity $\boldsymbol{\omega}$ specifies the direction and rate of the body frame's rotation with respect to time at a fixed position s, as illustrated in Fig. 3.2D.

Multiplying Eqs. (3.11) and (3.12) with the rotation matrix $\boldsymbol{Q}$ from the left yields

$$\boldsymbol{Q}\,\partial_s \boldsymbol{Q}^T \boldsymbol{e}_i = \bar{\boldsymbol{\kappa}} \times \boldsymbol{e}_i, \tag{3.13}$$

$$\boldsymbol{Q}\,\partial_t \boldsymbol{Q}^T \boldsymbol{e}_i = \bar{\boldsymbol{\omega}} \times \boldsymbol{e}_i, \tag{3.14}$$

where we used Eq. (3.4) to express the body frame vector $\boldsymbol{d}_i$ in terms of the lab frame vector $\boldsymbol{e}_i$, and Eq. (3.8) to transform $\boldsymbol{k}$ and $\boldsymbol{\omega}$ into the body frame. From Eqs. (3.13) and (3.14), we deduce the following relationship:

$$[\bar{\boldsymbol{\kappa}}]_\times = \boldsymbol{Q}\partial_s\boldsymbol{Q}^T, \tag{3.15}$$

$$[\bar{\boldsymbol{\omega}}]_\times = \boldsymbol{Q}\partial_t\boldsymbol{Q}^T. \tag{3.16}$$

Here, we introduced the notation $[\bar{\boldsymbol{\kappa}}]_\times$ and $[\bar{\boldsymbol{\omega}}]_\times$ to represent the skew-symmetric matrix associated with the vector cross products $\bar{\boldsymbol{\kappa}} \times \circ$ and $\bar{\boldsymbol{\omega}} \times \circ$, respectively. Substituting Eq. (3.3) for $\boldsymbol{Q}$ on the r.h.s. of Eqs. (3.15) and (3.16), and performing a cumbersome calculation, we arrive at the following concise expression for $\bar{\boldsymbol{\kappa}}$ and $\bar{\boldsymbol{\omega}}$:

$$\bar{\boldsymbol{\kappa}} = \boldsymbol{A}\,\partial_s\boldsymbol{\theta}, \tag{3.17}$$

$$\bar{\boldsymbol{\omega}} = \boldsymbol{A}\,\partial_t\boldsymbol{\theta}. \tag{3.18}$$

We find that $\bar{\boldsymbol{\kappa}}$ and $\bar{\boldsymbol{\omega}}$ are both linearly proportional to the derivative of the Euler angles $\boldsymbol{\theta}$ with respect to s and t, respectively. The matrix $\boldsymbol{A}$ depends on $\boldsymbol{\theta}$ and its functional form depends on the chosen rotation sequence. For the sequence defined by Eq. (3.1), matrix $\boldsymbol{A}$ takes the following form:

$$\boldsymbol{A}(\boldsymbol{\theta}) = \begin{bmatrix} 0 & \sin\alpha & -\cos\alpha\cdot\cos\beta \\ 0 & -\cos\alpha & -\sin\alpha\cdot\cos\beta \\ -1 & 0 & \sin\beta \end{bmatrix}. \tag{3.19}$$

A similar expression has been derived in Wang *et al.* [136] who used a slightly different rotation sequence.

In the body frame, the first two components $\bar{\kappa}_1$ and $\bar{\kappa}_2$ of the curvature vector determine the rotation rate around the in-plane body-frame vectors $\boldsymbol{d}_1$ and $\boldsymbol{d}_2$. Thus, they measure how the rod bends while we move along the centreline. The third component $\bar{\kappa}_3$ determines the rotation rate around the cross-section's normal vector $\boldsymbol{d}_3$, i.e. it measures twist.

To conclude, this section introduced two key vectors: the strain vector $\boldsymbol{\sigma}$ and the generalized curvature vector $\boldsymbol{\kappa}$. Together, they determine the rod's shape at any given time t. Specifically, the strain vector $\boldsymbol{\sigma}$ measures shear and extensions, while the generalized curvature vector $\boldsymbol{\kappa}$ measures bend and twist. In the body frame, $\boldsymbol{\sigma}$ and $\boldsymbol{\kappa}$ can be determined from the rod's state variables via Eqs. (3.10) and (3.15), respectively.

3.1.3 Equations of Motion

This section presents the Cosserat rod's equations of motion and defines all terms necessary to describe its dynamic behavior. Under the simplifying assumptions made in Section

3.1, the equations of motion for an active Cosserat rod immersed in a Newtonian fluid environment are given by

$$\mathbf{0} = \boldsymbol{f}_{\mathrm{F}} + \partial_s \boldsymbol{N} + \partial_s \boldsymbol{F}_A, \tag{3.20}$$

$$\mathbf{0} = \boldsymbol{l}_{\mathrm{F}} + \partial_s \boldsymbol{r} \times \boldsymbol{N} + \partial_s \boldsymbol{M} + \partial_s \boldsymbol{L}_A, \tag{3.21}$$

where $\boldsymbol{f}_{\mathrm{F}}$ and $\boldsymbol{l}_{\mathrm{F}}$ are the fluid drag force and drag torque line densities per unit reference length, $\boldsymbol{N}$ and $\boldsymbol{M}$ are the internal force and torque resultants, and $\boldsymbol{F}_{\mathrm{A}}$ and $\boldsymbol{L}_{\mathrm{A}}$ are the effective actuation force and torque, respectively [9, 121]. The first of the two equations states that an infinitesimal rod segment's local change in linear momentum must be equal to the sum of internal and external forces acting on its center of mass. Likewise, the second equation states that an infinitesimal rod segment's local change in angular momentum must equal the sum of internal and external torques acting on it. Therefore, the equations of motion are commonly referred to as the linear and the angular balance equations.

We approximate the swimmer's passive body as a homogeneous linear viscoelastic material, a well-established and effective model for *C. elegans* [13, 42, 45, 125, 126], the primary study object in this work (see Chapter 2). For a linear viscoelastic material, the internal force resultant is linearly proportional to the rod's strains and the temporal strain rates. Likewise, the internal torque resultant is linearly proportional to the rod's curvature and temporal curvature rate. Within the context of Cosserat rods, Lang *et al.* [80] rigorously derived the constitutive laws for a Kevin-Voigt-type viscoelastic Cosserat rod based on a three-dimensional continuum model. In the body frame, the internal stress-strain and torque-curvature relations can be succinctly written in vector notation as follows [52, 80, 88]:

$$\bar{\boldsymbol{N}} = \boldsymbol{S}\bar{\boldsymbol{\sigma}} + \tilde{\boldsymbol{S}}\partial_t \bar{\boldsymbol{\sigma}}, \tag{3.22}$$

$$\bar{\boldsymbol{M}} = \boldsymbol{B}\bar{\boldsymbol{\kappa}} + \tilde{\boldsymbol{B}}\partial_t \bar{\boldsymbol{\kappa}}. \tag{3.23}$$

Here, the elements of the rigidity matrix $\boldsymbol{S}$ are the proportionality coefficients between the elastic stress resultant and the strain vector $\bar{\boldsymbol{\sigma}}$, and the elements of the viscosity matrix $\tilde{\boldsymbol{S}}$ are the proportionality factors between the viscous stress resultant and strain rate vector $\partial_t \bar{\boldsymbol{\sigma}}$. Likewise, the elements of the rigidity matrix $\boldsymbol{B}$ are the proportionality factors between the elastic torque resultant and the curvature vector $\bar{\boldsymbol{\kappa}}$, and the elements of the viscosity matrix $\tilde{\boldsymbol{B}}$ are the proportionality factors between the viscous torque resultant and the curvature rate vector $\partial_t \bar{\boldsymbol{\kappa}}$. For simplicity, we assume that the body material is isotropic, in which case the rigidity and viscosity matrices are diagonal and take the following form [80]:

$$\boldsymbol{S} = \varphi^2 \begin{bmatrix} GA & 0 & 0 \\ 0 & GA & 0 \\ 0 & 0 & EA \end{bmatrix}, \quad \tilde{\boldsymbol{S}} = \varphi^2 \begin{bmatrix} \nu A & 0 & 0 \\ 0 & \nu A & 0 \\ 0 & 0 & \eta A \end{bmatrix}, \tag{3.24}$$

$$\boldsymbol{B} = \varphi^4 \begin{bmatrix} EI & 0 & 0 \\ 0 & EI & 0 \\ 0 & 0 & GI \end{bmatrix}, \quad \tilde{\boldsymbol{B}} = \varphi^4 \begin{bmatrix} \eta I & 0 & 0 \\ 0 & \eta I & 0 \\ 0 & 0 & \nu I \end{bmatrix}. \tag{3.25}$$

The diagonal elements of the matrices are referred to as

1. $\boldsymbol{S}$: the (effective) shearing and extensional rigidities
2. $\tilde{\boldsymbol{S}}$: the (effective) shearing and extensional viscosities
3. $\boldsymbol{B}$: the (effective) bending and twisting rigidities
4. $\tilde{\boldsymbol{B}}$ the effective bending and twisting viscosities.

The geometric model parameters include:

1. The shape function $0 < \varphi(s) \leq 1$, which defines the profile of the cross-sectional radius $R(s) = R_{\text{max}}\varphi(s)$ along the centreline, where R_{max} denotes maximal cross-sectional radius
2. The maximal cross-sectional area $A = \pi R_{\text{max}}^2$
3. The maximal second moment of area $I = \pi R_{\text{max}}^4/4$.

The material model parameters include:

1. Young's modulus $E > 0$ (force per unit area)
2. Shear modulus $G > 0$ (force per unit area)
3. Extensional viscosity $\eta \geq 0$ (force times time per unit area)
4. Shear viscosity $\nu \geq 0$ (force times time per unit area)

It is important to note that for circular cross-section, the second moment of areas with respect to rotations around the in-plane body frame vectors $\boldsymbol{d}_1$ and $\boldsymbol{d}_2$ are equal due to the cross-section's rotational symmetry.

The Rivlin-Ericksen theorem states that a linear elastic, isotropic, and homogeneous material can only have two independent elasticity parameters [95]. Similarly, a linear viscoelastic, isotropic, and homogeneous material has only two independent viscosity parameters [88]. In particular, the shear modulus G and shear viscosity ν can alternatively be expressed in terms of Poisson's ratio ϱ via the following equations:

$$G = \frac{E}{2(1+\varrho)}, \quad \nu = \frac{\eta}{2(1+\varrho)}, \tag{3.26}$$

Using Eq. (3.26), we define the dimensionless material parameter ratio p as follows:

$$p = \frac{G}{E} = \frac{\nu}{\eta} = \frac{1}{2(1+\varrho)}. \tag{3.27}$$

Having established the constitutive equations for the rod, we proceed by specifying the drag force and drag torque that the surrounding fluid exerts onto the rod. For a slender microswimmer, whose breadth is much smaller than its length, the interaction of its body surface with the surrounding fluid environment can be approximated by resistive-force theory (RFT) [17, 38, 55, 60]. As we discussed in Section 2.3, RFT approximates the fluid drag force line density $\boldsymbol{f}_\mathrm{F}$ and torque line density $\boldsymbol{l}_\mathrm{F}$ to be linearly proportional to the centreline velocity $\boldsymbol{u}$ and angular velocity $\boldsymbol{\omega}$, i.e.

$$\boldsymbol{f}_\mathrm{F} = -\mu \left[c_{||} \left(\boldsymbol{d}_3 \otimes \boldsymbol{d}_3 \right) + c_{\perp} \left(\boldsymbol{1} - \boldsymbol{d}_3 \otimes \boldsymbol{d}_3 \right) \right] \cdot \boldsymbol{u}, \tag{3.28}$$

$$\boldsymbol{l}_\mathrm{F} = -\mu \left[\gamma_{||} \left(\boldsymbol{d}_3 \otimes \boldsymbol{d}_3 \right) + \gamma_{\perp} \left(\boldsymbol{1} - \boldsymbol{d}_3 \otimes \boldsymbol{d}_3 \right) \right] \cdot \boldsymbol{\omega}, \tag{3.29}$$

where μ is the fluid's viscosity, and $\otimes$ denotes the outer vector product. Please note that in Eqs. (3.28) and (3.29), we have substituted the centreline tangent vector $\boldsymbol{t}$ with the normal vector $\boldsymbol{d}_3$ of the cross-section. This substitution is made because $\boldsymbol{d}_3$ represents the longitudinal axis of the infinitesimal cylindrical rod segments, which may not necessarily align with $\boldsymbol{t}$ in a Cosserat rod.

We distinguish four drag coefficients:

1. Linear longitudinal drag coefficient $c_{||}$: This coefficient determines the drag force experienced by the body segment when it moves longitudinally
2. Linear transverse drag coefficient $c_{\perp}$: This coefficient determines the drag force experienced by the body segment when it moves transversely (laterally)
3. Angular longitudinal drag coefficient $\gamma_{||}$: This coefficient determines the drag torque experienced by the body segment when it rotates around its longitudinal axis.
4. Angular transverse drag coefficient $\gamma_{\perp}$: This coefficient determines the drag torque

experienced by the body segment when it rotates around its transverse axis

Numerous analytic approximations for the drag coefficients have been proposed. As outlined in Section 2.3, we use the drag coefficients derived by Garg & Kumar [51], stated as:

$$c_{\parallel} = \frac{2\pi}{\ln(1/\varepsilon) - \frac{1}{2}}, \quad c_{\perp} = \frac{4\pi}{\ln(1/\varepsilon) + \frac{1}{2}}, \quad \gamma_{\parallel} = \pi\varphi^2 R_{\max}^2, \quad \gamma_{\perp} = 4\pi\varphi^2 R_{\max}^2, \tag{3.30}$$

where $\varepsilon = 2 \cdot R_{\max}/L_0$ is referred to as the rod's slenderness parameter.

Now that we have determined the internal and external force and torque resultants, the next step is to define how to actuate our model in order to achieve active deformation. As we discussed in Section 2.1, swimmers actively deform their body shape to generate propulsion. In the animal kingdom, such deformations are typically generated by muscle contractions, whereas on the microscopic level, molecular motors within cilia and flagella generate shear forces that result in local bending. In our model, rather than directly simulating those contractile or shear forces, we apply an effective actuation force $\boldsymbol{F}_{\mathrm{A}}$ and an effective actuation torque $\boldsymbol{L}_{\mathrm{A}}$ to reproduce the body deformations generated by those forces. The appropriate spatio-temporal pattern of $\boldsymbol{F}_{\mathrm{A}}(s,t)$ and $\boldsymbol{L}_{\mathrm{A}}(s,t)$ depends on the particular locomotion gait under investigation. This work focuses on undulatory locomotion, which we will discuss in more detail in Section 3.2.

To summarize, in this section, we introduced the equations of motion Eqs. (3.20) and (3.21), which govern the Cosserat rod's dynamics and are commonly referred to as the linear and angular balance equation. Furthermore, we formulated the rod's constitutive laws given by Eqs. (3.22) and (3.23) under the assumption that the swimmer's passive body can effectively be described as a linear viscoelastic homogeneous isotropic material. Lastly, we used RFT to approximate the fluid-structure interaction between the swimmer's deformable body surface and its surrounding fluid environment by Eqs. (3.28) and (3.29). Thus, for a given actuation force and actuation torque, our model provides a complete description for analyzing the dynamic behavior of slender microswimmers, taking into account both the deformation mechanics and fluid dynamics of the system.

3.1.4 Energy Expenditure

To explore gait optimality, our analysis focuses on two key objectives: swimming speed and energy efficiency. To estimate the swimmer's energy expenditure within the framework of our Cosserat rod model, it is essential to establish definitions for all relevant energetic terms. Given the model equations introduced in the previous section, the relevant energetic terms include:

1. The elastic potential energy V stored in the rod's shape
2. The internal dissipation rate $\dot{D}_\mathrm{I}$ associated with the viscosity of the body material
3. The external dissipation rate $\dot{D}_\mathrm{F}$ associated with the viscous fluid environment
4. The mechanical power $\dot{W}$ generated by the actuation force and actuation torque

Note that V has unit energy, whereas the dissipation rates and the mechanical power have unit energy per time. All energetic terms can be directly derived from the equations of motion, as we demonstrate in the Appendix A.2.1. The final expressions are identical to the one derived in Linn *et al.* [88]:

$$V(t) = \frac{1}{2}\int_0^{L_0} (\bar{\boldsymbol{\kappa}}\cdot\boldsymbol{B}\bar{\boldsymbol{\kappa}} + \bar{\boldsymbol{\sigma}}\cdot\boldsymbol{S}\bar{\boldsymbol{\sigma}})\,ds, \tag{3.31}$$

$$\dot{D}_\mathrm{I}(t) = -\int_0^{L_0} \left(\partial_t\bar{\boldsymbol{\kappa}}\cdot\tilde{\boldsymbol{B}}\,\partial_t\bar{\boldsymbol{\kappa}} + \partial_t\bar{\boldsymbol{\sigma}}\cdot\tilde{\boldsymbol{S}}\,\partial_t\bar{\boldsymbol{\sigma}}\right)\,ds, \tag{3.32}$$

$$\dot{D}_\mathrm{F}(t) = \int_0^{L_0} (\boldsymbol{f}_F\cdot\boldsymbol{u} + \boldsymbol{l}_F\cdot\boldsymbol{\omega})\,ds, \tag{3.33}$$

$$\dot{W}(t) = \int_0^{L_0} (\boldsymbol{f}_\mathrm{A}\cdot\boldsymbol{u} + \boldsymbol{l}_\mathrm{A}\cdot\boldsymbol{\omega})\,ds, \tag{3.34}$$

where we defined the actuation force and torque line densities per unit reference arc-length, $\boldsymbol{f}_\mathrm{A}(s,t) = \partial_s F_\mathrm{A}(s,t)$ and $\boldsymbol{l}_\mathrm{A}(s,t) = \partial_s L_\mathrm{A}(s,t)$, respectively.

Eq. (3.32) implies that $\dot{D}_I \leq 0$, which follows from the positive semi-definiteness of the viscosity matrices $\tilde{\boldsymbol{B}}$ and $\tilde{\boldsymbol{S}}$. Similarly, from Eq. (3.33), it follows that $\dot{D}_F \leq 0$ as the fluid drag force and drag torque line densities $\boldsymbol{f}_\mathrm{F}$ and $\boldsymbol{l}_\mathrm{F}$ are negatively proportional to the centreline velocity $\boldsymbol{u}$ and the angular velocity $\boldsymbol{\omega}$, respectively. Consequently, the system's total dissipation rate $\dot{D} = \dot{D}_I + \dot{D}_F$ is also $\dot{D} \leq 0$.

Energy conservation dictates that the dynamics of the Cosserat rod must fulfill the instantaneous power balance

$$\dot{E} = \dot{D} + \dot{W}, \tag{3.35}$$

where $\dot{E}$ is the change of the rod's total energy per unit of time. The rod's total energy $E = K + V$ is equivalent to the sum of its kinetic energy K and its elastic potential energy V. For an inertia-less rod, the contribution of the kinetic energy K to the rod's total energy E is approximated to be zero, i.e. Eq. (3.35) simplifies to

$$\dot{V} = \dot{D} + \dot{W}. \tag{3.36}$$

Integrating Eq. (3.36) from t_1 to t_2 results in the energy balance equation

$$V(t_2) - V(t_1) = D(t_1, t_2) + W(t_1, t_2), \tag{3.37}$$

where we introduced the short-hands:

$$D(t_1, t_2) = \int_{t_1}^{t_2} \dot{D} dt, \quad W(t_1, t_2) = \int_{t_1}^{t_2} \dot{W} dt. \tag{3.38}$$

The energies $D(t_1, t_2)$ and $W(t_1, t_2)$ represent the dissipated energy and mechanical actuation work over the time interval $[t_1, t_2]$, respectively.

To model a cyclic locomotion gait characterized by the period T, the actuation force and actuation torque should follow the same periodicity, i.e.

$$\boldsymbol{F}_{\mathrm{A}}(t) = \boldsymbol{F}_{\mathrm{A}}(t+T), \quad \boldsymbol{L}_{\mathrm{A}}(t) = \boldsymbol{L}_{\mathrm{A}}(t+T). \tag{3.39}$$

Assuming time invariant geometric, material, and environmental parameters, Eq. (3.39) implies that the swimmer's body undergoes periodic shape changes, from which follows that $V(t) = V(t+T)$. Thus, substituting $t_1 = t$ and $t_2 = t + T$ in Eq. (3.37) yields the simplified energy balance equation for a cyclic gait:

$$0 = W + D. \tag{3.40}$$

Here, W represents the mechanical actuation work performed by the swimmer, and D represents the total energy dissipated during one gait cycle. Hence, for the special case of a periodic gait, the energy injected into the system through the mechanical work done by the actuation force and torque balances the energy lost due to dissipation. For the remainder, the actuation work W per gait period T will serve as our proxy for the energetic cost associated with a periodic swimming gait.

3.2 Modelling the Undulation Gait

Undulatory swimmers utilize shear or contractile actuation forces to bend their body, generating a wave-like curvature profile that propagates along their body or propulsion appendages [1, 19, 83]. This gives rise to the characteristic wave-like body shape referred to as undulatory locomotion. In our model, we achieve a propagating curvature wave by modeling the effective actuation torque $\boldsymbol{L}_\mathrm{A}$ as a traveling wave:

$$\boldsymbol{F}_\mathrm{A}(s,t) = 0 \tag{3.41}$$

$$\boldsymbol{L}_\mathrm{A}(s,t) = A\, S(q_0 s - \omega_0 t)\boldsymbol{d}_1. \tag{3.42}$$

The undulation parameters are the actuation torque amplitude A, the wave number $q_0 = 2\pi/\lambda_0$, the angular undulation frequency $\omega_0 = 2\pi f_0$ and the shape function S, usually taken to be sinusoidal. Here, we defined the undulation wavelength λ_0 and undulation frequency $f_0 = 1/T$.

The effective actuation force $\boldsymbol{F}_\mathrm{A}$ is associated with active shearing, stretching, and compression, which we assume to play a negligible role in the context of undulatory locomotion. Consequently, it is approximated to be zero. Furthermore, we assume that the swimmer's initial configuration is planar with the body frame vector $\boldsymbol{d}_1$ being parallel to $\boldsymbol{e}_1$ everywhere along the body. In this scenario, the swimmer's motion is confined to the plane spanned by $\boldsymbol{e}_1$ and $\boldsymbol{e}_3$, which we refer to as the dorsal-ventral plane.

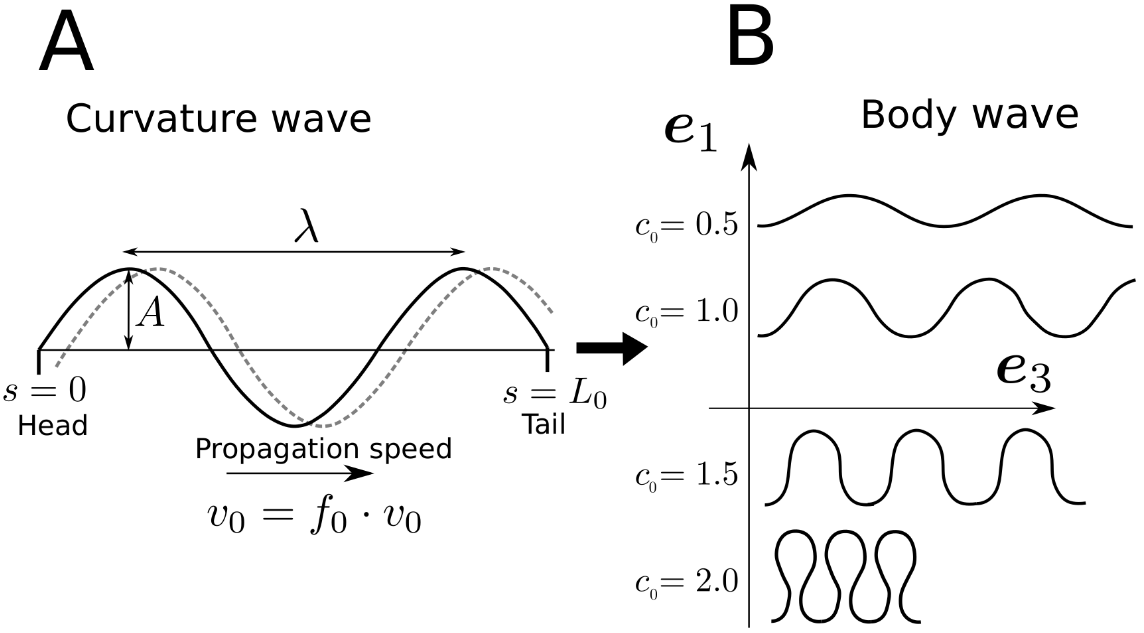

Figure 3.3: Schematic of the relationship between the swimmer's curvature and body wave. (**A**): Illustration of the preferred curvature wave $\boldsymbol{k}_0$, characterized by the preferred curvature amplitude A_0, wavelength λ_0, frequency f_0 and the wave's propagation speed v_0 . (**B**): Sketch of the body waves in the dorsal-ventral plane for different preferred shape factors $c_0 = A_0/q_0$. Please note that the body waves in panel B are plotted in dimensionless coordinates, i.e. they are not scaled to accurate size.

In order for the actuation torque $\boldsymbol{L}_\mathrm{A}$ to be strong enough to overcome the resistance of the passive internal torque resultant $\boldsymbol{M}$, the actuation torque amplitude A must be in the order of the maximum dorsal-ventral bending rigidity B. In our model, B corresponds to the first diagonal element of the rigidity matrix $\boldsymbol{B}$, defined in Eq. (A.47). To simplify our notation, we introduce the preferred curvature amplitude $A_0 = -A_\mathrm{M}/B$ so that Eq. (3.42) can be written as:

$$\boldsymbol{L}_\mathrm{A}(s,t) = -B\boldsymbol{\kappa}_0(s,t), \quad \boldsymbol{\kappa}_0(s,t) = A_0\, S(q_0 s - \omega_0 t)\boldsymbol{d}_1. \tag{3.43}$$

The vector $\boldsymbol{\kappa}_0$ is commonly referred to as the preferred curvature [52, 125]. Hence, the actuation torque can be understood as a preferred curvature wave propagating along the swimmer's body, see Fig. 3.3A. This curvature wave generates a body wave in the dorsal-ventral plane, as illustrated in Fig. 3.3B. The shape of this body wave is contingent on the curvature wave's dimensionless shape factor $c_0 = A_0/q_0$, where smaller c_0 values lead to shallower body waves while larger values lead to highly curved Ω-shapes [21, 106]. Please note that the body waves for different c_0 in Fig. 3.3B are drawn in dimensionless coordinates to illustrate the shape of the body wave and are not scaled to the accurate size.

A priori, it is uncertain whether the swimmer's emergent body curvature $\boldsymbol{\kappa}$ can track the preferred curvature $\boldsymbol{\kappa}_0$ prescribed by the actuation torque $\boldsymbol{L}_\mathrm{A}$. This will depend on how fast the body's response time is compared to the time scale of actuation torque $\boldsymbol{L}_\mathrm{A}$, which is set by the undulation frequency f_0. In the next section, we nondimensionalize the equations of motion to explore how the system's response time depends on its model parameters.

However, before we proceed, we conclude this section by deriving an expression for the average swimming speed during undulatory locomotion. For this purpose, we introduce the centreline's centroid $\boldsymbol{R}(t)$, which is defined as the normalized integral of the centreline coordinates

$$\boldsymbol{R}(t) = \frac{1}{L_0}\int_0^{L_0} \boldsymbol{r}(s,t)ds. \tag{3.44}$$

Given $\boldsymbol{R}(t)$, we define the instantaneous swimming speed $U(t)$ as

$$U(t) = \boldsymbol{e}_\mathrm{S} \cdot \partial_t \boldsymbol{R}, \tag{3.45}$$

where $\boldsymbol{e}_\mathrm{S}$ is the swimming direction defined as:

$$\boldsymbol{e}_\mathrm{S} = \frac{\boldsymbol{R}(t_0+T) - \boldsymbol{R}(t_0)}{|\boldsymbol{R}(t_0+T) - \boldsymbol{R}(t_0)|}. \tag{3.46}$$

Given $U(t)$, the average swimming U is obtained from the time average integral

$$U = \frac{1}{T}\int_t^{t+T} U(t'), dt', \tag{3.47}$$

3.3 Nondimensionalization

The properties of many dynamical systems do not depend on the specific numerical values of each of its parameters individually but rather on the relative values, proportions, or combinations of these parameters. Nondimensionalizing the equations of motion provides a generic method to identify the key dimensionless parameters that characterize the system's dynamic behavior. We refer to the classical textbook by Courant & Hilbert [37] for a more in-depth discussion.

Here, we follow the standard protocol to derive a dimensionless form of the equations of motion introduced in Section 3.1.3. First, we choose the rod's reference length L_0 and the gait period T as the system's characteristic length and time scales, respectively. This allows us to define the dimensionless coordinates s^* and t^* as follows:

$$s^* = \frac{s}{L_0}, \quad t^* = \frac{t}{T}. \tag{3.48}$$

Next, we define the rod's dimensionless state variables $\boldsymbol{r}^*$ and $\boldsymbol{\theta}^*$, along with its dimensionless strain and curvature measures $\bar{\boldsymbol{\sigma}}^*$ and $\bar{\boldsymbol{\kappa}}^*$ as follows:

$$\boldsymbol{r}^* = \frac{\boldsymbol{r}}{L_0}, \quad \boldsymbol{\theta}^* = \boldsymbol{\theta}, \quad \bar{\boldsymbol{\sigma}}^* = \bar{\boldsymbol{\sigma}}, \quad \bar{\boldsymbol{\kappa}}^* = L_0 \bar{\boldsymbol{\kappa}}. \tag{3.49}$$

Given the above definitions, we use the chain rule to derive the following expressions for the dimensionless centreline velocity $\boldsymbol{u}^*$, dimensionless angular velocity $\boldsymbol{\omega}^*$, and dimensionless temporal strain rate $\partial_{t^*} \bar{\boldsymbol{\sigma}}^*$ and curvature rate $\partial_{t^*} \bar{\boldsymbol{\kappa}}^*$:

$$\boldsymbol{u}^* = \frac{T \boldsymbol{u}}{L_0}, \quad \boldsymbol{\omega}^* = \frac{\boldsymbol{\omega}}{T}, \quad \partial_{t^*} \bar{\boldsymbol{\sigma}}^* = T \partial_t \bar{\boldsymbol{\sigma}}, \quad \partial_{t^*} \bar{\boldsymbol{\kappa}}^* = T_0 L_0 \partial_t \bar{\boldsymbol{\kappa}} \tag{3.50}$$

Lastly, we replace all variables and their derivatives in the linear balance equation Eq. (3.20) and angular balance equation Eq. (3.21) by their dimensionless counterparts, which yields the following dimensionless equations of motion (see Section A.2.2 in the Appendix for a detailed derivation):

$$0 = \boldsymbol{f}^*_{\mathrm{F}} + \partial_{s^*} \boldsymbol{N}^* + \partial_{s^*} \boldsymbol{F}^*_M, \tag{3.51}$$

$$0 = \boldsymbol{l}^*_{\mathrm{F}} + \partial_{s^*} \boldsymbol{r}^* \times \boldsymbol{N}^* + \partial_{s^*} \boldsymbol{M}^* + \partial_{s^*} \boldsymbol{L}^*_{\mathrm{M}}. \tag{3.52}$$

Here, we defined the dimensionless internal force and torque resultants $\bar{\boldsymbol{N}}^*$ and $\bar{\boldsymbol{M}}^*$ in the body frame as:

$$\bar{\boldsymbol{M}}^* = \boldsymbol{S}^* \bar{\boldsymbol{\sigma}}^* + \tilde{\boldsymbol{S}}^* \partial_{t^*} \bar{\boldsymbol{\sigma}}^*, \quad \bar{\boldsymbol{N}}^* = \boldsymbol{B}^* \bar{\boldsymbol{\kappa}}^* + \tilde{\boldsymbol{B}}^* \partial_{t^*} \bar{\boldsymbol{\kappa}}^*. \tag{3.53}$$

The dimensionless rigidity and viscosity matrices take the following form:

$$\boldsymbol{S}^* = \frac{\varphi^2}{ga}\begin{bmatrix}\alpha_c p & 0 & 0\\ 0 & \alpha_c p & 0\\ 0 & 0 & 1\end{bmatrix}, \quad \tilde{\boldsymbol{S}}^* = \frac{\varphi^2 b}{ga}\begin{bmatrix}\alpha_c p & 0 & 0\\ 0 & \alpha_c p & 0\\ 0 & 0 & 1\end{bmatrix}, \tag{3.54}$$

$$\boldsymbol{B}^* = \frac{\varphi^4}{a}\begin{bmatrix}1 & 0 & 0\\ 0 & 1 & 0\\ 0 & 0 & 2\alpha_T p\end{bmatrix}, \quad \tilde{\boldsymbol{B}}^* = \frac{\varphi^4 b}{a}\begin{bmatrix}1 & 0 & 0\\ 0 & 1 & 0\\ 0 & 0 & 2\alpha_T p\end{bmatrix}, \tag{3.55}$$

where we introduced the system's intrinsic time scales τ and ξ which are defined in terms of the physical model parameters

$$\tau = \frac{\mu\, c_{\parallel} L_0^4}{EI}, \qquad \xi = \frac{\eta}{E}, \tag{3.56}$$

and the dimensionless time scale ratios a and b, the dimensionless geometric ratio g, and material parameter ratio p (see Eq. (3.27)) as:

$$a = \frac{\tau}{T}, \qquad b = \frac{\xi}{T}, \qquad g = \frac{I}{L_0^2 A}, \qquad p = \frac{1}{2(1+\varrho)}, \tag{3.57}$$

Here, T is the gait period associated with the actuation torque.

The time scale τ quantifies the relative importance of viscous fluid and elastic stresses and is proportional to the fourth power of the sperm number [43, 93]. The time scale ξ, on the other hand, quantifies the relative importance of the internal viscous and the elastic stresses. Recall that actuation is achieved by applying an external actuation force and torque to our model with period T. Hence, a and b are defined as the time scale ratios between the system's response times τ and ξ with the input time scale T, respectively. Consequently, a and b can be understood as the system's effective response times. They predict how quickly or slowly the rod will be able to respond to actuation and thus play a crucial role in determining the system's dynamic behavior.

The dimensionless parameter p quantifies the relative importance of shear and extensional deformations and is defined in terms of Poisson's ratio ϱ. Since cells can be considered nearly incompressible, the Poisson's ratio of biological tissue is typically close to 0.5 [57, 133]. From Eq. (3.57), it follows then that p is of the order $\mathcal{O}(1)$. Hence, we infer the following scaling relations from Eq. (3.54):

$$\frac{\boldsymbol{B}^*}{\boldsymbol{S}^*} \sim g, \qquad \frac{\tilde{\boldsymbol{B}}^*}{\tilde{\boldsymbol{S}}^*} \sim g, \tag{3.58}$$

where $\boldsymbol{A}/\boldsymbol{B}$ denotes the element-wise division of two matrices. The dimensionless parameter

g quantifies the rod's geometric properties. For circular cross-sections, it is proportional to squared slenderness parameter ε^2. From Eq. (3.58), it follows then

$$\frac{\boldsymbol{B}^*}{\boldsymbol{S}^*} \sim \varepsilon^2, \quad \frac{\tilde{\boldsymbol{B}}^*}{\tilde{\boldsymbol{S}}^*} \sim \varepsilon^2 \tag{3.59}$$

Thus, for slender rods with $\varepsilon \ll 1$, the swimmer's passive body exhibits considerably greater shear and extension resistance than bend and twist. This property is an exclusive consequence of the swimmer's slender geometry. It enables the swimmer to maintain a small strain vector while it actively bends.

The dimensionless fluid drag force and torque line densities $\boldsymbol{f}_\mathrm{F}^*$ and $\boldsymbol{l}_\mathrm{F}^*$ are defined as

$$\boldsymbol{f}_\mathrm{F}^* = -\left[\boldsymbol{d}_3^* \otimes \boldsymbol{d}_3^* + K_c\left(\boldsymbol{1} - \boldsymbol{d}_3^* \otimes \boldsymbol{d}_3^*\right)\right] \cdot \boldsymbol{u}^*, \tag{3.60}$$

$$\boldsymbol{l}_\mathrm{F}^* = -K_\| \left[\boldsymbol{d}_3^* \otimes \boldsymbol{d}_3^* + K_\gamma\left(\boldsymbol{1} - \boldsymbol{d}_3^* \otimes \boldsymbol{d}_3^*\right)\right]\right] \cdot \boldsymbol{\omega}^*, \tag{3.61}$$

where we introduced the dimensionless drag coefficient ratios K_c, K_γ and $K_\|$ as follows:

$$K_c = \frac{c_\perp}{c_\|}, \quad K_\gamma = \frac{\gamma_\perp}{\gamma_\|}, \quad K_\| = \frac{\gamma_\|}{L_0^2 c_\|}. \tag{3.62}$$

Using the definition of the drag coefficients from Eq. (3.30), we derive the following scaling with respect to ε:

$$c_\|, c_\perp \sim \frac{1}{\ln(1/\varepsilon)}, \quad \gamma_\|, \gamma_\perp \sim \varepsilon^2, \quad K_c, K_\gamma \sim 1, \quad K_\| \sim \varepsilon^2 \ln(1/\varepsilon). \tag{3.63}$$

From Eqs. (3.60) and (3.61) it follows than that

$$\frac{\boldsymbol{l}_\mathrm{F}^*}{\boldsymbol{f}_\mathrm{F}^*} \sim \varepsilon^2 \ln(1/\varepsilon). \tag{3.64}$$

This implies that for slender rods with $\varepsilon \ll 1$, the fluid drag force density $\boldsymbol{f}_\mathrm{F}^*$ dominates over fluid drag torque density $\boldsymbol{l}_\mathrm{F}^*$. It is, therefore, common practice to neglect $\boldsymbol{l}_\mathrm{F}^*$ in the study of slender microswimmers [23, 42, 45, 55, 58, 125, 126]. However, we find that including $\boldsymbol{l}_\mathrm{F}^*$ improves the numerical stability of our model implementation, especially in the limit of small internal viscosities.

The dimensionless actuation force $\boldsymbol{F}_A^*$ and torque $\boldsymbol{L}_A^*$ are defined as:

$$\boldsymbol{F}_A^* = \frac{T}{\mu\, c_\| L_0^2} \boldsymbol{F}_A, \tag{3.65}$$

$$\boldsymbol{L}_A^* = \frac{T}{\mu\, c_\| L_0^3} \boldsymbol{L}_A. \tag{3.66}$$

For the special case of an undulatory gait as introduced in Section 3.2, the expressions for $\boldsymbol{F}^*_A$ and $\boldsymbol{L}^*_A$ are

$$\boldsymbol{F}^*_A(s^*,t^*) = 0, \tag{3.67}$$

$$\boldsymbol{L}^*_{\mathrm{A}}(s^*,t^*) = -\boldsymbol{B}^*\boldsymbol{\kappa}^*_0(s^*,t^*), \quad \boldsymbol{\kappa}_0(s^*,t^*) = A^*_0\, S(q^*_0 s^* - 2\pi t^*)\boldsymbol{d}^*_1, \tag{3.68}$$

where we used Eqs. (3.42), (3.66) and (3.55). The dimensionless undulation parameters include the preferred dimensionless curvature amplitude $A^*_0 = L_0 A_0$, wave-number $q^*_0 = L_0\, q_0$, wavelength $\lambda^*_0 = 2\pi/q^*_0$ and undulation frequency $f^*_0 = T f_0 = 1$.

Having defined all terms for the dimensionless equations of motion, we conclude this section by deriving dimensionless expressions for the energetic terms introduced in Section 3.1.4, as well as the swimming speed. In their dimensionless form, the elastic potential, dissipation rates, and actuation power can be expressed as follows:

$$V^*(t^*) = \frac{1}{2}\int_0^1 (\bar{\boldsymbol{\kappa}}^* \cdot \boldsymbol{B}^*\bar{\boldsymbol{\kappa}}^* + \bar{\boldsymbol{\sigma}}^* \cdot \boldsymbol{S}^*\bar{\boldsymbol{\sigma}}^*)\, ds^*, \tag{3.69}$$

$$\dot{D}^*_{\mathrm{I}}(t^*) = -\int_0^1 \left(\partial_{t^*}\bar{\boldsymbol{\kappa}}^* \cdot \tilde{\boldsymbol{B}}^*\, \partial_{t^*}\bar{\boldsymbol{\kappa}}^* + \partial_{t^*}\bar{\boldsymbol{\sigma}}^* \cdot \tilde{\boldsymbol{S}}^*\, \partial_{t^*}\bar{\boldsymbol{\sigma}}^*\right)\, ds^*, \tag{3.70}$$

$$\dot{D}^*_{\mathrm{F}}(t^*) = \int_0^1 (\boldsymbol{f}^*_F \cdot \boldsymbol{u}^* + \boldsymbol{l}^*_F \cdot \boldsymbol{\omega}^*)\, ds^*, \tag{3.71}$$

$$\dot{W}^*(t^*) = \int_0^1 (\boldsymbol{f}^*_{\mathrm{A}} \cdot \boldsymbol{u}^* + \boldsymbol{l}^*_{\mathrm{A}} \cdot \boldsymbol{\omega}^*)\, ds^*. \tag{3.72}$$

Integrating over one undulation period yields dimensionless energies

$$D^*_{\mathrm{I}} = \int_0^1 \dot{D}^*_{\mathrm{I}}\, dt^*, \quad D^*_{\mathrm{F}} = \int_0^1 \dot{D}^*_{\mathrm{F}}\, dt^*, \quad W^* = \int_0^1 \dot{W}\, dt^*, \tag{3.73}$$

where D^*_{I} is the dimensionless internal dissipated energy, D^*_{F} the dimensionless external (fluid) dissipated energy and W^* the dimensionless the actuation work per undulation period.

The dissipation rates and actuation power in physical units can be obtained from their dimensionless equivalents by applying the conversion factor

$$[\dot{D}_{\mathrm{I}}, \dot{D}_{\mathrm{F}}, \dot{W}] = \frac{\mu c_{\parallel} L_0^3}{T^2}\, [\dot{D}^*_{\mathrm{I}}, \dot{D}^*_{\mathrm{F}}, \dot{W}^*]. \tag{3.74}$$

Similarly, the dissipative energies and the actuation work in physical units can be recovered from their dimensionless counterparts by applying the conversion factor

$$[D_I,\, D_F,\, W] = \frac{\mu c_{\parallel} L_0^3}{T} [D^*_{\mathrm{I}},\, D^*_{\mathrm{F}},\, W^*] \tag{3.75}$$

Lastly, the dimensionless average swimming speed U^* per undulation period can be defined as the integral

$$U^* = \int_{t^*}^{t^*+1} \partial_{t^*} \boldsymbol{R}^* \cdot \boldsymbol{e}_{\mathrm{S}}^* \, dt_0^* ., \tag{3.76}$$

where we introduced the dimensionless centreline centroid $\boldsymbol{R}^*(t^*) = \boldsymbol{R}(t)/L_0$, and the dimensionless swimming direction $\boldsymbol{e}_{\mathrm{S}}^* = \boldsymbol{e}_{\mathrm{S}}$. From Eq. (3.47) it follows than that the physical speed U can be recovered from U^* through the equation

$$U = \frac{L_0}{T} U^*. \tag{3.77}$$

To conclude, this section derived the dimensionless forms of the linear and angular balance equation, which have the same functional form as the physical equations of motion introduced in Section 3.1.3. The system's dimensionless parameters include the dimensionless time scale ratios a and b, the material parameters ratio p, the geometric ratio g, and the drag coefficient ratios K_c, K_γ and $K_{\|}$. We will provide a detailed exploration of how these parameters influence the system's dynamical properties in Chapter 4. However, before we do so, we derive a numerical implementation of our model and present validation experiments to demonstrate its accuracy and stability.

3.4 Numerical Implementation

In this section, we employ a finite element scheme to solve the dimensionless equations of motion, derived in Section 3.3. A general introduction to the application of finite element methods to differential equations can be found in the textbook by Li *et al.* [85]. Here, our approach closely follows the methodology outlined by Ranner [111], who developed a finite element scheme for the special case of an unshearable, inextensible Kirchhof rod.

As the first step, we derive the weak form of the dimensionless equations of motion for the appropriate boundary conditions. Subsequently, we proceed by discretizing the weak form in space and time. This is where the advantage of rod models becomes evident. As a Cosserat rod only has a single spatial coordinate s, the spatial discretization of the model is significantly simpler compared to a three-dimensional continuum model. As a last step, we linearize the discretized representation of the weak form, so that it can be reduced to a linear matrix problem.

3.4.1 Weak Formulation

In this section, our objective is to derive the weak form of the dimensionless equations, which we previously introduced in Section 3.3. For this purpose, we multiply the dimensionless linear balance equation Eq. (3.51) and the angular balance equation Eq. (3.52) with the vector-valued test function $\boldsymbol{\phi}(s)$. We then integrate the balance equations over the domain of the dimensionless reference arc-length, resulting in the following weak form:

$$0 = \int_0^1 \boldsymbol{f}_{\mathrm{F}} \cdot \boldsymbol{\phi}\, ds - \int_0^1 (\boldsymbol{N} + \boldsymbol{F}_{\mathrm{A}}) \cdot \partial_s \boldsymbol{\phi}\, ds + [(\boldsymbol{N} + \boldsymbol{F}_{\mathrm{A}}) \cdot \boldsymbol{\phi}]|_0^1 , \tag{3.78}$$

$$0 = \int_0^1 \boldsymbol{l}_{\mathrm{F}} \cdot \boldsymbol{\phi}\, ds + \int_0^1 (\partial_s \boldsymbol{r} \times \boldsymbol{N}) \cdot \boldsymbol{\phi}\, ds - \int_0^1 (\boldsymbol{M} + \boldsymbol{L}_{\mathrm{A}}) \cdot \partial_s \boldsymbol{\phi}\, ds + [(\boldsymbol{M} + \boldsymbol{L}_{\mathrm{A}}) \cdot \boldsymbol{\phi}]|_0^1 . \tag{3.79}$$

Here, we omitted the star superscript associated with the dimensionless variables for the sake of brevity. For the last integral on r.h.s. of both equations, we used partial integration to shift the reference arc-length derivative onto the test function. This step introduces an additional boundary term in both of the equations.

As boundary conditions, one typically specifies the translational and rotational degrees of freedom at the rod's end. For our model, we assume that the rod's ends are not constrained or fixed in any way, commonly referred to as a free-end boundary condition. The internal force resultant $N(s)$ and the torque resultant $M(s)$ are defined such that they specify the force and the torque that the material in the interval $(s, 1]$ exerts on the infinitesimal segment at position s [9]. From Newton's action-reacgradualtion principle then follows that the force and torque that the material in the interval $[0, s)$ exerts on the same segment must be equal in magnitude but opposite in direction to $N(s)$ and $M(s)$, as illustrated in Fig. 3.4A. This implies that the internal force and torque resultant at the rod's boundaries must be zero. This is because there is no material beyond those boundary points that could exert an internal force or torque on the outer boundary segments. Thus, the appropriate boundary conditions for $\boldsymbol{N}$ and $\boldsymbol{M}$ are:

$$\boldsymbol{M}(0, t) = \boldsymbol{N}(0, t) = \boldsymbol{M}(1, t) = \boldsymbol{N}(1, t) = 0. \tag{3.80}$$

Furthermore, we restrict the actuation force $\boldsymbol{F}_A$ and actuation torque $\boldsymbol{L}_A$ to functions which are zero at the boundaries:

$$\boldsymbol{F}_A(0, t) = \boldsymbol{L}_A(0, t) = \boldsymbol{F}_A(1, t) = \boldsymbol{F}_A(1, t) = 0 \tag{3.81}$$

In the case of an undulatory gait, as defined in Section 3.2, this boundary condition can be achieved by a gradual spatial onset of the actuation torque at the head and tail of the swimmer, as depicted in Fig. 3.4B. Here, we use two sigmoidal functions

$$\mathrm{sig}_{\mathrm{H}}(s) = \frac{1}{1 + \exp\left(-\frac{s - s_{\mathrm{H}}}{\Delta_s}\right)}, \quad \mathrm{sig}_{\mathrm{T}}(s) = \frac{1}{1 + \exp\left(\frac{s - s_{\mathrm{T}}}{\Delta_s}\right)}, \tag{3.82}$$

to mask the actuation torque $\boldsymbol{L}_{\mathrm{A}}(s) \cdot \mathrm{sig}_{\mathrm{H}}(s) \cdot \mathrm{sig}_{\mathrm{T}}(s)$. The masking parameter are set to $s_{\mathrm{H}} = 0.05$, $s_{\mathrm{T}} = 0.95$ and $\Delta_s = 0.1$. For *C. elegans*, this choice is justified since the longitudinal body wall muscles do not extend into the head and tip of the tail.

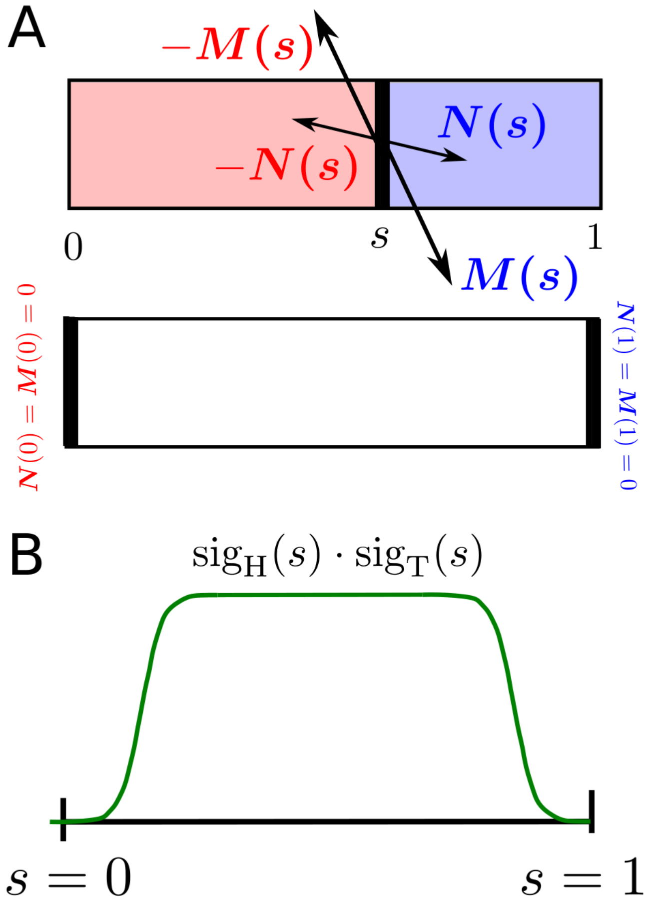

Figure 3.4: Schematic of the rod's free end boundary condition and the actuation torque masking function. (**A**): Illustration of the free-end boundary conditions. Newton's action-reaction principle stipulates that the internal force and torque resultants exerted by the material $[0, s)$ (red) onto a cross-section at body position s must equate to the torque and force resultants exerted by the material $(s, 1]$ (blue). From this follows that the internal force and torque resultants must be zero at the boundaries. (**B**): The masking function $\mathrm{sig}_{\mathrm{H}}(s) \cdot \mathrm{sig}_{\mathrm{T}}(s)$ ensures that the actuation torque $\boldsymbol{L}_A$ is zero at boundaries.

For the boundary conditions as specified in Eqs. (3.80) and (3.81), the boundary term in Eqs. (3.78) and (3.79) vanishes, and the weak form simplifies to

$$0 = \int_0^1 \boldsymbol{f}_{\mathrm{F}} \cdot \boldsymbol{\phi}\, ds - \int_0^1 (\boldsymbol{N} + \boldsymbol{F}_{\mathrm{A}}) \cdot \partial_s \boldsymbol{\phi}\, ds, \tag{3.83}$$

$$0 = \int_0^1 \boldsymbol{l}_{\mathrm{F}} \cdot \boldsymbol{\phi}\, ds + \int_0^1 (\partial_s \boldsymbol{r} \times \boldsymbol{N}) \cdot \boldsymbol{\phi}\, ds - \int_0^1 (\boldsymbol{M} + \boldsymbol{L}_{\mathrm{A}}) \cdot \partial_s \boldsymbol{\phi}\, ds. \tag{3.84}$$

In summary, this section presented the weak form of the dimensionless equations of motion, considering free-end boundary conditions and zero actuation force and torque at both the head and tail of the swimmer's body.

3.4.2 Discretization

In this section, our goal is to derive a discrete representation of the weak form introduced in the previous Section 3.4.1. For this purpose, we take an equidistant partition of $[0, 1]$ by N points $s_1 = 0 < s_2 < ... < s_N = 1$ which we call the mesh. Because our model's weak form only contains first-order derivatives with respect to s, it is sufficient to approximate the system's state variables $\boldsymbol{r}$ and $\boldsymbol{\theta}$ as continuous piecewise linear functions. More precisely, we define the scalar function space V as follows:

$$V = \{x(s) \in C([0,1]) : x(s) \text{ piecewise linear on } [s_i, s_{i+1}] \text{ for } i = 1, \ldots, N-1\}, \tag{3.85}$$

Given V, we define the three-dimensional vector-valued function space V^3 as

$$V^3 = \{(x_1(s), x_2(s), x_3(s)) : x_k \in V \text{ for } k = 1, 2, 3\}, \tag{3.86}$$

whose vector components are functions in V.

To discretize in time, we choose a constant time increment Δt and label the n-th time step as $t_n = n \cdot \Delta t$. Furthermore, we denote the piecewise linear approximation of an arbitrary vector-valued function $\boldsymbol{x}(t)$ at time t_n as $\boldsymbol{x}_n \in V^3$. Thus, discretizing the weak form merely involves adding a n subscript to all variables in Eqs. (3.83) and (3.84), resulting in:

$$0 = \int_0^1 \boldsymbol{f}_{\mathrm{F},n} \cdot \boldsymbol{\phi}\, ds - \int_0^1 (\boldsymbol{N}_n + \boldsymbol{F}_{\mathrm{A},n}) \cdot \partial_s \boldsymbol{\phi}\, ds \tag{3.87}$$

$$0 = \int_0^1 \boldsymbol{l}_{\mathrm{F},n} \cdot \boldsymbol{\phi}\, ds - \int_0^1 (\partial_s \boldsymbol{r}_n \times \boldsymbol{N}_n) \cdot \boldsymbol{\phi}\, ds - \int_0^1 (\boldsymbol{M}_n + \boldsymbol{L}_{\mathrm{A},n}) \cdot \partial_s \boldsymbol{\phi}\, ds \tag{3.88}$$

To approximate the first-order time derivatives implicitly contained in the discrete weak form, we employ a finite backwards difference of order $k > 0$, defined as follows:

$$\partial_t \boldsymbol{x}_n = \frac{1}{\Delta t} \sum_{i=0}^{k} c_{n-i}\, \boldsymbol{x}_{n-i} + \mathcal{O}(\Delta t^k) \tag{3.89}$$

Here, the weighting coefficient c_n determines the relative contribution of the function value at the n-th time step to the finite difference calculation. The order k specifies the number of past time steps included in the calculation. To calculate the finite difference order at the first time steps $n = 1, 2, \ldots$, we assume the rod's state variables $(\boldsymbol{r}_n,\, \boldsymbol{\theta}_n)$ to be equal to the initial values $(\boldsymbol{r}_0, \boldsymbol{\theta}_0)$ for $n \leq 0$.

As the order of the finite difference scheme increases, the accuracy of the approximation improves; however, this requires caching more previous solutions. For example, for $k = 1$, Eq. (3.89) simplifies to an simple Euler step

$$\partial_t \boldsymbol{x}_n = \frac{\boldsymbol{x}_n - \boldsymbol{x}_{n-1}}{\Delta t} + \mathcal{O}(\Delta t). \tag{3.90}$$

We introduce the shorthand $\tilde{\partial}_t^k$ to represent the k-th order finite backward difference approximation of a first-order time derivative. Lastly, we substitute all variables in the discrete weak form defined by Eqs. (3.87) and (3.88) with the expressions derived in Section 3.3, and formulate the following problem statement. **Problem**: Given the actuation force $\boldsymbol{F}_{\mathrm{A}}$ and actuation torque $\boldsymbol{L}_{\mathrm{A}}$, and the rod's initial configuration $\boldsymbol{r}_0(s,0)$ and $\boldsymbol{\theta}_0(s,0)$, find the unknown variables $(\boldsymbol{r}_n,\, \boldsymbol{\theta}_n) \in V^3$ such that for all t_n:

$$\begin{aligned} 0 = &- \int_0^1 \left[\boldsymbol{d}_{3,n} \otimes \boldsymbol{d}_{3,n} + K_c \left(\boldsymbol{1} - \boldsymbol{d}_{3,n} \otimes \boldsymbol{d}_{3,n}\right)\right] \tilde{\partial}_t^{(k)} \boldsymbol{r}_n \cdot \boldsymbol{\phi}\, ds \\ &- \int_0^1 \left[\boldsymbol{Q}_n^T \left[\boldsymbol{S} \left(\boldsymbol{Q}_n \partial_s \boldsymbol{r}_n - \boldsymbol{e}_3\right) + \tilde{\boldsymbol{S}} \left(\boldsymbol{Q}_n \partial_s \tilde{\partial}_t^{(k)} \boldsymbol{r}_n - \left(\boldsymbol{A}_n \tilde{\partial}_t^{(k)} \boldsymbol{\theta}_n\right) \times \boldsymbol{Q}_n \partial_s \boldsymbol{r}_n\right)\right] + \boldsymbol{F}_{\mathrm{A},n}\right] \cdot \partial_s \boldsymbol{\phi}\, ds \end{aligned} \tag{3.91}$$

$$\begin{aligned} 0 = &- \int_0^1 K_{\|} \boldsymbol{Q}_n^T \left[\boldsymbol{e}_3 \otimes \boldsymbol{e}_3 + K_\gamma \left(\boldsymbol{1} - \boldsymbol{e}_3 \otimes \boldsymbol{e}_3\right)\right] \boldsymbol{A}_n \partial_t^{(k)} \boldsymbol{\theta}_n \cdot \boldsymbol{\phi}\, ds \\ &+ \int_0^1 \left\{\partial_s \boldsymbol{r}_n \times \boldsymbol{Q}_n^T \left[\boldsymbol{S} \left(\boldsymbol{Q}_n \partial_s \boldsymbol{r}_n - \boldsymbol{e}_3\right) + \tilde{\boldsymbol{S}} \left(\boldsymbol{Q}_n \partial_s \tilde{\partial}_t^{(k)} \boldsymbol{r}_n - \left(\boldsymbol{A}_n \tilde{\partial}_t^{(k)} \boldsymbol{\theta}_n\right) \times \boldsymbol{Q}_n \partial_s \boldsymbol{r}_n\right)\right]\right\} \cdot \boldsymbol{\phi}\, ds \\ &- \int_0^1 \left\{\boldsymbol{Q}_n \left[\boldsymbol{B} \boldsymbol{A}_n \partial_s \boldsymbol{\theta}_n + \tilde{\boldsymbol{B}} \left(\boldsymbol{A}_n \partial_s \tilde{\partial}_t^{(k)} \boldsymbol{\theta}_n + \left(\tilde{\partial}_t^{(k)} \boldsymbol{A}_n\right) \partial_s \boldsymbol{\theta}_n\right)\right] + \boldsymbol{L}_{\mathrm{A},n}\right\} \cdot \partial_s \boldsymbol{\phi}\, ds \end{aligned} \tag{3.92}$$

for all $\boldsymbol{\phi} \in V^3$.

A detailed derivation of the equations is given in Section A.2.3 of the Appendix for interested readers. However, it is important to note that the variables $\boldsymbol{d}_{3,n}$, $\boldsymbol{Q}_n$ and $\boldsymbol{A}_n$ implicitly depend on the Euler angles $\boldsymbol{\theta}_n$, which renders the problem nonlinear in the unknowns $(\boldsymbol{r}_n, \boldsymbol{\theta}_n)$. To solve this nonlinear problem, we use Picard's iteration, which can be summarized by the following steps [90]:

1. Start with an initial guess to approximate the solution to the PDE at the current time step
2. Linearize the nonlinear terms in the PDE using the current approximation
3. Solve the linearized PDE to obtain an updated approximation
4. Repeat steps 2 and 3 until the solution converges to a desired accuracy

Following these outlined steps, we denote the solution at time step n after the i-th Picard iteration step as $(\boldsymbol{r}_n^{i+1},\, \boldsymbol{\theta}_n^{i+1})$. As the initial guess for the Picard iteration, we chose the solution at the previous time step, i.e.

$$(\boldsymbol{r}_n^0,\, \boldsymbol{\theta}_n^0) = (\boldsymbol{r}_{n-1},\, \boldsymbol{\theta}_{n-1}). \tag{3.93}$$

To linearize the equations in the weak form of the problem statement defined by Eqs. (3.91) and (3.92), we approximate all nonlinear terms by using the solution $(\boldsymbol{r}_n^i,\, \boldsymbol{\theta}_n^i)$ from the previous Picard iteration step. Please note that there is no unique way of doing this, but we acknowledge that some linearizations may have better-fixed point convergence properties than others. Here, we derive the following form of the linearized weak form (see Section A.2.3 in the Appendix for details):

$$\begin{aligned}0 = &-\int_0^1 \left[\boldsymbol{d}_{3,n}^i \otimes \boldsymbol{d}_{3,n}^i + K_c \left(\boldsymbol{1} - \boldsymbol{d}_{3,n}^i \otimes \boldsymbol{d}_{3,n}^i\right)\right] \tilde{\partial}_t^{(k)} \boldsymbol{r}_n^{i+1} \cdot \boldsymbol{\phi}\, ds \\ &-\int_0^1 \left\{\boldsymbol{Q}_n^{i,T} \left[\boldsymbol{S}\left(\boldsymbol{Q}_n^i \partial_s \boldsymbol{r}_n^{i+1} - \boldsymbol{e}_3\right) + \tilde{\boldsymbol{S}}\left(\boldsymbol{Q}_n^i \partial_s \tilde{\partial}_t^{(k)} \boldsymbol{r}_n^{i+1} - \boldsymbol{A}_n^i \left(\tilde{\partial}_t^{(k)} \boldsymbol{\theta}_n^{i+1}\right) \times \boldsymbol{Q}_n^i \partial_s \boldsymbol{r}_n^i\right)\right] + \boldsymbol{F}_{\mathrm{A},n}^{i+1}\right\} \cdot \partial_s \boldsymbol{\phi}\, ds,\end{aligned} \tag{3.94}$$

$$\begin{aligned}0 = &-\int_0^1 K_{\|} \boldsymbol{Q}_n^{i,T} \left[\boldsymbol{e}_3 \otimes \boldsymbol{e}_3 + K_\gamma \left(\boldsymbol{1} - \boldsymbol{e}_3 \otimes \boldsymbol{e}_3\right)\right] \boldsymbol{A}_n^i \tilde{\partial}_t^{(k)} \boldsymbol{\theta}_n^{i+1} \cdot \boldsymbol{\phi}\, ds \\ &+\int_0^1 \left\{\partial_s \boldsymbol{r}_n^i \times \boldsymbol{Q}_n^{i,T} \left[\boldsymbol{S}\left(\boldsymbol{Q}_n^i \partial_s \boldsymbol{r}_n^{i+1} - \boldsymbol{e}_3\right) + \tilde{\boldsymbol{S}}\left(\boldsymbol{Q}_n^i \partial_s \tilde{\partial}_t^{(k)} \boldsymbol{r}_n^{i+1} - \boldsymbol{A}_n^i \left(\tilde{\partial}_t^{(k)} \boldsymbol{\theta}_n^{i+1}\right) \times \boldsymbol{Q}_n^i \partial_s \boldsymbol{r}_n^i\right)\right]\right\} \cdot \boldsymbol{\phi}\, ds \\ &-\int_0^1 \left\{\boldsymbol{Q}_n^{i,T} \left[\boldsymbol{B} \boldsymbol{A}_n^i \partial_s \boldsymbol{\theta}_n^{i+1} + \tilde{\boldsymbol{B}}\left(\boldsymbol{A}_n^i \partial_s \tilde{\partial}_t^{(k)} \boldsymbol{\theta}_n^{i+1} + \left(\tilde{\partial}_t^{(k)} \boldsymbol{A}_n^{i+1}\right) \partial_s \boldsymbol{\theta}_n^i\right)\right] + \boldsymbol{L}_{\mathrm{A},n}^{i+1}\right\} \cdot \partial_s \boldsymbol{\phi}\, ds,\end{aligned} \tag{3.95}$$

which converges for most combinations of physical model parameters in the range of interest. In cases where the fixed point does not converge, the solution of the nonlinear weak form can be approximated by the solution to the linearized weak form. We show in Section 3.5.2 that the solution of the linearized weak form converges to the nonlinear solution in the limit of small time steps and large numbers of mesh points.

The variables $\boldsymbol{d}^i_{3,n}$, $\boldsymbol{Q}^i_n$ and $\boldsymbol{A}^i_n$ implicitly depend on the state variables from the previous iteration step as indicated by the i superscript. To solve the linearized problem for the unknowns $(\boldsymbol{r}^{i+1}_n, \boldsymbol{\theta}^{i+1}_n)$, we use the open-source platform FEniCS, which implements an automated finite element scheme for solving partial differential equations numerically [4, 90]. At each time step, the linear system yields a band matrix problem since the equations of motion only involve local interactions.

To decide whether the Picard iteration has converged, we require the normalized mean absolute error integral between the solutions of two consecutive iteration steps to be smaller than the desired tolerance tol. This can be expressed as follows:

$$\frac{\int_0^1 \left|\boldsymbol{r}^{i+1}_n - \boldsymbol{r}^i_n\right| \, ds}{\int_0^1 \left|\boldsymbol{r}^{i+1}_n - \boldsymbol{r}_{n-1}\right| \, ds} < \text{tol}, \qquad \frac{\int_0^1 \left|\boldsymbol{\theta}^{i+1}_n - \boldsymbol{\theta}^i_n\right| \, ds}{\int_0^1 \left|\boldsymbol{\theta}^{i+1}_n - \boldsymbol{\theta}_{n-1}\right| \, ds} < \text{tol}, \tag{3.96}$$

where we used the mean absolute error integral between the current iteration's solution and the solution from the previous time step as normalization. This ensures that the error is relatively small compared to the average change of the state variables per time step. Throughout this study, we will employ a tolerance of $\text{tol} = 10^{-3}$.

To conclude, this chapter derived a fully discretized expression for the linearized weak form of the dimensionless equations of motion, as formulated in Eqs. (3.94) and (3.95). Adopting free-end boundary conditions, we constrain the internal force and torque to be zero at both ends of the rod. Additionally, we require the actuation force and torque to be zero at these boundaries, a choice motivated by the typical absence of muscles or molecular motors at the swimmer's head and tail tips. To obtain a solution for the initial nonlinear weak form of our model, we employ the Picard iteration as a solution strategy. With the numerical scheme of our model established, we proceed to test its numerical accuracy.

3.5 Numerical Validation

The main goal of this section is to validate the numerical scheme introduced in the previous section. For this purpose, we simulate undulation experiments, systemically varying the time step Δt, number of mesh points N, and finite difference order k. To compare the results of these simulations, we define a set of metrics suitable in the context of undulatory locomotion. Our analysis demonstrates that these metrics converge to a baseline solution as spatial and temporal resolution increase. Based on this convergence analysis, we establish a relationship between the scheme's numerical accuracy and the discretization parameters Δt, N, and k. This understanding allows us to make an informed choice for the discretization parameters, ensuring sufficient numerical accuracy while being computationally efficient.

The discretization parameters selected through this process will be employed in subsequent chapters for simulations.

3.5.1 Simulation Showcase

To set the stage, we first showcase an exemplary simulation result of an undulatory locomotion experiment; see Fig. 3.5 and Vid. 3.1. In the experiment, the swimmer starts in a straight, stress-free configuration. To generate undulatory locomotion, we apply a sinusoidal actuation torque $\boldsymbol{F}_{\mathrm{A}}$ traveling along the swimmer's body as defined in Eq. (3.42). During the first undulation cycle, the swimmer transitions from its initial straight configuration to a wave-like body shape. In the subsequent undulation cycles, it deforms its body in a consistent and periodic manner. For this simulation, the physical model parameters are chosen to match the available experimental data for *C. elegans*. As discretization parameters, we select the time step $\Delta t = 0.001$, the number of mesh points $N = 750$, and the finite difference order $k = 3$; a choice we will motivate in the next section.

Having presented an overview of the experiment setup, we now discuss the specific simulation results in more detail. Fig. 3.5A shows the trajectory of the centreline's centroid $\boldsymbol{R}(t)$ and the centreline's midpoint $\boldsymbol{r}(t, 0.5)$ in the dorsal-ventral plane. Those trajectories qualitatively resemble the experimental data presented in Sznitman *et al.* [126]. The centroid $\boldsymbol{R}(t)$ exhibits an oscillatory pattern around the constant swimming direction $\boldsymbol{e}_{\mathrm{S}}$, commonly referred to as wobbling. This characteristic of the centroid's trajectory can be observed across a wide range of undulating swimmers [91, 94].

In our model, the wobbling of the centroid's trajectory can be explained as follows: First, we define the transverse direction $\boldsymbol{e}_{\mathrm{T}}$ as orthogonal to the swimming direction $\boldsymbol{e}_{\mathrm{S}}$. Next, we consider the projection of the centreline velocity $\boldsymbol{u}(s)$ onto $\boldsymbol{e}_{\mathrm{T}}$, shown in Fig. 3.5C. Here, we only show the centreline velocity profile at the onset and the midpoint of an undulation period. Integrating these velocity distributions over s yields the transverse centroid velocity, defined as $\boldsymbol{e}_{\mathrm{T}} \cdot \partial_t \boldsymbol{R}$. The velocity $\boldsymbol{e}_{\mathrm{T}} \cdot \partial_t \boldsymbol{R}$ is not zero, but it changes periodically with the undulation period, as shown in Fig. 3.5D. This explains the wobbling of the swimmer's centroid. However, its magnitude is one order of magnitude smaller compared to the centroid's velocity in the swimming direction $\boldsymbol{e}_{\mathrm{S}}$, which is denoted as $U(t)$ and is shown in Fig. 3.5B. This explains why the swimmer's centroid's lateral side-to-side movement is small compared to its movement in the primary swimming direction. As $\boldsymbol{e}_{\mathrm{T}} \cdot \partial_t \boldsymbol{R}$ is centered around zero, see Fig. 3.5D, its time average of over one undulation period is zero. Consequently, the net movement of the centroid in the transverse direction $\boldsymbol{e}_{\mathrm{T}}$ during one undulation cycle is zero. This explains why the swimming direction remains constant throughout the simulation.

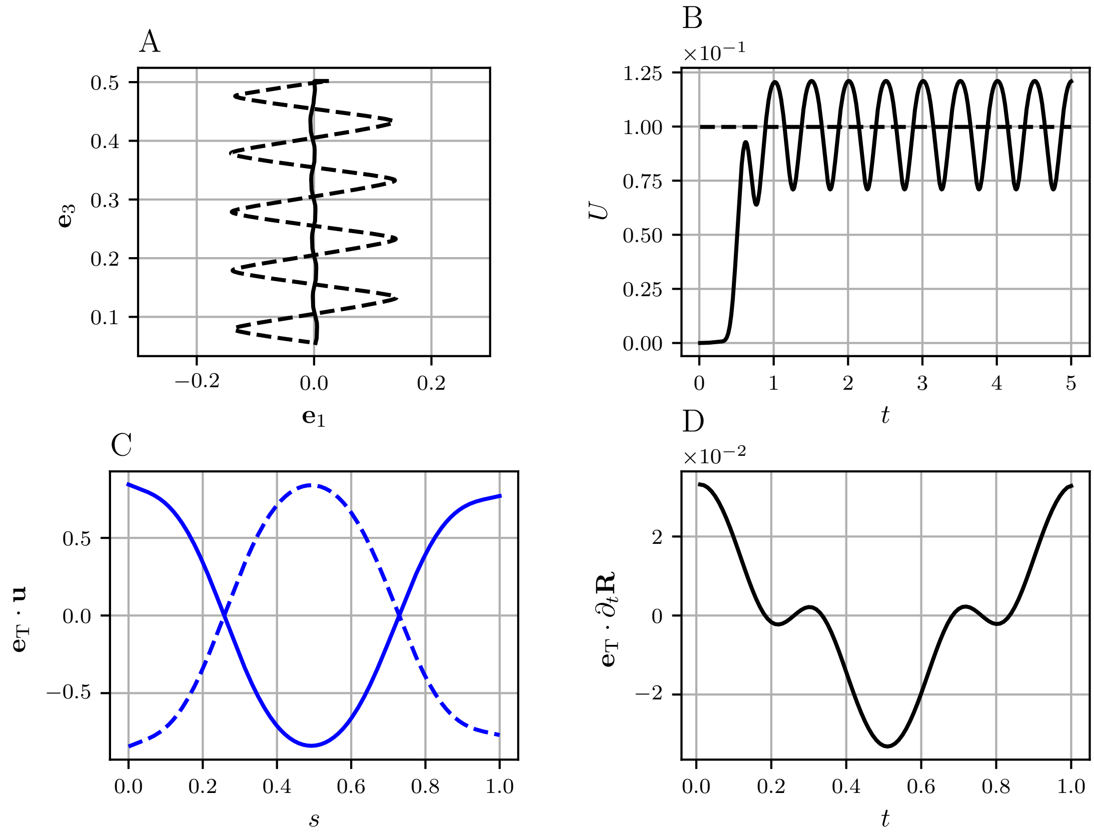

Figure 3.5: Centreline trajectory and swimming speed during undulatory locomotion. (**A**): Trajectories of the centreline's centroid $\boldsymbol{R}(t)$ (solid) and the centreline's midpoint $\boldsymbol{r}(0.5, t)$ (dashed). (**B**): Instantaneous swimming speed $U(t)$ (solid) and average swimming speed U (dashed). (**C**): Transverse centreline velocity $\boldsymbol{e}_\mathrm{T} \cdot \boldsymbol{u}$ along the body at the onset (solid) and the midpoint of the undulation cycle (dashed). (**D**): Transverse centroid velocity $\boldsymbol{e}_\mathrm{T} \cdot \partial_t \boldsymbol{R}$ during one undulation cycle. Physical model parameters: Young's modulus $E = 1.2 \times 10^5\,\mathrm{Pa}$ [13, 45], ratio of the extensional viscosity to Young's modulus $\xi = 1 \times 10^{-2}\,\mathrm{s}$ [45], Poisson's ratio $\varrho = 0.5$ [48], reference length $L_0 = 1130\,\mu\mathrm{m}$ [5], maximal cross-sectional radius $R_\mathrm{max} = 32\,\mu\mathrm{m}$ [13], fluid viscosity $\mu = 1 \times 10^{-3}\,\mathrm{Pa\,s}$, undulation frequency $f = 1\,\mathrm{Hz}$. From the physical model parameters, we derive the following values for the dimensionless model parameters using Eqs. (3.57), (3.30) and (3.62): $a = 0.033$, $b = 0.01$, $p = 0.33$, $g = 2.0 \times 10^{-4}$. Drag coefficient ratios, $K_c = 1.5$, $K_\gamma = 4.0$ and $K_\| = 1.2 \times 10^{-3}$ Preferred dimensionless undulation parameters are $A_0 = 2\pi$ and $\lambda_0 = 1$.

After having analyzed the trajectory of the swimmer's centroid, we now consider its instantaneous swimming speed $U(t)$ illustrated in Fig. 3.5B. In the first undulation cycle, the swimmer transitions from its initial straight configuration to periodic undulatory locomotion, and $U(t)$ exhibits a sharp increase. Following this initial transient, $U(t)$ undergoes oscillations at a consistent frequency around a steady baseline value, denoted as the average swimming speed U. For the specific model parameters, the dimensionless swimming speed is $U = 0.1$, i.e. the swimmer covers a distance of 0.1 body length L_0 per undulation cycle, which follows from Eq. (3.77). This value is comparable to the experimentally measured swimming speed of *C. elegans* [50, 126]. However, we acknowledge that the experimentally observed swimming speeds are slightly larger than 0.1. A possible explanation for this discrepancy lies in our assumption of an unconfined fluid environment. In the cited experiments, *C. elegans* swim within a narrow walled chamber filled with liquid, constraining their motion to a planar trajectory. This narrow confinement alters the fluid dynamics, resulting in a larger linear drag coefficient ratio K_c and, consequently, faster swimming speeds [21].

Following our discussion of the swimmer's centroid kinematics, we now shift our focus to the swimmer's deformation kinematics. As we discussed in Section 3.1.2, they are characterized by the curvature vector $\bar{\boldsymbol{\kappa}}$ and the strain vector $\bar{\boldsymbol{\sigma}}$ in the body frame. Throughout the undulation experiment, the swimmer's configuration remains planar and twist-free. This implies that only the first component $\bar{\kappa}_1$ of the curvature vector, which measures the bending in the dorsal-ventral plane, is nonzero. Henceforth, we will refer to $\bar{k}_1$ as the body curvature $\bar{k}$. The first component $\bar{\sigma}_1$ of the shear vector, which measures shearing perpendicular to the dorsal-ventral plane, is zero. Hence, it is sufficient to only consider the shear vector's second component $\bar{\sigma}_2$ and the third component $\bar{\sigma}_3$.

Fig. 3.6A presents a color plot of the body curvature $\bar{\kappa}$ as a function of time t and body coordinate s, referred to as a kymogram. The kymogram's distinct striped patterns are indicative of the curvature wave, propagating from the swimmer's head to its tail while it actively deforms its body. We emphasize that similar curvature kymograms to the one shown in Fig. 3.6A have been observed in a multitude of experimental studies of undulatory locomotion [40, 45, 125, 126]. Each stripe is composed of diagonal lines of equal curvature, except at the body boundaries, where the curvature rapidly decreases to zero. This sharp decrease in curvature is a consequence of the actuation torque being constrained to zero at the boundaries, as we discussed in Section 3.4.1. The slope of the stripes is equivalent to the curvature wave's propagation speed v. The undulation frequency f can be determined by dividing the number of undulation cycles visible in the kymogram by the simulation time T_{sim}=5. With knowledge of v and f, the undulation wavelength λ can be determined from the relationship $v = \lambda \cdot f$. Here, we assume that the wave's propagation speed is constant along the body, which is not necessarily the case, as we will discuss in Chapter 4.

Fig. 3.6B shows a kymogram of the preferred curvature $\kappa_0(s,t)$, which is defined as the first component of the preferred curvature $\boldsymbol{\kappa}_0(s,t)$, introduced in Section 3.2. The preferred curvature kymogram closely resembles the kymogram of the emergent body curvature in Fig. 3.6A. This is because, for the chosen model parameters, the system's response time is relatively fast compared to the undulation frequency f_0 of the preferred curvature, i.e. the body curvature κ tracks the preferred curvature κ_0 instantaneously. In such a scenario, the preferred and actual undulation parameters are approximately equivalent, which can be expressed as follows:

$$A \approx A_0, \quad \lambda \approx \lambda_0, \quad f \approx f_0 = 1. \tag{3.97}$$

A detailed analysis of the relationship between κ and κ_0 as a function of the model parameters will be undertaken in Chapter 4.

Fig. 3.6C and Fig. 3.6D show the kymograms of the swimmer's body shear strain $\bar{\sigma}_2$ and extensional strain $\bar{\sigma}_3$, respectively. Both kymograms display a similar stripy pattern to the one observed for the body curvature in Fig. 3.6A. This is not surprising because the shear and extensional deformations are an indirect consequence of the bending deformation initiated by the actuation torque. Note that the stripes are not straight lines, i.e. the propagation speed of the shear and extension wave changes with the position s along the swimmer's body. Importantly, the order of magnitude of $\bar{\sigma}_2$ and $\bar{\sigma}_3$ is much smaller compared to the body curvature $\bar{\kappa}$. This is a consequence of the large linear viscoelastic resistance the swimmer's slender body exhibits with respect to shear and extensional deformations, as discussed in Section 3.3. Consequently, we hypothesize that shear and strain deformations only play a marginal role in the context of undulatory locomotion in the parameter regime of *C. elegans*.

Having presented exemplary evidence that our model generates centroid trajectories, swimming speeds, and body posture qualitatively reminiscent of those experimentally observed in *C. elegans*, we further verify the reliability of our numerical scheme by demonstrating that it is energy-conserving up to a small relative error. In Fig. 3.6A, we plot the powers defined in Section 3.1.4 as a function of time. These powers include the actuation power $\dot{W}$ (green), the dissipation rate $\dot{D}$ (red), and the temporal rate of change in potential energy $\dot{V}$ (black). After the first initial undulation cycle, these powers oscillate around a constant baseline value with undulation frequency f. This periodic behavior is expected, given that the powers are defined in terms of the swimmer's kinematic and shape parameters, which themselves are periodic functions in f. Specifically, the rate of change in potential energy $\dot{V}$ oscillates around zero, signifying that there is no net increase or decrease in the swimmer's potential energy V within a single undulation cycle. Furthermore, we confirm that the total dissipation rate $\dot{D}$ is strictly negative as predicted by Eq. (3.32).

The instantaneous power balance, given by Eq. (3.36), demands that the signed sum of all powers must equate to zero for all t. In Fig. 3.6B, we confirm that our numerical scheme fulfills the instantaneous power balance at each time step up to a relative error in the order of $\mathcal{O}(10^{-2})$. Here, we normalized the absolute error by the time-averaged actuation power $\text{avg}(\dot{W})$ such that it is relative to the order of magnitude of the powers depicted in Fig. 3.6A.

Integrating the power balance from the start of the last undulation cycle at $t = 4$ to the

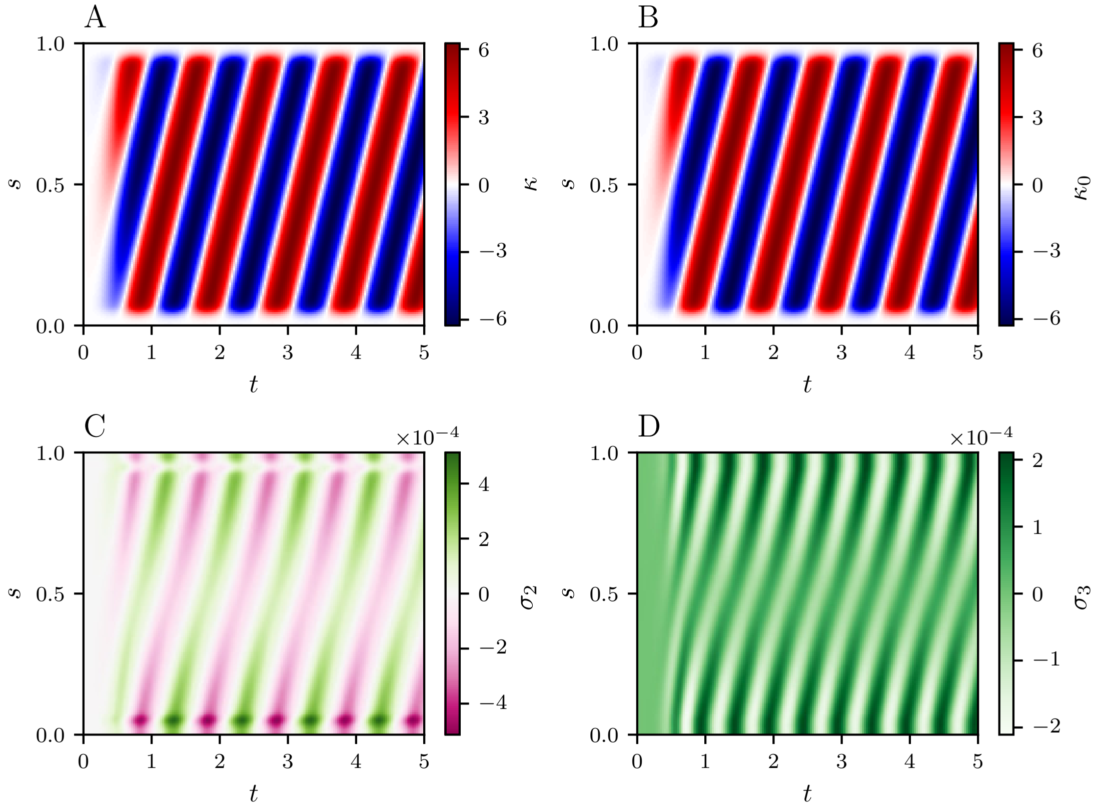

Figure 3.6: Strain measures of the swimmer's body during undulatory locomotion. (**A**): Kymogram of the emergent body curvature $\kappa(s,t)$. (**B**): Kymogram of the preferred curvature $\kappa_0(s,t)$. (**C**): Kymogram of the dorsal-ventral shear strain $\sigma_2(s,t)$. (**D**) Kymogram of the dorsal-ventral extensional strain $\sigma_3(s,t)$. Model parameters are identical to those in Fig. 3.5.

time point $4+t$ yields the energy balance equation

$$\Delta V(4,t) = D(4,4+t) + W(4,4+t), \tag{3.98}$$

where $\Delta V(4,t)$, $D(4,t)$ and $W(4,t)$ are the change in potential energy, the dissipated energy, and the actuation work during the time interval $[4,4+t]$, respectively. For brevity's sake, we will suppress the starting point 4 in the energy function's argument. Fig. 3.6C shows $\Delta V(t)$, $D(t)$ and $W(t)$ as a function of time in t. We confirm that the net change in potential energy after one undulation cycle is zero. Furthermore, the dissipated energy D decreases monotonically as expected. The energy balance Eq. (3.37) states that the change in potential energy $\Delta V(t)$ must equal the sum of dissipated energy $D(t)$ and actuation work $W(t)$ at any time t. Fig. 3.6D confirms that our numerical scheme fulfills this energy balance up to a small relative error of the order of $\mathcal{O}(10^{-3})$. Here, we used the mechanical actuation work $W = W(T)$ per undulation cycle as our normalization. We remind the reader that W

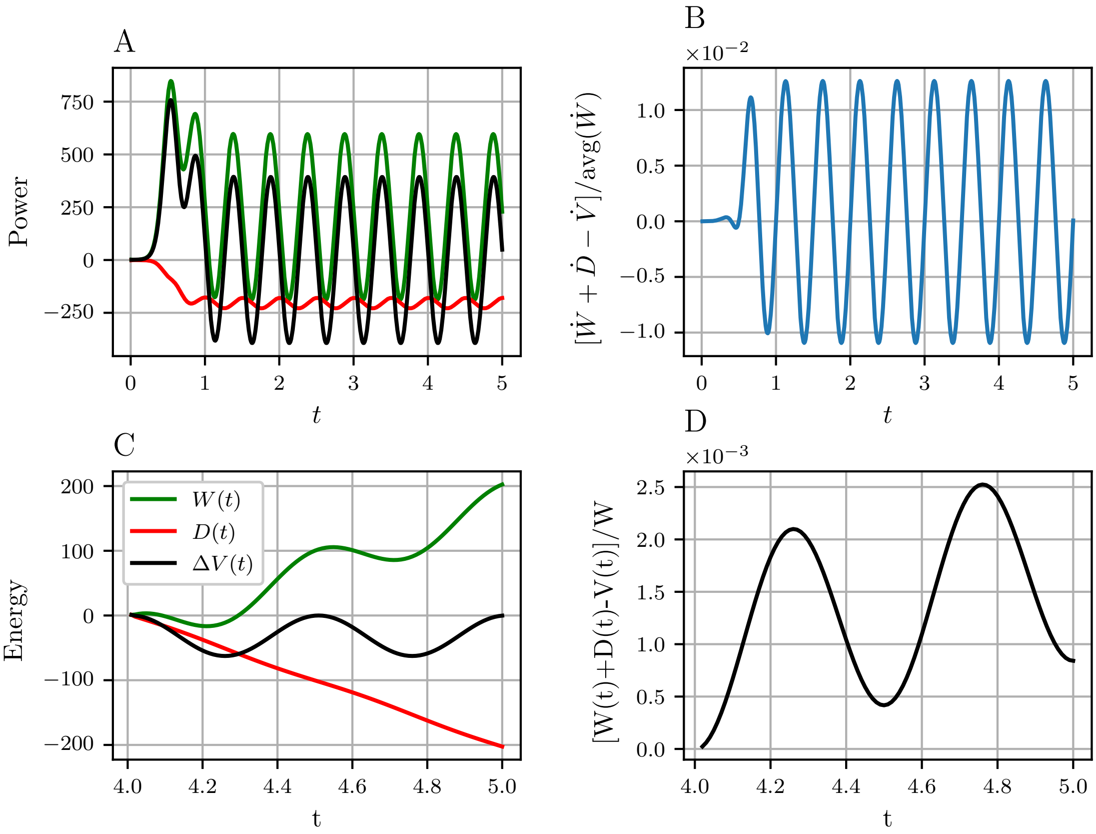

Figure 3.7: Power and energy balance during undulatory locomotion. (**A**): Actuation power $\dot{W}$ (green), net dissipation rate $\dot{D}$ (red), and change in potential energy per unit time $\dot{V}$ (black) as a function of time. (**B**): Instantaneous power balance $0 = \dot{W} + \dot{D} - \dot{V}$ as a function of time, normalized by the time-averaged actuation power avg($\dot{W}$). (**C**): The actuation work $W(t)$ (green), dissipated energy $\dot{D}(t)$ (red) and change in potential energy $\Delta V(t)$ (black) as a function of time during the last undulation period. (**D**): Energy balance $0 = W(t) + D(t) - \Delta V(t)$ as a function time normalized by actuation $W = W(T)$ required during one undulation cycle. Model parameters are identical to those in Fig. 3.5.

will serve as our proxy to estimate the energetic cost of swimming, as discussed in Section 3.1.4.

After showcasing the simulation results for an exemplary undulation experiment that illustrates realistic undulatory locomotion and affirms that our numerical scheme conserves energy up to a small relative error, we now conduct a thorough convergence analysis of our scheme. The goal is to determine optimal discretization parameters that achieve the desired accuracy while being computationally efficient.

3.5.2 Convergence Analysis

In the preceding section, we showcased the simulation results of an undulation experiment featuring fixed model and undulation parameters. This section systematically analyses the convergence properties of our numerical scheme with respect to discretization parameters Δt and N and k. For this purpose, we repeat the previously presented undulation experiment for different Δt, N and k values. The outcome of these experiments is asset based upon the following three metrics:

1. The final position of the centreline's centroid, denoted as $\boldsymbol{R}$
2. The swimmer's average swimming speed U
3. The energetic swimming cost W

Here, we choose U and W as performance metrics, as they are the key objectives we will consider when comparing the performance of different undulation gaits in the upcoming sections. Furthermore, we consider $\boldsymbol{R}$ to ensure that our scheme produces reliable straight trajectories and does not introduce a bias.

To establish a benchmark for comparison, we designate the numerical solution for the smallest time step $\Delta t_{\mathrm{min}} = 10^{-4}$, the maximum number of mesh points $N_{\mathrm{max}} = 1000$, and the highest finite difference order $k_{\mathrm{max}} = 5$ as our reference solution. Using this reference solution, we calculate the reference centroid position $\boldsymbol{R}_{\mathrm{ref}}$, the reference swimming speed U_{ref} and the energetic reference cost W_{ref}. Subsequently, for any given combination of discretization parameters N, dt and k, we denote the relative error between the metrics and their corresponding reference values as follows:

$$\varepsilon_{\boldsymbol{R}} = \frac{|\boldsymbol{R} - \boldsymbol{R}_{\mathrm{ref}}|}{|\boldsymbol{R}_{\mathrm{ref}}|}, \quad \varepsilon_U = \frac{|U - U_{\mathrm{ref}}|}{U_{\mathrm{ref}}}, \quad \varepsilon_W = \frac{|W - W_{\mathrm{ref}}|}{W_{\mathrm{ref}}} \tag{3.99}$$

Here, $\boldsymbol{R}$, $\bar{\boldsymbol{U}}$, and W are functions of Δt, N and k. In Fig. 3.8A-C, we plot $\varepsilon_{\boldsymbol{R}}$, ε_U and ε_W as functions of the time step Δt, while maintaining a constant number of mesh points N. Different markers correspond to distinct values of the finite difference order k, as indicated by the legend in panel D. For $k = 1$, all three errors decrease linearly over the full range of Δt, suggesting a power-law relationship of the form $\varepsilon_{\boldsymbol{R}}, \varepsilon_U, \varepsilon_W \propto \Delta t^{\alpha}$. For $k > 1$, the errors initially decrease linearly; however, for sufficiently small Δt, they plateau and fluctuate around a constant saturation value, which we represent by the dotted horizontal yellow lines. The higher the order k, the steeper the slope in the linear regime, and the faster the error reaches its plateau.

To determine the scaling exponent α, we perform a linear regression for the data points within the linear regime in each panel. The result of these linear regressions is shown by the dashed red lines. Note that we only consider the first and second finite difference orders, which both exhibit a clearly visible linear behavior for all three errors. The linear regressions yield an average scaling exponent of $\alpha = 1.00$ for $k = 1$ and $\alpha = 2.06$ for $k = 2$. This suggests that the temporal discretization error is determined by the error of the finite difference approximation, which scales as $\mathcal{O}(\Delta t^k)$.

The saturation of the temporal discretization errors hints at additional error sources inherent in our numerical scheme. These errors, apparently independent of the time step Δt, must lead to errors in the centroid position, swimming speed, and energy cost, which are in the same order of magnitude as the saturation values displayed by the horizontal yellow dotted lines in Fig. 3.8A-C. Possible error sources include the tolerance of the linear solver used by FEniCS and the tolerance that determines the convergence of the Picard iteration. In Fig. 3.8A-C, the errors $\varepsilon_{\boldsymbol{R}}$ and ε_U and ε_W saturate at orders of magnitude of 10^{-4}, 10^{-5} and 10^{-8}, respectively. These orders fall well below our desired level of accuracy, as we will motivate in a subsequent paragraph. Consequently, further investigation into the origin of these additional error sources will not be pursued.

Having analyzed the temporal accuracy of our numerical scheme, we now turn our attention to its spatial discretization errors. In Fig. 3.8D-F, we present the relative errors $\varepsilon_{\boldsymbol{R}}$, ε_U and ε_W as a function of the number of mesh points N while maintaining a constant time step $\Delta t = 10^{-4}$. The errors in Fig. 3.8D-F decrease linearly on a log-log scale, indicating a power-law relationship of the form $\varepsilon_{\boldsymbol{R}}$, ε_U, $\varepsilon_W \propto N^{-\beta}$. Furthermore, we observe that the errors in Fig. 3.8D-F are independent of k, which is to be expected since the finite difference order should only change the scaling of the temporal discretization error. Notably, for $k = 1$, the error ε_W in Fig. 3.8F remains constant while N increases. This behavior can be explained by the fact that for $k = 1$, the temporal discretization error dominates over the spatial discretization error even when the finest time step Δt_{min} is employed.

To determine the scaling exponent β, we perform a linear regression on all the data points in each of the panels in Fig. 3.8D-F, excluding ε_W for $k = 1$. The resulting fits yield an average scaling exponent $\beta = 2.18$. Note that each of the metrics $\boldsymbol{R}$, $\bar{U}$ and W involves an integral over the body coordinate s. For piecewise linear basis functions, this body integral introduces an error that scales with order $\mathcal{O}(N)$. The larger value of the scaling exponent β indicates additional factors contributing to the spatial discretization errors, which will not be investigated.

Based on the convergence analysis presented in Fig. 3.8, our objective is to select a temporal-spatial resolution that balances accuracy with computational efficiency. It is essential to underscore that our model functions as a simplified representation of actual biological microswimmers. Consequently, our primary goal is to attain a qualitative under-

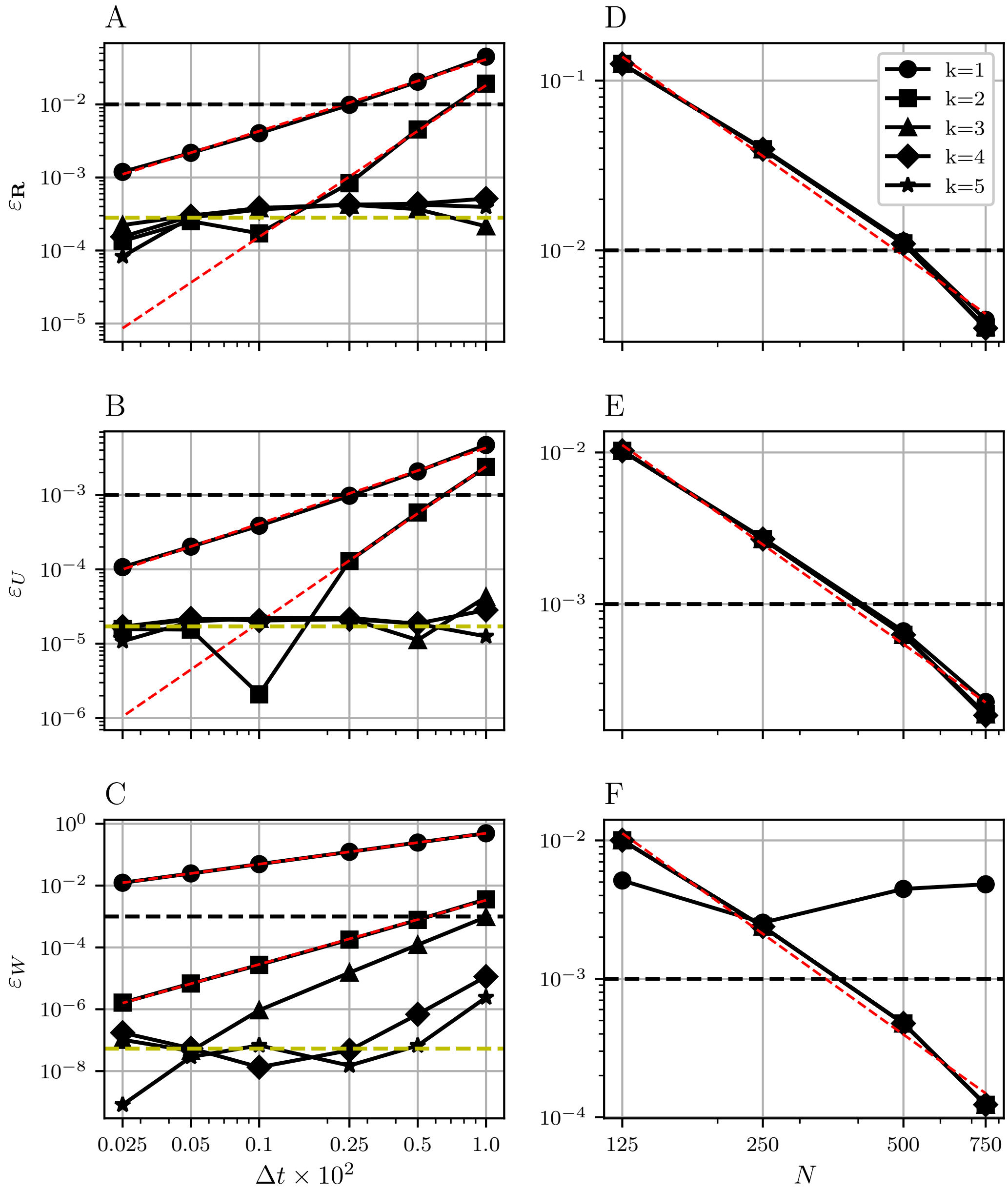

Figure 3.8: Convergence analysis of the numerical model scheme with respect to its discretization parameters in undulation experiments. (**A**, **B**, **C**): Relative errors $\varepsilon_{\boldsymbol{R}}$, ε_U and ε_W as a function of the time step Δt for maximum meshsize of $N_{\max} = 1000$. (**D**, **E**, **F**): Relative errors $\varepsilon_{\boldsymbol{R}}$, ε_U and ε_W as a function of mesh points N with minimum time step $\Delta t_{\min} = 0.0001$. The different markers correspond to different finite difference order k as indicated by the legend in panel D. Linear fits, depicted by the red dashed lines, yield average scaling exponents x of x=1.00 for $k = 1$ and x=2.08 for $k = 2$. Saturation values, represented by the yellow dashed lines, are estimated by averaging data points in the non-linear saturation regime. The saturation values in panel A-C are 2.81×10^{-4}, 1.71×10^{-5} and 5.32×10^{-8}, respectively. The average scaling exponent calculated from the linear fits in D-F is x=-2.18. Black dashed lines represent the upper bounds of the relative errors $\varepsilon_{\boldsymbol{R}}$, ε_U and ε_W which are set to 10^{-2}, 10^{-3} and 10^{-3}, respectively. For all simulations, the same model parameters as in Fig. 3.5 have been used.

standing of their undulatory behavior rather than striving for a highly accurate numerical scheme tailored to the specific model equations outlined in Section 3.4.1. However, in Chapter 6, we conduct a quantitative comparison between simulated undulation experiments and the available experimental data for *C. elegans*. Acknowledging the inherent simplifications in our model, we do not anticipate a perfect alignment between the simulated and experimental data. Moreover, the experimental data introduces its own set of uncertainties stemming from factors such as small sample sizes, variations among individual specimens, and measurement uncertainties. To account for these uncertainties, we adopt a conservative estimate, assuming that the relative uncertainty of the experimental measurements is on the order of percent [45, 50, 126]. Consequently, it is sufficient to select the discretization parameters Δt, N and k such that the relative errors $\varepsilon_{\boldsymbol{R}}$, ε_U and ε_W remain below 10^{-2}. Here, we opt for an upper error bound of 10^{-2} for the centroid's position and an upper bound of 10^{-3} for the swimming speed and the energetic cost. These thresholds are displayed as the black dashed lines in Fig. 3.8.

One should point out that the temporal discretization error and the spatial discretization error compound, i.e. there is no benefit in refining the temporal resolution if the total error is dominated by the spatial discretization error and vice versa. From Fig. 3.8A-C, we infer that for $k \geq 3$, the relative errors remain smaller than their respective upper bounds over the entire range of time steps Δt. From Fig. 3.8D-F, we infer that for $N = 750$, the relative errors are lower than their respective upper bounds.

Among the subset of discretization parameters that yield the desired accuracy, we want to select a combination that is computationally fastest. As outlined in Section 3.4.2, to solve the nonlinear equations of motion, we first linearize their discretized weak form. We then use the Picard iteration to iteratively solve the linearized weak form until the solution convergence to the solution of the nonlinear problem. In Fig. 3.9A, we plot the simulation runtime T_{run} as a function of the time step Δt, for different number mesh points N and finite difference orders k with and without Picard iteration.

To clarify, solving the problem without Picard iteration means that we approximate the solution to the nonlinear weak form by the solution of its linearized form. This effectively equates to only performing the first iteration step of the Picard iteration at every time step. It is clear that this linear approximation demands a smaller time step to preserve the numerical scheme's accuracy in the absence of the iterative refinement provided by the Picard iteration, as we will demonstrate later.

With Picard iteration, the simulation runtime T_{run} increases approximately linearly with Δt on a log-log scale, indicating a power-law relationship of the form $T_{\text{run}} \propto c\Delta t^{\gamma}$. We observe that the constant c increases with the number of mesh points N. Moreover, we note that the runtime depends only marginally on the finite difference order k. A higher

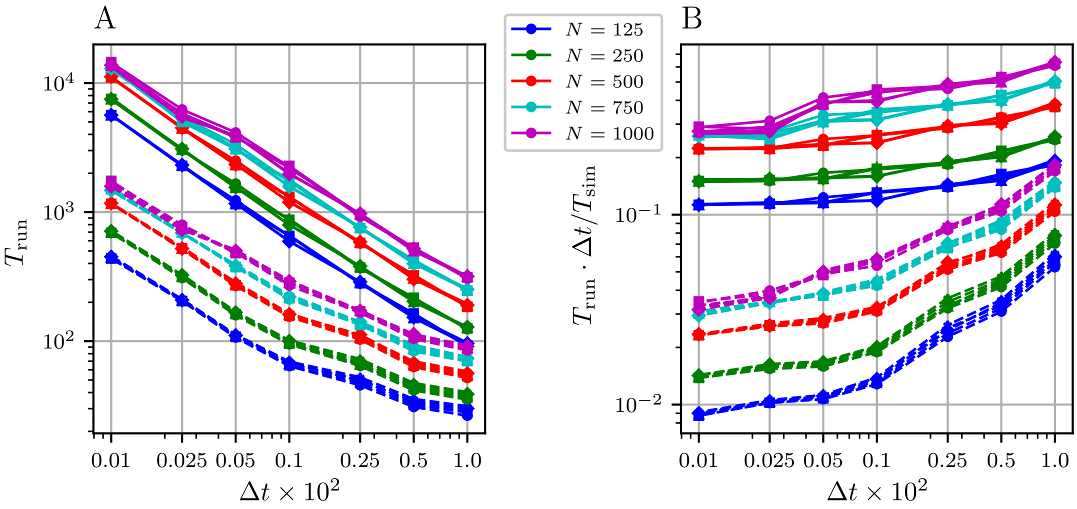

Figure 3.9: Model runtime analysis with respect to the discretization parameters in undulation experiments. (**A**): Simulation runtime T_{run} as a function of the time step Δt. The different colors represent different mesh sizes N, as depicted in the legend. The solid lines correspond to simulations with Picard iteration, and the dashed lines correspond to simulations without Picard iteration. Markers correspond to the same finite difference order k as in Fig. 3.8. For the simulation without Picard iteration, the solution to the nonlinear weak form is approximated by the solution to its linearized form. (**B**): The average runtime time per time step, defined as $T_{\mathrm{run}} \cdot \Delta t / T_{\mathrm{sim}}$, where $T_{\mathrm{sim}} = 5$ is the dimensionless simulation. The same model parameters as in Fig. 3.5 have been used for all simulations.

order k increases the assembly complexity of the matrix problem, which represents the linearized weak form at each iteration step. Consequently, we deduce that the computational complexity of the numerical scheme is primarily dominated by the solution process of the matrix problem rather than its assembly.

In Fig. 3.9B, the average runtime $T_{\mathrm{run}} \Delta t / T_{\mathrm{sim}}$ per time step Δ is shown for different values of Δt, where T_{sim} is the dimensionless simulation time. Interestingly, there is a small reduction in the average runtime as Δt decreases. In simulations employing the Picard iteration, this trend is explained by the fact that Picard iteration requires fewer iteration steps to converge as Δt decreases. This is because for smaller Δt, the solution from the previous time step, which we use as the initial guess for Picard iteration, is in closer proximity to the solution of the subsequent time step. Surprisingly, a similar trend is observed for the simulations without Picard iteration. One plausible explanation is that the matrix problem can be solved more efficiently if the time step is smaller.

Not surprisingly, the simulation runtime is significantly reduced if the Picard iteration is omitted, as shown by the dashed lines in Fig. 3.9AB. To judge if the linear approximation is computationally more efficient than the Picard iteration, we need to determine the temporal and spatial resolution, which is required for the linear approximation to undercut the previously defined upper error bounds. With this intention, we simulate the undulation experiment without Picard iteration for different discretization parameters Δt, N, and k and compare the results against the reference solution. In Fig. 3.10A-C, we plot the relative errors $\varepsilon_{\boldsymbol{R}}$, ε_U and ε_W as a function of the time Δt.

If we select a time step of $\Delta t = 10^{-3}$, number of mesh points $N = 750$, and finite difference order $k \geq 2$, the relative errors are comfortably below the respective upper error bounds. Note that we deliberately made a conservative selection to enhance the chance that our numerical scheme achieves the desired accuracy across a wide range of model parameters. With these discretization parameters, the simulation runtime without Picard iteration stands at $T_{\text{run}} = 218\,\text{s}$. In contrast, even for the largest time step $\Delta t = 10^{-2}$, the simulation's runtime with Picard iteration extends to $T_{\text{run}} = 250\,\text{s}$, surpassing the runtime of the simulation conducted without Picard iterations.

We conclude with some overarching remarks: We are surprised by the large number of mesh points required to achieve the desired accuracy. This may be attributed to the sharp sigmoidal onset of the actuation torque at the swimmer's head and tail introduced in Section 3.4.1. Accurately capturing this sharp sigmoidal onset demands a finer mesh at the swimmer's head and tail compared to its central body region. Consequently, implementing a non-uniform mesh could potentially reduce the total number of required mesh points. Such a non-uniform mesh should have a finer resolution at the swimmer's head and tail and a coarser resolution at its central body region.

Our analysis reveals that the simulation runtime is approximately independent of the finite difference order k. Additionally, the memory cost associated with storing the state variables from the k preceding time steps required for the finite difference calculation is marginal. This is because the rod's mesh is one-dimensional. Therefore, when employing the Picard iteration to solve the problem, we recommend selecting a large k, which allows for a larger time step Δt to achieve the desired accuracy. However, it is important to acknowledge that a maximum value for k will exist above which the scheme's accuracy plateaus. This saturation is caused by other error sources inherent within the scheme. Specifically, for the centroid position, swimming speed, and energy cost, opting for values larger than $k = 4$ yields minimal benefits in accuracy.

Opting to bypass the Picard iteration and approximating the solution to the nonlinear problem with the solution of the linearized problem necessitates a smaller time step to achieve comparable accuracy. However, omitting the Picard iteration reduces the runtime of the simulation, i.e. it is not a priori clear which scheme is preferable. For the specific model parameters and desired accuracy chosen in this section, skipping the Picard iteration yields at least a 10% gain in runtime. Thus, we opt to solve the problem without Picard iteration. However, according to our results, neither of the two methods demonstrates a

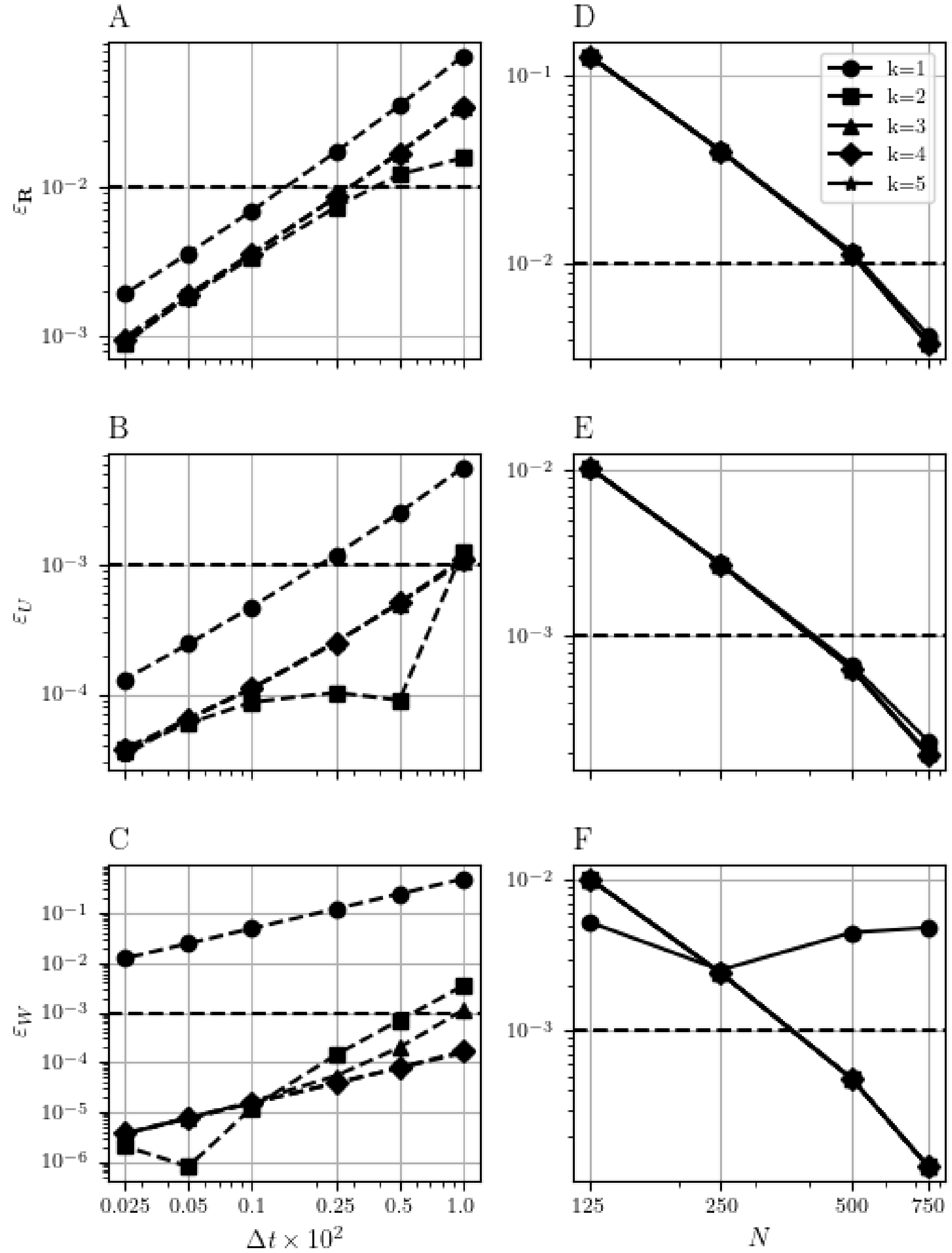

Figure 3.10: Convergence analysis of the numerical model scheme with respect to its discretization parameters in undulation experiments without Picard iteration. (**A**, **B**, **C**): Relative errors $\varepsilon_{\boldsymbol{R}}$, ε_U and ε_W as a function of the time step Δt for maximum meshsize $N_{\max} = 1000$. (**D**, **E**, **F**): Relative errors $\varepsilon_{\boldsymbol{R}}$, ε_U and ε_W as a function of the mesh points N with minimum time step $\Delta t_{\min} = 0.0001$. Markers correspond to distinct finite difference orders k, as displayed by the legend in panel D. Black dashed lines represent the upper bounds of the relative errors $\varepsilon_{\boldsymbol{R}}$, ε_U and ε_W which are set to 10^{-2}, 10^{-3} and 10^{-3}, respectively. For all simulations, the same model parameters as in Fig. 3.5 have been used.

significant advantage. For the remainder, we adopt $\Delta t = 10^{-3}$, $N = 750$, and $k = 3$ as our default parameters unless otherwise stated.

To give the reader a better sense of the run times required to perform extensive parameter sweeps with our model, we report the run times of two sweeps performed to obtain the results presented in the upcoming chapters. In Chapter 4, we perform a parameter sweep over the dimensionless response times a and b while keeping all other model parameters fixed. This sweep includes 61 points within the range $a \in [10^{-2}, 10^{4}]$ and 31 points within the range $b \in [10^{-3}, 10^{0}]$, using uniform logarithmic spacing. Thus, a total of 1891 simulations are required, each taking on average $T_{run} = 9.77\,\mathrm{min}$ to complete five undulation cycles. Therefore, the overall runtime for the parameter sweep approximates 308 h. However, individual simulations can be executed in parallel to reduce the effective run time. Thus, employing ten cores in parallel reduces the run time to approximately 30.8 h, and with a hundred cores, it diminishes further to 3.08 h.

To give another example, in Chapter 6, we sweep over the preferred shape factor $c_0 = A_0/q_0$, preferred wavelength λ_0, and the fluid viscosity μ to compare the performance of *C. elegans* undulation gait as a function of its waveforms in fluids with different viscosities. For the undulation parameters, we select a uniform grid spacing $\Delta\lambda_0 = 0.1$ within the range $\lambda_0 \in [0.5, 2.0]$ (16 points) and $\Delta c_0 = 0.1$ within the range $c_0 \in [0.4, 2.0]$ (17 points). For the fluid viscosity, we use a uniform logarithmic spacing with 21 points within the range $\mu \in [10^{-3}, 10^{1}]\mathrm{Pa\,s}$. Hence, the sweep includes 5712 simulations, each taking on average $T_{run} = 10.03\,\mathrm{min}$ to complete five undulation cycles, resulting in an overall runtime of approximately 955 h. This runtime is the longest among all parameter sweeps conducted in this thesis.

With the numerical scheme established, we proceed to analyze our model's dynamical properties in the context of undulatory locomotion. Specifically. we aim to understand how these properties are determined by the dimensionless and, consequently, physical model parameters.

Chapter 4

Model Exploration

Effortless undulation or persistent struggle

4.1 Overview

In the previous chapter, we provided a detailed description of our model formulation. Our model aims to describe the undulatory locomotion of a slender limbless microswimmer immersed in a Newtonian fluid environment. This chapter explores how our model responds to actuation. The swimmer's response properties are determined by its geometry, material parameters, and the viscosity of its surrounding fluid environment. Hence, we consider the swimmer's body and the surrounding fluid as an integrated system. For readers who prefer to start with the results, we provide a brief and non-technical model overview.

The swimmer's passive body is modeled as a linear viscoelastic Cosserat rod. Elastic behavior refers to a material's ability to return to its original shape post-deformation. In the context of a Cosserat rod, a linear elastic material is characterized by a linear relationship between the rod's strain and curvature (deformation) and its internal elastic stress and torque resultants. Conversely, a linear viscous material is characterized by a linear relationship between the rod's strain and curvature rates (deformation speed) and the internal viscous stress and torque resultants. A linear viscoelastic material combines both behaviors, simultaneously resisting and damping deformation. The proportionality factors between stress and strain, as well as strain rates, are determined by the rod's geometry and the material parameters. Tab. 4.1 provides an overview of all physical model parameters.

The swimmer's body geometry is approximated as a tapered rod with a circular cross-section. Consequently, its geometry is determined by its natural length L_0 in its stress-free configuration, the maximal cross-sectional radius $R_{\max}$, and the radius shape-function φ. The shape function φ governs how the cross-sectional radius varies along the swimmer's length. To generate actuation, we apply an effective actuation force and torque distribution along the centreline of the swimmer's body. The spatio-temporal pattern of the actuation force and torque distribution determines the swimmer's locomotion pattern. In the case of undulatory locomotion, the actuation torque is modeled as a traveling wave propagating along the swimmer's body opposite to the direction of motion.

The fluid drag force and torque distribution along the swimmer's body is approximated by resistive-force theory. In resistive force theory, the drag force and the drag torque that acts on a local rod segment are assumed to be linearly proportional to the fluid viscosity and to the segment's linear and angular velocities, respectively. The proportionality factors are called drag coefficients (see Tab. 4.1).

To simplify our model formulation, we derived a dimensionless form of the rod's equations of motion. This involved introducing a set of dimensionless model parameters, which determine the dynamic properties of our system. An overview of all dimensionless model parameters is provided in Tab. 4.2.

In this chapter, our objective is to characterize the system's dynamical behavior and to identify the dimensionless model parameters that have the most impact on its response properties. To this end, it is helpful to conceptualize the system as a dynamical filter, which takes the actuation torque as an input and generates a body curvature as an output, as illustrated in Fig. 4.1.

Following this conceptual approach, Section 4.2 explores how the system's response properties depend on its effective response times a and b. To characterize the system's response properties, Section 4.2 demonstrates that the parameter space of a and b can be divided into distinct dynamical regimes. In each of these regimes, our system exhibits distinct filter characteristics, determining the input-output relationship between the actuation torque and the emergent body curvature. The effective response time a and b are defined as ratios of the physical model parameter (see Tab. 4.2). Consequently, variations in a and b can be interpreted as changes in the swimmer's body geometry, material model parameters, fluid viscosity, or undulation frequency, as illustrated by Fig. 4.1B. Conversely, depending on how the physical model parameters influence a and b, we can discern which parameters exhibit similar or opposing dynamical roles. This underscores the key advantage of our dimensionless formulation, providing a unified description across a wide range of scenarios.

Naturally, the question arises: If there are distinct dynamical regimes, in which regimes do microswimmers operate, and what motivates this evolutionary "choice"? To explore this question, Section 4.3 analyses the swimmer's performance across the different regimes.

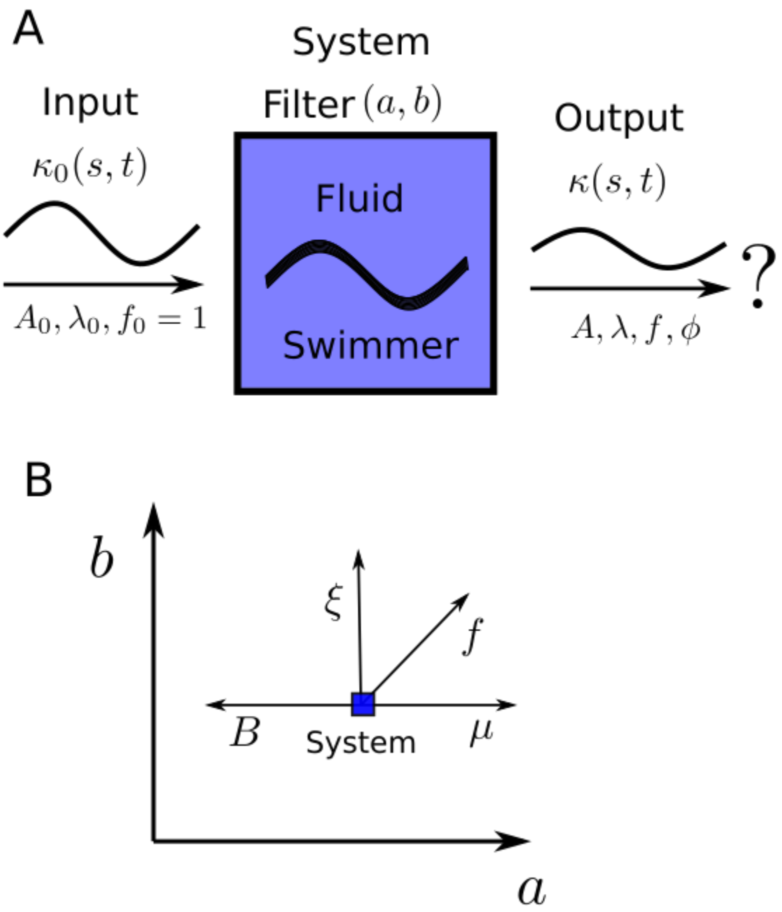

Figure 4.1: Conceptualizing the rod model as a dynamical filter. (**A**): Together, the swimmer and the fluid environment form a system that behaves akin to a dynamic filter, which takes the preferred curvature $\kappa_0(s, t)$ as an input and generates the emergent body curvature $\kappa(s, t)$ as an output. The input is characterized by the preferred curvature amplitude A_0, preferred wavelength λ_0, and preferred undulation frequency f_0. The output is characterized by the emergent curvature amplitude A, wavelength λ, undulation frequency f, and phase lag ϕ. The characteristics of the filter depend on the system's effective response times a and b. (**B**): Schematic of how the system's operating point, characterized by the effective response times a and b, changes when the undulation frequency f, relative internal damping coefficient ξ, bending rigidity B and fluid viscosity μ are varied, respectively.

Drawing from this analysis, we hypothesize that gait modulation can be understood as the swimmer's effort to maintain an optimal operating point while adapting to changing behavioral objectives or environmental conditions. We will explore this hypothesis in more detail in Chapter 5.

Physical Parameters

Parameter	Definition	SI Unit	Description
L_0	-	m	Natural body ength
$R_{\max}$	-	m	Maximum cross-sectional radius
ε	$\frac{2R_{\max}}{L_0}$	-	Slenderness parameter
φ	-	-	Radius shape-function
I	$\frac{\pi R_{\max}^4}{4}$	m^4	Second moment of area
E	-	Pa	Young's modulus
ϱ	-	-	Poisson's ratio
G	$\frac{E}{2(1+\rho)}$	Pa	Shear modulus
η	-	Pa s	Extensional viscosity
ν	$\frac{\eta}{2(1+\rho)}$	Pa s	Shear viscosity
μ	-	Pa s	Fluid viscosity
$c_{\parallel}$	$\frac{2\pi}{\ln(1/\varepsilon)-\frac{1}{2}}$	-	Linear longitudinal drag coefficient
$c_{\perp}$	$\frac{2\pi}{\ln(1/\varepsilon)+\frac{1}{2}}$	-	Linear transverse drag coefficient
$\gamma_{\parallel}$	$\pi\varphi^2 R_{\max}^2$	-	Angular longitudinal drag coefficient
$\gamma_{\perp}$	$4\pi\varphi^2 R_{\max}^2$	-	Angular transverse drag coefficient
τ	$\frac{\mu c_{\parallel} L_0^4}{EI}$	s	Fluid-structure response time
ξ	$\frac{\eta}{E}$	s	Internal viscous-elastic response time
A_0	-	m^{-1}	Preferred curvature amplitude
λ_0	-	m	Preferred undulation wavelength
T_0	-	s	Undulation period
f_0	$\frac{1}{T_0}$	Hz	Undulation frequency

Table 4.1: Physical model parameter: The internal viscoelastic response time ξ is also called the relative damping coefficient.

Dimensionless Parameters		
Parameter	**Definition**	**Description**
a	$\dfrac{\tau}{T_0}$	Effective fluid-structure response time
b	$\dfrac{\xi}{T_0}$	Effective internal viscous-elastic response time
p	$\dfrac{1}{2(1+\varrho)}$	Viscoelastic shear to extension ratio
g	$\dfrac{I}{AL_0^2}$	Geometric ratio
K_c	$\dfrac{c_\perp}{c_\|}$	Linear drag coefficient ratio
K_γ	$\dfrac{\gamma_\perp}{\gamma_\|}$	Angular drag coefficient ratio
$K_\|$	$\dfrac{\gamma_\|}{L_0^2 c_\|}$	Longitudinal drag coefficient ratio
A_0^*	$\dfrac{A_0}{L_0}$	Normalized preferred curvature amplitude
λ_0^*	$\dfrac{\lambda_0}{L_0}$	Normalized preferred undulation wavelength
T_0^*	1	Dimensionless undulation period
f_0^*	1	Dimensionless undulation frequency

Table 4.2: Dimensionless model parameters. All dimensionless model parameters are defined in terms of the physical parameters summarized in Tab. 4.1.

4.2 Dynamical Regimes

This section analyses how the swimmer's actuation response depends on the dimensionless model parameters. Specifically, we focus on the system's effective response times a and b, which prove to have the most significant impact on how the system responds to actuation. As we discussed in Chapter 3, swimmers achieve propulsion by actively deforming their bodies in a synchronized manner. In our model, this active deformation is generated by an actuation torque, whose spatio-temporal pattern can be expressed in terms of the preferred curvature $\kappa_0(s,t)$. Hence, we conceptualize the system as a dynamic filter that takes the preferred curvature $\kappa_0(s,t)$ as an input and generates the body curvature $\kappa(s,t)$ as an output, as illustrated in Fig. 4.1A. To study undulatory locomotion, we model the dimensionless preferred curvature $\kappa_0^*(s,t)$ as a sinusoidal traveling wave, i.e. $\kappa_0^*(s,t) = A_0 \sin(q_0^* s - 2\pi t)$. Here, the dimensionless undulation parameters are the preferred curvature amplitude A_0^*, the preferred wavenumber $q_0^* = 2\pi/\lambda_0^*$, and the preferred wavelength λ_0^*. Be aware that the preferred undulation frequency is $f_0^* = 1$ in dimensionless coordinates. In what follows, we will omit the star superscript that denotes dimensionless variables for the sake of brevity unless otherwise stated.

It is important to stress that the functional form of the emergent body curvature $k(s,t)$ is unknown at this stage. However, we will demonstrate in the following that in the case of a sinusoidal preferred curvature κ_0, the emergent body curvature κ can also be described as a sinusoidal traveling wave, taking the form $\kappa(s,t) = A \sin(qs - 2\pi f t + \phi)$. Here, the dimensionless undulation parameters are the emergent curvature amplitude A, wavenumber $q = 2\pi/\lambda$, wavelength λ, undulation frequency f and the phase lag ϕ often dubbed the neuromechanical phase lag [42]. Contingent on the choice of a and b, we will demonstrate that the emergent undulation parameters are not necessarily equivalent to their preferred counterparts. Furthermore, we show that the emergent undulation parameters are not necessarily uniform but can vary continuously along the swimmer's body.

To characterize the filter properties of our system, our goal is to establish a relationship between input (preferred) undulation parameters A_0, λ_0 and output undulation parameters A, λ, f, ϕ. To this end, we conduct undulation experiments with constant input parameters $A_0 = 2\pi$ and $\lambda_0 = 1$, while systematically varying the parameters a and b. For every experiment, we determine the undulation amplitude A, wavelength λ, undulation frequency f, and phase lag ϕ. All other model parameters are held constant throughout the experiments.

As we discussed in Section 3.4, we constrain the actuation torque to be zero at both ends of the swimmer's body. As a result, the body curvature $\kappa(s,t)$ converges to zero in the head and tail region. Hence, we restrict our analysis to the midsection of the swimmer's body, which we define as the interval from s_1=0.1 to s_2=0.9. Before presenting the results of our experiments, we underscore that our initial discussion will be primarily descriptive. A unified interpretation of results will be given at the end section when we identify distinct dynamical regimes of the system.

Initially, we focus our discussion on the swimmer's undulation frequency f and the phase lag ϕ. To illustrate our methodology, Fig. 4.2A-D showcases the simulation result for a specific value of a and b represented by the green cross in panels E and F. Panel A compares the preferred curvature to the body curvature at the swimmer's midpoint ($s = 0.5$) as a function of time. The following observations can be made: Similar to the preferred curvature, the body curvature $\kappa(0.5, t)$ exhibits a sinusoidal profile. However, the body curvature lags behind the preferred curvature, and its amplitude is smaller than that of the preferred curvature.

To determine the undulation frequency f, we perform a fast Fourier transform of the body curvature $\kappa(s,t)$ at all body positions $s \in [s_1, s_2]$. In Panel C, the power spectrum of the Fourier transform is shown as a function of s. Irrespective of the value of s, the power spectrum remains zero except for the frequency $f = 1.0$, which we identify as the undulation frequency. This confirms that $\kappa(s,t)$ can be represented as a sinusoidal function, characterized by a single frequency component. This observation holds true over the entire parameter range of a and b. Hence, we conclude that our system preserves the frequency of the input signal, i.e. $f = f_0 = 1.0$.

To determine the phase lag ϕ between the preferred and the body curvature, we calculate their cross-correlation function defined as

$$\mathrm{CC}(s, \Delta t_{\mathrm{lag}}) = \frac{\int_t^{t+1} \kappa_0(s,t)\kappa(s, t + \Delta t_{\mathrm{lag}})\, dt}{\sigma_{\kappa_0}(s)\sigma_k(s)}. \tag{4.1}$$

Here, we normalized the cross-correlation function by the standard deviations σ_{κ_0} and σ_k defined as

$$\sigma^2_{\kappa_0}(s) = \int_t^{t+1} \kappa_0^2(s,t)dt - \left(\int_t^{t+1} \kappa_0(s,t)dt\right)^2, \tag{4.2}$$

$$\sigma^2_{\kappa}(s) = \int_t^{t+1} \kappa^2(s,t)dt - \left(\int_t^{t+1} \kappa(s,t)dt\right)^2. \tag{4.3}$$

Panel B displays the cross-correlation between the preferred and body curvature at the swimmer's midpoint, shown in panel A. The phase lag ϕ is proportional to the time lag of maximum correlation $\Delta t^{\max}_{\mathrm{lag}}$, represented by the vertical red dashed line. In dimensionless coordinates, the phase lag is given by $\phi = 2\pi\Delta t^{\max}_{\mathrm{lag}}$, as $f = 1$. Panel D displays the cross-correlation spectrum as a function of the body position s. For the sake of illustration, we selected values of a and b where the maximum correlation band is not a perfectly vertical straight line. This indicates that ϕ is non-uniform across the length of the swimmer's body. Hence, to quantify the variability of ϕ, we introduce the average phase lag $\bar{\phi}$ and phase lag's standard deviation σ_ϕ as follows:

$$\bar{\phi} = \int_{s_0}^{s_1} \phi(s)\, ds, \quad \sigma_\phi = \sqrt{\int_{s_0}^{s_1} \left(\phi(s) - \bar{\phi}\right)^2 ds}. \tag{4.4}$$

To examine how $\bar{\phi}$ and σ_ϕ depend on the model parameters, their contour plots as a function of a and b are shown in Fig. 4.2E and F. Most notably, the contour bands in Fig. 4.2E display rotational "symmetry", suggesting that a and b play similar dynamical roles. This is not surprising, considering that both a and b represent one of the two intrinsic time scales of the system. We observe, that for small values of a and b, both $\bar{\phi}$ and σ_ϕ

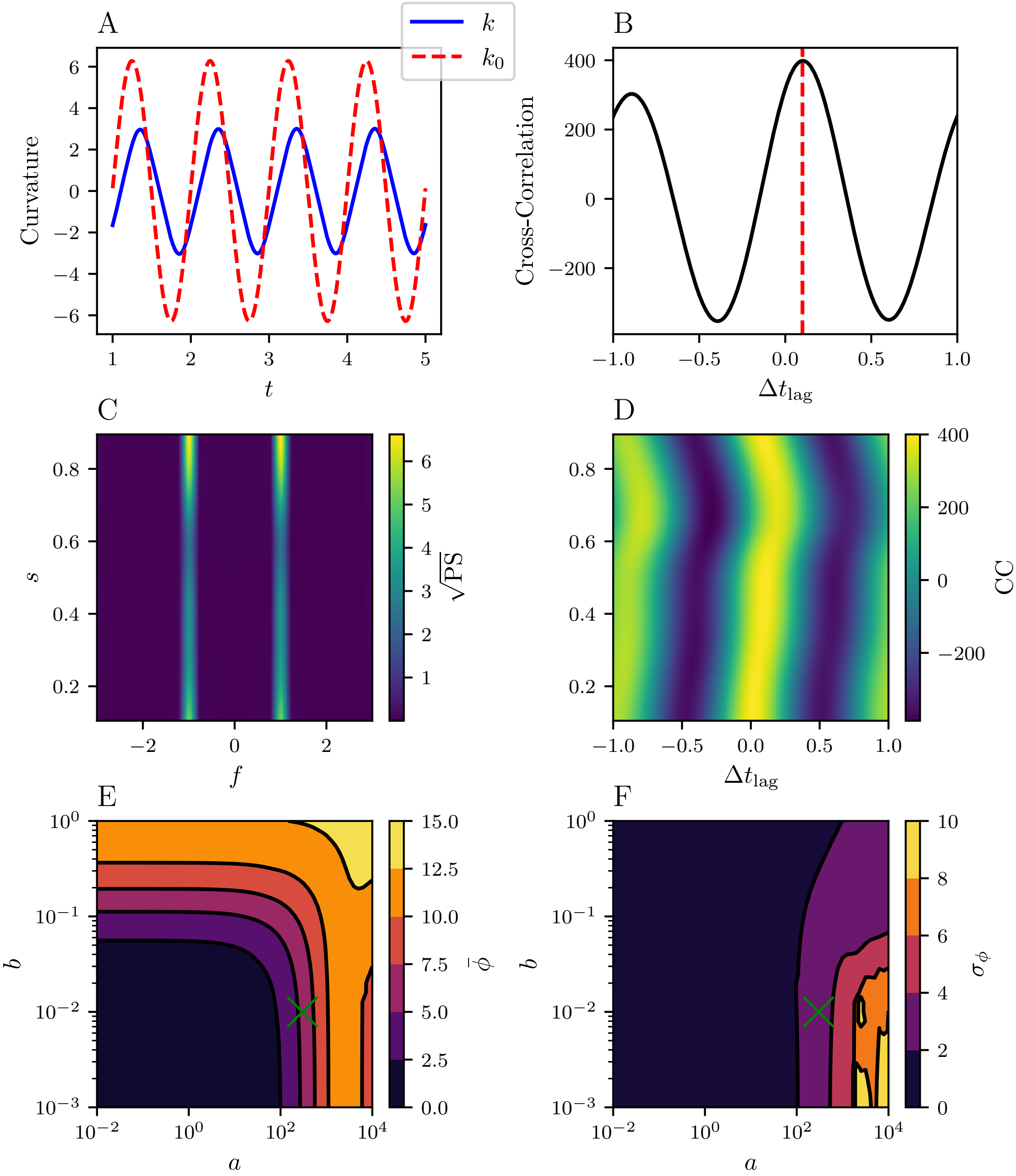

Figure 4.2: The phase lag ϕ between preferred and actual body curvature as a function of the system's effective response times a and b. Panel A-D showcases the simulation results for effective response times $a = 300$ and $b = 0.01$, represented by the green cross in panels E and F. (**A**): Preferred curvature $\kappa_0(0.5, t)$ (red dashed line) and body curvature $\kappa(0.5, t)$ (blue line) both evaluated at the swimmer's body midpoint $s = 0.5$ within the time interval $t = [1, 4]$. (**B**): Cross-correlation (black line) between $\kappa_0(0.5, t)$ and $\kappa(0.5, t)$ for varying time lags Δt_{lag}. The red dashed line denotes the cross-correlation's maximum. (**C**): Body curvature power spectrum calculated from its fast Fourier transform for different body coordinates s. (**D**): Cross-correlation spectrum between $\kappa_0(s, t)$ and $\kappa(s, t)$ for varying time lags Δt_{lag} for different body coordinates s. (**E**): Contour plot of the average phase lag $\bar{\phi}$ as a function of a and b. (**F**): Contour plot of the phase lag's standard deviation σ_ϕ as a function of a and b. Other dimensionless model parameters include $g = 2.00 \times 10^{-4}$, $p = 0.33$, $K_c = 1.51$, $K_\gamma = 4.0$ and $K_\| = 1.22 \times 10^{-3}$ (see Tab. 4.2).

converge to zero. Consequently, in this parameter region, the body curvature $\kappa(s,t)$ follows the preferred curvature $\kappa_0(s,t)$ instantaneously at every point along the swimmer's body. As a or b become larger, the average phase lag $\bar{\phi}$ increases gradually, indicating that the body curvature lags behind the preferred curvature.

For very large values of a, at the bottom right corner of Fig. 4.2E, the rotational symmetry is broken, evident by a decrease in $\bar{\phi}$. As we will show in the following, in this parameter region, the undulation parameters display the most variability along the swimmer's body. As a result, the spatio-temporal pattern of κ exhibits a greater dissimilarity compared to that of κ_0, whose undulation parameters are constant. This enhanced dissimilarity typically leads to smaller cross-correlations and shorter lag of maximum correlation $\Delta t_{\text{lag}}^{\text{max}}$ [96], explaining the decrease in $\bar{\phi}$.

Notably, the contour plot of σ_ϕ in Fig. 4.2F lacks the rotation "symmetry" of the plot in panel E. Roughly speaking, the contour plot in panel F can be divided into two parameter regions. For a values smaller than a certain threshold value, σ_ϕ converges to zero irrespective of the value of b, signifying a uniform phase lag ϕ along the entire length of the swimmer's body. As a exceeds this threshold, σ_ϕ starts to increase gradually. Within this parameter range, as b increases, σ_ϕ becomes smaller, implying that internal damping has a homogenizing effect on ϕ. In the following, we show that the same holds true for the other undulation parameters.

After having analyzed the phase lag ϕ, we now focus on the body curvature amplitude A. In our presentation, we will follow a similar outline to that previously used for ϕ. First, to illustrate our methodology, we showcase the simulation results for two specific value pairs of a and b in Fig. 4.3A-D. Those value pairs are represented by the green cross and green star in panels E and F. To determine A as a function of the body position s, we calculate the Fourier transform of the body curvature $\kappa(s,t)$. Panels A and C display the power spectrum of $\kappa(s,t)$ for each of the two value pairs, respectively. Taking the square root of the power spectrum at frequency $f = 1$ yields the curvature amplitude A as a function s, displayed in Fig. 4.3B and D.

Panel D, we choose a value of a and b for which the curvature amplitude A is not uniform across the swimmer's body. Thus, we introduce the average amplitude $\bar{A}$ and the amplitude's standard deviation σ_A as follows:

$$\bar{A} = \int_{s_1}^{s_2} A(s)\, ds, \quad \sigma_A = \sqrt{\int_{s_1}^{s_2} \left(A(s) - \bar{A}\right)^2 ds} \tag{4.5}$$

In panel B, the average curvature amplitude $\bar{A}$ is approximately equal to the preferred curvature amplitude A_0, and the normalized standard deviation $\sigma_A/\bar{A}$ is approximately

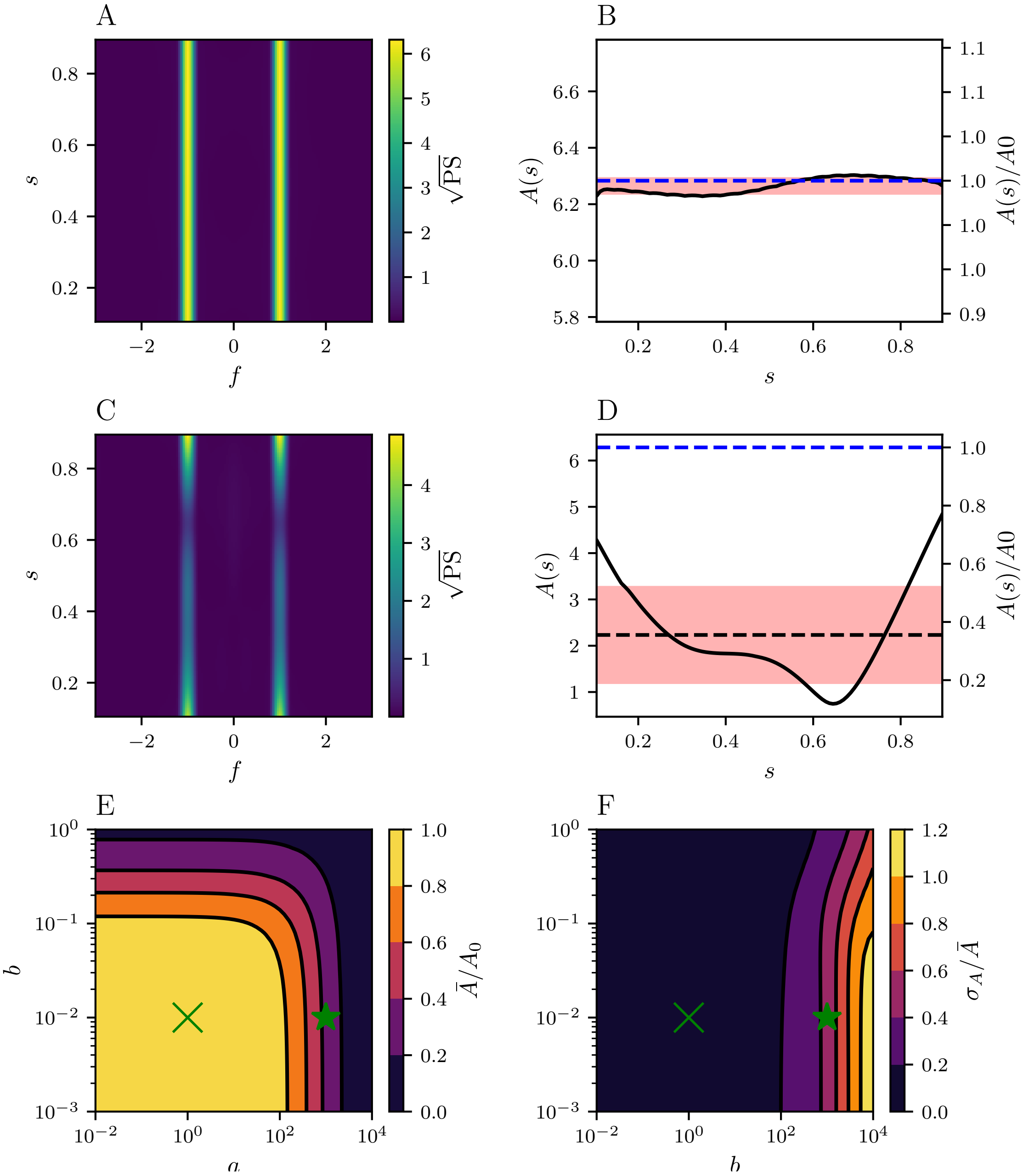

Figure 4.3: The mapping from the preferred A_0 to actual A curvature amplitude as a function of the system's effective response times a and b. Panels A and B showcase the simulation results for the effective response times $a = 1$ and $b = 0.01$, represented by the green cross in panels E and F, whereas panels C and D correspond to $a = 300$ and $b = 0.01$, represented by the green star. (**A**, **C**): Power spectrum calculated from the fast Fourier transform of the body curvature $\kappa(s,t)$ as a function of the body coordinate s. (**B**, **D**): Curvature amplitude $A(s)$ as a function of the body position s (black line), average amplitude A (black dashed line), amplitude's standard deviation σ_A (red band) and preferred amplitude A_0 (blue dashed line). (**E**): Contour plot of the relative curvature amplitude A/A_0 for varying a and b. (**F**): Contour plot of the standard deviation σ_A normalized preferred curvature amplitude A_0 for varying a and b. Other dimensionless model parameters are identical to those in Fig. 4.2.

zero. Conversely, in panel D, $\bar{A}$ is significantly smaller than A_0, i.e. the system damps the input amplitude. Furthermore, A displays significant variations along the swimmer's body length, resulting in a large standard deviation σ_A, represented by the red band. Notably, A is largest in the head and tail region and smallest at the body centre.

To analyze the dependence of $\bar{A}$ and σ_A on the parameters a and b, their contour plots are shown in panels E and F, respectively. Here, we normalized the average amplitude $\bar{A}$ by the preferred amplitude A_0, and the standard deviation σ_A by $\bar{A}$. Notably, the contour plot of $\bar{A}$ displays the same rotational "symmetry" as the plot of the average phase lag $\bar{\phi}$, shown in Fig. 4.2E. As a or b decreases, the average amplitude $\bar{A}$ converges to A_0, and the normalized standard deviation σ_A converges to zero. Hence, in this parameter region, the system acts as a pass-through filter, preserving the amplitude of the input signal across the entire length of the swimmer's body. As a or b increase, the average amplitude $\bar{A}$ decreases gradually and eventually converges to zero. This damping behavior is reminiscent of a low-pass filter. As the damping becomes stronger for larger values of a and b, it suggests that the system's filter time constant increases with these parameters. This makes intuitive sense, as a and b can be interpreted as the effective response time of the system.

Notably, the contour plot of σ_A coarsely resembles the plot of the phase lag's standard deviation σ_ϕ in Fig. 4.2F. Particularly, the contour plot of σ_A can also be divided roughly into two regions. For a smaller than a certain threshold, σ_A is zero irrespective of the value of b. Beyond this threshold, σ_A increases gradually with a. Within this region, σ_A exhibits a minor dependency on b, diminishing as b increases. This supports our previous hypothesis that internal damping enhances the uniformity of the swimmer's undulation parameters but results in stronger damping of the curvature amplitude.

Having analyzed the system's filter properties with respect to the curvature amplitude A, we now focus on the wavelength λ. Our presentation of the results will follow the same outline previously used for ϕ and A. First, we illustrate our methodology in Fig. 4.4A-C by showcasing the simulation results for the same value pairs of a and b featured in Fig. 4.3. Those value pairs are represented by the green cross and the green star in Fig. 4.4E and F. In panels A and B, we display the kymograms of the body curvature κ during the last undulation cycle for each value pair, respectively.

To determine the undulation wavelength λ from these kymograms, we follow the method presented in Fang Yen *et al.* [45]. The black dots in the kymograms represent the time and body point coordinates where κ is zero, highlighting distinct curves of zero curvature. By aligning the points of the individual curves, a unified B-spline can be fitted to all the data points, as depicted in the upper graphs of panels C and D. Note we exchanged the body and the time axis in these graphs compared to the kymograms. Hence, the curvature wave's propagation speed v is equal to the inverse of the B-spline's derivative. From the relationship

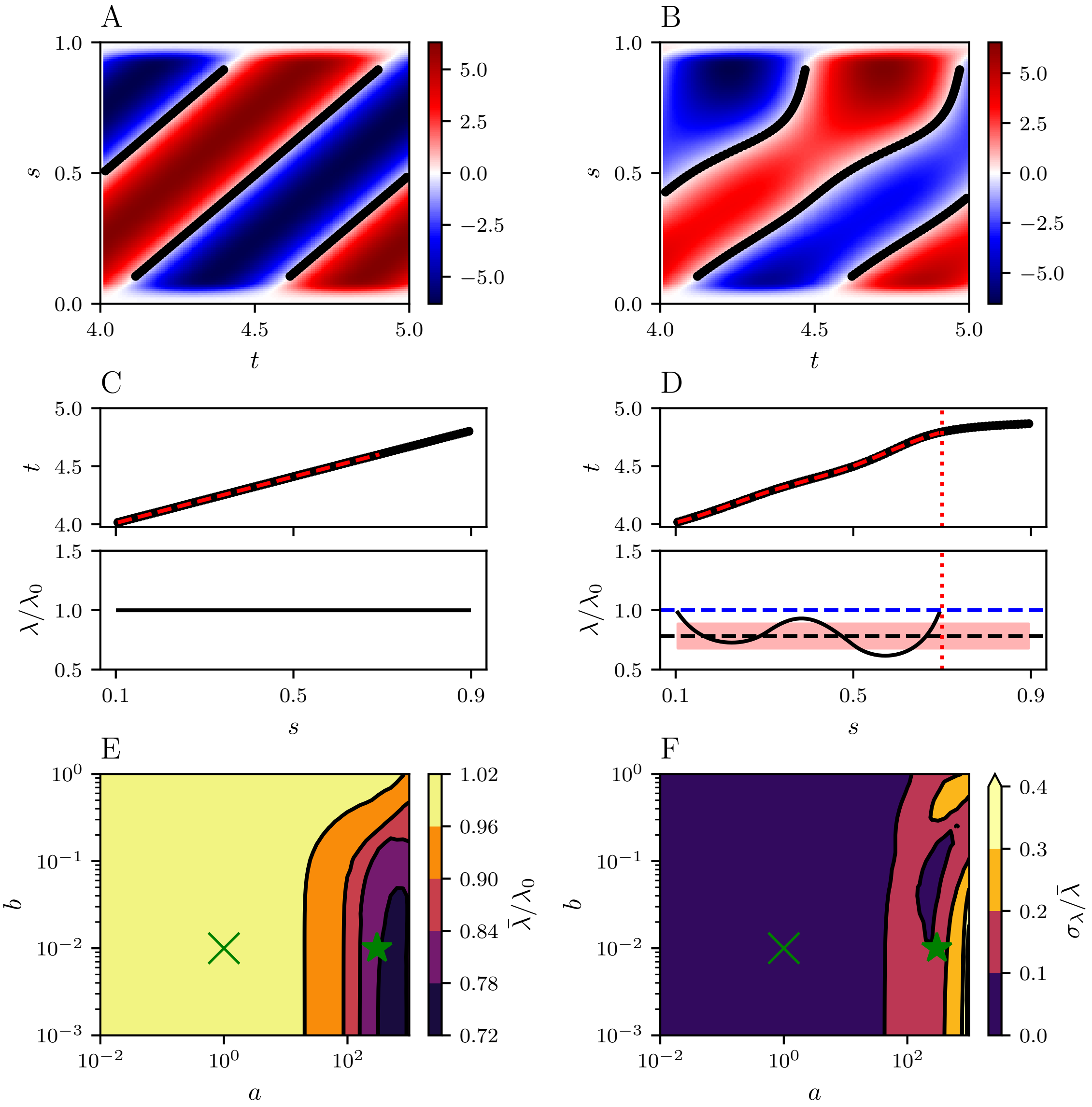

Figure 4.4: The mapping from the preferred λ_0 to actual λ wavelength as a function of the system's effective response times a and b. (**A**): Kymogram of the body curvature $\kappa(s,t)$ for the effective response times $a = 1$ and $b = 0.01$, represented by the green cross in panels E and F. (**B**): Kymogram for effective response times $a = 300$ and $b = 0.01$, represented by the green star. The black dots in both kymograms denote isolines of zero curvature, $\kappa(s,t) = 0$. (**C**): Aligned isolines (black dots) extracted from panel A. We perform a B-spline fit (red dashed line) to the data points that make up the aligned isolines. The inverse derivative of this fit yields the undulation wavelength $\lambda(s)$ as a function of the body coordinate s, shown in the lower C panel (black line). (**D**): Aligned isolines (black dots) extracted from panel B and corresponding B-spline fit (red dashed line). The lower panel D displays the wavelength $\lambda(s)$ (black line), average wavelength $\bar{\lambda}$ (dashed black line), standard deviation σ_λ (red band), preferred wavelength λ_0 (blue dashed line) and the cut off $s_{\text{cut}} = 0.7$ (red dotted line). (**E**): Contour plot of the normalized undulation wavelength λ/λ_0 for varying a and b. (**F**): Contour plot of the normalized standard deviation σ_λ for varying a and b. Other dimensionless model parameters remain consistent with those in Fig. 4.2.

$v = \lambda \cdot f$, it then follows that $\lambda = v$ because $f = 1$ in dimensionless coordinates. Hence, we can estimate λ at position s as the inverse of B-spline's derivative.

In panel C, the data points are well described by a straight line, i.e. the wavelength λ is constant along the length of the swimmer's body. Furthermore, the bottom graph of panel C shows that λ matches the preferred wavelength λ_0. Therefore, for the specific values of a and b in panel C, our system preserves the wavelength of the input signal.

Conversely, in panel D, the data points do not conform to a straight line. As a result, the wavelength λ varies significantly along the length of the swimmer's body, which can be seen in the bottom graph of panel D. Hence, following the same approach taken for ϕ and A, we introduce the average wavelength $\bar{\lambda}$ and the wavelength's standard deviation σ_λ as follows:

$$\bar{\lambda} = \int_{s_1}^{s_2} \lambda \, ds, \quad \sigma_\lambda = \sqrt{\int_{s_1}^{s_2} \left(\lambda - \bar{\lambda}\right)^2 ds} \tag{4.6}$$

Notably, in the upper graph in panel D, the curve's derivative approaches zero within the posterior part of the swimmer's body $s > 0.7$. Consequently, the propagation speed v and wavelength λ diverge to infinity. This can be seen in the kymogram in panel B, where the curves of zero curvature align vertically in the posterior part of the swimmer's body.

For very large values of a, we find that the curvature wave's propagation speed v first diverges and then changes sign in the posterior part of the swimmer's body. This could be interpreted as two curvature waves propagating simultaneously along the length of the swimmer's body. One propagates from head to tail and the other from tail to head, both clashing in the posterior part of the body. Within this parameter range, no meaningful average wavelength $\bar{\lambda}$ or standard deviation σ_λ can be calculated across the full length of the swimmer's body. To address this problem, we introduce a cutoff $s_\theta = 0.7$, illustrated by the red dashed line in panel D. Substituting s_θ as the upper integral boundary in Eq. (4.6) yields the anterior average wavelength and standard deviation, which will refer to $\bar{\lambda}$ and σ_λ for the rest of thesis. Both are represented by the black dashed line and the red band in the bottom graph of panel D, respectively. Notably, the anterior average wavelength is smaller than the preferred wavelength λ_0.

To analyse how $\bar{\lambda}$ and σ_λ depend on the parameters a and b, their contour plots are shown in Fig. 4.4E and F. Note that we normalized $\bar{\lambda}$ by the preferred wavelength λ_0 and σ_λ by $\bar{\lambda}$. Again, we find that both contour plots in panels E and F can be roughly divided into two parameter regions. For a values smaller than a certain threshold, irrespective of the value of b, the average wavelength $\bar{\lambda}$ converges to λ_0, and σ_λ converges zero. Consequently, within this parameter region, the kymogram of the body curvature resembles the one in panel A, with straight diagonal stripes whose slope is equivalent to λ_0. Hence, within this region, the system preserves the preferred wavelength of the actuation signal.

As a becomes larger than the threshold, $\bar{\lambda}$ gradually decreases. Yet, it converges to λ_0 with increasing b, indicating that internal damping helps to preserve the input wavelength. Within this parameter region, the curvature wave's propagation speed diverges to infinity in the posterior part of the body. Consequently, it must become slower in the anterior part to preserve the undulation frequency. This explains why the anterior wavelength $\bar{\lambda}$ is reduced, as it is equivalent to the propagation speed.

Notably, the contour plot of σ_ϕ does not display a similar clean and continuous trend if compared to the plot in panel E. This is most likely a consequence of our numerical method, which depends on the arbitrary value of the cutoff $s_\theta = 0.7$, as well the parameters of the clustering and fitting routines. In the region where a is very large, hydrodynamic viscous forces dominate over the internal elastic stresses generated by the swimmer's passive body. Thus, perhaps a more accurate model than RFT must be used to describe the fluid dynamics in this parameter range. Nonetheless, despite the less clean contour plot in panel F, we can clearly identify the parameter region where σ_ϕ is nonzero.

By comparing to the contour plots of Fig. 4.2F, Fig. 4.3F, and Fig. 4.4F, we find that the parameter regions where the standard deviations σ_ϕ, σ_A and σ_λ are nonzero approximately overlap. This demonstrates that there exists a distinct parameter region, characterized by large a and small b values, where undulation parameters exhibit significant variability along the swimmer's body. These variations are accompanied by a non-uniform curvature wave propagation speed, diverging to infinity in the posterior part of the swimmer's body. Naturally, this symmetry breaking proves disadvantageous for the generation of propulsion. Hence, microswimmers are incentivized to avoid this parameter region through gait modulation, as we will discuss in more detail in Chapters 5 and 6.

Building upon our preceding analysis, we are now able to identify distinct dynamical regimes within the a and b parameter space based on the system's characteristic response properties. In Fig. 4.5A and B, we present the contour plots of the average phase lag $\bar{\phi}$ and the average curvature amplitude $\bar{A}$. Additionally, the contour plot of the normalized swimming speed $U/U_{\max}$ is shown in panel C, where $U_{\max}$ is the maximum swimming speed $U_{\max}$ within the specified parameter range of a and b. Notably, all three contour plots look remarkably similar. This motivates us to introduce three dynamical regimes, whose boundaries are displayed by the blue dashed lines in Fig. 4.5D. These regimes are defined as follows:

I: **Pass-through regime** $U/U_{\max} \geq 0.95$: Characterized by an undamped curvature amplitude $\bar{A} \approx A_0$, approximately zero phase lag $\bar{\phi} \approx 0$, and fast swimming speeds.

II: **Low-pass regime** $0.95 > U/U_{\max} > 0.05$: Characterized by a damped curvature amplitude $\bar{A} < A_0$, non-zero phase lag $\bar{\phi} > 0$, and reduced swimming speed.

III: **Struggle regime** $U/U_{\max} \leq 0.05$: Characterized by a strongly damped curvature amplitude $\bar{A} \ll A_0$, large phase lag $\bar{\phi}$, and approximately zero swimming speed.

As regime boundaries, we selected the contour lines $U/U_{\max} = 0.95$ and $U/U_{\max} = 0.05$ since the swimming speed will be one of the primary focuses of our analysis. Recognizing the arbitrariness of these cutoff values, we consider them a practical choice to distinguish the different dynamical behaviors of the system.

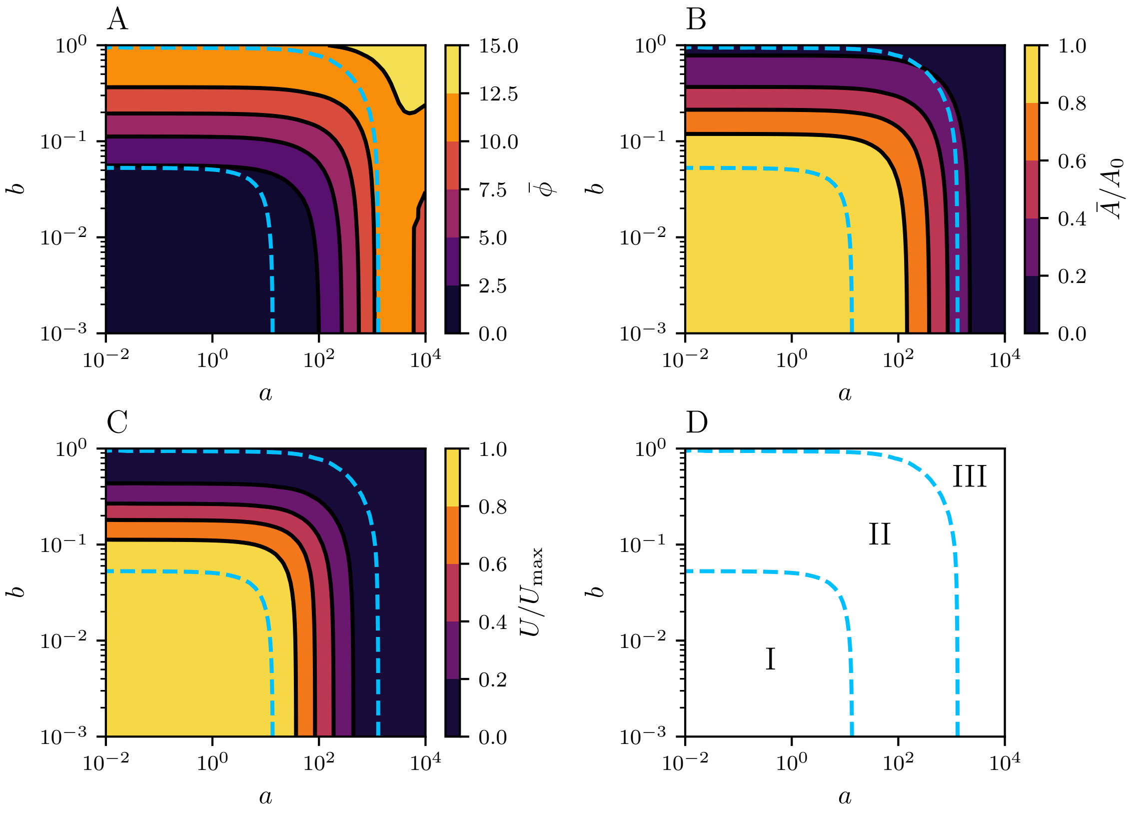

Figure 4.5: The dynamical regimes of the system (representation 1). (**A**): Contour plot of the averaged time lag $\bar{\phi}$ between the preferred curvature $\kappa_0(s,t)$ and the emergent curvature $\kappa(s,t)$ adopted from Fig. 4.2E. Blue dashed lines show contour lines $U/U_{\max} = [0.1, 0.9]$, respectively. (**B**): Contour plot of the normalized curvature amplitude A/A_0 adopted from Fig. 4.3E. (**C**): Contour plot of the normalized average swimming speed $U/U_{\max}$, where $U_{\max}$ is the maximum swimming in the specified range of a and b. (**D**): Depiction of the Pass-through (I), low-pass (II), and struggle (III) regimes, which are defined as: $U/U_{\max} \geq 0.95$, $0.05 > U/U_{\max} > 0.95$, and $U/U_{\max} \leq 0.05$, respectively. Other dimensionless model parameters are identical to those in Fig. 4.2.

In the pass-through regime, a and b are small, i.e. the system's effective response time is much shorter than the actuation time scale. As a result, the system effectively behaves as a pass-through filter, i.e. it generates a body curvature $\kappa(s,t)$ that tracks the preferred curvature $\kappa_0(s,t)$ instantaneously. Consequently, the phase lag $\bar{\phi}$ between preferred and body curvature converges to zero, and the curvature amplitude $\bar{A}$ converges to preferred amplitude A_0. The latter explains why the swimming speed U is maximal in the pass-through regime.

As a or b become larger, the system's response time becomes slower, and it is not able to instantaneously track the preferred curvature $\kappa_0(s,t)$ anymore. Hence, we refer to this parameter region as the low-pass regime. It is characterized by non-zero phase lag, dampened curvature amplitude and a reduced swimming speed. In this regime, the system behaves akin to a low-pass filter. The filter's time constant increases with a or b, resulting in a stronger damping effect and a larger phase lag.

For very large values of a, the system's response time becomes so slow that the curvature amplitude is almost completely damped out. As a result, the swimmer can no longer generate a meaningful body wave. Hence, we refer to this parameter region as the struggling regime, as the swimmer remains almost stationary. This explains why the swimming U converges to zero in the struggling regime.

Together, the pass-through, low-pass, and struggle regimes provide a concise characterization of the swimmer's dynamic response to actuation. However, they do not quantify how uniform the undulation parameters are across the length of the swimmer's body. Hence, in Fig. 4.6 A-C, we revisit the contour plots of standard deviations σ_ϕ, σ_A, and σ_λ. In addition, the contour plot of the average wavelength $\bar{\lambda}$ is shown again in panel D, as it displays a similar dependency on a and b. Upon comparing panel A-C, we distinguish two parameter regions, as discussed previously. One is characterized by zero standard deviations, while the other exhibits nonzero values. Hence, we introduce two additional dynamical regimes, which are defined as follows:

(a) **Homogeneous regime** $\sigma_A/\bar{A} \leq 0.15$: In this regime, the undulation parameters remain constant along the length of the swimmer's body, as σ_ϕ, σ_A and σ_λ are approximately zero. Here, the system preserves the preferred wavelength, as $\bar{\lambda} \approx \lambda_0$.

(b) **Heterogeneous regime** $\sigma_A/\bar{A} > 0.15$: In this regime, the undulation parameters vary across the length of the swimmer's body, as σ_ϕ, σ_A and σ_λ are nonzero. Here, the system shortens the preferred wavelength, as $\bar{\lambda} < \lambda_0$.

Here, we choose the contour line $\sigma_A/\bar{A} = 0.15$ as the regime boundary, as σ_A displays the smoothest contour plot among the three standard deviations presented in panels A-C. Again, the specific value of the cutoff is arbitrary, i.e. it should be understood as a practical choice to distinguish between both regimes.

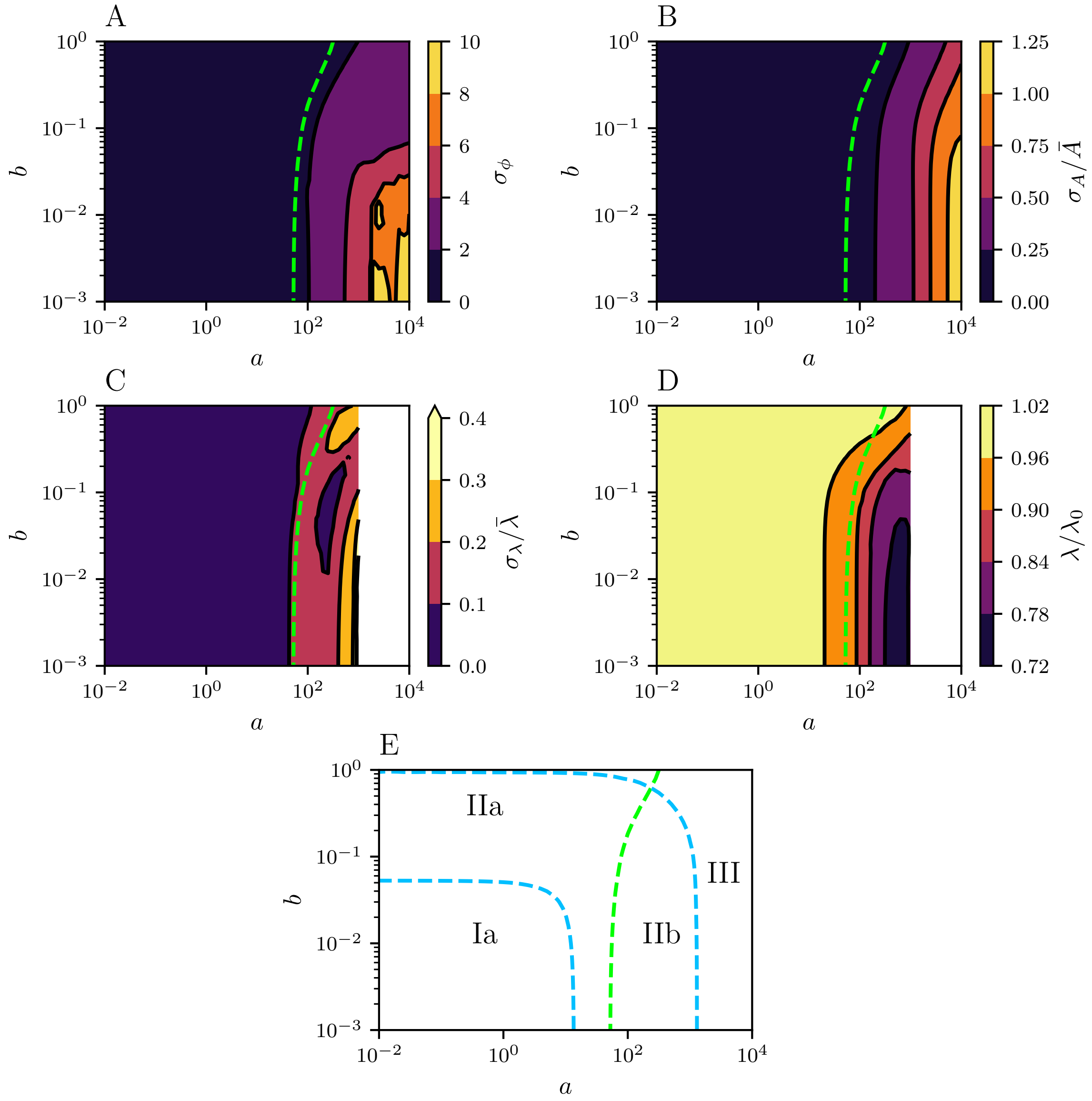

Figure 4.6: The dynamical regimes of the system (representation 2). (**A**): Contour plot of the phase lag standard deviation σ_ϕ as function of effective response times a and b adopted from Fig. 4.2F. (**B**): Contour plot of the normalized curvature amplitude standard deviation $\sigma_A/\bar{A}$ adopted from Fig. 4.3F. (**C**): Contour plot of the normalized wavelength standard deviation $\sigma_\lambda/\bar{\lambda}$ adopted from Fig. 4.4F. For $a > 10^3$, the curvature wave's propagation speed becomes negative in the posterior part of the body, and no meaningful undulation wavelength can be determined (white area). (**D**): Contour plot of the average wavelength $\bar{\lambda}/\lambda_0$ adopted from Fig. 4.4E. The Green dashed curve represents the boundary between the homogeneous and heterogeneous undulation regime, defined as $\sigma_A/\bar{A} = 0.15$. (**E**): Depiction of the homogeneous pass-through and low-pass regime (Ia) and (IIa), and the heterogeneous low-pass and the struggling regime (IIb) and (III). Homogeneous and heterogeneous regimes are defined as: $\sigma_A/\bar{A} \leq 0.15$ and $\sigma_A/\bar{A} \geq 0.15$, respectively. Other dimensionless model parameters are identical to those in Fig. 4.2.

To summarize, we established two distinct classes of regimes that govern the dynamic behavior of the swimmer. The first class encompasses the pass-through, low-pass, and struggle regime, characterizing the system's filter properties. They determine the swimmer's speed, curvature amplitude, and phase lag compared to actuation. The second class, comprised of the homogeneous and heterogeneous regime, characterizes the variability of the undulation parameters along the length of the swimmer's body. The boundaries between the regimes within each class are displayed in Fig. 4.6E. Together, those boundaries give rise to four distinct dynamical regimes, each characterized by the combined response properties of each class. Those regimes concisely characterize the system's dynamical response properties to actuation.

To illustrate how the swimmer looks in the different dynamical regimes, Fig. 4.7 displays snapshots of the swimmer's waveform in each regime for different time points during the last undulation cycle of the simulation. As discussed, the preferred curvature amplitude is damped in the low-pass regime (II) and the struggling regime (III). This damping results in the damping of the amplitude of the swimmer's body waveform in the position space, as can be seen in panels C-E. Notably, in the struggling regime, the amplitude is approximately zero, and the swimmer makes almost no progress when compared to its initial configuration $\boldsymbol{r}(s,0) = s\boldsymbol{e}_3$ at the beginning of the simulation. By comparing panels B and D, we notice that in the heterogeneous low-pass regime (IIb), the swimmer's waveform has a higher curvature in the head and tail when compared to the homogeneous regime (IIa). This variability in curvature amplitude along the swimmer's body in the heterogeneous low-pass regime is consistent with our findings in Fig. 4.3.

Notably, the swimmer's operating regime is determined by the values of the parameters a and b, which are defined in terms of the physical model parameters; see Tab. 4.2. Thus, the swimmer's operating point is determined by its material parameters, such as Young's modulus E, relative internal damping coefficient ξ, body geometry, fluid viscosity μ and undulation frequency f. This implies that a swimmer can maintain an advantageous operating point by modulating its undulation frequency. This is specifically relevant if the swimmer is exposed to environments with different viscosities, as we will discuss in more detail in Chapter 5. Naturally, the question arises: Which operating regime is optimal in what context? For a fixed undulation frequency, we demonstrated that the pass-through regime enables maximum swimming speed, homogeneous undulation parameters, and a one-to-one instantaneous mapping between actuation (preferred curvature) and body curvature without lag. The latter should be advantageous for maneuverability and quick behavioral adaptations. However, despite these benefits, it is unclear whether the pass-through regime is favorable from an energetic point of view - a question we will address in Section 4.3.

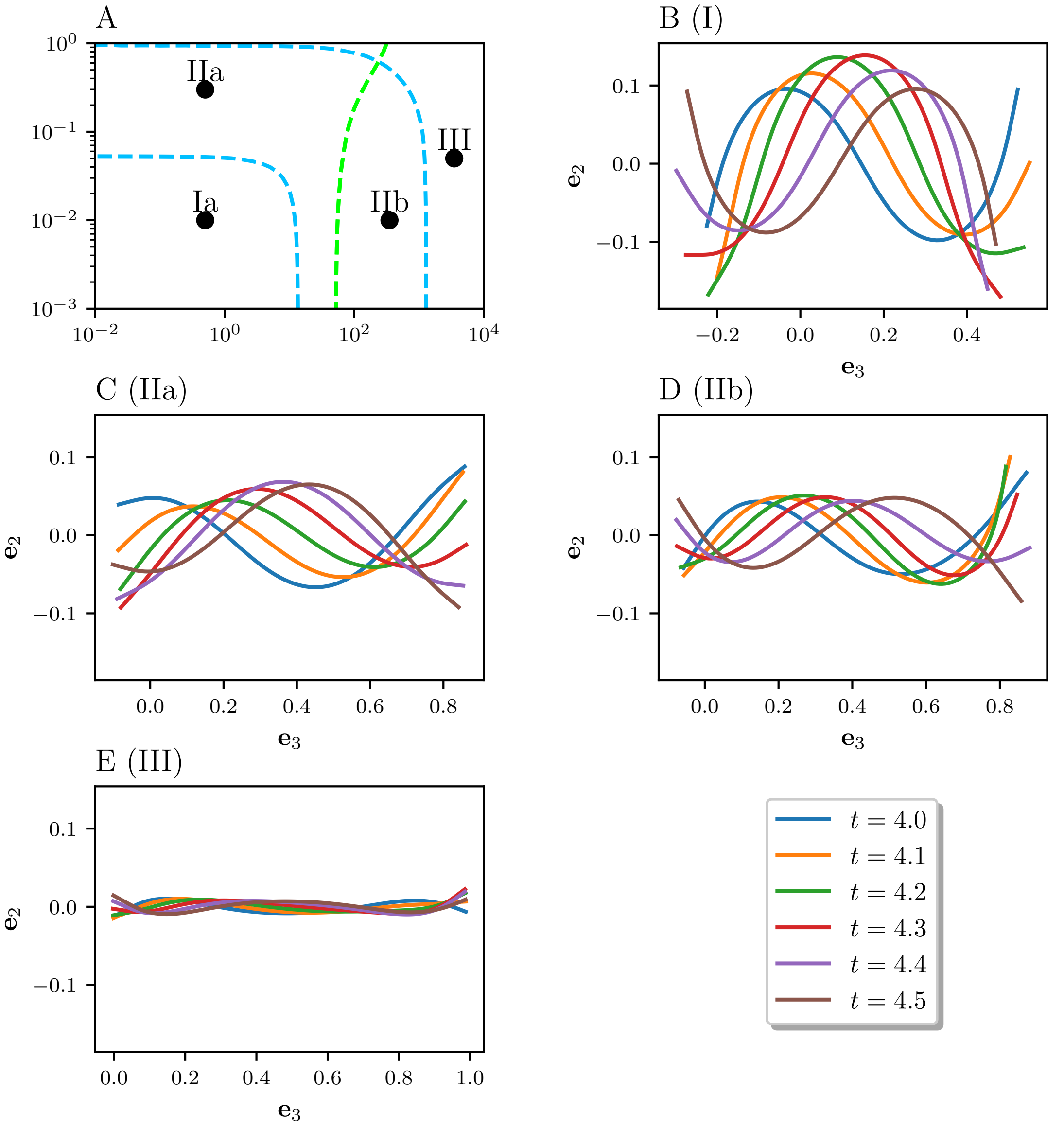

Figure 4.7: Snapshots of the swimmer's body waveforms in different dynamical regimes with preferred curvature waveform ($\lambda_0 = 1$, $A_0 = 2\pi$) and initial configuration $\boldsymbol{r}(s, 0) = s\boldsymbol{e}_3$ where $s \in [0, 1]$. (**A**): Depiction of the different dynamical regimes introduced in Fig. 4.6. We select an exemplary operating point (a, b) for each regime represented by the black dots. The swimmer's waveforms at those operating points are illustrated by plotting the swimmer's centreline coordinate $r_3(s, t)$ and $r_2(s, t)$ in the dorsal-ventral (undulation) plane. Colors represent six different time points (see legend bottom right) in the last undulation cycle of the simulation. (**B**): Emergent waveform in the pass-through regime (I). (**C**): Emergent waveform in the homogeneous low-pass regime (IIa). (**D**): Emergent waveform in the heterogeneous low-pass regime (IIb). (**E**): Emergent waveform in the struggling regime (III). We use the same y-axis range in each panel to illustrate the damping of the waveform's amplitude. Other dimensionless model parameters are identical to those in Fig. 4.2.

4.3 Performance Analysis of Dynamic Regimes

In the previous section, we defined four distinct dynamical regimes, each characterized by their unique response properties to actuation. The swimmer's operating point in relationship to those regimes is contingent upon the values of the system's effective response times a and b. From the definitions provided in Tab. 4.1, it follows that $a \propto f\mu/B$ and $b \propto f\xi$, with f being the undulation frequency, μ the fluid viscosity, B the bending rigidity and ξ the relative internal damping coefficient. Hence, if we assume that f and μ are constant, then an increase in a can be understood as a decrease in the swimmer's bending rigidity B. Similarly, an increase b can be understood as an increase in the relative damping coefficient ξ. Conversely, decreasing the rigidity B of the swimmer's passive body shifts its operating point $(a,\ b)$ in the horizontal direction while increasing its viscous damping ξ induces a shift in the vertical direction, as illustrated in Fig. 4.8A. The blue dashed lines represent the regime boundaries between the pass-through, low-pass, and struggle regimes. Hence, we conclude that the swimmer's operating regime is contingent on the geometric and material properties of its body. For the remainder, we make the simplifying assumption that the material parameters of the swimmer's body are time-invariant and homogeneous across the swimmer's body. However, the material properties of the body are known to be dependent on the state of the muscles or molecular motors [66], implicitly represented by the spatio-temporal pattern of the actuation torque.

Naturally, the following questions arise: Can we identify values of B and ξ that enable our model to reproduce the undulatory behavior observed in biological microswimmers across different fluid environments? Do different species of microswimmers exhibit similar values for B and ξ? If indeed, what evolutionary advantages might drive the selection of these specific values? Addressing the latter question, it is well established that evolutionary pressures shape body anatomies that optimize movement speed, energy efficiency, and adaptability to environmental conditions [2, 19]. Hence, to compare the performance of the different dynamical regimes, we consider two objectives: The swimming speed U and the mechanical actuation work W during one undulation period.

To illustrate how W depends on the swimmer's operating point, Fig. 4.8B displays the contour plot of the normalized actuation work $W/W_{\max}$ as a function of a and b. Here, $W_{\max}$ refers to the maximum value of W within the specified range of a and b. Remarkably, we find that the actuation work varies by seven orders of magnitude across this range. To understand this considerable variation, it is instructive to consider the energy balance equation $W = D_{\mathrm{I}} + D_{\mathrm{F}}$, derived in Section 3.1.4. Here, D_{I} and D_{F} represent the energy lost to internal dissipation and to fluid dissipation, respectively. In Section 3.3, we showed that dimensionless internal dissipation rate, scales proportional to $\dot{D}_{\mathrm{I}} \propto b\dot{\kappa}^2/a$. Consequently, as a and b span a combined range of nine orders of magnitude, we expect D_{I} to exhibit variation over a comparable range. To verify, we plot D_{I} as a function of the swimmer's operating point a and b in Fig. 4.8C, which shows that D_{I} varies by ten orders of magnitudes within the specified range a and b.

To gain physical insight from our observations, we recall that $a \propto E^{-1}$ and $b \propto \xi$. From $a \propto E^{-1}$, it follows that the swimmer's Young's modulus E changes by six orders of magnitude across the given range of a. Similarly, from $b \propto \xi$, it follows that the swimmer's relative damping coefficient ξ changes by three orders of magnitude across the given range of b. Consequently, the internal viscosity η, defined as $\eta = \xi E$, changes by nine orders of magnitudes across the combined range of a and b. Hence, the physical explanation for why D_{I} varies by ten orders of magnitude is simply that we are comparing swimmers with vastly different body stiffness and internal viscosity. Notably, a six-order magnitude change in Young's modulus equates to comparing the elastic properties of rubber and diamond [67, 123]. Clearly, the range of biologically plausible values for Young's modulus must be constrained to a narrower range. However, the effective bending rigidity of microswimmers is not only determined by the combined material properties of their structural elements but also their size [13]. Hence, as $a \propto \varepsilon^{-4}$, it is conceivable that a large range of a values has been evolutionarily accessible. Here, $\varepsilon = 2R_{\mathrm{max}}/L_0$ is the slenderness parameter.

For a more comprehensive understanding, we showcase the contour plot of D_{F} as a function of the swimmer's operating point $(a,\, b)$ in Fig. 4.8D. Remarkably, D_{F} closely resembles the contour plot of the curvature amplitude, shown in Fig. 4.5. In restive-force theory, the fluid dissipation rate is proportional to $\dot{D}_{\mathrm{F}} \propto u^2$, where u denotes the magnitude of the centreline velocity averaged across the length of the swimmer's body. To infer the scaling of u, note that the swimmer generates its centreline velocity by actively bending its body. The speed of its deformation is, therefore, characterized by the curvature rate $\dot{\kappa}$, which is proportional to the curvature amplitude $\dot{\kappa} \propto A$. Hence, we conclude that $u \propto A$, from which follows that $D_{\mathrm{F}} \propto A^2$, which explains why the contour plot of D_{F} resembles that of the curvature amplitude. As A varies by 1.5 orders of magnitude over the specified range of a and b; we expect D_{F} to exhibit variations of approximately three orders of magnitude, which is confirmed by Fig. 4.8D.

To assess whether the energetic cost of swimming is dominated by losses due to internal or fluid dissipation, we plot the ratio D_{I}/D as a function of the swimmer's operating point $(a,\, b)$ in Fig. 4.8E. If the ratio is close to one, internal dissipation dominates and $W \approx D_{\mathrm{I}}$. Conversely, if it is close to zero, fluid dissipation dominates and $W \approx D_{\mathrm{F}}$. Hence, we can identify three parameter regions: In the upper-left corner of Fig. 4.8E, characterized by small a and large b, internal dissipation dominates the energetic cost of swimming. As $\eta \propto b/a$, this region corresponds to swimmers with large internal viscosity η. Consequently, in the bottom-right corner, characterized by small a and large b, fluid dissipation dominates.

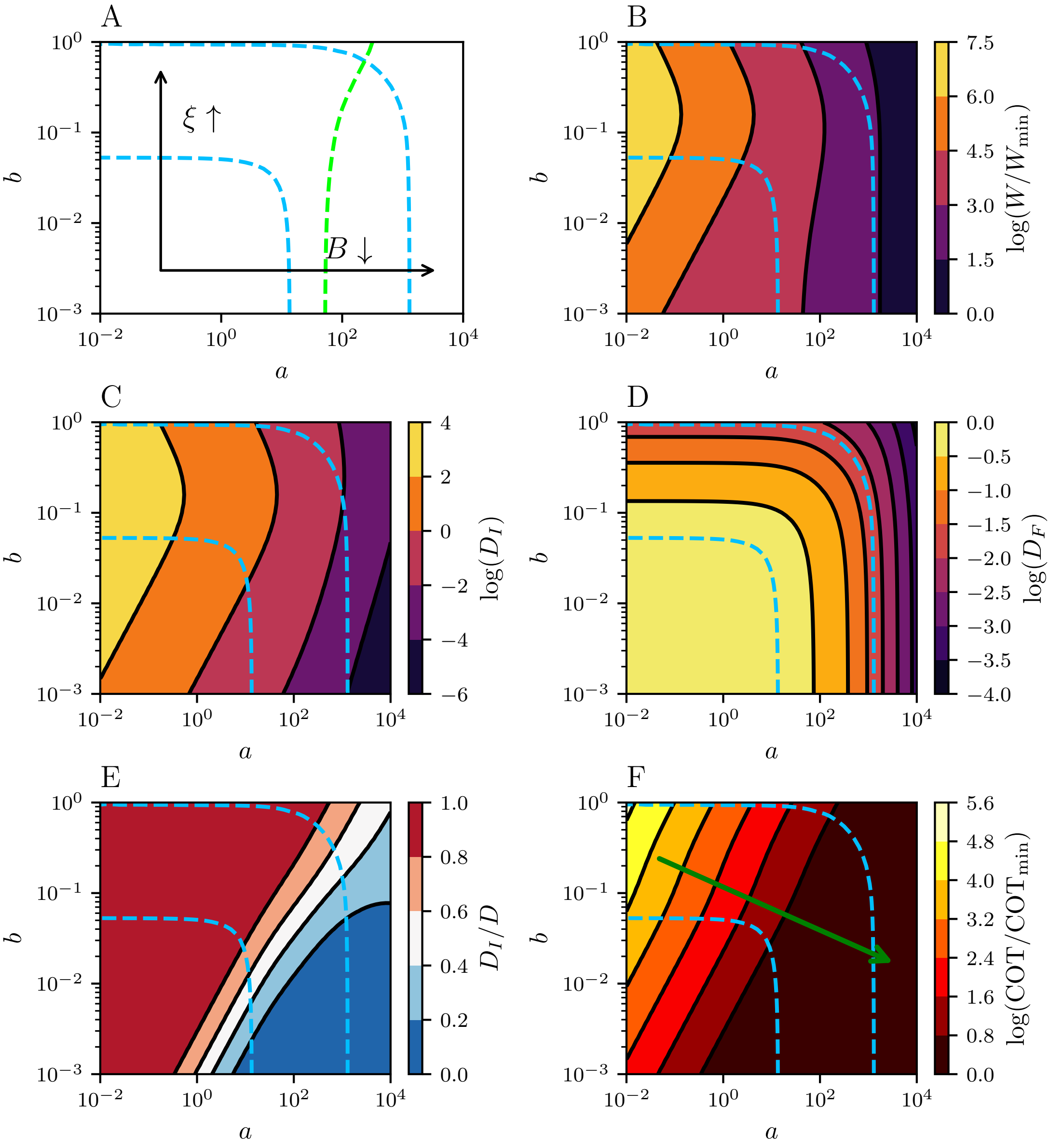

Figure 4.8: Dependency of different energy components on the swimmer's operating point characterized the by effective response times a and b. (**A**): The blue and green dashed lines represent the dynamical regime boundaries introduced in Section 4.2. If the fluid viscosity μ, undulation frequency f, and slenderness parameter ε are assumed constant, then increasing a and b lead to a decrease in the bending rigidity B (horizontal black arrow) and an increase in the relative damping coefficient ξ (vertical black arrow), respectively. (**B**): Contour plot of the actuation work W per undulation cycle normalized by the minimum actuation work $W_{\min}$ within the specified range of a and b. (**C**): Contour plot of the internally dissipated energy $\log(D_{\mathrm{I}})$ per undulation cycle. (**D**): Contour plot of the energy $\log(D_{\mathrm{F}})$ dissipated into the fluid per undulation cycle. (**E**): Ratio between the internally dissipated energy D_{I} and total dissipated energy $D = D_{\mathrm{I}} + D_{\mathrm{F}}$. (**F**): Contour plot of Cost of Transport (COT) (Eq. (4.7)), normalized by the minimum $\mathrm{COT}_{\min}$ within the specified range of a and b. Other dimensionless model parameters are identical to those chosen in Fig. 4.2.

Between both corners, there is a transition region where both internal and fluid dissipation contribute meaningfully to the energy cost of swimming.

Notably, for $b > 10^{-3}$, internal dissipation makes a significant contribution to the total energy cost within the entire pass-through regime. Therefore, even if the internal viscosity η is considerably smaller than Young's modulus E, our model demonstrates that internal dissipation can contribute meaningfully to the swimmer's energy cost. In such a scenario, the swimmer's body should not be approximated as purely elastic, even if its internal viscosity η is up to a thousand times smaller than its Young's modulus E. This is because the value of η needs to be compared to the value of the fluid viscosity μ to judge whether its contribution to the energy cost is negligible or not.

To estimate the swimmer's energy efficiency, we define the Cost of Transport (COT) as the required actuation work per unit distance

$$\mathrm{COT} = \frac{W}{S}, \tag{4.7}$$

where $S = U\,T$ is the distance the swimmer travels per undulation cycle T. The r.h.s. of Eq. (4.7) can be expressed in terms of dimensionless variables, which yields the expression

$$\mathrm{COT} = \mu c_{||} L_0^2 f \cdot \mathrm{COT}^*, \tag{4.8}$$

where we defined the dimensionless Cost of Transport COT^* as follows:

$$\mathrm{COT}^* = \frac{W^*}{U^*}. \tag{4.9}$$

To derive Eq. (4.8), we converted W to W^* using the conversion factor defined in Eq. (3.75) and used Eq. (3.77) to express the distance S in terms of the dimensionless swimming speed U^*. Note that U^* is equivalent to the dimensionless distance $S^* = U^*\,T^*$, as $T^* = 1$. For the remainder, we will omit the star superscript for brevity unless otherwise stated.

The COT is commonly used as an efficiency measure in the study of biological and engineered systems [14, 19, 75, 140]. Only recently, Anastasiadis *et al.* [8] designed a bio-inspired anguilliform robot and showed that live anguilliforms optimize their waveform to minimize their COT. To get a more intuitive understanding of the COT, we draw the following analogy: Envision a car trip from Leeds to London. The COT of our trip is given by the amount of fuel expended divided by the road distance traveled. Clearly, the COT depends on the speed at which the car is driven. Generally, cars have an optimal speed at which they achieve the best fuel efficiency. At higher speeds, the air resistance increases significantly. At low speeds, the car's engine performs less efficiently. Hence, for a typical car, the optimum velocity range is between 55 - 80 km/h. Similar to our car analogy, we seek to identify the operating regime that minimizes the swimmer's COT during undulatory locomotion.

The dimensionless COT as a function of the swimmer's operating point (a, b) is displayed in Fig. 4.8F. The contour lines are straight and parallel, indicating a uniform gradient direction, represented by the green arrow. Notably, the width of the contour bands expands as a becomes larger, implying a decrease in the gradient's magnitude. Surprisingly, our model predicts that the swimmer's COT is minimal at the bottom right corner of the contour plot. This implies that the swimmer operates most cost-effectively in the struggle regime. This may appear counterintuitive since the struggling regime is characterized by very slow swimming speeds. However, as we discussed previously, the parameter region at the bottom right corner corresponds to small values of the internal viscosity η. Consequently, in this region, the swimmer loses significantly less energy to internal dissipation compared to the pass-through regime. This reduction in energy loss makes up for the slower swimming speed, explaining why the COT is minimized in the struggle regime. In our car analogy, this would mean that to minimize fuel expenditure on our journey from Leeds to London, the optimal strategy would be to drive at a walking pace with a chugging engine. This counterintuitive result reveals a shortcoming of our model, as it only accounts for the energy cost required by the swimmer to actively deform its body.

However, it is clear that biological organisms also expend energy to maintain essential physiological functions such as metabolic processes, neural activity, digestion and so forth [2, 19]. Analogously, running a car idle will consume fuel without generating any productive movement. Therefore, assuming that it would take us ten days to drive from Leeds to London at a walking pace, this idle baseline consumption would accumulate over time, significantly contributing to the total fuel cost. In the same vein, if a microswimmer swims at a lower speed, the travel time to cover a unit distance increases, i.e. it requires more energy to maintain its physiological functions over the course of its journey.

To incorporate this idea into our model, we introduce the Basal Metabolic Rate (BMR), which represents an organism's energy expenditure per unit of time at rest, necessary to uphold its essential physiological functions [68]. For the sake of simplicity, we assume the swimmer's BMR to be constant. Hence, in physical units, the refined COT takes the form:

$$\mathrm{COT} = \frac{W + \mathrm{BMR} \cdot T}{S}. \tag{4.10}$$

The dimensionless COT is then given by

$$\mathrm{COT}^* = \frac{W^* + \mathrm{BMR}^*}{U^*}, \tag{4.11}$$

where we defined dimensionless BMR, denoted as BMR*, as follows:

$$\mathrm{BMR} = \mu c_{||} L_0^3 f^2 \mathrm{BMR}^*. \tag{4.12}$$

We note that the conversion factor is identical to the one we derived for the internal and the fluid dissipation rate as well as the actuation power in Eq. (3.74). From Eq. (4.12), it follows that BMR* is not a constant, but it depends on the fluid's viscosity μ, drag coefficient $c_{||}$, the swimmer's body length L_0 and its undulation frequency f. Note that this dependency must be taken into account when comparing the swimmer's COT across different environments and for varying undulation frequencies.

Naturally, the following question arises: What constitutes a plausible range of values for an organism's BMR, and how does this range compare to its actuation work W? Or, drawing on our analogy, how does the fuel consumption of an idle car compare to that of a driving car? To investigate this question, the Vid. 4.1A shows how the contour plot of the COT changes as we continuously increase the BMR. Here, we limit BMR to values within the range BMR $\in [W_{\mathrm{min}}, W_{\mathrm{max}}]$, where W_{min} is the minimum and W_{max} the maximum value of W within the specified range of a and b. The video demonstrates that irrespective of the value of the BMR, the minimum COT is always located at the bottom boundary of the contour plot, corresponding to $b = 10^{-3}$. This is not surprising as $b \propto \xi$. Consequently, decreasing b reduces the relative internal friction within the swimmer's body and is, therefore, always energetically advantageous.

Clearly, the relative internal damping coefficient ξ cannot be arbitrarily small, given that the deformation of biological material invariably generates internal friction. In the case of microswimmers, only a few experimental studies have attempted to estimate ξ [13, 45, 125, 126]. For *C. elegans*, Fang Yen *et al.* [45] estimated an upper bound of $\xi = 5 \times 10^{-3}$ and observed undulation frequencies in the range $f \in [0.3, 1.76]$ Hz, which corresponds to b values within the range $b \in [1.5, 9] \times 10^{-3}$. Thus, for illustrative purposes, we assume that $b = 5 \times 10^{-3}$, as represented by the horizontal dashed red line in Vid. 4.1A.

On this horizontal line, the red cross represents the a value that minimizes the COT, which will be referred to as the swimmer's most cost-effective operating point. We make the following observations: For small BMR values, the swimmer operates most cost-effectively in the struggling regime, characterized by very slow swimming speeds. As the BMR increases, the most cost-effective operating point moves gradually to the left, passing from the struggle through the low-pass to the pass-through regime, where the swimmer achieves its maximum swimming speed. This makes intuitive sense, as a larger BMR incentivises the swimmer to reach its destination faster. Hence, we conclude that the relative cost-effectiveness of the different operating regimes varies based on the value of the BMR.

To quantify the relationship between the BMR and actuation work W, we introduce the Metabolic Equivalent of Task (MET). In general, the MET is defined as the ratio between the organism's energy expenditure during a specific physical task and its energy expenditure during rest [3]. Thus, in the context of our model, we define the MET for undulatory locomotion as

$$\mathrm{MET} = 1 + \frac{W}{\mathrm{BMR} \cdot T} = 1 + \frac{W^*}{\mathrm{BMR}^*}. \tag{4.13}$$

To clarify, an MET value of X means that the swimmer expends X times more energy during undulatory locomotion compared to its resting state. Consequently, if $\mathrm{BMR} \cdot T \gg W$, then $\mathrm{MET} \approx 1$, i.e. the actuation work is negligible and undulatory locomotion requires as much energy as resting. Conversely, if $\mathrm{BMR} \cdot T \ll W$, then $\mathrm{MET} \gg 1$, i.e. undulatory locomotion requires significantly more energy than resting.

Vid. 4.1B illustrates the changes in the contour plot of the MET as the BMR gradually increases. Similar to panel A, the red cross represents the swimmer's most cost-effective operating point if we assume that $b = 5 \times 10^{-3}$. As the BMR increases, the MET at the most cost-effective operating point operating point gradually decreases by three orders of magnitude. For BRM values close to W_{min}, the swimmer operates most cost-effectively in the struggling regime, where $\mathrm{MET} = \mathcal{O}(10^2)$, i.e. undulatory locomotion requires at least a hundred times more energy than resting. As the BMR increases, the most cost-effective operating point moves towards the pass-through regime, and the MET converges to one.

To summarize the results presented in Vid. 4.1, we showcase the contour plots of the swimmer's COT for a relatively small and large BMR value in Fig. 4.9A and B, respectively. In Fig. 4.9C and D, we plot the normalized COT and the normalized swimming speed as a function of the swimmer's operating point a assuming that $b = 5 \times 10^{-3}$. The vertical black dashed line denotes the most cost-effective operating point, where the COT is minimal. Hence, the intersection of this vertical dashed line and red curve yields the most cost-effective swimming speed. In panel C, the swimmer operates most efficiently in the low-pass regime, i.e. the most cost-effective swimming speed is lower than the maximum swimming speed. In this scenario, shifting the operating point to the left, as indicated by the black arrow, enhances the swimming speed at the expense of increasing the COT. Therefore, in the region to the left of the vertical dashed line, there exists a trade-off between swimming speed and COT. Conversely, in Panel D, the swimmer operates most cost-effectively in the pass-through regime. In this scenario, the maximum swimming speed is also the most cost-effective. Hence, the swimmer has no incentive to change its operating point because it optimizes both objectives, speed and efficiency.

To provide a comprehensive analysis covering the entire range of BMR values, we plot the most cost-effective swimming speed (red), operating point a_{opt} (yellow), and the associated

MET value (green) against the BMR in Fig. 4.9E. As the BMR increases, the a value of the most cost-effective operating point increases and the swimmer transitions from the struggle through the low-pass to the pass-through regime. Simultaneously, the most cost-effective normalized swimming speed gradually increases from approximately zero in the struggling regime until it eventually converges to one in the pass-through regime. In the struggling regime, the MET is of the order of 10^2, i.e. undulatory locomotion requires at least a hundred times more energy than resting. As the BMR increases, the MET decreases gradually until it eventually converges to one in the pass-through regime. At this point, the BMR is so large that the actuation work is negligible, and the swimmer is incentivized to swim as fast as possible to reduce its COT.

Naturally, the question arises: What is a plausible range for the MET value of undulating biological microswimmers? To address this question, it is important to acknowledge that the MET has been primarily developed to study human fitness and health. For example, during light, moderate, and intensive physical activities like walking, jogging and running, the MET of humans is typically between 2 and 12 [3]. However, microswimmers such as *C. elegans* and humans have vastly different physiological and biomechanical characteristics; therefore, no direct comparison should be drawn. Obviously, it would be desirable to constrain the MET of microswimmers through experimental measurements. To study the metabolism of microorganisms, researchers typically use indirect measures such as oxygen consumption or carbon dioxide production to estimate the organism's metabolic rate [98]. Regardless of the chosen metric, if it can be measured at rest and during locomotion, then by comparison, the microswimmer's MET could be estimated. Hence, to test the hypothesis that the bending rigidity of slender microswimmers has evolved to enable cost-effective undulatory locomotion in their natural habitat, experimental estimates of the bending rigidity, relative internal damping, and MET are required. For *C. elegans*, Laranjeiro *et al.* [82] measured the MET by using a highly sensitive microcalorimeter chamber. They compared the energy expenditure of anesthetized worms to worms in an active state in both buffer solution (akin to water) and a solid medium (agar). In water and on agar, they estimated a general MET of the order of 3 and 1.7, respectively, which is comparable to the MET of humans during mild physical activity. Similar values have been confirmed by Hur *et al.* [69]. According to Fig. 4.9E, this would translate to an optimal operating point in the low-pass regime (II) close to the boundary of the pass-through regime (I). In this regime, there does not exist an optimal solution that maximizes the swimming speed and minimizes the COT simultaneously. Thus, our model predicts a parameter region where a trade-off between swimming speed and COT exists. This finding has interesting consequences as a swimmer can actively shift its operating point by modulating its undulation parameters, as will be discussed in more detail in the following chapter.

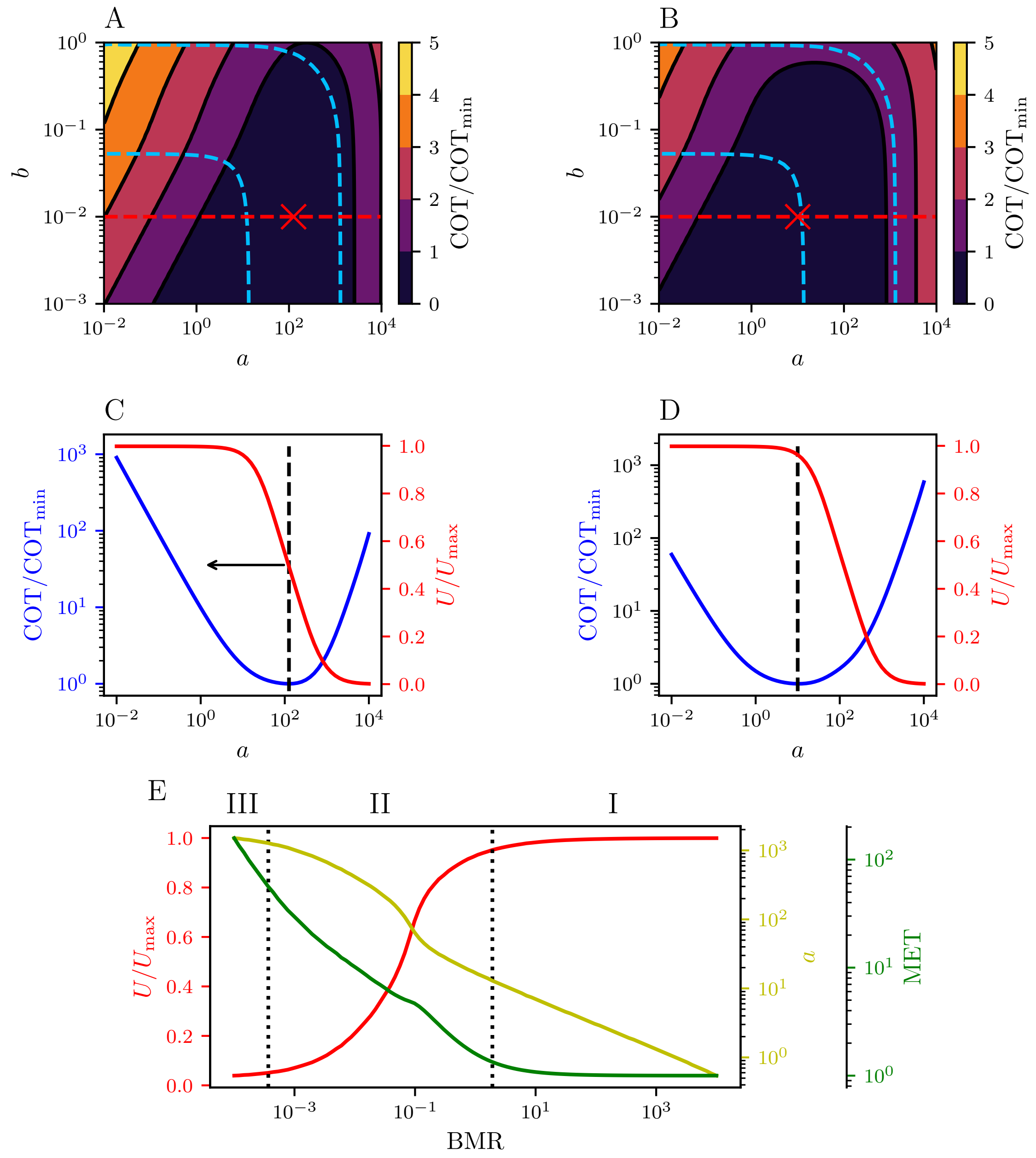

Figure 4.9: Dependency of the swimmer's optimal operating regime on its Basal Metabolic Rate (BMR). (**A**, **B**): Contour plots depicting the refined normalized Cost of Transport (COT) (Eq. (4.10)) as a function of the swimmer's operating point a and b. For normalization, we use the minimum $\mathrm{COT}_{\min}$ within the specified range of a and b. BMR in both panels is set to 0.1 and 10, respectively. The blue dashed lines display the boundaries of the dynamical regimes introduced in Section 4.2. The horizontal red line in panels A and B corresponds to the value $b = 10^{-2.5}$. The red cross represents the most cost-effective operating point on this line. (**C**, **D**): Normalized COT (blue) and the normalized swimming speed (red) as a function of the swimmer's operating point a for fixed $b = 10^{-2.5}$. The vertical dashed line represents the minimum COT. (**E**): The most cost-effective normalized swimming speed $U/U_{\max}$ (red), optimal operating point a (yellow) that minimizes COT, Metabolic Equivalent of Task (MET) (Eq. (4.13)) (green). The dotted lines illustrate the most cost-effective operating regime as the BMR increases. Other dimensionless model parameters are identical to those chosen in Fig. 4.2.

4.4 Discussion

To characterize the response properties of our model, we conceptualized the microswimmer and its surrounding fluid environment as a dynamical filter, which takes the actuation torque as an input and generates the swimmer's body curvature as an output. We defined the spatio-temporal pattern of the actuation torque in terms of the preferred curvature [52, 111, 125, 126]. To achieve undulatory locomotion, we modeled the preferred curvature as a sinusoidal traveling wave [45, 52, 58, 125], characterized by a constant curvature amplitude, wavelength, and undulation frequency. Employing this simple model, we demonstrated that the swimmer's response to actuation is primarily governed by the system's effective (dimensionless) response times a and b. Note that a is proportional to the fourth power of the sperm number, a dimensionless parameter first introduced to describe the biomechanical properties of sperm flagella [43, 93]. However, we adopt the definition of a because it can be interpreted as a ratio of timescales. In studies of active and passive filament fibers, a is also commonly referred to as the effective viscosity [129], bending relaxation time scale [44, 47], effective flow forcing [100]. It determines the time scale of fast a bend filament relaxes back into its natural stress free configuration in a given fluid environment. The effective response time b has been referred to as the swimmer's mechanical timescale [71]. Within the parameter space of a and b, we identified four different dynamical regimes, each characterized by their distinct filter properties.

To the best of our knowledge, these regimes have not been previously identified and characterized. Importantly, we showed that the specific regime a microswimmer operates in is contingent on its body geometry, material parameters, undulation parameters, and the viscosity of the surrounding fluid. Furthermore, we demonstrated that the operating regimes are characterized by different swimming speeds and energy efficiency. Hence, they provide a pathway to understanding the evolutionary selection of a swimmer's body parameters and gait parameters within a given habitat. In particular, our model predicts that if evolution has prioritized swimming speed, the swimmer's body stiffness should have evolved to be sufficiently rigid for it to operate in the pass-through regime, which is characterized by maximum swimming speed and instantaneous response to actuation. However, once the swimmer operates in the pass-through regime, any further increase in stiffness offers no speed advantage, as the swimmer already operates at maximum speed. On the contrary, increasing the body stiffness would be energetically disadvantageous, as it increases the internal viscosity and, thereby, the energy loss due to internal dissipation. Our assumption here is that the internal viscosity scales with body stiffness. Furthermore, a larger stiffness also requires stronger muscles, as the actuation torque's amplitude must scale with the body's bending rigidity to overcome elastic resistance to deformation.

Hence, if a swimmer is geared towards swimming at maximum speed in a fixed environment, our model predicts that its body stiffness should have evolved to position its operating point in the pass-through regime, precisely at the right part of the boundary to the low-pass regime. The spermatozoa of sea urchins would be an ideal model organism to test this hypothesis, as both sperm and eggs are directly released into the surrounding water. If an organism has evolved to navigate a spectrum of fluid viscosities, its stiffness would need to be adapted to the most viscous environment to enable fast swimming across the entire range. Alternatively, a swimmer can also reduce its undulation frequency to sustain an optimal operating point in more viscous surroundings. This adaptive behavior has been observed in *C. elegans* and sperm [18, 45, 79, 114, 126] and will be further explored in Chapter 5.

To quantify the swimmer's energy efficiency, we defined the Cost of Transport (COT) as the energy cost per undulation cycle divided by the distance traveled [8, 19]. Previous studies by Korta *et al.* [79] and Berri *et al.* [18] only used the fluid dissipation rate to estimate the swimming power of *C. elegans*. However, our model reveals that internal dissipation can significantly contribute to the swimmer's energy cost even if the swimmer's internal viscosity is much smaller than its Young's modulus. This is because it is not the ratio between the internal viscosity and Young's modulus that determines the relative contribution of internal friction to the swimmer's energy cost, but rather the ratio of internal viscosity to fluid viscosity. This observation aligns with the findings by Fang Yen *et al.* [45], who measured and modelled the undulatory locomotion of *C. elegans* across a wide range of fluid viscosities. Their model showed that in low fluid viscosities, the energy cost of *C. elegans* is dominated by internal friction, whereas in high viscosity fluids, it is dominated by external friction with the fluid environment. We will revisit this point in Chapter 5 and 6 when we explore gait adaptation in response to variations in fluid viscosity.

Other studies that considered the contribution of internal friction to the organism's energy cost include the work by Guo *et al.* [58] and Yaqoob *et al.* [141], both of whom modeled the undulatory locomotion of limbless organisms on land. Guo *et al.* utilized a continuous rod model, whereas Yaqoob *et al.* employed a model featuring a small number of discrete coupled joints. Specifically, Guo *et al.* defined the organism's mechanical efficiency as the power required to move an inactive limbless organism in the direction of motion to the power lost due to internal and external friction forces. The definition by Guo *et al.* is similar to the standard definition by Lighthill [87], who defined the hydrodynamic efficiency of a swimming organism as the ratio between the power required to drag the organism with constant velocity through a fluid and the power this organism dissipates into the fluid when it actively swims at the same velocity.

However, when evaluating the energy efficiency of locomotion, it is essential to not only account for how much energy an organism expends per unit of time but also for the distance it covers within the same time period. This is especially important when considering the gait modulation of undulatory microswimmers, as changes in waveform and undulation frequency impact both the swimming power and the swimming speed. This is why we opt for the Cost of Transport (COT) as an efficiency measure. Furthermore, by including the organism's Basal Metabolic Rate (BMR) as an additional energy cost, we account for the energy expended by the organism to sustain its essential physiological functions. The energy cost associated with the BMR during one undulation cycle is inversely proportional to the swimming speed. i.e. it penalizes slow swimming speeds. This penalty introduces a lower bound for the undulation frequency and swimming speed, as we will show in the next chapter.

So far, our analysis has been based on the assumption that the swimmer maintains a constant frequency and waveform. To understand how the swimmer's undulation frequency and waveform affect its swimming speed and energy efficiency, we will explore gait modulation in the next chapter.

Chapter 5

Gait modulation

How to be fast and how to go far

5.1 Overview

This chapter explores gait modulation in undulatory microswimmers, characterized by changes in the swimmer's undulation frequency and waveform. Our exploration focuses on two distinct waveforms: the fastest and most cost-effective. The former is the waveform that maximizes the swimmer's swimming speed, whereas the latter minimizes the swimmer's Cost of Transport (COT). A comprehensive analysis is presented of how these two waveforms change as a function of the undulation frequency and the fluid viscosity. This analysis will be instrumental in Chapter 6, where we compare our model to available experimental data for *C. elegans* to infer whether its gait prioritizes swimming speed or energy efficiency.

This chapter is organized into two parts: The first part focuses on gait modulation in a static environment characterized by a constant fluid viscosity. The second part explores gait modulation in response to changing environmental conditions represented by different fluid viscosities. To simplify our analysis, we start our exploration by focusing exclusively on frequency modulation, assuming a fixed waveform. The goal is to provide a comprehensive understanding of how the undulation frequency influences the swimming speed and the COT of the swimmer in a static environment. Subsequently, we extend our analysis by allowing the swimmer to modulate its undulation frequency and waveform. First, we conduct a comprehensive sweep across the swimmer's shape space to identify its fastest and most cost-effective waveform. This exploration includes a detailed discussion of the relationship between the swimmer's waveform, angle of attack, and deformation speed.

Finally, we discuss how swimmers can modulate their undulation frequency to achieve efficient swimming across a wide range of fluid viscosities. Building upon these results, we explore how the swimmer's fastest and most cost-effective waveform changes as a function of the fluid viscosity. We find that the most cost-effective waveform undergoes a continuous transition from the low viscosity to the high viscosity regime. This transition can be understood by comparing the relative strength of internal and external friction, as we will discuss in detail.

5.2 Static Environment

This section explores the gait modulation of an undulatory microswimmer in a static environment characterized by a constant fluid viscosity μ. In our model, gait modulation is achieved by adjusting the spatio-temporal pattern of the actuation torque. To simulate undulatory locomotion, we model the actuation torque as a sinusoidal traveling wave, characterized by the preferred curvature amplitude A_0, wavelength λ_0, and undulation frequency f.

In Section 4.2, we demonstrated that the swimmer's response to actuation is primarily determined by the effective dimensionless response times a and b. By our definition, a and b are both proportional to the undulation frequency. Consequently, changes in the undulation frequency f shift the swimmer's operating point $(a,\, b)$ as illustrated in Fig. 4.1. On the other hand, variations in preferred curvature amplitude A_0 and wavelength λ_0 result in changes in the swimmer's waveform, characterized by the body curvature amplitude A and wavelength λ. As discussed in Section 4.2, the preferred waveform and the swimmer's emergent waveform are not necessarily equivalent, a distinction we will emphasize throughout this chapter.

To simplify our analysis, Section 5.2.1 focuses exclusively on frequency modulation while maintaining a constant preferred curvature amplitude A_0 and wavelength λ_0 constant. Subsequently, Section 5.2.2 explores frequency and waveform modulation.

5.2.1 Frequency Modulation

Throughout this chapter, we assume that the swimmer's body geometry, material parameters, and fluid viscosity are known and constant. Consequently, for a generalized microswimmer that undulates with the characteristic frequency f_c, we can calculate its characteristic operating point $(a_c,\, b_c)$; refer to Tab. 4.2. For illustrative purposes, we assume that the swimmer's characteristic operating point sits at the boundary between the pass-through and the low-pass regime, represented by the more prominent dotted marker in Fig. 5.1A. As discussed in the last chapter, such a scenario corresponds to a microswimmer whose rigidity has evolved to enable fast swimming while minimizing energy losses due to internal friction. As a and b are both proportional to f, frequency modulation shifts the swimmer's operating point in a diagonal direction as indicated by the black arrow in Fig. 5.1A. Thus, the smaller dotted markers represent the swimmer's operating point for different values of the normalized frequency $f/f_\mathrm{c} \in [10^{-1}, 10^{1}]$. In this analysis, undulation frequencies span a range of two orders of magnitude. We note that microswimmers such as sperm and *C. elegans* typically only display frequency modulations across one order of magnitude [45, 113, 114]. However, we choose a broader range to capture extreme cases.

To investigate how the swimmer's speed scales with its undulation frequency, we plot the dimensionless normalized swimming speed U^*/U^*_max against the normalized undulation frequency f/f_c in Fig. 5.1B. The dotted markers correspond to the operating points shown in panel A. Notably, as the swimmer increases its undulation frequency, the normalized dimensionless swimming speed decreases from one to zero, indicating a transition from the pass-through to the struggling regime. To clarify, with a constant body geometry, material parameters and fluid viscosity, the system's characteristic response times τ and ξ remain constant; see Tab. 4.1. Consequently, as the undulation frequency increases, it becomes increasingly difficult for the swimmer's body to keep up the time scale set by the actuation torque, explaining why the system transitions to the struggling regime.

According to Eq. (3.77), multiplying the dimensionless swimming speed U^* with the undulation frequency f yields the physical swimming speed per unit body length, which we will refer to as U. The characteristic physical swimming speed per unit body length is, therefore, defined as $U_\mathrm{c} = U^*_\mathrm{c} \cdot f_\mathrm{c}$, where U^*_c is dimensionless swimming speed associated with the swimmer's characteristic operating point $(a_\mathrm{c},\, b_\mathrm{c})$. To illustrate how the physical swimming scales with the undulation frequency, Fig. 5.1B plots the normalized physical swimming speed U/U_c (dashed line) as a function of f/f_c on the secondary y-axis. The dotted markers represent the operating points in panel A. In the pass-through regime, the physical swimming speed scales linearly with f, as the dimensionless swimming speed remains constant. This linear relationship was first shown by Taylor, who considered an infinite waving swimming sheet [127] and a finite tube [128] immersed in a Newtonian fluid. His work on the locomotion of such simplified geometries laid important foundations for understanding fluid dynamics and propulsion mechanisms in biological systems.

As the swimmer's undulation frequency surpasses its characteristic frequency f_c, the swimmer transitions from the pass-through to the low-pass regime, characterized by a damped curvature amplitude and shallower body wave. Consequently, the dimensionless swimming speed decreases in the low-pass regime, resulting in a sublinear scaling of the

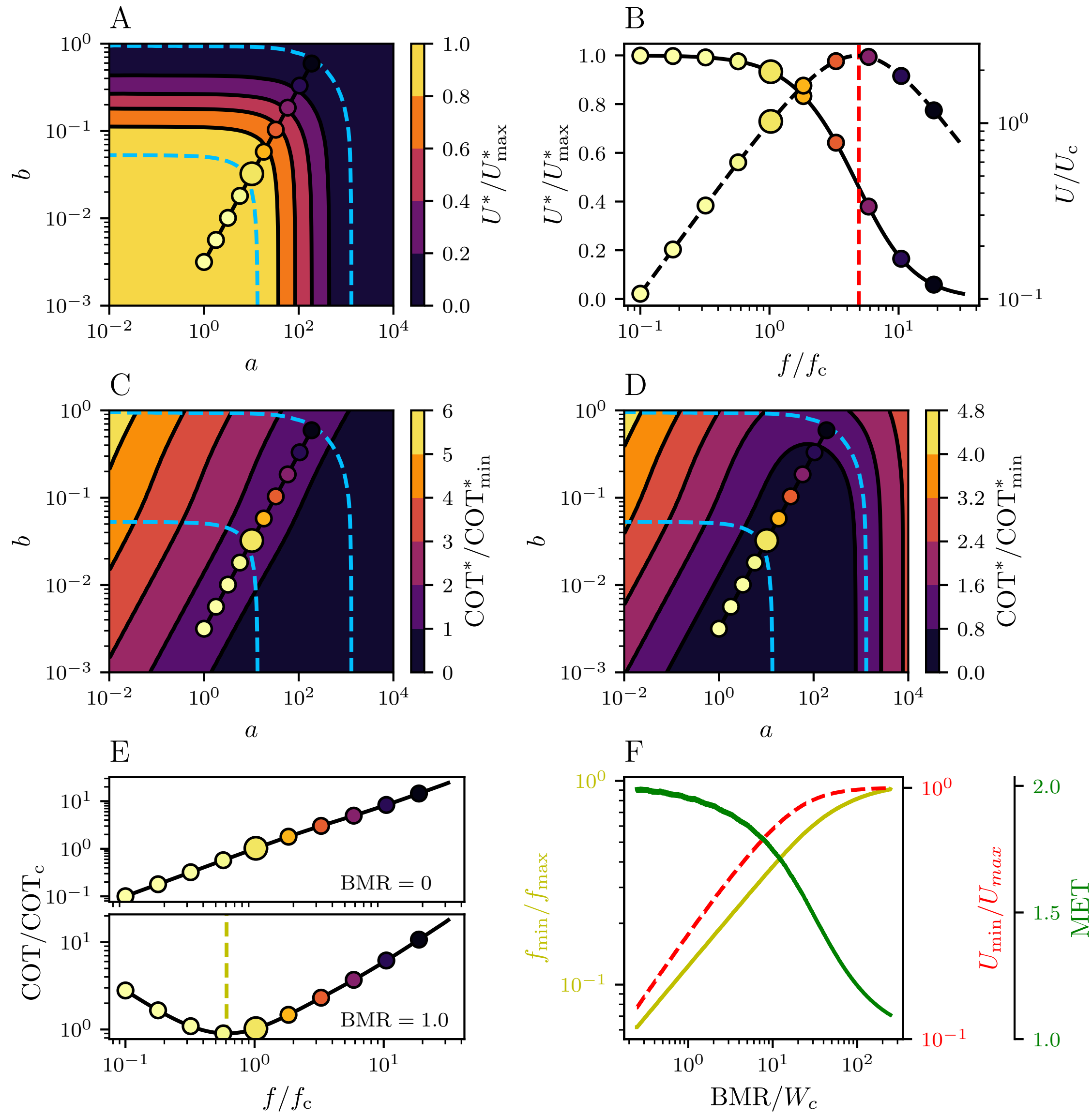

Figure 5.1: Frequency modulation in a static environment with constant fluid viscosity. (**A**): Contour plot of the normalized dimensionless swimming speed $U^*/U^*_{\max}$ as a function of the swimmer's operating point (a, b). The blue dashed lines represent the regime boundaries between the pass-through, low-pass, and struggle regimes introduced in Section 4.2. Large dotted marker represents the characteristic operating point (a_c, b_c) associated with the swimmer's characteristic undulation frequency f_c. Frequency modulation shifts the swimmer operating point along the diagonal represented by the smaller dotted markers color-coded for the operating regime. (**B**): Normalized dimensionless swimming speed $U^*/U^*_{\max}$ (solid) and normalized physical swimming speed U/U_c (dashed) at the operating points in panel A, plotted against the normalized undulation frequency f/f_c. The red dashed line represents the frequency $f_{\max}$ at which the swimmer achieves maximum speed $U_{\max}$. (**C**, **D**): Contour plot of the normalized dimensionless Cost of Transport $\mathrm{COT}^*/\mathrm{COT}^*_{\min}$ without and with Basal Metabolic Rate (BMR). (**E**): Physical Cost of Transport $\mathrm{COT}/\mathrm{COT}_{\min}$ associated with the markers in C and D. The yellow dashed line in the bottom graph represents the most cost-effective undulation frequency $f_{\min}$ associated with speed $U_{\min}$. (**F**): Most cost-effective undulation frequency (yellow), normalized physical swimming speed $U/U_{\max}$ (red), and Metabolic Equivalent of Task (MET) (green) as a function of the normalized Basal Metabolic rate BRM/W_c.

physical swimming with f.

The physical swimming speed peaks at a distinct frequency $f_{\text{max}} > f_{\text{c}}$, represented by the red dashed line in Fig. 5.1B. In this example, f_{max} is approximately five times larger than the swimmer's characteristic frequency f_{c}, whereas the maximum swimming U_{max} is only 2.4 larger than U_{c}, underscoring the sublinear scaling in the low-pass regime. Beyond f_{max}, the swimming speed diminishes despite the swimmer undulating at a higher frequency. This results in the peculiar situation that any swimming speed lower than U_{max} can be achieved by two undulation frequencies, one below and one above f_{max}. In the following, we will demonstrate that the lower undulation frequency is the more energy-efficient one, as one would intuitively expect.

To assess the swimmer's energy efficiency, we calculate the swimmer's Cost of Transport (COT) as a function of the swimmer's undulation frequency f. The contour plot of the normalized dimensionless COT, denoted as $\text{COT}^*/\text{COT}^*_{\text{min}}$, is presented as a function of the swimmer's operating point (a, b) in Fig. 5.1C and D, with and without Basal Metabolic Rate (BMR), respectively. Here, $\text{COT}^*_{\text{min}}$ is the minimum dimensionless COT in the specified range of a and b. In panel D, we select an exemplary value of $\text{BMR}^* = W^*_{\text{c}}$ for the dimensionless BMR, where W^*_{c} is the dimensionless actuation work required to swim at the characteristic frequency f_{c}. To calculate the physical COT, we multiply COT^* with the conversion factor provided in Eq. (4.8). First, we define the characteristic Cost of Transport COT_{c} as

$$\text{COT}_{\text{c}} = \mu c_{||} L_0 f_{\text{c}} \text{COT}^*_{\text{c}}, \tag{5.1}$$

where COT^*_{c} refers to the dimensionless COT associated with the swimmer's characteristic operating point $(a_{\text{c}}, b_{\text{c}})$. From the above equation, it follows that the ratio between physical COT and COT_{c} is given by

$$\frac{\text{COT}}{\text{COT}_{\text{c}}} = \frac{f}{f_{\text{c}}} \frac{\text{COT}^*}{\text{COT}^*_{\text{c}}}, \tag{5.2}$$

where we used that μ, $c_{||}$ and L_0 are constant. Eq. (5.2) will be referred to as the normalized COT. To investigate how the swimmer's COT changes as it modulates its undulation frequency, we plot the normalized COT as a function of f/f_{c} in Fig. 5.1E with and without BMR, respectively. Without BMR, we find that the COT scales linearly with the undulation frequency. This can be understood from Fig. 5.1C, which shows that COT^* remains approximately constant across the entire range of frequencies, represented by the dotted markers. Consequently, from Eq. (5.2), it follows then that $\text{COT}/\text{COT}_{\text{c}} \propto f$. Therefore, our model predicts that undulating with a lower frequency is more cost-effective. This makes intuitive sense, as decreasing the undulation frequency reduces the speed at which the swimmer deforms its body. Consequently, less energy is lost due to internal friction and external friction with the surrounding fluid environment. Thus, to minimize the COT, our model predicts that the swimmer should undulate with zero frequency, essentially taking an infinite time to travel a unit distance.

Beyond energy efficiency, it is evident that biological organisms, including microswimmers, are driven by many objectives, such as foraging, mating and escaping predators. These other objectives require the organism to maintain a reasonable swimming speed and are, therefore, in conflict with undulating at a zero frequency. However, even if we assume that energy efficiency is the swimmer's only objective, our model prediction is counterintuitive. Clearly, a lower limit for the undulation frequency must exist, below which swimming becomes energetically inefficient. Indeed, the bottom panel in Fig. 5.1E shows that when the swimmer's BMR is included as an additional cost, the normalized COT displays a minimum at a distinct frequency f_{min}, represented by the yellow vertical dashed line. Consequently, the swimmer has no incentive to adopt a lower frequency than f_{min} since this would lead to an increase in COT and a decrease in physical swimming speed. On the other hand, undulating at a faster frequency than f_{min} allows the swimmer to enhance its swimming speed at the cost of increasing its COT. Hence, including the BMR in our model constrains the plausible value of undulation frequency f to the range $[f_{\mathrm{min}}, f_{\mathrm{max}}]$. The swimmer can modulate its frequency within this range to prioritize speed or cost-effectiveness. This implies that the range of plausible swimming speeds U is given by $[U_{\mathrm{min}}, U_{\mathrm{max}}]$, where U_{min} is the swimming speed associated with the most cost-effective frequency f_{min}.

To understand how f_{min} depends on the value of the BMR, the yellow curve in Fig. 5.1F plots the ratio $f_{\mathrm{min}}/f_{\mathrm{max}}$ as a function of the normalized BMR, denoted as BMR/W_{c}. Here, W_{c} represents the actuation work required to swim at the characteristic frequency f_{c}. Reducing the BMR leads to a smaller energy penalty for slow swimming speeds. Consequently, the BMR becomes smaller, the ratio $f_{\mathrm{min}}/f_{\mathrm{max}}$ decreases, i.e. the range of plausible undulation frequencies becomes larger. As the normalized BMR increases, f_{min} continuously converges to f_{max} as the swimmer is incentivized to adopt a faster swimming speed. For exceedingly large BMR values, f_{min} becomes equivalent to f_{max}. In such a case, the range of plausible frequencies narrows down to the single value f_{max}, optimizing both speed and energy efficiency.

To compare the swimmer's energy expenditure at rest to undulatory locomotion, the green curve in Fig. 5.1F displays the swimmer's Metabolic Task Equivalent (MET) as a function of the normalized BMR. Here, we consider the MET associated with the most cost-effective undulation frequency f_{min}. For small BMR values, the swimmer's MET has a value of approximately two, signifying that the energy expenditure during undulation is twice as large compared to resting. This value is comparable to the MET of humans during walking. It is slightly smaller than the reported estimate of 3 Laranjeiro *et al.* [82] for *C. elegans* swimming activity. As the BMR increases, the MET converges to one from above, indicating that the energy cost of actuation becomes negligible compared to the one associated with the swimmer's BMR.

To conclude, our model predicts that, within a static environment, the undulation frequency of the microswimmer should be confined to the range $[f_{\mathrm{min}},\ f_{\mathrm{max}}]$. At the lower limit f_{min}, the swimmer's COT is minimal, while at the upper limit f_{max}, the swimmer's speed is maximal. Consequently, within this range, the swimmer can increase its undulation frequency to enhance its swimming speed at the expense of increased COT and vice versa. Moreover, we demonstrated that the value of f_{min} increases with the organism's BMR, whereas f_{max} is only determined by the swimmer's characteristic operating point. The latter depends on physical model parameters including the material and geometric properties of the swimmer's body. Consequently, those properties play a crucial role in determining the maximum swimming speed and frequency of a microswimmer within a given environment. This will be discussed in more detail in the discussion section at the end of the chapter.

5.2.2 Waveform Modulation

In the preceding section, we discussed how the swimmer's operating point $(a,\ b)$ changes as it modulates its undulation frequency. Specifically, we considered normalized undulation frequencies within the range $f/f_{\mathrm{c}} \in [10^{-1}, 10^{1}]$, where f_{c} denotes the swimmer's characteristic frequency. In this section, we consider the same range of undulation frequencies. However, we broaden the scope of our analysis by allowing the swimmer to not only modulate its undulation frequency but also its waveform. To explore how the swimming speed and COT depend on the swimmer's waveform, we simulate undulation experiments encompassing the full range of plausible wavelengths and curvature amplitudes A_0 (or shape-factor c_0). By analyzing these experiments, we aim to identify the swimmer's fastest and most cost-effective waveform. Furthermore, we aim to understand how these distinct waveforms change as the swimmer modulates its undulation frequency.

To better understand how the swimmer's waveform affects its swimming speed, we initially focus on the simulation result for the characteristic undulation frequency f_{c}. For this specific frequency, the contour plot of the normalized swimming speed U/U_{max} as a function of the preferred wavelength λ_0 and shape factor $c_0 = A_0\lambda_0/2\pi$ is shown in Fig. 5.2A. Here, U_{max} denotes the swimmer's maximum swimming speed within the specified range of λ_0 and c_0. Notably, the contour plot reveals a unique maximum at a distinct preferred waveform, represented by the black cross. This waveform, denoted as $(\lambda_{0,\mathrm{max}},\ c_{0,\mathrm{max}})$, will be referred to as the fastest preferred waveform. Note that the swimmer's emergent waveform is not necessarily equivalent to the preferred waveform, as we showed in Chapter 4. Thus, we denote the swimmer's emergent fastest waveform as $(\lambda_{\mathrm{max}},\ c_{\mathrm{max}})$.

Naturally, we want to understand why the waveform $(\lambda_{\mathrm{max}},\ c_{\mathrm{max}})$ achieves maximum

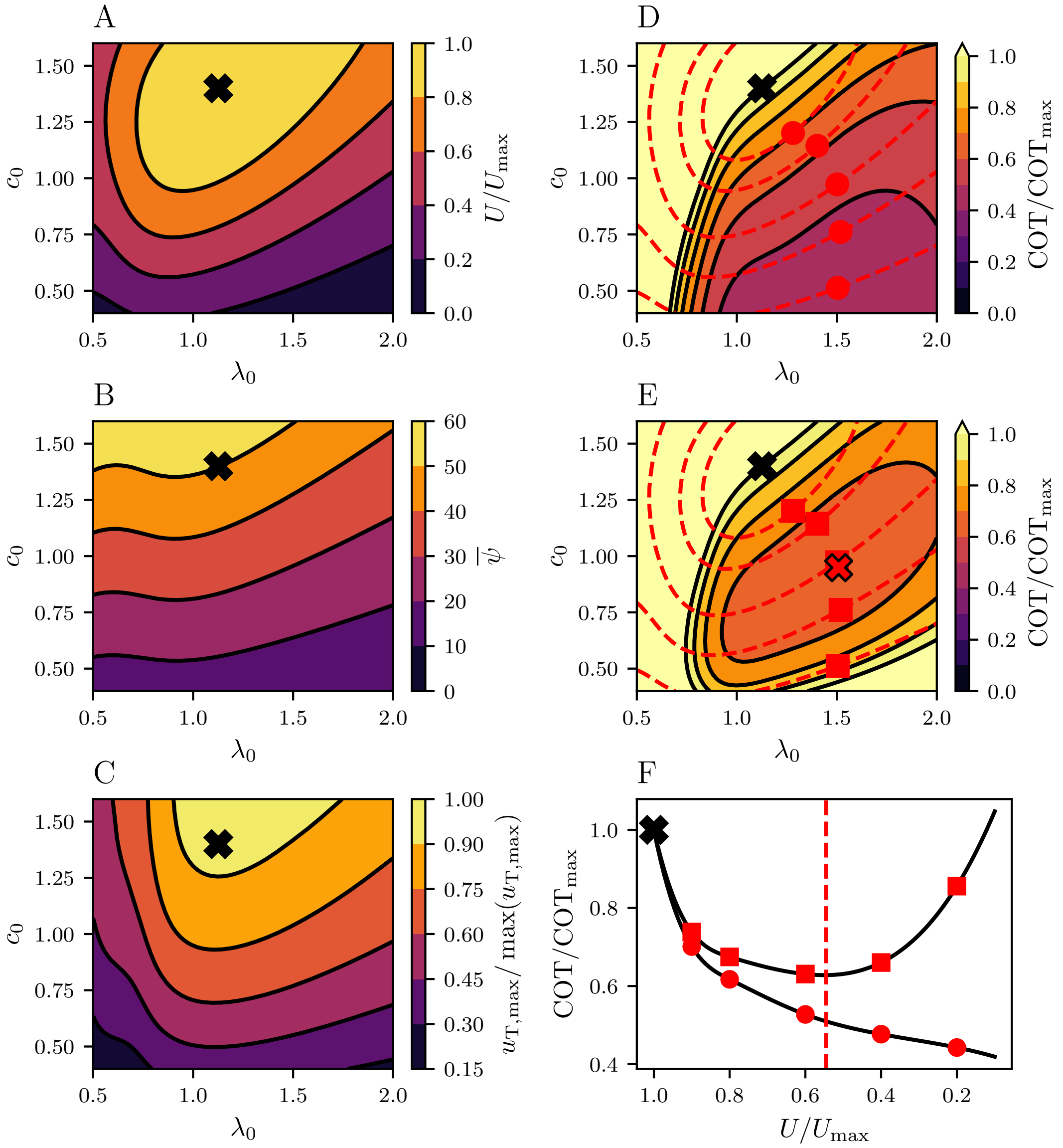

Figure 5.2: Waveform modulation in a static environment with constant fluid viscosity. We adopt the characteristic operating point (a_c, b_c) and frequency f_c introduced in Fig. 5.1A. (**A**): Contour plot of the normalized swimming speed $U/U_{\max}$ as a function of the preferred undulation wavelength λ_0 and shape factor c_0. Here, $U_{\max}$ denotes the maximum swimming speed within the specified range of λ_0 and c_0. The black cross represents the preferred waveform $(\lambda_{0,\max},\ c_{0,\max})$ at which the swimmer achieves maximum speed. (**B**): Contour plot of the average angle of attack $\bar{\psi}$. (**C**): Contour plot of maximum transversal centreline velocity $u_{\mathrm{T,max}}$. (**D**): Contour plot of normalized Cost of transport $\mathrm{COT}/\mathrm{COT}_{\max}$ for $\mathrm{BMR} = 0$, where $\mathrm{COT}_{\max}$ is the Cost of Transport associated with the fastest preferred waveform $(\lambda_{0,\max},\ c_{0,\max})$. Red dashed lines represent contour lines of constant swimming speed displayed in panel A. Red dots and rectangles display the most cost-effective waveform on each of the contour lines. (**E**): Contour plot of normalized $\mathrm{COT}/COT_{\max}$ for $\mathrm{BMR} = 0.1 \cdot W_{\max}$, where $W_{\max}$ is the actuation work required to swim with the fastest waveform. Red cross denotes waveform $(\lambda_{0,\min},\ c_{0,\min})$ that minimizes the COT. (**F**): Normalized Cost of Transport $\mathrm{COT}/\mathrm{COT}_{\max}$ without BMR (dots) and with BMR (rectangles) plotted against normalized swimming speed $U/U_{\max}$. The vertical red dash line represents the speed $U_{\min}$ that minimizes the COT with BMR.

swimming speed. To address this question, we employ a simple geometric model, discussed in detail in Appendix A.3.1. This model reproduces the well-known approximation by RFT that the propulsive force $f_\mathrm{p}(s,t)$, generated by the body segment at position s and time t is proportional to

$$f_\mathrm{p}(s,t) \propto \sin(2\psi) \cdot u_\mathrm{T}, \tag{5.3}$$

where $\psi(s,t)$ and $u_T(s,t)$ are the angle of attack and the body segment's transversal velocity at body position s and time t. Analog to Chapter 3, we define the transversal direction $\boldsymbol{e}_\mathrm{T}$ perpendicular to the swimming direction $\boldsymbol{e}_\mathrm{S}$. From Eq. (5.3), it follows that $\psi = 45°$ maximizes the propulsive force generated by the body segment independent of its velocity u_T. We refer to the book by Lauga [83] for an alternative derivation of Eq. (5.3).

The local angle of attack ψ of a body segment is typically defined as the angle between its centreline tangent $\boldsymbol{t} = \partial_s \boldsymbol{r}$ and the swimming direction $\boldsymbol{e}_\mathrm{S}$. Hence, it can be expressed as follows:

$$\cos(\psi) = \frac{\boldsymbol{t} \cdot \boldsymbol{e}_\mathrm{s}}{|\boldsymbol{t}|}. \tag{5.4}$$

Note that $\boldsymbol{t}$ does not necessarily have unit length, as a Cosserat rod is extensible. To calculate the swimmer's average angle of attack $\bar{\psi}$, we integrate ψ across the length of the swimmer's body and one undulation period:

$$\bar{\psi} = \int_t^{t+1} \int_0^1 \psi(s,t)\, ds\, dt. \tag{5.5}$$

Naturally, We want to understand how $\bar{\psi}$ depends on the swimmer's waveform. Our simple geometric model predicts that $\bar{\psi}$ is primarily proportional to the wave's shape factor c while exhibiting a less pronounced and nontrivial dependency on the undulation wavelength λ. This prediction is confirmed by the contour plot in Fig. 5.2C, which displays $\bar{\psi}$ as a function of λ_0 and c_0. It closely resembles the contour plot generated from the analytic derivation of our geometric model in Fig. A.1C.

In Fig. 5.2C, the fastest preferred waveform ($\lambda_{0,\mathrm{max}}$, $c_{0,\mathrm{max}}$) is represented by the black cross. We observe that the swimmer's fastest waveform has an average angle of attack of approximately 50°, close to the theoretically predicted optimum of 45°. Notably, the contour band for angles between 40° and 50° extends over the entire range of λ_0. Hence, considering the average angle of attack $\bar{\psi}$ alone is insufficient to explain why the swimming speed is maximal at a preferred wavelength of $\lambda_{0,\mathrm{max}} \approx 1.1$. To understand why this wavelength achieves maximum speed, it is helpful to consider the transversal centreline velocity u_T, which is proportional to the propulsion force (see Eq. (5.3)). It is defined as the projection of the centreline velocity $\boldsymbol{u}(s,t)$ onto the transversal body direction $\boldsymbol{e}_\mathrm{T}$. To estimate the magnitude of u_T, we determine its maximum across the length of the swimmer's body during one undulation period

$$u_{\mathrm{T,max}} = \max_{t\in[t_0,\,t_0+1]} \left[\max_{s\in[0,\,1]} \left(u_{\mathrm{T}}(s,t) \right) \right]. \tag{5.6}$$

Our geometric model predicts that $u_{\mathrm{T,max}} \propto c\lambda$, which can be explained as follows: Increasing the emergent shape factor $c = A\lambda/2\pi$ of the curvature wave translates to a body wave with larger amplitude, as illustrated in Fig. A.1A. For a given shape factor c, increasing the wavelength λ reduces the number of waves $n = 1/\lambda$ along the swimmer's body. Thus, as n decreases, the overall size of the swimmer's body wave must increase to ensure that the length of the swimmer's body is conserved.To conclude, both the shape factor c and the wavelength λ enhance the amplitude of the swimmer's body wave, explaining why $u_{\mathrm{T,max}} \propto c\lambda$.

The contour plot of $u_{\mathrm{T,max}}$ as a function of λ_0 and c_0 is presented in Fig. 5.2E. Interestingly, the maximum of $u_{\mathrm{T,max}}$ is not located in the top right corner as predicted by our geometric model; see Fig. A.1D for a comparison. Instead, $u_{\mathrm{T,max}}$ is maximal at the centre of the contour plot's top boundary, with $\lambda_0 \approx 1.3$ and $c_0 = 1.6$. Our geometric model fails to predict the correct wavelength because it assumes that the swimmer's head is fixed at the origin. This assumption ensures that the body wave always propagates in the opposite swimming direction. It is comparable to the experiment setup used in Backholm *et al.* [12], where the tail position of *C. elegans* was secured with a pipette. In contrast, in our Cosserat model, both ends of the swimmer can move freely, allowing its body to undergo global rotations. This implies that the swimmer's longitudinal body axis is not always aligned with the swimming direction. However, the angle between the swimmer's longitudinal body axis and the swimming direction is typically periodic, constrained to small values and centred around zero. This is a result of the body wave's symmetry. This symmetry ensures that the transversal propulsion force integrates to approximately zero across the length of the swimmer's body. However, when λ becomes larger than one, the swimmer's body expresses only a fraction of a curvature wave at any given time. This leads to a more asymmetric body shape, resulting in a more pronounced global rotation of the swimmer's longitudinal body axis. On average, this periodic rotation results in a larger misalignment between the propagation direction of the curvature wave and the swimming direction. This explains why $u_{\mathrm{T,max}}$ gradually decreases as λ_0 exceeds one. We conclude that to achieve maximum swimming speed, the swimmer must select a waveform that maximizes its transversal centreline velocity while maintaining an optimal average angle of attack.

Having identified the swimmer's fastest waveform, we now focus on the most cost-effective waveform that minimizes the COT. Fig. 5.2D presents the contour plot of the swimmer's normalized COT as a function of λ_0 and c_0. As normalization we use $\mathrm{COT}_{\mathrm{max}}$, the COT associated with the fastest preferred waveform ($\lambda_{0,\mathrm{max}}$, $c_{0,\mathrm{max}}$). Consequently, in the shape-space region where $\mathrm{COT}/\mathrm{COT}_{\mathrm{max}} > 1$, the swimmer's COT is larger compared to the COT required to swim at maximum speed U_{max} (black cross). Thus, the swimmer has no incentive to occupy this region of the shape-space, as its slower and less energy efficiency than the fastest waveform. Conversely, in the shape-space region where $\mathrm{COT}/\mathrm{COT}_{\mathrm{max}} < 1$, the swimmer is slower than U_{max} but more energy-efficient. Thus, within this region, the swimmer can modulate its waveform depending on whether it prioritizes swimming speed or energy efficiency. We observe that the COT is minimal at the right half of the shape-space's bottom boundary, characterized by a large preferred wavelength $\lambda_0 > 1$ and small preferred shape factor $c_0 = 0.4$. This implies that a swimmer can optimize energy efficiency by opting for a waveform with a small shape factor c_0. However, doing so leads to a shallow body wave and slow swimming speed, as shown in Fig. 5.2A. Hence, our model predicts that undulating with zero amplitude and taking infinite time minimizes the COT. This result is counterintuitive, as a minimum curvature amplitude should exist below which swimming becomes energetically inefficient.

Notably, if we incorporate the organism's BMR as an additional energy cost, the contour plot of the normalized COT reveals a distinct minimum within the interior of the shape space, as shown in Fig. 5.2E. The position of this minimum is displayed by the red cross, representing the most cost-effective waveform, denoted as $(\lambda_{0,\mathrm{min}}, c_{0,\mathrm{min}})$. The most cost-effective swimming speed and associated COT will be referred to as U_{min} and $\mathrm{COT}_{\mathrm{min}}$, respectively. This implies that there is no incentive for the swimmer to adopt a waveform with a slower swimming speed than U_{min}, as this would increase its COT relative to $\mathrm{COT}_{\mathrm{min}}$. Thus, for a given undulation frequency and fluid viscosity, our model constrains the plausible range of swimming speeds to the interval $[U_{\mathrm{min}}, U_{\mathrm{max}}]$. Within this range, the swimmer can increase its swimming speed at the cost of increasing its COT.

To quantify the trade-off between swimming speed and energy efficiency, we plot the constant swimming speed contour lines from panel A as red dashed lines in Fig. 5.2D and F. On each of these contour lines, the red marker represents the optimal waveform that minimizes the swimmer's COT, denoted as $(\lambda_{0,\mathrm{opt}}, c_{0,\mathrm{opt}})$. The COT associated with this optimal waveform, $\mathrm{COT}_{\mathrm{opt}}$, is plotted as a function of the normalized swimming speed in Fig. 5.2F. The rectangular and dotted markers represent $\mathrm{COT}_{\mathrm{opt}}$ with and without BMR, respectively.

In the absence of BMR, it is apparent that the trade-off between speed and COT is not linear; instead, the gain in energy efficiency diminishes as the swimmer decreases its swimming speed. To illustrate, reducing the swimming speed from U_{max} by 10% reduces the COT by approximately 35%. However, reducing the swimming speed by another 10% only yields an approximately 10% gain in efficiency. This observation suggests that microswimmers are incentivized to operate within a specific range of swimming speeds. Below this optimal range, the diminishing returns indicate that additional reductions in speed do not result in meaningful gains in efficiency (reduction of the COT).

When the BMR is included, $\mathrm{COT}_{\mathrm{opt}}$ displays a distinct minimum, illustrated by the vertical red dashed line in Fig. 5.2E. This minimum corresponds to the most cost-effective swimming speed U_{min}. This confirms that swimming at a speed slower than U_{min} increases the COT, i.e. it is energy inefficient. It is important to note that the value of U_{min} is contingent on the organism's BMR. As the BMR increases, the swimmer is incentivized to swim faster, i.e. U_{min} converges to U_{max}, which results in a narrower range of plausible swimming speeds.

We remark that the BMR's contribution to the swimmer's COT is given by the term BMR/U. Consequently, since U is constant along each of the red dashed contour lines in Fig. 5.2E, the term BMR/U is also. Thus, including the BMR does not change the position of the optimal waveform ($\lambda_{0,\mathrm{opt}}$, $c_{0,\mathrm{opt}}$) on the respective contour lines. This can be confirmed by the identical positions of the dotted and rectangular markers in panels D and E. Therefore, by determining the optimal waveform ($\lambda_{0,\mathrm{opt}}$, $c_{0,\mathrm{opt}}$) for different swimming speeds $U < U_{\mathrm{max}}$, we implicitly determine the most cost-effective waveform ($\lambda_{0,\mathrm{min}}$, $c_{0,\mathrm{min}}$) without explicitly incorporating the swimmer's BMR. Lastly, we notice that $\lambda_{0,\mathrm{opt}}$ is consistently larger compared to the fastest wavelength $\lambda_{0,\mathrm{max}}$. Hence, we can clearly distinguish between the optimal and the fastest waveform. Hence, by comparing our model with existing experimental data, we can try to infer whether a microswimmer maximizes its swimming speed or compromises between speed and energy efficiency, as we will demonstrate in Chapter 6.

Having presented the simulation results for a specific undulation frequency, we now consider the entire range of normalized frequencies $f/f_{\mathrm{c}} \in [10^{-1}, 10^{1}]$. For this purpose, it is more convenient to consider the curvature amplitude than the shape factor, as we will explain shortly. Thus, we introduce the fastest preferred curvature and actual curvature amplitude $A_{\mathrm{max},0}$ and A_{max}, alongside the optimal curvature amplitudes $A_{\mathrm{opt},0}$ and A_{opt}. To examine whether the fastest waveform undergoes changes as the swimmer modulates its undulation frequency, Fig. 5.3A and B display A_{max} and λ_{max} as a function of f/f_{c}, respectively. Observing the trends, both plots can be divided into two regions, indicated by the green and the red shaded areas. The green area corresponds to the frequency range where the swimmer is not power-limited. In this region, the fastest waveform remains approximately constant with respect to f, exhibiting only a slight increase in A_{max} along with a minor decrease in λ_{max}. On the other hand, the red area corresponds to the frequency range where the swimmer is power-limited. Power-limited means we cannot specify an arbitrarily large preferred curvature amplitude A_0 because the actuation torque biological swimmers can generate is limited, as we will explain in more detail in the next paragraph. In power-limited region, A_{max} decreases rapidly with f, mirrored by a rapid increase in

$\lambda_{\max}$.

This can be understood as follows: In the pass-through regime, the swimmer's body curvature instantaneously tracks the preferred curvature. Consequently, preferred curvature amplitude $A_{0,\max}$ and the body curvature amplitude $A_{\max}$ are approximately equal for frequencies $f/f_{\mathrm{c}} < 1$. However, for frequencies $f/f_{\mathrm{c}} > 1$, the swimmer transitions into the low-pass regime, which leads to a damping of the curvature amplitude, i.e. $A_{\max}/A_{0,\max} < 1$. This damping intensifies as the frequency increases. Hence, to maintain its optimal waveform, the swimmer must gradually increase the preferred curvature amplitude $A_{0,\max}$ to counterbalance the growing damping effect, as can be seen by the dashed blue line in Fig. 5.3A. However, since $A_{0,\max}$ is proportional to the actuation torque amplitude, it must have an upper limit because the swimmer's molecular motors or muscles can not generate arbitrarily strong bending torques. Here, we choose an upper limit of $A_{0,\max} = 12$ for illustrative purposes. This choice is motivated by experimental findings where normalized curvature amplitudes are consistently measured to be below ten [45, 106, 113].

To analyze how the physical swimming speed scales with the undulation frequency, we plot the normalized maximum swimming speed $U_{\max}/U_{\max,\mathrm{c}}$ (red line) as a function of f/f_{c} in Fig. 5.3C, where $U_{\max,\mathrm{c}}$ is the maximum swimming speed associated with the characteristic undulation frequency f_{c}. Not surprisingly, the physical swimming speed exhibits the same trend as in Fig. 5.1B, where we imposed a fixed waveform. If the swimmer is not power-limited, the swimming speed scales linearly with undulation frequency f. This is because the swimmer can sustain its fastest waveform, characterized by an optimal average angle of attack (blue line) of approximately 50°. In the power-limited regime, the swimming speed scales sublinearly with f, eventually peaking at the frequency $f_{\max}$, represented by the vertical red dashed line.

To summarise, assuming the swimmer is not power-limited, our model shows that the fastest waveform ($\lambda_{\max}$, $A_{\max}$) remains largely unaffected by variations of the undulation frequency. This result is unsurprising, as the fastest waveform is characterized by an optimal angle of attack and a high degree of body symmetry, and these geometric properties are expected to be independent of the undulation frequency. Furthermore, for a power-limited swimmer, our model predicts that there must exist an upper limit $f_{\max}$ for the undulation frequency beyond which the swimming speed starts to decrease. The value of $f_{\max}$ is contingent on the upper limit of the actuation torque amplitude.

Having analyzed the effect of the swimmer's undulation frequency on the fastest waveform, we now explore how the undulation frequency affects the optimal waveform (λ_{opt}, A_{opt}). To simplify our analysis, we assume that the swimmer undulates within a frequency range where it is not power-limited, i.e. $f/f_{\mathrm{c}} < 4$. Fig. (5.3)D and E display λ_{opt} and A_{opt} as a function of f/f_{c}, respectively. The colored lines represent different values of the normal-

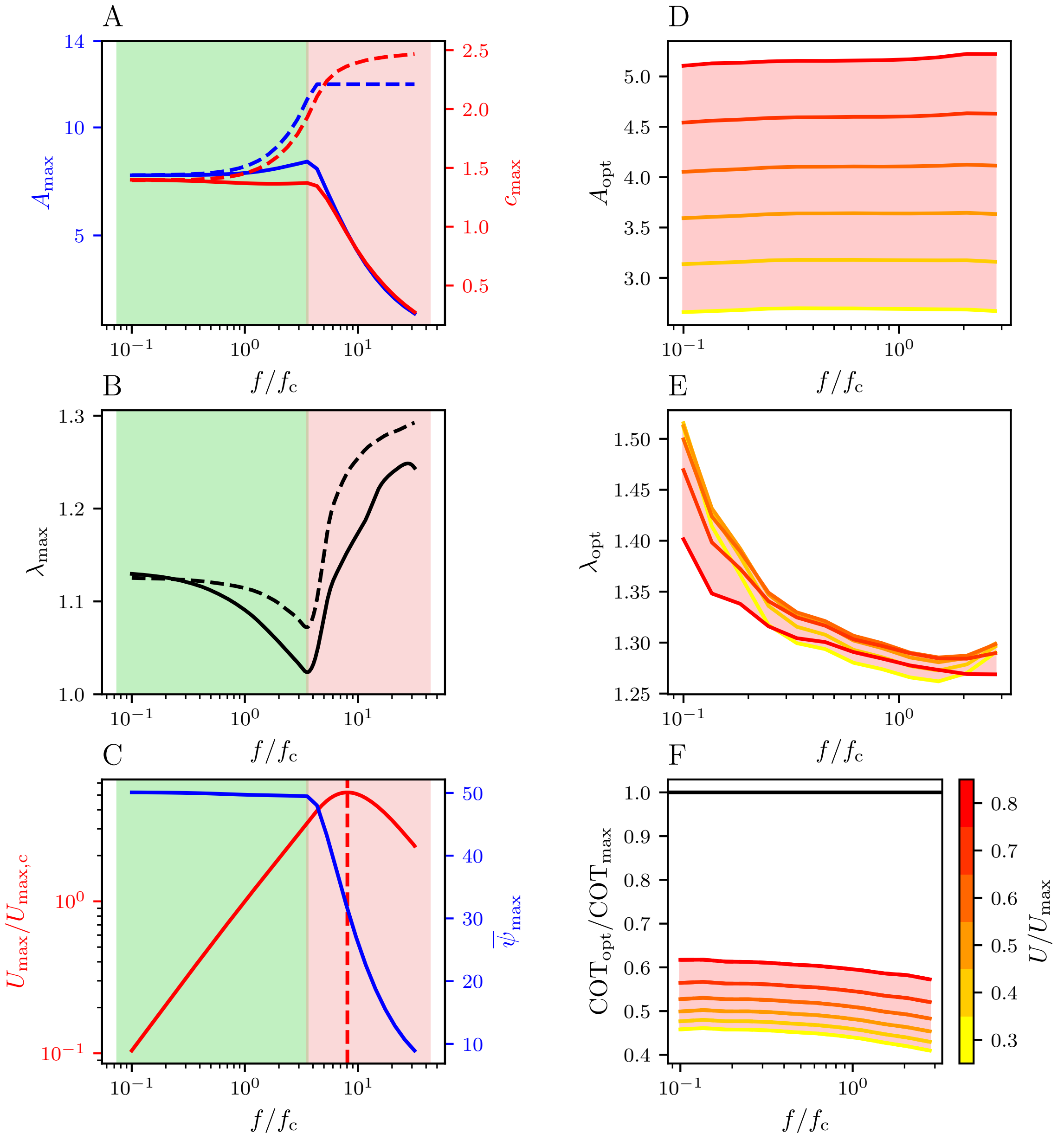

Figure 5.3: Fastest and optimal waveform as a function of the normalized undulation frequency. (**A**): Fastest preferred curvature amplitude $A_{0,\max}$ (blue dashed), actual curvature amplitude $A_{\max}$ (blue solid), preferred shape factor $c_{0,\max}$ (red dashed), and actual shape factor $c_{\max}$ (red solid) as a function of the normalized undulation frequency f/f_c. Two distinct regions are highlighted: in the green area, the swimmer is not power-limited, while in the red area, it is. (**B**): Fastest preferred wavelength $\lambda_{0,\max}$ (black dashed) and actual wavelength $\lambda_{0,\max}$ (black solid). (**C**): Normalized physical swimming speed $U_{\max}/U_{\max,c}$ (red) and average angle of attack $\bar{\psi}_{\max}$ (blue). The vertical red dashed line represents the frequency $f_{\max}$, which achieves maximum speed. (**D**): Optimal curvature amplitude A_{opt} (solid) as function of f/f_c. Colored lines correspond to different values of the normalized swimming speed $U/U_{\max}$, presented by the colorbar in panel F. (**E**): Optimal wavelength wavelength λ_{opt}. (**F**): Normalized Cost of Transport $\mathrm{COT_{opt}/COT_{max}}$ associated with optimal waveforms.

ized swimming speed U/U_{max}, represented by the color bar in panel F. For a given speed, Fig. (5.3)D shows that A_{opt} remains approximately constant across the entire frequency range. Furthermore, the height of the vertical gaps between the colored lines remains constant, which implies that swimming speed is proportional to the curvature amplitude. In contrast, Fig. (5.3)E shows that λ_{opt} decreases with f, exhibiting a convex trend. Notably, λ_{opt} only displays a minor dependency on the swimming speed, with all colored lines falling into a narrow band. Consequently, at a given frequency, our model predicts that the swimming speed can be modulated most efficiently by adjusting the curvature amplitude while maintaining a constant wavelength close to λ_{opt}.

To illustrate the trade-off between swimming speed and energy efficiency, we compare $\mathrm{COT}_{\mathrm{opt}}$ to $\mathrm{COT}_{\mathrm{max}}$ in Fig. 5.3F. Consistent with our earlier observation in Fig. 5.2F, reductions of the swimming speed have diminishing returns. Across the entire frequency range, reducing the maximum swimming speed by 20% decreases the COT by approximately 40%, whereas lowering it by another 20% only yields an additional 10% decrease. Consequently, the vertical gaps between the colored lines become smaller as U decreases. Notably, the gain in energy efficiency is negligible for normalized swimming speed lower than $U/U_{\mathrm{max}} < 0.3$. Consequently, the swimmer has no incentive to swim at a lower speed, providing us with a lower bound for U_{min}, irrespective of the swimmer's BMR.

To conclude, our model predicts that a swimmer should modulate its waveform (wavelength) together with its frequency to optimize efficiency. However, if it prioritizes speed, we expect a more or less constant waveform. Having addressed the scenario of a static environment, we now explore gait adaptation in response to changing environmental conditions characterized by the fluid's viscosity.

5.3 Changing Environments

This section explores the gait modulation of an undulatory microswimmer in response to changing environmental conditions. Remarkably, undulatory microswimmers are capable of navigating a wide range of environmental conditions. While human sperm navigate the diverse fluid environments of the female reproductive system during fertilization, nematodes like *C. elegans* can thrive in aquatic environments, soil, and transitional zones [5, 49]. Previous studies by Rikmenspoel [114] and Fang Yen *et al.* [45] have examined the undulatory locomotion of sea urchin sperm and *C. elegans* in Newtonian fluid environments, respectively. Their experiments revealed that sperm and *C. elegans* are both capable of swimming in fluids across a broad range of viscosities. Interestingly, both exhibit a continuous gait transition, dynamically adjusting their undulation frequency and waveform to variations in fluid viscosity. Understanding this gait adaptation from the viewpoint of optimality will be the goal of this section.

It will follow a structure similar to the previous section, which discussed the static environment case. In the first Subsection 5.3.1, we focus exclusively on frequency modulation assuming a constant waveform. We discuss how frequency modulation enables the swimmer to maintain an efficient operating point in more viscous fluids. Building upon these results, Subsection 5.3.2 explores waveform modulation, again distinguishing between the swimmer's fastest and most efficient (optimal) waveform. We will explore how both of these waveforms depend on the viscosity of the surrounding fluid environment.

5.3.1 Frequency Adaptation

In this section, we use our model to simulate undulatory locomotion within fluids with different viscosities. To simplify our initial analysis, we assume a constant waveform ($\lambda_0 = 1$, $A_0 = 2\pi$) throughout this section. Mimicking the experimental study by Fang Yen *et al.* [45], we consider fluid viscosities μ spanning four orders of magnitude $\mu/\mu_0 \in \cdot[1, 10^4]$. Here, μ_0 represents the viscosity of the least viscous fluid that the swimmer is exposed to, e.g. water. In this reference viscosity, we assume that the swimmer undulates with the characteristic frequency f_0. Furthermore, consistent with Section 5.2.1, we assume that the swimmer's body geometry and material parameters remain constant throughout. Hence, given the values of μ_0 and f_0, we can determine the swimmer's characteristic operating point (a_0, b_0) at the lower limit of the viscosity spectrum (see Tab. 4.1). We make the assumption that (a_0, b_0) lies within the interior of the pass-through regime, represented by the large dotted marker in Fig. 5.4B. As we discussed in Chapter 4, this choice implies that the swimmer's body stiffness has evolved to facilitate swimming in environments with higher viscosities than μ_0, thereby enhancing the swimmer's adaptability.

Notably, as the fluid becomes more viscous, the friction force due to the relative motion between the fluid and the body surface becomes stronger, making it more difficult for the swimmer to actively deform its body. Consequently, the system's response time τ, which is proportional to μ, becomes slower. To adapt to this slowed response, microswimmer decreases their undulation frequency in more viscous fluids. This adaptation allows them to maintain a functional ratio between response time and actuation time scale, thereby sustaining an efficient operating point. This leads to higher energy efficiency, as we will demonstrate in the following.

We compare two scenarios: In the first scenario, the swimmer does not modulate its characteristic undulation frequency, i.e. f_0 remains constant across the entire range of fluid viscosities, as illustrated by the dotted markers in Fig. 5.4A. In the second scenario, the swimmer decreases its undulation frequency as the fluid viscosity increases. Here, we choose

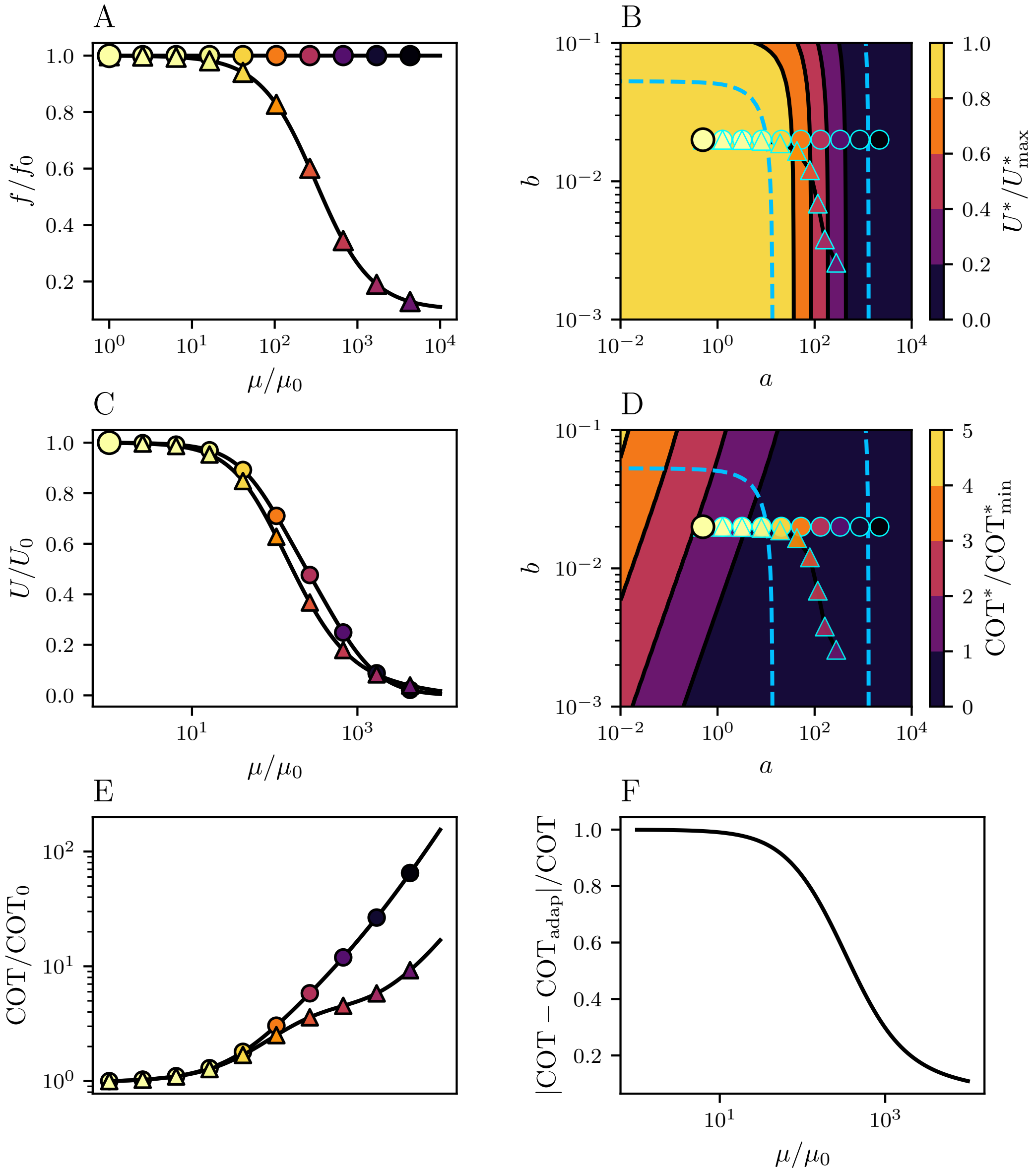

Figure 5.4: Frequency adaptation enhances energy efficiency in more viscous fluids. (**A**): Normalized undulation frequency f/f_0 as a function of the normalized fluid viscosity μ/μ_0 with (rectangles) and without adaptation (dots). Here, μ_0 is the lowest viscosity associated with frequency f_0 and swimming speed U_0. (**B**): Swimming speed as a function of the effective response times a and b. Dashed blue lines represent regime boundaries introduced in Section 4.2. Here, we choose a characteristic operating point ($a_0 = 0.5$, $b_0 = 0.02$) (large dotted marker) so that the swimmer operates in the pass-through regime at the lowest viscosity μ_0. Without frequency adaptation, increasing μ shifts the operating point in the positive horizontal direction (dotted markers). With frequency adaptation, operating points shift in horizontal and in negative diagonal directions (triangular markers). (**C**): Normalized physical swimming speed U/U_0 with (triangles) and without (dots) frequency modulation as a function of the normalized fluid viscosity μ/μ_0. (**D**): Contour plot of the dimensionless Cost of Transport COT* as a function of a and b without BMR. (**E**): Normalized physical COT with (dots) and without (triangles) frequency adaptation as a function of μ/μ_0. Top panel without BMR bottom panel with $\mathrm{BMR}/W_0 = 0.1$ (**F**): Relative difference between the physical Cost of Transport with ($\mathrm{COT}_{\mathrm{adap}}$) and without frequency (COT) modulation plotted against μ/μ_0.

a simple sigmoidal relationship between undulation frequency f and the logarithm of the fluid viscosity μ, illustrated by the triangular markers in Fig. 5.4A. The parameters of the sigmoid are chosen such that its inflection point is located at the midpoint of the viscosity range at $\mu/\mu_0 \approx 10^2$. Furthermore, the sigmoid's slope parameter is chosen such that f gradually decreases from the maximum value f_0 to the minimum value f_{min} across the entire range of μ/μ_0. Here, we opt for a ratio of $f_0/f_{\mathrm{min}} = 0.1$, i.e. the swimmer decreases its undulation frequency by one order of magnitude. This choices are motivated by the experimental study of Fang Yen *et al.* [45], who reported a similar range for *C. elegans*.

Recall that the swimmer's effective response time a is proportional to μ. Hence, in the first scenario where the swimmer does not adapt its undulation frequency, the swimmer's operating point $(a_0,\ b_0)$ shifts in a positive horizontal direction as μ increases. Consequently, the swimmer transitions from the pass-through through the low-pass to the struggling regime, as depicted by the dotted markers in Fig. 5.4A. In the second scenario, where the swimmer adapts its undulation frequency, two opposing factors superimpose. Similar to the first scenario, increasing μ shifts the swimmer's operating point in a positive horizontal direction. In contrast, a decrease in f results in a shift in a negative diagonal direction, as illustrated earlier in Fig. 5.1A. Combining both of these factors, the swimmer's operating point follows a "sigmoidal" curve illustrated by the triangular markers in Fig. 5.4B. Thus, by lowering its undulation frequency in more viscous environments, the swimmer effectively delays its transition into the struggling regime.

To compare the performance of both scenarios, we consider the swimming speed and the COT. The normalized physical swimming speed U/U_0 is plotted against μ/μ_0 in Fig. 5.4C with (triangles) and without (dots) frequency adaptation. Here, U_0 refers to the swimming speed in the least viscous fluid. For low viscosities, the swimmer maintains a constant undulation frequency in both scenarios and operates in the pass-through regime. In this regime, the physical swimming is constant, i.e. it is independent of the fluid viscosity μ. This finding is consistent with the classical result by Taylor [127], who considered a flexible two-dimensional sheet deforming as a traveling wave of transverse displacements. Taylor demonstrated that the swimming speed of the sheet is independent of μ. A detailed derivation of this result can be found in Chapter 3 of Eric Lauga's book [83]. In the case of *C. elegans*, our result aligns with the experimental data, which shows that *C. elegans* swimming speed is approximately constant in the low viscosity regime where it undulates with constant frequency [50, 126]. See Section A.4.2 of the appendix for a more detailed discussion.

As the fluid viscosity μ increases, Fig. 5.4C shows that swimming speed decreases in both scenarios following a sigmoidal trend. In the first scenario, this decrease is caused by the swimmer's transition to the struggling regime, which is characterized by a strongly damped curvature amplitude and a slow swimming speed. In the second scenario, the swimmer's prevents the transition to the struggling regime. However, this comes at the cost of a lowering its undulation frequency f, resulting in a gradual decrease in physical swimming. Thus, judging from the swimming speed alone, neither of the two scenarios can be considered superior.

To compare the energy efficiency of both scenarios, Fig. 5.4D displays the contour plot of the normalized dimensionless COT as a function of the swimmer's operating point (a, b). Here, $\mathrm{COT}^*_{\mathrm{min}}$ denotes the minimal dimensionless COT in the specified range of a and b. To calculate the physical COT, we first consider the swimmer's characteristic COT in the least viscous fluid μ_0, denoted as COT_0. According to Eq. (4.8), it is defined as

$$\mathrm{COT}_0 = \mu_0 c_{||} L_0^2 f_0 \mathrm{COT}^*_0, \tag{5.7}$$

where COT^*_0 denotes the dimensionless COT in the least viscous fluid μ_0, represented by the large dotted marker in Fig. 5.4D. Using COT_0 as our normalization, we define the normalized physical COT as

$$\frac{\mathrm{COT}}{\mathrm{COT}_0} = \frac{\mu}{\mu_0}\frac{f}{f_0}\frac{\mathrm{COT}^*}{\mathrm{COT}^*_0}, \tag{5.8}$$

where we used that $c_{||}$ and L_0 are constant. Fig. 5.4E, shows $\mathrm{COT}/\mathrm{COT}_0$ as a function of μ/μ_0 for both scenarios. Without frequency adaptation (dotted markers), the swimmer's COT increases by approximately two orders of magnitude over the entire range of μ. Hence, in the most viscous fluid, the swimmer requires a hundred times more energy to travel a unit distance compared to the least viscous environment μ_0. With frequency adaptation (triangular markers), the COT only increases by one order of magnitude over the entire range of μ. Hence, the swimmer only requires ten times more energy in the most viscous fluid. Thus, the swimmer significantly reduces its COT in higher viscosities by adapting its undulating frequency. To quantify the efficiency gain, we plot the ratio between the COT with and without frequency adaptation against μ/μ_0 in Fig. 5.4F. At low viscosities, the ratio converges to one, indicating that both scenarios are equally efficient. As μ increases, the ratio gradually decreases to a value of approximately 0.1, which shows that frequency adaption is up to ten times more energy efficient in more viscous fluids.

Additional considerations: The efficiency gain achieved by the swimmer through frequency modulation is contingent on its BMR. If the organism's energy cost is dominated by the BMR, its COT simplifies to the expression $\mathrm{COT} \approx \mathrm{BMR}/U$. In such a case, the COT with and without frequency adaptation would be approximately equivalent. This follows from the fact that the swimming speed is approximately equivalent in both scenarios. This suggests that the energy cost of microswimmers is not dominated by their BMR, as they are observed to adapt their undulation frequency in more viscous environments.

5.3.2 Waveform Adaptation

In the preceding section, we showed that microswimmers can improve their efficiency in more viscous environments by lowering their undulation frequency. We used a simple sigmoidal function to modulate the frequency such that it decreases gradually from the upper limit f_0 to the lower limit f_{min} over a generic range of fluid viscosities $\mu/\mu_0 \in [1, 10^4]$. To simplify our analysis, we assumed that the swimmer's waveform ($\lambda_0 = 1$, $A_0 = 2\pi$) remains constant across the entire viscosity range. However, experimental studies have shown that microswimmers do not only modulate their undulation frequency but also adapt their waveform when exposed to fluids with different viscosities [18, 45, 79, 114, 126]. Therefore, we extend our analysis by considering both its frequency and waveform adaptation. In particular, our goal is to determine the swimmer's fastest and optimal waveform as a function of μ/μ_0. To accomplish this, we simulate a series of undulation experiments, spanning viscosities in the range $\mu/\mu_0 \in \cdot[1, 10^4]$. To determine the undulation frequency f as a function of μ, we use the sigmoidal function defined in the previous section. For each value of μ, we systematically vary the preferred undulation wavelength λ_0 and the preferred shape factor c_0.

We begin our initial analysis by focusing on two simulation results: the first corresponds to the lower limit of the viscosity range $\mu = \mu_0$, and the second corresponds to its upper limit $\mu/\mu_0 = 10^4$. In both cases, the contour plot of the normalized swimming speed U/U_{max} is shown as a function of λ_0 and c_0 in Fig. 5.5A and B, respectively. Here, U_{max} is defined as the maximum swimming speed within the specified range of λ_0 and c_0. In each plot, the black cross represents the fastest preferred waveform ($\lambda_{0,\text{max}}$, $c_{0,\text{max}}$). Notably, $\lambda_{0,\text{max}}$ is nearly identical in both limits, measuring 1.13 in the low and 1.04 in the high viscosity limit, respectively. In contrast, $c_{0,\text{max}}$ is noticeably larger in the high viscosity limit, with respective values of 1.40 and 1.75. As the fluid becomes more viscous, the swimmer transitions into the low-pass regime, characterized by a damped curvature amplitude. To counterbalance this damping, the value of $c_{0,\text{max}}$ must increase in more viscous fluids. However, the value of the swimmer's actual shape factor c_{max} is approximately 1.40 in both limits. This suggests that the swimmer's fastest waveform (λ_{max}, c_{max}) is more or less independent of μ.

To determine the swimmer's most cost-effective waveform, the contour plot of the normalized COT as a function of λ_0 and c_0 is displayed in the low and high viscosity limit in Fig. 5.5C and D, respectively. As normalization, we use COT_{max}, the COT associated with the fastest preferred waveform $(\lambda_{0,\text{max}}, c_{0,\text{max}})$ displayed by the black cross. In panels E and F, we included the organism's BMR as an additional energy cost, which is set to zero in panels C and D. Consistent with our discussion in Section 5.2.2, without including the BMR, the swimmer's COT has no minimum within the shape space interior. Instead,

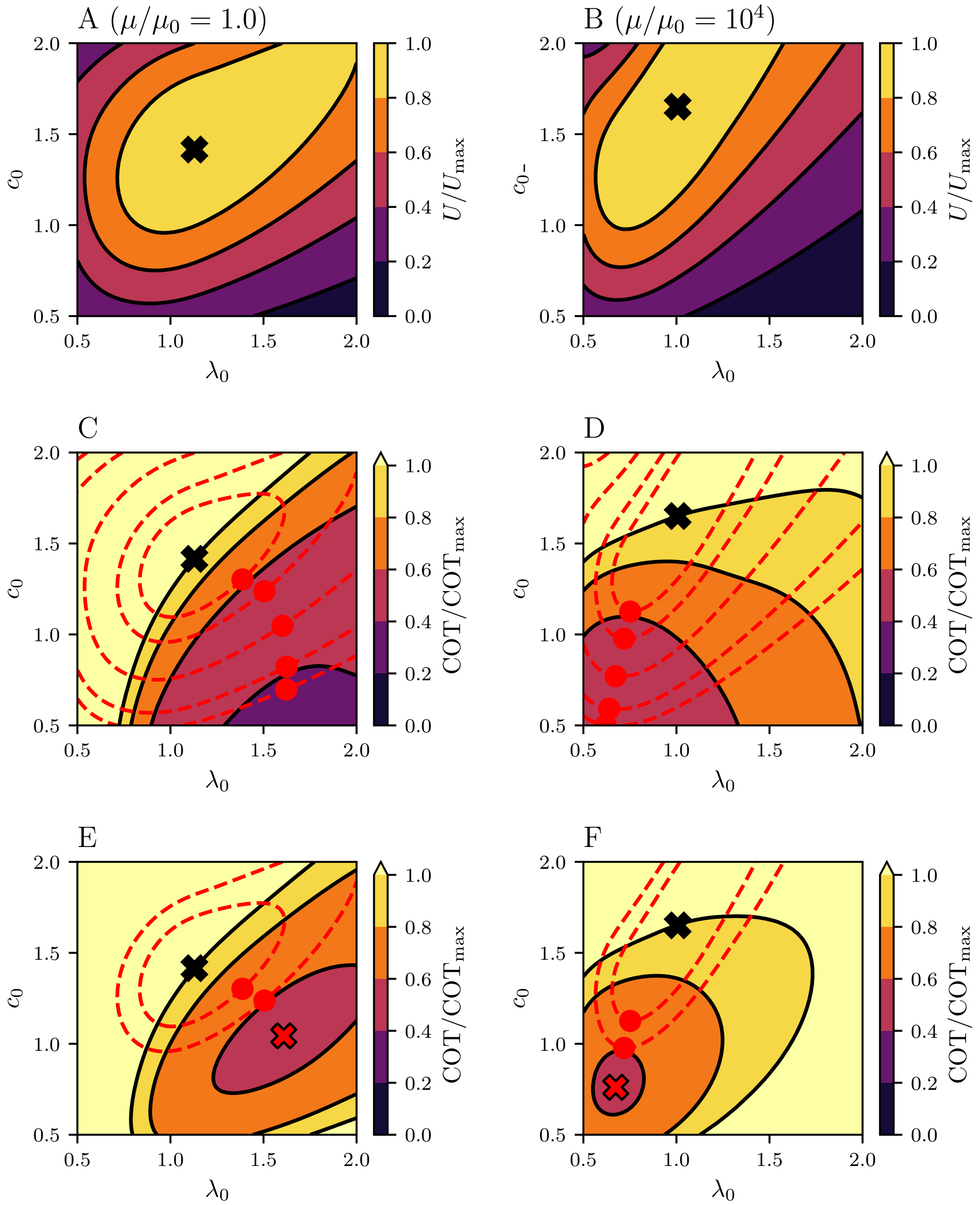

Figure 5.5: Waveform modulation in the low μ_0 (left column) and high $\mu/\mu_0 = 10^4$ (right column) fluid viscosity limit. (**A**, **B**): Normalized swimming speed $U/U_{\max}$ as a function of the preferred undulation wavelength λ_0 and shape factor c_0. Here, $U_{\max}$ is the maximum swimming speed within the specified range of λ_0 and c_0. The fastest preferred waveform ($\lambda_{0,\max}$, $c_{0,\max}$) is represented by the black cross. (**C**, **D**): Normalized Cost of Transport $\mathrm{COT}/\mathrm{COT}_{\max}$, where $\mathrm{COT}_{\max}$ is the COT required to swim at the fastest speed $U_{\max}$. Red dashed lines represent contour lines of constant swimming speed shown in panels A and B, respectively. Red dotted markers represent the optimal preferred waveform ($\lambda_{0,\mathrm{opt}}$, $c_{0,\mathrm{opt}}$) that minimizes the COT on each contour line. (**E**, **F**): Contour plot of the normalized dimensionless COT as a function of λ_0 and c_0 for an exemplary value of $\mathrm{BMR}^*/W^*_{\max} = 0.1$, where $W^*_{\max}$ is the actuation work required to swim with maximum speed $U_{\max}$. The red cross corresponds to the most cost-effective preferred waveform ($\lambda_{0,\min}, c_{0,\min}$) that minimizes the swimmer's COT.

the COT is minimal at the bottom boundary of the shape space, where the preferred shape factor c_0 is small. This boundary region is associated with shallow body waves and slow swimming speeds. In contrast, for BMR > 0 in panels E and F, the contour plot of the COT displays a distinct minimum within the interior of the shape space, represented by the red cross in panels E and F. We refer to this waveform as the most cost-effective preferred $(\lambda_{0,\mathrm{min}}, c_{0,\mathrm{min}})$ and emergent $(\lambda_{\mathrm{min}}, c_{\mathrm{min}})$ waveform, respectively.

The red dashed lines in panels C-F represent the contour lines of constant swimming speed, as shown in black in panels A and B. Thus, each red dashed contour line represents a constant swimming speed value. The red dotted marker on the contour line represents the most cost-effective preferred waveform, minimizing the swimmer's COT for this specific speed. This preferred and emergent waveform will be referred to as optimal and denoted $(\lambda_{0,\mathrm{opt}}, c_{0,\mathrm{opt}})$ and $(\lambda_{\mathrm{opt}}, c_{\mathrm{opt}})$, respectively. Thus, by modulating its waveform, the swimmer can transition from the most cost-effective $(\lambda_{0,\mathrm{min}}, c_{0,\mathrm{min}})$ (red cross) to the fastest $(\lambda_{0,\mathrm{max}}, c_{0,\mathrm{max}})$ (black cross) waveform to prioritize between swimming speed and energy efficiency. To achieve the most efficient trade-off between speed and efficiency, our model predicts that the swimmer should modulate its waveform such that it minimizes the COT for a given speed, i.e. follow the curve that connects the optimal waveforms (red markers) in Fig. 5.5C-F. In low viscosity, we find that the optimal wavelength $\lambda_{0,\mathrm{opt}}$ is consistently larger than $\lambda_{0,\mathrm{max}}$, converging to a value of approximately 1.6 as the swimmer decreases its swimming speed. Conversely, in high viscosity, $\lambda_{0,\mathrm{opt}}$ is consistently smaller than $\lambda_{0,\mathrm{max}}$, converging to a value of 0.6. Therefore, our model predicts that shorter wavelengths are more energy-efficient in low viscosities, whereas in higher viscosities, longer wavelengths are. In contrast, the optimal shape factor $c_{0,\,\mathrm{opt}}$ decreases gradually with slower swimming speeds, corresponding to a shallower body wave.

To illustrate how the swimmer looks if it is actuated with the fastest (black cross) or the most cost-effective (red cross) preferred curvature waveform from Fig. 5.5E and F, Fig. 5.6 shows snapshots of the swimmer's centreline at different time points in the last undulation cycle of the simulation. As predicted, the fastest body waveform looks similar for low (panel A) and high (panel B) fluid viscosities. However, in high viscosity, we find that the curvature of the centreline in the swimmer's tail appears larger compared to low viscosity. This discrepancy is because, in high viscosity, the swimmer operates in the heterogeneous low-pass regime, which is associated with higher curvature amplitudes in the head and tail region compared to the body's midsection, as we discussed in Section 4.2. In contrast, the most cost-effective emergent body waveform looks very different in low (panel C) and high (panel D) viscosities. In low viscosity, the most cost-effective waveform has a larger amplitude and significantly longer wavelength than in high viscosity. The waveforms in panels C and D are reminiscent of the swimming and crawling gait of *C. elegans*, respectively [45]. This similarity suggests that *C. elegans* gait adaptation in different fluid viscosities aims to optimize energy efficiency, as will be discussed in more detail in Chapter *C. elegans*.

To conclude, our findings indicate that the swimmer's fastest waveform remains mainly unaffected by changes in fluid viscosity, while the optimal waveform changes significantly. This prediction is independent of the swimmer's BMR, as can be seen in Fig. 5.5E and F. When the BMR is included as an additional energy cost, the contour plot of the COT displays a distinct minimum within the interior of the shape space (red cross). This minimum sets a lower bound U_{min} for the swimming speed. However, as we discussed previously, it does not change the optimal waveform at a given speed. The fact that the fastest waveform changes very little with fluid viscosity, whereas the most energy-efficient does, suggests that energy efficiency is the primary drive behind gait adaptation.

To test this hypothesis, we determine the fastest and the optimal waveform for different swimming speeds across the entire viscosity spectrum. In Fig. 5.7A and B, A_{max} (red line) and λ_{max} (black line) are plotted against μ/μ_0, respectively. We confirm that A_{max} and λ_{max} exhibit minor to moderate relative changes of approximately 10% and 20% across the entire viscosity range, respectively. The fastest waveform (λ_{max}, A_{max}) is characterized by an average angle of attack of approximately $\bar{\psi} \approx 50^\circ$ as shown by the blue line in Fig. 5.7C. Nonetheless, the normalized maximum swimming speed $U_{\mathrm{max}}/U_{0,\mathrm{max}}$ (red line) significantly decreases as the fluid becomes more viscous. This is because the swimmer lowers its frequency in more viscous environments.

For comparison, the optimal curvature amplitude A_{opt} and wavelength λ_{opt} are plotted against μ/μ_0 in Fig. 5.7D and E, respectively. Each colored line corresponds to a constant value of the normalized swimming speed U/U_{max} represented by the colorbar at the bottom of panel F. All colored lines exhibit the same general trend as μ increases. Consequently, our model predicts that the swimmer should increase its curvature amplitude and decrease its wavelength in higher viscosities to achieve optimal energy efficiency.

To quantify the trade-off between swimming speed and energy efficiency, the ratio $\mathrm{COT}_{\mathrm{opt}}/\mathrm{COT}_{\mathrm{max}}$ is plotted against μ/μ_0 in Fig. 5.7F. The colored lines are approximately horizontal, which implies that the trade-off between swimming speed and energy efficiency is largely independent of μ. Consistent with our results from the previous section, our model predicts that the gain in efficiency diminishes as the swimmer reduces its swimming speed. For example, reducing the maximum swimming speed U_{max} by 10% yields an approximately 35% reduction in COT. However, reducing it by another 10% only yields another approximately 10% reduction. For swimming speeds slower than $U/U_{\mathrm{max}} < 0.3$, the efficiency gain is negligible, which sets a lower bound $U_{\mathrm{min}}/U_{\mathrm{max}} \approx 0.3$ for the swimming speed.

So far, we have not provided an explanation for why longer wavelengths are more energy-efficient in low viscosities, whereas shorter wavelengths are more efficient in high viscosities.

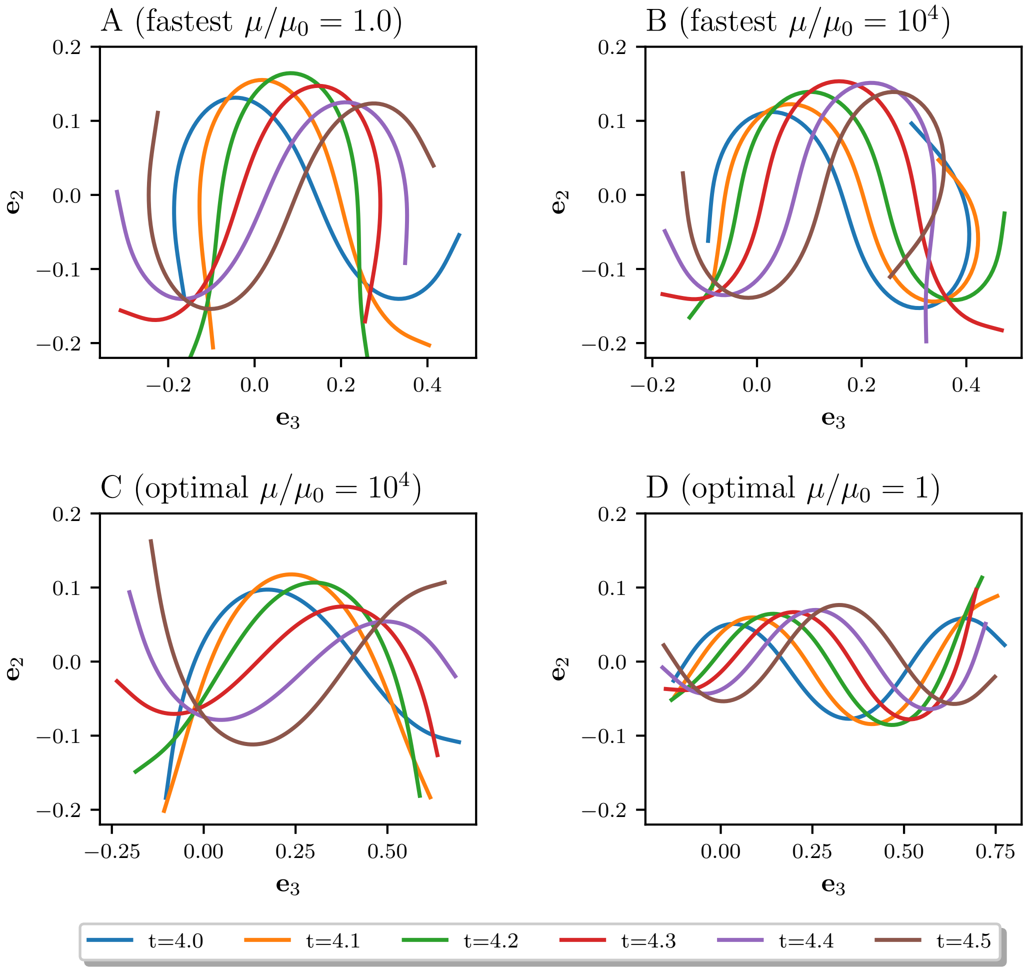

Figure 5.6: Snapshots of the fastest and the most efficient body waveform predicted by our model for low ($\mu/\mu_0 = 1$) and high ($\mu/\mu_0 = 10^4$) fluid viscosities. For each viscosity, the fastest body waveform corresponds to the fastest preferred curvature waveform ($\lambda_{0,\max}, c_{0,\max}$) depicted by the black cross in Fig. 5.5E, while the most efficient body waveform aligns with the most efficient preferred curvature waveform ($\lambda_{0,\min}, c_{0,\min}$) indicated by the red cross. The swimmer's waveforms are illustrated by plotting the swimmer's centreline coordinate $r_3(s,t)$ and $r_2(s,t)$ in the dorsal-ventral (undulation) plane. Colors represent six different time points (see bottom legend) in the last undulation cycle of the simulation. (**A**): Fastest waveform for low fluid viscosity. (**B**): The fastest waveform for high fluid viscosity. (**C**): The most efficient waveform that minimizes the swimmer's COT in low viscosity. (**D**): Most efficient waveform in high viscosities. We use the same y-axis range in each panel to illustrate the difference in amplitude between the fastest and most efficient waveform.

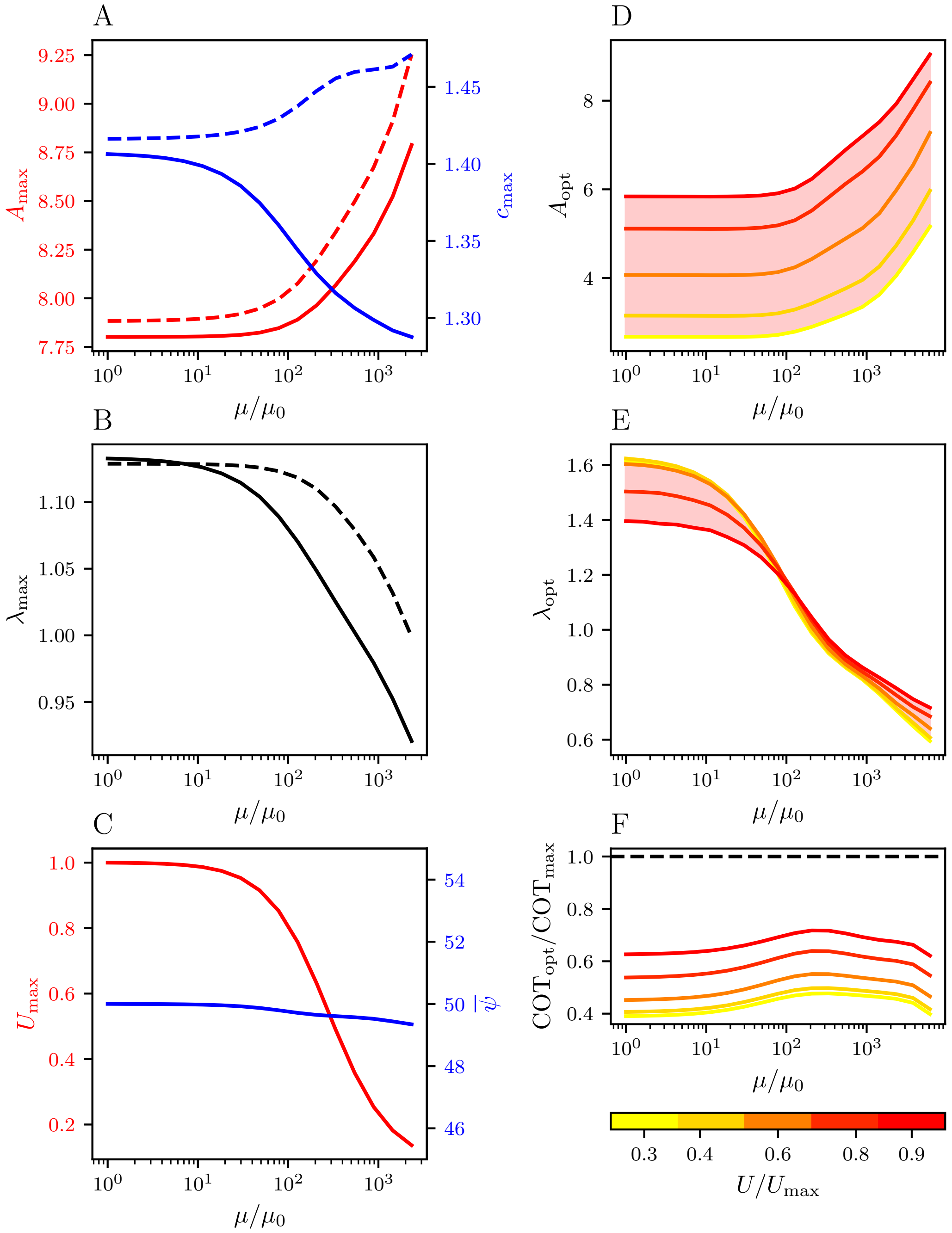

Figure 5.7: Influence of the fluid viscosity on the fastest and optimal waveform. (**A**): Fastest preferred curvature amplitude $A_{\max,0}$ (red dashed), preferred shape factor $c_{\max,0}$ (blue dashed), curvature amplitude $A_{\max}$ (red solid) and shape factor $c_{\max}$ (blue solid) as a function of the normalized fluid viscosity μ/μ_0. (**B**): Fastest preferred wavelength $\lambda_{\max,0}$ (black dashed) and fastest wavelength $\lambda_{\max}$ (solid black). (**C**): Normalized maximum swimming speed $U_{\max}/U_{0,\max}$ (red) and average angle of attack $\bar{\psi}$ (blue). (**D**): Optimal curvature amplitude A_{opt} as a function of μ/μ_0. Colored lines correspond to different values of the normalized swimming speed $U/U_{\max}$ represented by the colorbar below panel F. (**E**): Optimal undulation wavelength λ_{opt}. (**F**): Ratio $\text{COT}_{\text{opt}}/\text{COT}_{\max}$ between the Cost of Transport associated with optimal and the fastest waveform.

To address this question, it is helpful to compare the energy losses due to internal and external friction during undulatory locomotion. To do so, we consider the ratio D_{I}/D, where D_{I} and D are the internal and total dissipated energy during one undulation cycle, respectively. The ratio is plotted against the normalized fluid viscosity μ/μ_0 in Fig. 5.8. Each colored line corresponds to one of the optimal waveforms (A_{opt}, λ_{opt}) shown in Fig. 5.7D. Notably, all these lines display a sigmoidal trend similar to that of the optimal waveform λ_{opt} shown in Fig. 5.7E. In the low viscosity regime, the ratio D_{I}/D converges to one, i.e. the swimmer's energy cost is dominated by the internal friction. As the fluid viscosity increases, D/D gradually decreases and eventually converges to zero in the high viscosity limit. Unsurprisingly, in this regime, the swimmer's energy cost is dominated by external (fluid) friction.

This implies the following: The waveform that minimizes internal dissipation is characterized by a long wavelength and small curvature amplitude. In contrast, the waveform that minimizes external dissipation is characterized by a short wavelength and large curvature amplitude. Consequently, the optimal waveform (A_{opt}, λ_{opt}) exhibits a continuous transition from the internal dissipation-optimal waveform to the external dissipation-optimal waveform as μ increases. The transition region between both optima is characterized by the inflection point and the slope factor of the sigmoid in Fig. 5.8. As we will discuss in Chapter 6, the position of the inflection point depends on the ratio between the internal and fluid viscosity.

To conclude, our model shows that frequency and waveform modulation are crucial to enable efficient undulatory across changing environmental conditions. We conclude this Chapter with a summary and discussion of all the relevant results.

5.4 Discussion

This section provides a critical discussion of the key findings presented in this chapter. We started this chapter by exploring the gait modulation of an undulatory microswimmer in a static environment characterized by a constant fluid viscosity. This exploration had three main objectives: Firstly, to determine the range of plausible undulation frequencies for our physical model. Secondly, to derive the scaling behavior between the swimming speed and undulation frequency. Lastly, to establish a relationship between the swimmer's undulation frequency, waveform, swimming speed, and COT.

Concerning the first objective, our model constraints the swimmer's undulation frequency to the range $f \in [f_{\mathrm{min}}, f_{\mathrm{max}}]$, where f_{min} minimizes the swimmer's Cost of Transport (COT) and f_{max} maximizes its swimming speed. Within this range, lower frequencies are

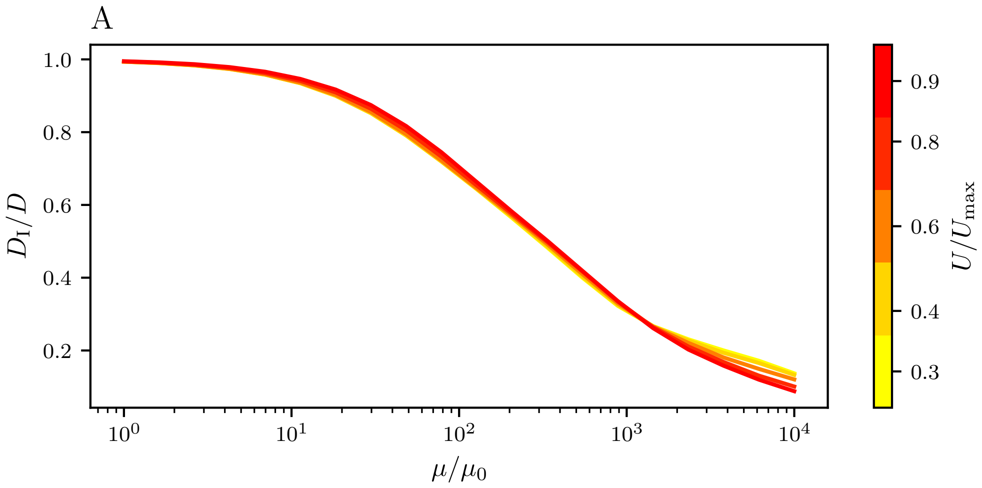

Figure 5.8: Comparison between the internal and external dissipation loss during undulatory locomotion in varying fluid viscosities. Ratio D_{I}/D between internal D_{I} and total D dissipation loss as a function of normalized fluid viscosity μ/μ_0. Colored lines correspond to the optimal waveforms (see Fig. 5.7) associated with different normalized swimming speeds $U/U_{\max}$, as depicted in the colorbar.

found to be more energy efficient, whereas higher frequencies lead to a faster swimming speed. The specific values of $f_{\min}$ and $f_{\max}$ are contingent on the swimmer's operating point and Basal Metabolic Rate (BMR). As the swimmer increases its frequency, it transitions from the pass-through to the low-pass regime, characterized by a damped curvature amplitude and shallow body wave. The precise frequency at which this transition occurs is determined by the system's intrinsic response times τ and ξ, which, in turn, are defined in terms of the physical model parameters, as detailed in Tab. 4.1. Generally speaking, the quicker the swimmer's response time, the larger the value of $f_{\max}$ and, consequently, the maximum achievable swimming speed.

This hypothesis can be tested by comparing microswimmers with different undulation frequencies. For instance, sea urchin sperm exhibit undulation frequencies in the range of 25-52 Hz [55, 113] when swimming in water, whereas the undulation frequencies of *C. elegans* are one order of magnitude smaller 0.2-2.0 Hz [18, 45, 120]. The body length and bending rigidity of the flagella of different sea urchin sperm have been estimated to be of the order $30\,\mu\mathrm{m}$ and $5 \times 10^{-22}\,\mathrm{N\,m^2}$ [103, 109, 112, 113], resulting in a response time of $\tau = 1.62\,\mathrm{s}$. To make a fair comparison, we consider the most viscous environment *C. elegans* typically inhabit, which is comparable to that of agar. The drag coefficients of agar have been estimated by Niebur *et al.* [101] and Boyle *et al.* [23]. Using these estimates together with values for the body length and bending rigidity given in Tab. 6.1 yields a response time of $\tau = 48.60\,\mathrm{s}$ — an order of magnitude slower than the time scale of sea urchin sperm. To the best of our knowledge, the viscoelastic response time (relative damping coefficient)

ξ of sea urchin sperm has not been estimated, but we expect it to be faster than that of *C. elegans* due to sea urchin sperm's faster undulation frequencies.

Regarding the lower frequency limit f_{min}, our model predicts that its value is contingent on the swimmer's BMR. Larger BMR values impose a greater penalty for slow swimming, resulting in a larger f_{min}. Therefore, comparing our model to experimental observations of a microswimmer's minimum undulation frequency enables us to estimate an upper bound for the swimmer's BMR. This process will be demonstrated for *C. elegans* in Chapter 6.

Concerning the scaling relationship between swimming speed and undulation frequency, we demonstrated that the frequency range $[f_{\mathrm{min}}, f_{\mathrm{max}}]$ can be divided into intervals. In the lower interval, the swimming speed scales linearly with the undulation frequency. In the upper interval, where values are close to f_{max}, the swimming speed scales sublinear with the undulation frequency due to power limitations. In this context, power-limited means that the swimmer's effective response times a and b are too slow for the actuation torque to generate a meaningful curvature amplitude. Consequently, the scaling behavior between swimming speed and undulation frequency allows us to infer whether a swimmer undulates with a frequency close to f_{max} or not. For example, Deng *et al.* [40] measured the undulation frequency and swimming speed of *C. elegans* swimming in the water and crawling in agar. In both media, their data reveals a linear scaling between between swimming speed and undulation frequency. This suggests that the undulation frequency of *C. elegans* is significantly smaller than f_{max}, i.e. it is not optimized for achieving maximum speed, a claim we will substantiate in Chapter 6. Interestingly, Deng *et al.* reported a bimodal frequency distribution in agar, but a uni-modal distribution was observed in water. A bimodal distribution suggests a slow and fast gait, whereas a uni-modal distribution suggests a single gait with a distinct preferred frequency. According to our model, slower frequencies are more energy-efficient, as they exhibit a smaller COT, making them beneficial for long-distance travel.

Importantly, microswimmers not only modulate their undulation frequency but also their waveform. Our model predicts the fastest waveform that maximizes the swimming speed and the most energy-efficient waveform that minimizes the COT. By continuously transitioning between these two waveforms a swimmer can either prioritize swimming speed or energy efficiency. Consequently, these waveforms constrain the plausible values for the swimmer's wavelength and curvature amplitudes in a given environment. Thus, we can test the validity of our model by verifying whether the experimentally observed waveforms of a swimmer fall within the predicted range. Furthermore, based on whether the measured waveform aligns more with the fastest or energy-efficient waveform, we can infer the swimmer's prioritization, as will be demonstrated for *C. elegans* in Chapter 6.

To summarize, our model suggests that a swimmer can prioritize swimming speed or energy efficiency by modulating either its undulation frequency or its waveform. Thus, we are faced with a two-dimensional performance space defined by the swimming speed and the COT and a three-dimensional parameter space encompassing undulation frequency, wavelength, and curvature amplitude. Consequently, determining which combination of undulation parameters yields the optimal performance requires multivariate optimization, which is beyond the scope of this thesis. However, it would be very interesting to investigate whether frequency or waveform modulation enables a more efficient trade-off between speed and energy efficiency. Such an investigation could provide insight into whether and why swimmers choose one modulation strategy over the other.

To compare our model to the established literature, we reference an extensive body of work that combines flow simulations with evolutionary optimization [61, 62]. This body of research has explored the locomotion of various organisms from the viewpoint of optimality, including determining the optimal C-start escape of larval fish [53], optimizing the morphology of anguilliform swimmers [132], and optimizing the actuation torque of slithering snakes and undulating sea urchin sperm [52]. In the latter study, the authors developed an explicit numerical scheme for a purely elastic Cosserat rod. Consistent with our model, active deformation is achieved by applying an actuation torque across the length of the rod. Actuation torque optimization involves five parameters, with four determining the actuation torque profile across the rod's length, while the fifth represents the undulation wavelength. The authors optimized for maximum crawling and swimming speed, respectively, without taking the organism's energy expenditure into consideration. In the study of undulating aquatic animals, such as lamprey, ells, and trouts, the COT is commonly used to estimate energy efficiency [14, 119, 130]. In these studies, energy expenditure is estimated based on the power exerted by the animal's body against the fluid, with internal body friction not being accounted for. In a recent study, Anastasiadis *et al.* [8] developed an anguilliform bio-inspired robot comprising eight actuator modules to investigate the relationship between the kinematics of its body and the resulting swimming speed and efficiency. Their findings indicate that to achieve maximum swimming speed, the robot should use higher tail amplitude and larger wavelengths. For efficiency, it should use a lower wavelength moderate amplitude, resulting in a slower swimming speed. Thus, consistent with our Cosserat model, the robot can modulate its waveform to prioritize between speed and efficiency. To the best of our knowledge, the COT and BMR have so far not been considered for the study of microswimmers such as sperm or *C. elegans*. Notably, all of the previously mentioned studies focused on a static environment. The impact of environmental conditions on the undulatory locomotion of terrestrial organisms, such as snakes, has been explored by Guo *et al.* [58] and Yaqoob *et al.* [141]. The latter study used a model of coupled discrete viscoelastic joints passively driven by the head. In their model, waveform and crawling speed are contingent on the fine-tuning of physical parameters like stiffness, moment of inertia, external frictional anisotropy, and internal damping.

In our model, we demonstrated that the swimmer's fastest and most efficient waveform is contingent on the swimmer's undulation frequency and the fluid's viscosity. In a static environment, the swimmer's fastest waveform (λ_{max}, A_{max}) remains relatively unaffected by the undulation frequency, assuming that the swimmer is not constrained by power limitations. On the other hand, the most energy-efficient wavelength λ_{opt} decreases significantly with the frequency, exhibiting a concave trend. Meanwhile, the most energy-efficient curvature amplitude A_{opt} remains constant. A similar trend for the relationship between wavelength and frequency has been observed for sea urchin sperm [28, 113]. However, it is important to acknowledge that our model is not directly applicable to sperm, given that sperm consists of two distinct parts: the cell body and the flagellum, both connected by a mid-piece often referred to as the sperm's neck [49]. In the base region close to the neck, the flagellum typically has a very large curvature, giving rise to a body wave whose amplitude increases from head to tail [113]. Thus, a more accurate representation of sperm would require a model of its cell body that is connected to our Cosserat rod model using the appropriate boundary conditions, which is beyond the scope of this thesis. Since the primary goal of sperm is to reach the egg first, we anticipate its undulation frequency and waveform to be geared toward maximum speed. For *C. elegans*, there is currently insufficient experimental data available to conclusively determine whether undulatory gait modulation occurs in a static environment.

However, there is ample evidence that the frequency and waveform of sperm and *C. elegans* are modulated by their physical environment [18, 45, 114, 120, 126]. Most notably, both sea urchin sperm and *C. elegans* gradually decrease their undulation frequency in more viscous fluids. To understand the reason behind this behavior, we compared two scenarios: one where the swimmer maintains a constant frequency and another where it continuously adapts its frequency to the fluid viscosity. Notably, both scenarios achieve a similar swimming speed, while frequency adaptation proves to be significantly more energy-efficient, making it the superior strategy. Thus, we anticipate undulatory microswimmers to adapt their frequency in response to changes in fluid viscosity, irrespective of whether they prioritize speed or energy efficiency. Mammalian sperm would be an ideal model organism to test this hypothesis, as they must migrate through the numerous environments of the female reproductive tract, characterized by complex rheologies with varying viscosity [49].

Lastly, imposing a sigmoidal relationship between frequency and fluid viscosity, we examined how the fluid viscosity influences the swimmer's fastest and most energy-efficient waveform. Our model predicts that both waveforms undergo a continuous transition from low to high viscosity. In the low viscosity regime, internal friction dominates the energy expenditure, favoring large wavelengths and small curvature amplitudes. Conversely, in the high viscosity regime, external dissipation dominates, favoring small wavelengths and large curvature amplitudes. These distinct preferences must be a consequence of the fact that internal friction is proportional to the rate of body curvature, while external friction is proportional to the centreline velocity. However, further investigation is needed to understand why these proportionalities result in the observed optimal waveforms. As the viscosity increases, the waveform transitions from one optimum to the other. Hence, at each viscosity limit, we expect the fastest and optimal waveform to converge. For the simulations presented in this chapter, we did not explore high enough fluid viscosities to properly capture the convergent behavior associated with the external friction-dominated regime. As we demonstrated, the transition region from internal and external friction dominated can be determined by comparing the swimmer's internal to its total dissipation loss. In the next chapter, we will discuss in more detail how the transition region's location on the fluid viscosity scale depends on the physical model parameters.

Chapter 6

Model Application to *C. elegans*

Not a sprinter but a casual swimmer

6.1 Overview

In the previous chapter, we discussed the gait modulation and selection of a generalized undulating microswimmer. Building upon these results, this chapter focuses on the 1mm long slender nematode *C. elegans*. As discussed in Section 2.4, multiple studies have demonstrated that *C. elegans* adapts its undulation gait in response to changing environmental conditions, making it an ideal model organism to study gait modulation. Throughout this chapter, we will colloquially refer to *C. elegans* as the worm.

To model *C. elegans*, we must select appropriate physical model parameters, which are summarized in Tab. 6.1. Backholm *et al.* [13] estimated the bending rigidity B of *C. elegans* by measuring the force-deflection response of anesthetized animals using a three-point measuring device. By comparing the bending rigidity B and cross-sectional radius $R_{\max}$ of worms at different life stages, growing in size, the authors demonstrated that B is proportional to $R_{\max}^4$. This suggests that the stiffness of the worm's body is isotropic and self-similar; that is, it is rotationally symmetric and scales with the worm's size. This observation is consistent with the worm's anatomy described in Section 2.4. Consequently, the bending rigidity can be expressed as $B \sim EI$, where E is the effective Young's modulus of the worm's body material and $I \propto R_{\max}^4$ represents the cross-section's second moment of area. We refer to Chapter 3 for a detailed discussion of the material model parameters. At any life stage, Backholm *et al.* found that $R_{\max}$ and B vary across specimens. In adult worms, which will be the exclusive focus of this study, the bending rigidity B between specimens can vary by up to one order magnitude, illustrated by the range given in Tab.

6.1. Thicker worms with larger R_{max} are typically found to be more rigid, as $B \propto R_{\mathrm{max}}^4$. In an independent study, Fang Yen *et al.* [45] estimated the bending rigidity B and the internal damping coefficient $\tilde{B}$ by measuring the relaxation time scale of awake worms following bending deformation in Newtonian fluids with different viscosities. From these experiments, the authors calculated an average bending rigidity of $B = 9.5 \times 10^{-14}\,\mathrm{Pa\,m^4}$ for adult worms, which is consistent with the range reported by Backholm. For the internal damping coefficient, Fang Yen *et al.* estimated an upper bound of $\tilde{B} = 5 \times 10^{-16}\,\mathrm{Pa\,m^4 s}$, which yields a relative damping coefficient of $\xi = 0.005\,\mathrm{s}$. As this chapter will focus on the experimental data presented by Fang Yen *et al.*, we adopt their values as our defaults. For the worm's cross-sectional radius, we use the average value $R_{\mathrm{max}} = 32\,\mathrm{\mu m}$ of all adult specimens measured by Backholm *et al.* [13]. For the body length, we adopt the midpoint $L_0 = 1130\,\mathrm{\mu m}$ of the range for adult worms provided by the Wormatlas [5].

Given these values and assuming that the "worm material" is disturbed homogeneous and uniformly across the worm's cross-section, we calculate Young's modulus of $E = 0.12\,\mathrm{MPa}$. In reality, *C. elegans* is of cause not made up of a homogeneous material. On the contrary, it has a complex anatomy, which consists of multiple body parts such as the cuticle (outer body wall), pseudocolumn, muscles, and organs, all made up of different tissue types (see Section 2.4). However, the bending rigidity B is independent of these complexities, as it characterizes the response of the worm's body as a whole. Thus, to simplify matters, we model the worm as a uniform rod with a circular cross-section. Additionally, we assume that the internal viscosity η is directly proportional to Young's modulus E, i.e. the stiffer the worm, the stronger the damping. Under these assumptions, given the worm's cross-sectional radius, we determine can E and η from B and ξ.

The Poisson's ratio ϱ of *C. elegans* has been measured by Park *et al.* [108] by using piezoresistive cantilevers as force-displacement sensors. The authors estimated a value 0.5, which we adopt for our model. Note that the majority of materials have a Poisson ratio between 0 and 0.5, with 0.5 being characteristic of a perfectly incompressible isotropic material. As cells and extracellular matrix components are commonly considered incompressible, the Poisson ratio of most soft biological tissues is very close to 0.5 [57, 133] in line with the measure by [108] for *C. elegans*.

Having established values for the worm's body length L_0, cross-sectional radius R_{max}, bending rigidity B, relative damping coefficient ξ and Poisson ratio ϱ, all other model parameters such as the shear modulus G, shear viscosity ν and drag coefficient ratios can be determined using the formulas detailed in Tab. 4.1. All relevant physical model parameters for *C. elegans* are detailed in Tab. 6.1. The dimensionless model parameters can be determined from the physical model parameters using the equations detailed in Tab. 4.2. The values of the dimensionless model parameter for *C. elegans* are presented in Tab. 6.2. Note that Tab. 6.2 does not provide specific values for the system's effective response times a and b. This is because their values are contingent on the swimmer's undulation frequency and the viscosity of the surrounding fluid environment. Consequently, they need to be recalculated for different environments and undulation frequencies.

Having determined the values for all relevant dimensionless model parameters, we are now prepared to model the undulatory locomotion of *C. elegans*. As we discussed in Section 2.4.2, *C. elegans* adapts its undulation gait in response to its environment [18, 45, 50, 79, 126]. Until recently, swimming and crawling were considered to be distinct biomechanical gaits, although Niebur & Erdös already hypothesized that a single underlying circuit generates both swimming and crawling [102]. Berri *et al.* [18] and a large body of work that followed [22, 45, 126] now give a strong indication that the two behaviors are extremes of a continuous spectrum. Among the experimental studies, Fang Yen *et al.* [45] conducted the most comprehensive investigations on *C. elegans* undulation gait in Newtonian fluids, covering four orders of magnitude in viscosity. The authors demonstrated that the undulation frequency and waveform of *C. elegans* undergo a continuous transition from low to high fluid viscosity regime. This transition shows similar trends as the transition of the most energy-efficient gait, predicted for a generic microswimmer in Section 5.3. Therefore, to assess whether *C. elegans* gait transition can be deemed optimal, we conduct a quantitative comparison between our model predictions and Fang-Yen's experimental data.

Following a similar outline as in Chapter 5, we first explore frequency modulation within a static, low-viscosity, water-like environment. Subsequently, we analyze the gait transition of *C. elegans* in response to varying fluid viscosities. As a preliminary step, we fit our model parameters to match the experimental data recorded by Fang Yen *et al.* [45]. Finally, we compare the experimentally measured waveform of *C. elegans* against the fastest and most energy-efficient waveform predicted by our model across the full viscosity range.

6.2 Optimal Gait Transition

This chapter aims to provide an explanation for why *C. elegans* modulate their undulatory gait by assessing its performance. It builds upon our findings from Chapter 5, where we explored gait modulation of a generalized undulating microswimmer within our dimensionless framework. To set the scene, we start this chapter by presenting the experimental data from Fang Yen *et al.* [45], depicted in Fig. 6.1. In their experiments, the authors placed worms within a narrow wall chamber filled (effectively 2D) with Newtonian viscous fluid. They systematically increased the fluid's viscosity from 10^{-3} to $10^{4.45}$ Pa s, capturing the movement of the specimens with a microscope from a top-down perspective. From the resulting image sequences, they reconstructed the worms' centreline trajectories and showed

Physical Parameters					
Name	**Range**	**Value**	**SI Unit**	**Source**	Description
L_0	[1110 - 1150]	1130	µm	[5]	Natural length
R_{max}	[28 - 35]	32	µm	[13]	Max. cross-sectional radius
ε	-	0.057	-		Slenderness parameter
B	$[3.26 - 30.3]\times10^{-14}$	9.5×10^{-14}	$\mathrm{N\,m^2}$	[13, 45]	Bending rigidity
E	-	0.12	MPa	-	Young's modulus
ϱ	-	0.5	-	[108]	Poisson's ratio
G	-	0.04	MPa	-	Shear modulus
η	-	607	Pa s	[45]	Extensional viscosity
ξ	-	0.005	Pa s	[45]	Rel. damping coeff.
ν		202	Pa s	-	Shear viscosity
μ	$[10^{-3} - 10^{1}]$	-	Pa s	-	Fluid viscosity
$c_{\|\|}$	-	2.05	-	-	Linear longi. drag coeff.
$c_{\perp}$	-	3.09	-	-	Linear transv. drag coeff.
$\gamma_{\|\|}$	-	3.21×10^{-9}	$\mathrm{m^2}$	-	Angular longi. drag coeff.
$\gamma_{\perp}$	-	12.84×10^{-9}	$\mathrm{m^2}$	-	Angular transv. drag coeff.

Table 6.1: Physical model parameters for *C. elegans* sourced from literature. For a definition and description of the parameters, please refer to Tab. 4.1. Experimental measurements are available for the length L_0, maximal radius R_{max}, bending rigidity B, extensional viscosity (internal damping coefficient) η, and the Poisson ratio ϱ. All other model parameters can be calculated from the expression in Tab. 4.1.

Name	Definition	Value	Description
p	$\dfrac{1}{2(1+\varrho)}$	1/3	Viscoelastic shear to extension ratio
g	$\dfrac{I}{AL_0^2}$	0.00020	Geometric ratio
K_{c}	$c_{\perp}/c_{\|\|}$	1.51	Linear drag coefficient ratio
K_{γ}	$\gamma_{\perp}/\gamma_{\|\|}$	4	Angular drag coefficient ratio
$K_{\|\|}$	$\gamma_{\|\|}/L_0^2 c_{\|\|}$	0.0038	Longitudinal drag coefficient ratio

Table 6.2: Dimensionless model parameters for *C. elegans*. The dimensionless parameters are calculated from the physical model parameters in Tab. 6.1 using the equations in Tab. 4.2. The values of the dimensionless effective response times a and b are contingent on the fluid viscosity μ and undulation frequency f.

(consistent with Berri *et al.* [18]) that their body curvature could be accurately described as a traveling wave across the entire viscosity range. From the body curvature kymograms, they determined the curvature wave's amplitude, wavelength, and undulation frequency as a function of the fluid viscosity, shown in Fig. 6.1A. Notably, the amplitude, wavelength, and frequency all undergo a continuous transition from the low to the high viscosity regime. To describe this transition, we fit three sigmoidal functions to the experimental data — one for the curvature wave amplitude, another for the wavelength, and a third for the undulation frequency. Each of the sigmoidal functions is defined as follows:

$$Y(\mu) = \frac{\text{Amplitude}}{1 + e^{\alpha\left[\log(\mu) - \log(\mu_{\text{ip}})\right]}} + \text{Offset} \tag{6.1}$$

Relevant parameters include the sigmoid's amplitude, slope factor α, inflection point μ_{ip}, and offset. All three fits yield similar values for the slope factor α and the inflection point μ_{ip}. Thus, we calculate the average inflection point $\bar{\mu}_{\text{ip}}$ to characterize the transition region of the undulation parameters. See the vertical dashed black line in Fig. 6.1A. The fit of the curvature amplitude and wavelength are plotted against the undulation frequency in Fig. 6.1B. Both amplitude and wavelength change linearly with the frequency consistent with the experimental observation by Berri *et al.* [18]. The vertical dashed back line represents the worm's undulation frequency at the average inflection point in panel A. Notably, this vertical line coincides with the intersection point of the red and blue curve, suggesting that amplitude, wavelength, and frequency undergo a simultaneous transition. Lastly, the worm's maximum angle of attack is plotted as a function of the fluid viscosity in Fig. 6.1C.

Having presented the experimental data, we start our discussion by focusing on *C. elegans* swimming gait in water. In Section 5.2.1, we demonstrated that in a fixed environment, microswimmers can modulate their undulation frequency to prioritize either swimming speed or energy efficiency. Moreover, we predicted that the swimmer's undulation frequency should lie within the range $f \in [f_{\text{min}}, f_{\text{max}}]$, where f_{min} is the frequency that minimizes its Cost of Transport (COT) (see Eq. 4.10) and f_{max} is the frequency that maximizes its swimming speed. Naturally, we want to know where *C. elegans* undulation frequency falls within this interval to infer how it balances between energy efficiency and swimming speed. Water has a viscosity of $\mu_0 = 10^{-3}\,\text{Pa s}$, which corresponds to the lower viscosity limit in the experimental dataset. Thus, from fits (colored lines) in Fig. 6.1A, we obtain *C. elegans*' characteristic undulation frequency $f_{\text{c}} = 1.71\,\text{Hz}$, wavelength $\lambda_{\text{c}} = 1.46$ and curvature amplitude $A_{\text{c}} = 2.94$ in water $\mu_0 = 10^{-3}\,\text{Pa s}$. This characteristic frequency coincides with the peak of the frequency distribution measured by [40] *et al.* for wild-type *C. elegans* swimming in water. Given the fluid's viscosity μ_0, characteristic frequency f_{c}, and physical model parameters in Tab. 6.1, we determine the worm's characteristic operating point (a_{c}, b_{c}) in water. To explore why *C. elegans* undulate at a frequency of approximately $f_c = 1.71\,\text{Hz}$ in water, we simulate undulation experiments within the range

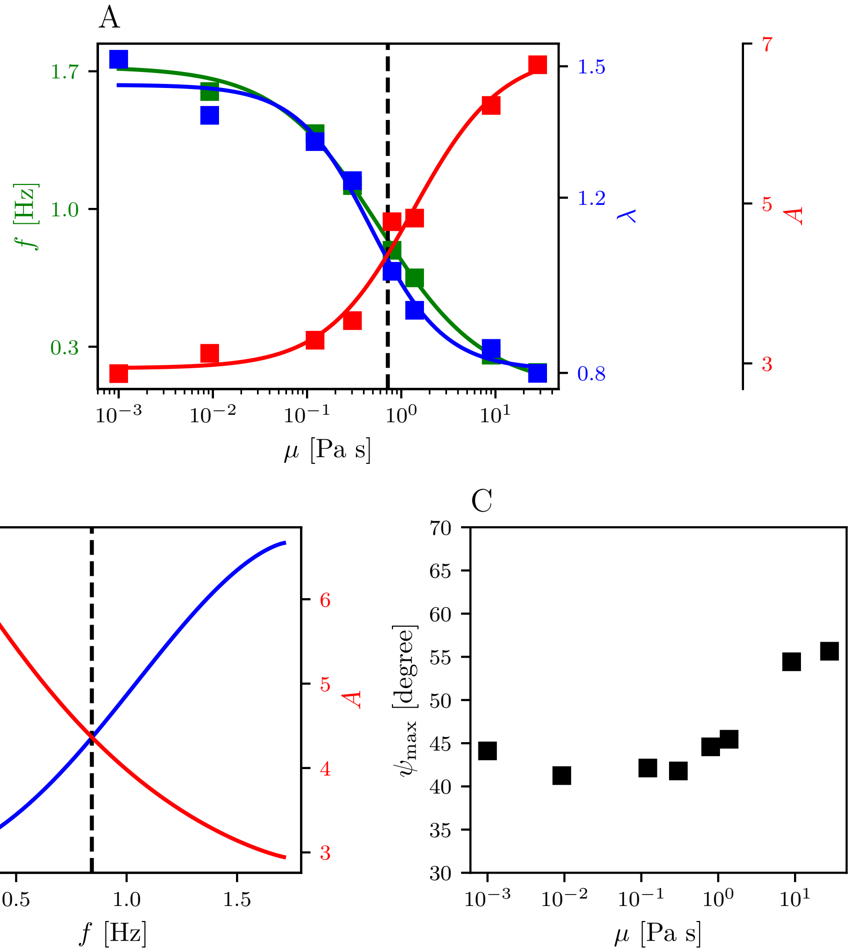

Figure 6.1: *C. elegans* gait modulation in Newtonian fluids with varying viscosity sourced from Fang Yen [45]. (**A**): Rectangular markers display the measured undulation frequency f (green), wavelength λ (blue), and curvature amplitude A (red) of *C. elegans* as a function of the fluid's viscosity μ. Both λ and A are normalized by the worm's body length L_0. We fit a sigmoidal function to the experimental data of each undulation parameter, represented by the colored lines, characterized by its inflection point and slope factor. The black vertical dashed line represents the average inflection point $\bar{\mu}_{\text{ip}}$ of all three sigmoidal fits. (**B**): Fitted normalized curvature amplitude A and wavelength λ as a function of the undulation frequency f. (**C**): Measured peak angle of attack $\psi_{\max}$ as a function of fluid viscosity μ.

$f/f_c \in [10^{-1}, 10^{1}]$. Independent of the frequency, we assume that the worm maintains its characteristic waveform (λ_{c}, A_{c}) in water.

The contour plot of the dimensionless normalized swimming speed $U^*/U^*_{\max}$ is depicted as a function of the worm's operating point (a, b) in Fig. 6.2A, where $U^*_{\max}$ is the maximum speed within the given range of a and b. The characteristic operating (a_{c}, b_{c}) of *C. elegans* in water is represented by the big dotted marker. This marker demonstrates that *C. elegans* operates in the pass-through regime close to the upper boundary of the low-pass regime, which is characterized by fast swimming speeds and instantaneous response time to actuation. As explained in Section 5.2.1, when the worm modulates its undulation frequency, its operating point shifts in a diagonal direction as illustrated by the small dotted markers in Fig. 6.2A.

For each operating point (frequency), the dimensionless (solid) and the physical swimming speed (dashed) are plotted against the worm's undulation frequency f in Fig. 6.2B. For frequencies lower than *C. elegans*' characteristic frequency, $f \leq f_\mathrm{c} = 1.71\,\mathrm{Hz}$, *C. elegans* operates in the pass-through regime, i.e. the dimensionless normalized swimming speed U^*/U^*_max is approximately one. Consequently, the physical swimming U increases linearly, as can be seen from Eq. (3.77). For $f > f_\mathrm{c}$, *C. elegans* transitions through the low-pass regime towards the struggle regime, which results in a damping of the curvature amplitude and a decrease of U^*. Initially, U^* decreases at a slower rate than $1/f$, i.e. the physical swimming speed still increases sublinearly because $U \sim fU^*$. However, as f increases further, *C. elegans* approaches the struggle regime, and U^* decreases at a faster rate than $1/f$, which results in a decrease of U. This explains why the physical swimming speed U peaks at the frequency $f_\mathrm{max} = 11\,\mathrm{Hz}$ represented by the vertical red dashed line.

Notably, for the given model parameters, f_max is significantly larger than the experimentally observed frequency range of *C. elegans*, which is highlighted by the blue shaded area in panel B. This discrepancy suggests that the undulation frequency of *C. elegans* is not optimized for achieving maximum swimming speed. This hypothesis is supported by the fact that *C. elegans* characteristic waveform ($\lambda_\mathrm{c} = 1.46$, $A_\mathrm{c} = 2.94$) deviates significantly from the fastest waveform ($\lambda_\mathrm{max} \approx 1.14$, $A_\mathrm{max} \approx 7.78$) predicted by our model (see Fig. A.2).

As discussed in Section 5.2.1, our model predicts that within the range $[f_\mathrm{min}, f_\mathrm{max}]$, a swimmer can increase its undulation frequency to enhance its swimming speed at the cost of being less energy efficiency and vice versa. Consistent with our previous discussion, we use the swimmer's Cost of Transport (COT) as an efficiency metric, referring to Section 4.3 for more details. The normalized Cost of Transport $\mathrm{COT}/\mathrm{COT}_c$ for *C. elegans* swimming in water is plotted against f in Fig. 6.2C. Here, COT_c is the model worm's characteristic COT at frequency $f_\mathrm{c} = 1.71\,\mathrm{Hz}$. The frequency f_min that minimizes the worm's COT is represented by the vertical yellow dashed line. As discussed in Section 4.3, the value of f_min is contingent on the organism's Basal Metabolic Rate (BMR), with a larger BMR resulting in a higher minimum frequency. The value of f_min as a function of the normalized Basal Metabolic Rate $\mathrm{BMR}/W_\mathrm{c}$ is depicted in Fig. 6.2D, where W_c denotes the characteristic actuation work required during one undulation cycle at frequency f_c in water. The BMR acts as an energy penalty that is inversely proportional to the swimming speed. Consequently,

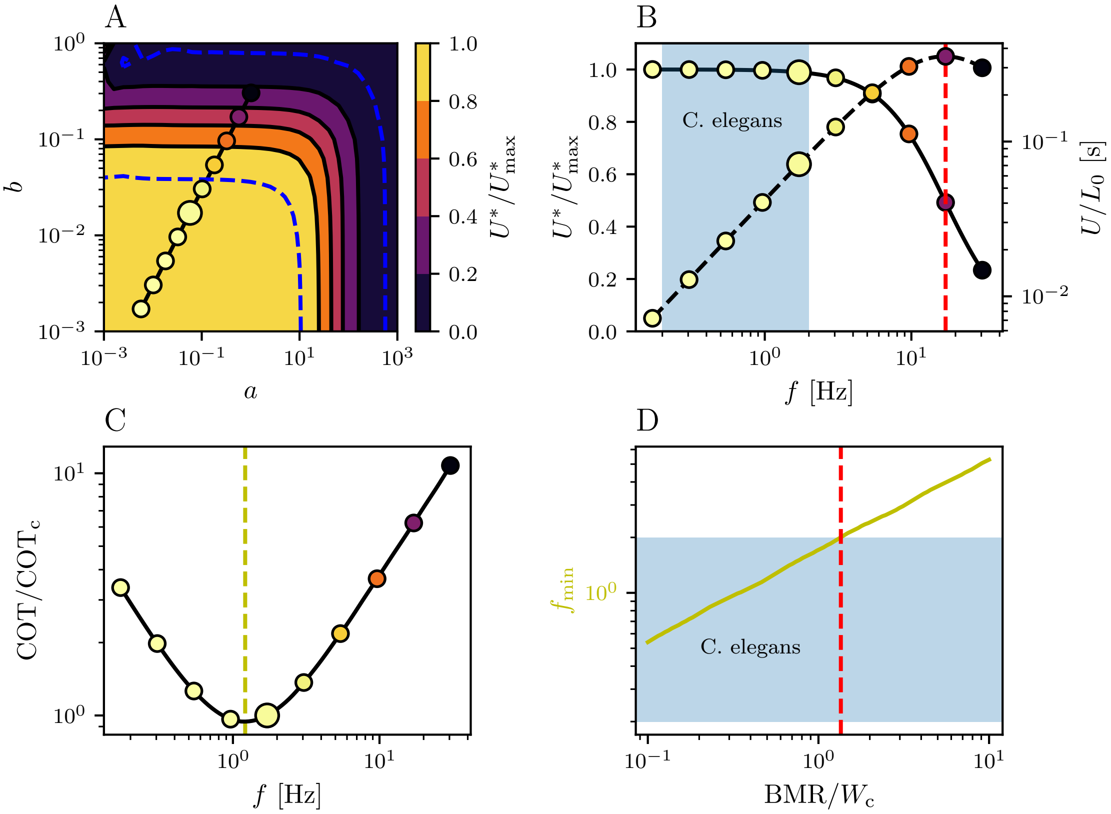

Figure 6.2: Frequency modulation of *C. elegans* in water-like fluid with viscosity $\mu = 1 \times 10^{-3}\,\mathrm{Pa}$. (**A**): Contour plot of the dimensionless normalized swimming speed U^*/U^*_{max}, where is the maximum speed U^*_{max} in specified range of a and b. Big dotted marker represents the characteristic operating point (a_c, b_c) of *C. elegans*, associated with its characteristic undulation frequency $f_c = 1.71\,\mathrm{Hz}$. Small dotted markers illustrate the shift in *C. elegans*' operating point when it modulates its undulation frequency within the range $f/f_c \in [10^{-1}, 10^1]$. The markers' color codes for the dimensionless swimming speed U^*/U^*_{max}. Regime boundaries are illustrated by blue dashed lines, introduced in Section 4.2. (**B**): Dimensionless normalized swimming speed U/U_{max} (solid) and physical swimming speed U (dashed) per unit body length plotted against f. The red dashed line represents undulation frequency $f_{\mathrm{max}} \approx 11\,\mathrm{Hz}$ that achieves the maximum physical swimming speed U_{max}. The blue shaded area depicts the range of experimentally observed undulation frequencies of *C. elegans* [45]. (**C**): Normalized Cost of Transport, COT/COT$_c$ plotted against f for an exemplary value of the normalized Basal Metabolic Rate of BMR/$W_c = 0.5$ [82], where COT$_c$ and W_c are the COT and actuation work associated with characteristic operating point (a_c, b_c) and frequency f_c. The undulation frequency f_{min} that minimizes the COT is represented by the yellow dashed line. (**D**): Optimal frequency f_{min} plotted against BMR/$W_c = 0.5$. The Red dashed line represents the upper bound for *C. elegans* BMR. Other dimensionless model parameters are taken from Tab. 4.2.

increasing the BMR incentivizes the worm to swim faster, resulting in a larger f_{min} value.

Conversely, if we know a swimmer's slowest characteristic undulation frequency $f_{\mathrm{c}}^{\mathrm{min}}$ within a specific environment, we can estimate an upper bound for the BMR from the inequality $f_{\mathrm{c}}^{\mathrm{min}} \leq f_{\mathrm{c}}$. Deng *et al.* [40] reported a unimodal frequency distribution for *C. elegans* swimming in water, with its peak value approximately equal to the characteristic frequency $f_{\mathrm{c}} = 1.71\,\mathrm{Hz}$ obtained from the experimental fit presented in Fig. 6.1A. Thus, we make the simplifying assumption that $f_{\mathrm{c}}^{\mathrm{min}} = 1.71\,\mathrm{Hz}$, which yields an upper bound of $\mathrm{BMR}/W_{\mathrm{c}} = 1.44$. This corresponds to a lower bound for the Metabolic Task Equivalent (MET) of $\mathrm{MET} = 1.70$. This lower bound is below the experimental measure of 3.0 reported by Laranjeiro *et al.* [82], who estimated *C. elegans*' energy expenditure during rest and locomotion using a microcalorimeter. Based on Laranjeiro *et al.*'s estimate $\mathrm{BMR}/W_{\mathrm{c}} \approx 0.5$, we infer $f_{\mathrm{min}} \approx 1.20\,\mathrm{Hz}$ from Fig. 6.2. This value is much closer to *C. elegans* actual frequency $f_{\mathrm{c}} = 1.71\,\mathrm{Hz}$ than f_{max}, which suggests that *C. elegans* undulation frequency optimizes energy efficiency. However, the experimental measures by [82] need to be taken with caution, as they do not specifically represent *C. elegans*' energy expenditure during undulatory locomotion but instead capture a general active state comprising a variety of locomotion patterns.

Having examined *C. elegans*' swimming gait in water in more detail, we now focus on its gait transition across different fluid viscosities. In Section 5.3.1, we hypothesized that microswimmers lower their undulation frequency in more viscous environments to accommodate a slower actuation response time. Additionally, we showed that in fluids with low viscosity, the swimmer's energetic cost is dominated by internal friction, whereas in high viscosities, external friction takes over. To test whether this holds true for *C. elegans*, we simulate undulation experiments in fluids with varying viscosity μ, spanning the same range accessed experimentally by Fang *et al.* [45]. At each μ value, we derive the worm's undulation frequency and waveform from the experimental fits presented in Fig. 6.1.

To determine whether internal or external friction is dominant, Fig. 6.3A displays the ratio D_{I}/D between the internally dissipated energy D_{I} and the total dissipated energy D during one undulation cycle as a function of μ. Each colored curve corresponds to a worm with different body stiffness (Young's modulus) E. All of these curves follow a sigmoidal trend, consistent with our presentation in Section 5.3. For low μ, the ratio D_{I}/D converges to one, which implies that the swimmer's energy loss is dominated by internal friction. Conversely, as μ increases, external friction becomes more dominant, and D_{I}/D gradually converges to zero. At intermediate viscosities, both internal and external friction make a significant contribution to the worm's energy loss. This intermediate transition region is characterized by the sigmoid's inflection point μ_{ip}, defined as $D_{\mathrm{I}}/D = 0.5$. On each sigmoid in Fig. 6.3A, μ_{ip} is represented by a black dot. Notably, as E increases and the worm becomes stiffer, μ_{ip} shifts to the right. This is because we choose the internal viscosity η to be proportional to Young's modulus E. Consequently, as the worm stiffens, internal damping becomes stronger, leading to a greater energy loss due to internal friction. Thus, higher fluid viscosities are required for fluid dissipation to surpass internal dissipation, explaining why μ_{ip} becomes larger.

As mentioned before, the undulation frequency, wavelength, and curvature amplitude of *C. elegans* also undergo a continuous "sigmoidal" transition from low to high fluid viscosities, mirroring the behavior of the ratio D_{I}/D. The transition region of the worm's undulation parameters is characterized by the average inflection point $\bar{\mu}_{\mathrm{ip}}$, calculated from the sigmoidal fits presented in Fig. 6.1A. For comparison, $\bar{\mu}_{\mathrm{ip}}$ is depicted by the vertical black dashed line in Fig. 6.3A. This comparison allows us to fit the model's Young's modulus by aligning inflection point μ_{ip} (black dot) with the experimental prediction $\bar{\mu}_{\mathrm{ip}}$ (vertical dashed line). This fit is based on the premise that the transition from the internal to the external friction-dominated regime is what triggers the worm's gait transition. Choosing an exemplary value of the relative damping coefficient of $\xi = 10^{-2.0}\,\mathrm{s}$, we determine the optimal Young's modulus to be $E = 10^{5.42}\,\mathrm{Pa}$, as illustrated in Fig. 6.1C. This value yields a bending rigidity of $B = 2.15 \times 10^{-13}\,\mathrm{N\,m^2}$, which is close to the upper range of the rigidities reported by Backholm *et al.* [13] (see Tab. 6.1).

It is important to note that the model's inflection point μ_{ip} is influenced not only by the worm's stiffness E but also by its relative damping coefficient ξ. Again, this can be understood from the fact that the internal viscosity η is proportional to ξ. Consequently, when ξ becomes larger, more energy is lost due to internal dissipation. Therefore, higher fluid viscosities are required for fluid dissipation to surpass internal dissipation. This is illustrated in Fig. 6.1B, where the colored curves display the ratio D_{I}/D for different values of ξ. As predicted, the inflection point μ_{ip} (black dot) shifts to the right as ξ increases. Thus, similar to panel A, we can fit the model's optimal relative damping coefficient ξ by aligning μ_{ip} (black dot) with $\bar{\mu}_{\mathrm{ip}}$ (vertical dashed line). Assuming that $E = 10^5\,\mathrm{Pa\,s}$, we determine the optimal relative damping coefficient to be $\xi = 10^{-1.7}\mathrm{s}$, as illustrated in Fig. 6.1D.

To conclude, our results show that the model's transition point μ_{ip} is contingent on Young's modules E and the relative damping coefficient ξ. To illustrate this, we plot the logarithmic error between μ_{ip} and the experimental prediction $\bar{\mu}_{\mathrm{ip}}$ as a function of E and ξ in Fig. 6.3E. There exists no single optimal solution for E and ξ that minimizes the error. Instead, a manifold of equally optimal solutions exists, represented by the red dashed line. This line has a slope of negative one, i.e. it corresponds to a constant value of the internal viscosity η. This value can be calculated from the line's y-intercept, which yields $\eta = 10^{3.35}\,\mathrm{Pa\,s}$. This corresponds to an internal damping coefficient of $\tilde{B} = 1.84 \times 10^{-15}\,\mathrm{N\,m^2\,s}$, which is an order of magnitude larger compared to the experimental value reported by Fang Yen *et al.* [45]. Possible reasons for this disparity will be discussed in the discussion section

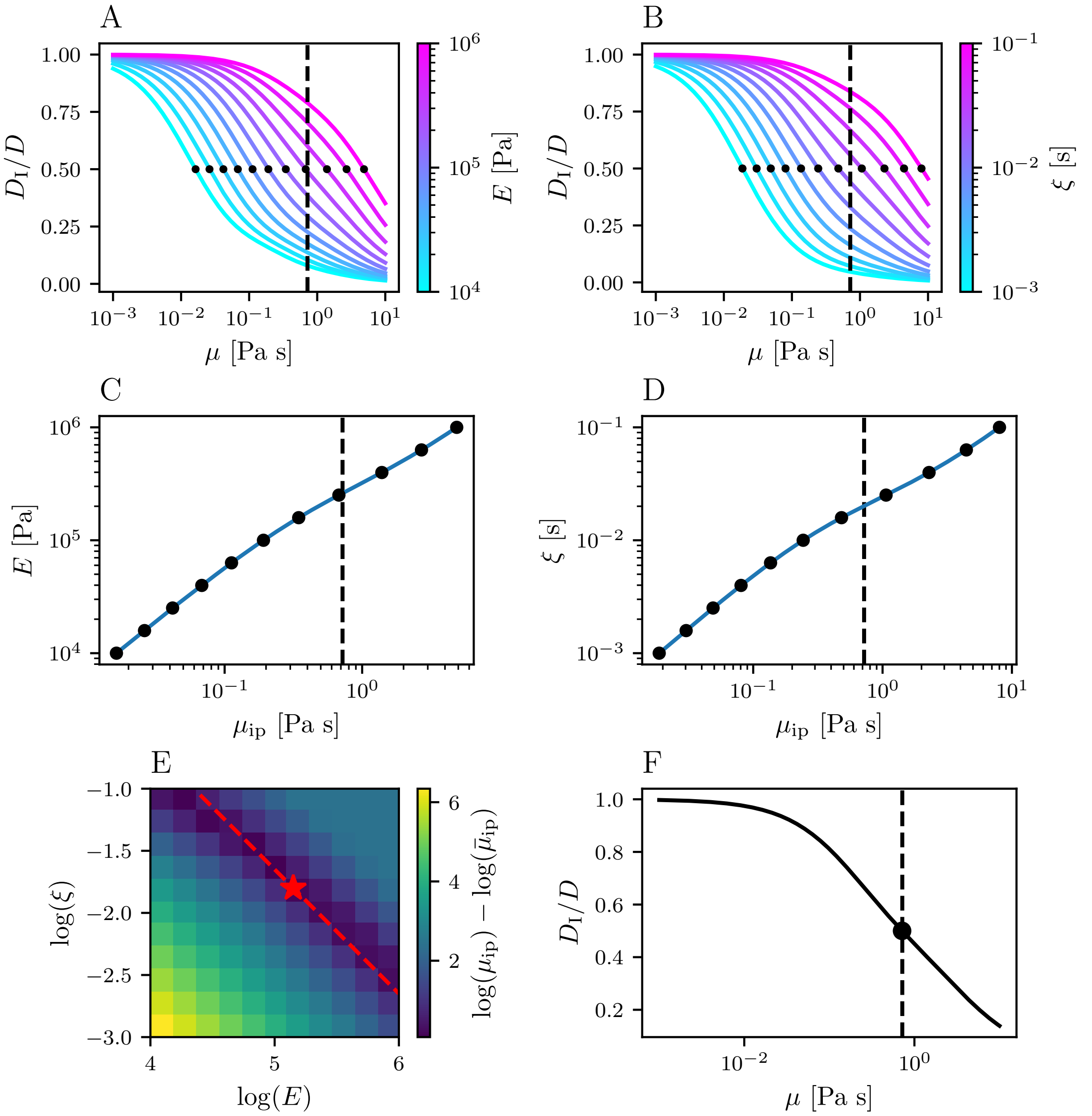

Figure 6.3: Simulation of *C. elegans*' gait transition across fluid viscosities ranging from $\mu \in [10^{-3}, 10^{1}]$ Pa s. Physical model parameters are extracted from Tab. 6.1. For each μ, the undulation frequency f and waveform parameters (λ, A) are determined from the fits to the experimental data presented in Fig. 6.1. (**A**): Ratio between internal and total dissipated energy per undulation cycle, D_I/D plotted against μ with fixed relative damping coefficient $\xi = 0.01$. The colored curves represent simulations for different values of Young's modulus E. The black dots mark each curve's inflection point μ_ip, defined as $D_\mathrm{I}/D = 0.5$. The black dashed line represents the inflection point $\bar{\mu}_\mathrm{ip}$ predicted from the experimental data showcased in Fig. 6.1. (**B**): Ratio D_I/D plotted against μ for fixed Young's modulus $E = 1 \times 10^{5}$ Pa. Each colored curve represents the simulation results for different values of the relative damping coefficients ξ. (**C**): Young's modulus E of each sigmoidal curve in panel A plotted against its inflection point μ_ip. Again, the black dashed line represents the experimental prediction $\bar{\mu}_\mathrm{ip}$. (**D**): Relative damping coefficient ξ of each sigmoidal curve in panel B plotted against its inflection point μ_ip. (**E**): Logarithmic error between experimentally predicted and simulated inflection point $\log(\mu_\mathrm{ip}) - \log(\bar{\mu}_\mathrm{ip})$ as a function of E and ξ. (**F**): Ratio D_I/D plotted against μ for an specific choice of material parameters $E = 10^{5.2}$ Pa and $\xi = 10^{-1.8}$ s that minimize logarithmic error shown in panel E.

at the end of this chapter. To validate our method, Fig. 6.3F showcases the ratio D_I/D as a function of μ for an exemplary optimal solution of E and ξ represented by the red star in panel E. We confirm that the model's inflection point μ_ip (black dot) closely aligns with the experimental prediction (vertical dashed line), as desired.

Naturally, the question arises: Which of the optimal solutions for E and ξ should we choose? Typically, measuring the bending rigidity of a material is easier than determining its damping coefficient. The former only requires force-deflection experiments, while the latter requires a dynamical mechanical analysis, e.g. by varying deflection speeds [13]. Therefore, we select the experimental estimate $B = 9.5 \times 10^{-14}\,\mathrm{N}^2\,\mathrm{m}$ by Fang Yen *et al.* [45] as our default value which yields a Young's modulus of $E = 10^{5.08}\,\mathrm{Pa}$. Based on our analysis in Fig. 6.3E, we assume that $\eta = 10^{3.35}\,\mathrm{Pa\,s}$, which yields a relative damping coefficient of $\xi = 10^{-1.73}\,\mathrm{s}$.

Given those values, we examine how the fluid viscosity influences the fastest and the most energy-efficient waveform of *C. elegans*. Following the same approach outlined in Section 5.3, we simulate undulation experiments covering the same viscosity range experimentally probed by Fang Yen *et al.* [45]. For each μ value within this range, we systematically vary the preferred undulation wavelength λ_0 and curvature amplitude A_0, covering the entire spectrum of plausible waveforms. Within this spectrum, we identify the worm's fastest waveform (λ_max, A_max) and its optimal waveform (λ_opt, A_opt) following the same approach as in Fig. 5.5. The optimal waveform is defined as the waveform that minimizes the worm's COT while maintaining a constant normalized swimming speed U/U_max. Here, U_max denotes the worm's maximum swimming speed in a given fluid environment. To analyse the trade-off between energy efficiency and swimming speed, we determine the worm's optimal waveform for normalized swimming speeds within the range $U/U_\mathrm{max} \in [0.3, 0.9]$.

To compare our model to experimental data by Fang Yen *et al.* [45], Fig. 6.4A displays the fastest wavelength λ_max (solid black), the optimal wavelength λ_opt (red band), and the experimental fit (dashed black). The colored curves within the red band represent different values of the normalized swimming U/U_max, illustrated by the colorbar at the bottom right. Notably, the band of optimal wavelengths is fairly narrow, which implies that λ_opt is approximately independent of the worm's swimming speed. The λ_opt band closely matches the fit of the experimental data, exhibiting a sigmoidal transition as μ increases. In contrast, the fastest wavelength λ_max does not align well with the experimental data, being significantly smaller in the low viscosity regime and showing only a slight decrease in more viscous fluids. This suggests that *C. elegans*' waveform is optimized for energy efficiency and not maximum speed.

This hypothesis is supported by Fig. 6.4B, which shows the fastest curvature amplitude A_max (solid black), optimal amplitude A_opt (red band), and the experimental fit (dashed black). Notably, the band of A_{opt} is significantly wider compared to that of λ_{opt}. Hence, across the entire μ range, our model predicts that *C. elegans* can modulate its swimming speed most efficiently by altering its curvature amplitude while maintaining a relatively constant wavelength. Comparing the experimental fit to A_{opt}, we find that *C. elegans* swims at a speed well below $U_{\max}$, ranging from $U/U_{\max} \in [0.3, 0.6]$ across the entire μ range. The increase in normalized swimming speed for high μ might be an attempt by *C. elegans* to compensate for the decrease in physical swimming speed caused by the lower undulation frequencies in more viscous fluids.

In Fig. 6.4C, we compare the worm's maximum angle attack $\psi_{\max}$ for both the fastest (solid black) and the optimal waveform (red band) with the experimental data (black rectangles). Consistent with panel B, the experimental measures fall within the band of optimal waveforms, corresponding to normalized swimming speed within the range of $U/U_{\max} \in [0.3.0.65]$. Furthermore, their values range from 45° to 55° which is significantly smaller than $\psi_{\max}$ of the fastest waveform, which is larger than 90° across the entire μ range. We stress that the maximum angle of attack $\psi_{\max}$ is not a good measure, and the average angle of attack $\bar{\psi}$ across the worm's body should be used instead. This is because the worm's net propulsion force is equivalent to the sum of propulsion forces generated by each individual body segment. Thus, to achieve maximum swimming speed, the average angle of attack must be close to the predicted optimum of 45° and not the maximum angle of attack. This can be seen in Fig. 6.4D, which shows the model worm's average angle of attack $\bar{\psi}$ for both the fastest (solid black) and the optimal waveform (red band). The average angle of attack $\bar{\psi}$ of the fastest waveform is approximately 50°, close to the theoretically predicted optimum. For slower swimming speeds within range $U/U_{\max} \in [0.3, 0.65]$, $\bar{\psi}$ falls within the range of 20° to 35°. This implies that *C. elegans* do not modulate their waveform to maintain an optimal angle of attack. Instead, they opt for a shallower body wave, characterized by smaller curvature amplitude and average angle of attack, to be more energy-efficient.

To illustrate the trade-off between swimming speed and energy efficiency, Fig. 6.4E displays the worm's normalized Cost of Transport $\text{COT}_{\text{opt}}/\text{COT}_{\max}$ as a function of μ. Here, COT_{opt} and $\text{COT}_{\max}$ represent the COT of the optimal and fastest waveform, respectively. Consistent with our discussion in Section 5.3.2, we find that the worm can opt for a waveform with a lower speed to reduce its COT. Note that the vertical gaps between the colored lines in Fig. 6.4E become smaller as the swimming speed decreases, which implies that efficiency gain diminishes. For speeds smaller than $U/U_{\max} = 0.3$ (yellow curve), our model predicts the efficiency gain to become negligible. Thus, there is no incentive for *C. elegans* to swim at a lower speed, which is consistent with the experimental observation.

Unfortunately, Fang-Yen *et al.* [45] did not measure the swimming speed of *C. elegans*.

However, there are two independent studies that measured the swimming speed of *C. elegans* in the low and intermediate viscosity regime [50, 126] under comparable experimental conditions. We refer to Appendix A.4.2 for a more detailed discussion. We conclude this chapter with a summary and critical discussion of the presented results.

6.3 Discussion

In this chapter, we assessed the performance of planar undulation gait *C. elegans* by comparing available experimental data against our model prediction. First, we focused on *C. elegans* swimming gait in water. Our specific objectives were twofold: firstly, to determine the operating regime of *C. elegans*, and secondly, to discern whether the undulation frequency of *C. elegans* is geared towards achieving maximum speed or being energy efficient. Using the available experimental data of the biomechanical properties of *C. elegans*, such as body length, cross-sectional radius, bending rigidity, internal damping coefficient, Poisson's ratio, and characteristic undulation frequency, we demonstrated that *C. elegans* operates in the pass-through regime close to the upper boundary to the low-pass regime. Moreover, its operating point is far to the left of the vertical part of the boundary pass-through regime. This implies that *C. elegans* body stiffness has evolved to facilitate undulatory locomotion in a more viscous environment than water. This is not surprising as *C. elegans* can be commonly found in moist soil, which is typically more viscous than water.

Using our model, we modulated *C. elegans*'s undulation frequency in water establishing a lower bound $f_{\text{min}} \approx 1.2\,\text{Hz}$ and upper bound $f_{\text{max}} \approx 11.0\,\text{Hz}$. To determine the lower bound, we used the estimate for the normalized Basal Metabolic Rate (BMR) $\text{BMR}/W_{\text{c}} \approx 0.5$ from Laranjeiro *et al.* [82]. By comparing *C. elegans* characteristic frequency $f_{\text{c}} = 1.71\,\text{Hz}$ to the values of the lower and upper bound, we conclude that *C. elegans* prioritizes energy efficiency rather than speed. We seek to understand the robustness of these results with respect to variations in the physical model parameters. The upper bound f_{max} is expected to be insensitive to changes in the worm's bending rigidity, cross-sectional radius, and body length. This is because changes in these parameters result in a horizontal shift of the worm's operating point, which is far to the left of the vertical boundary between the pass-through and low-pass regime. However, f_{max} will be sensitive to changes in the worm's relative damping coefficient ξ, with larger ξ values causing an upward shift of the worm's operating point toward the low-pass regime. Nevertheless, given that f_{max} only exhibits a logarithmic dependence on ξ, we are confident that $f_{\text{c}} \ll f_{\text{max}}$.

As we discussed in Section 5.2.1, the lower bound f_{min} is contingent on the BMR, which is assumed to be a constant in our model. However, Laranjeiro *et al.* [82] showed that the BMR of demobilized worms is significantly smaller in a liquid environment (M9 buffer

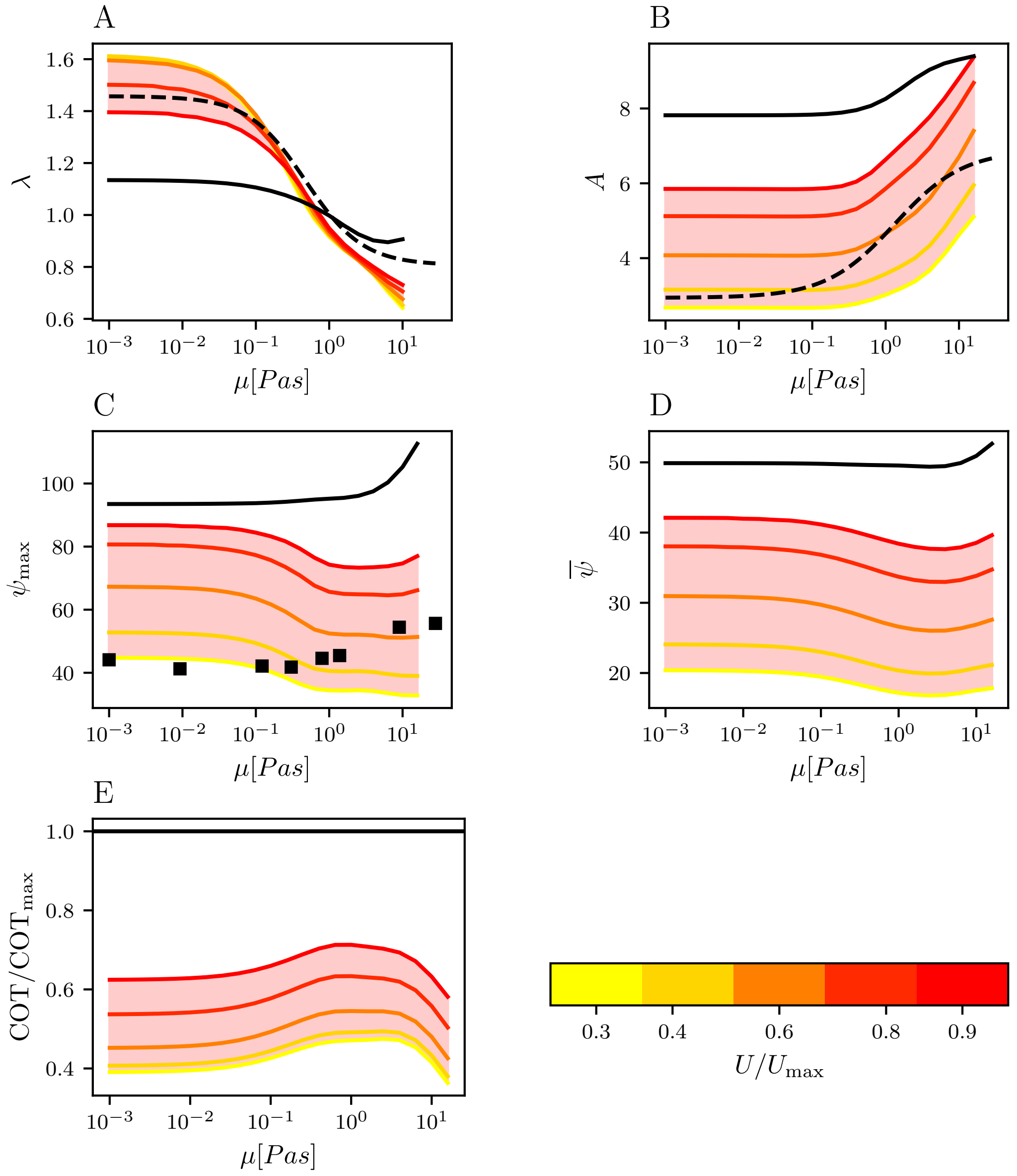

Figure 6.4: Comparison of *C. elegans*' gait transition with model predictions, assessing optimality. Physical model parameters are taken from Tab. 6.1. In all panels, the fastest waveform (λ_{max}, $A_{\max}$) is depicted by the solid black line, while the red band denotes the range of the most energy-efficient waveform (λ_{opt}, A_{opt}), referred to as optimal. Colored curves within the red band represent the optimal waveform for different values of the normalized swimming speed $U/U_{\max}$, as indicated by the bottom colorbar. Here, $U_{\max}$ corresponds to the maximum swimming speed associated with the fastest waveform (λ_{max}, $A_{\max}$). (**A**): Comparison of the fastest wavelength $\lambda_{\max}$ (black solid) and optimal wavelength λ_{opt} (red band) to the experimentally measured waveform (black dashed). (**B**): Comparison of fastest curvature amplitude $\lambda_{\max}$ (black solid) and the optimal curvature amplitude λ_{opt} (red band) to the experimentally measured curvature amplitude (black dashed). (**C**): Comparison of the maximum angle of attack $\psi_{\max}$ of the fastest (black solid) and optimal waveform (red band) to the experimentally measured maximum of angle attack (black dashed). (**D**): Average angle of attack of the fastest (black solid) and optimal waveform (red band) plotted against μ. (**E**): Ratio $\mathrm{COT}/\mathrm{COT}_{\max}$ between Cost of Transport associated with optimal waveform and fastest waveform (red band), plotted against μ.

solution) than on a solid substrate (agar). The authors argued that this discrepancy could be due to the differences in oxygen availability in liquid versus agar. To integrate the experimental estimate for the BMR into our model, we need to know the ratio between energy cost during undulatory locomotion and at rest, quantified by the MET. Given the MET, we can infer the worm's normalized dimensionless Basal Metabolic Rate, denoted as $\mathrm{BMR}/W_{\mathrm{c}}$, where W_{c} is the actuation work required during one undulation cycle. Laranjeiro *et al.* measured the energy cost of *C. elegans* in a generalized active state, encompassing a variety of locomotion patterns, including undulatory locomotion. Consequently, their measure is not directly applicable to our model but serves as a valuable reference point.

Hur *et al.* [69] developed a highly sensitive, bio-compatible calorimetric platform enabling time-resolved metabolic measurements and simultaneous optical imaging of individual worms. Hence, we envision the following experiment: measure the time-resolved metabolic activity of single worms in fluids with varying viscosities, covering the same range explored by Fang Yen *et al.* [45]. Conduct experiments with immobilized animals to test whether the BMR remains constant irrespective of the fluid's viscosity. Conduct experiments with free-moving animals and identify time epochs in which the worm displays planar undulatory locomotion. Using these epochs, estimate the MET for undulatory locomotion as a function of the fluid's viscosity. Those measures would allow us to derive a lower bound for the swimming speed, undulation frequency, and waveforms within a specified environment, which can be compared to available experimental data.

This brings us to the second part of our discussion, where we discuss our analysis of the continuous gait transition exhibited by *C. elegans* when exposed to more viscous fluid environments. As we increase the fluid viscosity, our model displays a transition from a regime where the worm's energy cost is dominated by internal friction to a regime where external friction takes precedence, consistent with the observation by Fang Yen *et al.* [45]. As we outlined in Section 5.3.2 of the previous chapter, this transition is characterized by the ratio between energy loss due to internal and external (fluid) dissipation, which exhibits a sigmoidal trend. This sigmoidal trend is defined by its inflection point and slope factor, which are mainly determined by the internal viscosity η. This stems from the fact that internal dissipation is directly proportional to η, while external dissipation is proportional to μ. Consequently, it is the ratio between η and μ that determines whether internal or external dissipation dominates in a given fluid environment. Therefore, we expect our results to be robust irrespective of the type of model that is used to describe the viscoelastic properties of the worm's passive body material and the fluid-structure interaction.

However, the model details will influence the shape of the most efficient waveform that minimizes the worm's COT. Particularly in low-viscosity fluids where internal friction dominates, we expect the shape of the most efficient waveform to be influenced by the viscoelastic properties of the worm material. Conversely, in high-viscosity fluids, where external friction dominates, we expect it to depend on the details of the fluid-structure interaction model. Therefore, our model details will likely influence the transition range of the most efficient wavelength and curvature amplitude from low to high fluid viscosities. However, a systematic exploration of alternative models, extending beyond the simplicity of a simple homogeneous Kelvin-Voigt material combined with resistive-force theory, is beyond the scope of this thesis. In Chapter 7, we discuss potential improvements over resistive-force theory, including considerations such as slender body theory and regularized Stokes flow [36, 72].

Nonetheless, despite our model's simplicity, it predicts an optimal waveform that displays a sigmoidal transition, showing good agreement with experimental observations. By fitting the physical model parameters to the experimental data, we obtain an optimal value for the worm's internal viscosity $\eta = 2.24 \times 10^3\,\mathrm{Pa\,s}$. Assuming a circular cross-section with radius $R_{\mathrm{max}} = 32\,\mu\mathrm{m}$ made of homogeneous worm material, this value translates to an internal damping coefficient of $\tilde{B} = 2.00 \times 10^{-15}\,\mathrm{N\,m^2\,s}$. This value for $\tilde{B}$ is a factor four larger compared to the upper bound $5 \times 10^{-16}\,\mathrm{N\,m^2\,s}$ predicted by Fang Yen *et al.* [45].

In [45], the authors used a simplified one-dimensional inextensible rod equation to describe the worm's body, which could explain why they predicted a different value for $\tilde{B}$. Their equation can be considered as the leading-order approximation in the limit of small body wave amplitudes. Specifically, it neglects the internal tension generated by the worm's passive body material and assumes the centreline tangent to be equivalent to the swimming direction [83]. However, in general, *C. elegans* body wave amplitude cannot be assumed to be small relative to its body length [18]. To test this assumption, we could fit our model to the experimental data from Fang Yen *et al.*'s deflection relaxation time scale experiments and check whether this procedure yields an internal damping coefficient consistent with our model prediction. This would necessitate simulating deflection release experiments clamping the worm at one end while applying an external force on the other, which is beyond the scope of this thesis.

To conclude, our study suggests that undulatory gait modulation of *C. elegans* in response to varying environmental conditions is primarily driven by energy considerations rather than swimming speed. We propose two key mechanisms to support this hypothesis. Firstly, we propose that *C. elegans* lower their undulation frequency in more viscous environments to align their actuation time scale (undulation frequency) with their body's response time, facilitating more energy-efficient swimming. Secondly, we propose that it modulates its waveform to maximize energy efficiency, depending on whether its energy cost is dominated by internal or external friction. However, these results are based on simplifying assumptions. We assume that internal losses can be effectively described in terms of a viscoelastic material. Yet, it is evident that there are additional sources of internal friction within the worm's body. For example, the worm's body wall muscles, commonly modeled as a spring-damper system [23, 42, 71], contribute to internal friction during contraction and relaxation processes. Furthermore, the movement of fluids within the worm's body, such as circulation or flow within the pseudocolumn, will generate internal friction. The impact of these additional energy losses on our results depends on their relative magnitude and whether their contribution is affected by the gait transition. Therefore, while our findings appear promising, it is necessary to quantify and incorporate these complexities, if necessary, to rigorously test the validity of our hypothesis.

Chapter 7

Conclusion and Outlook

This chapter summarizes the findings of this thesis (Section 7.1) and subsequently provides a critical discussion with an indication of future research perspective (Section 7.2)

7.1 Conclusion

This research aimed to provide insight into the underlying reasons that govern gait selection and modulation in slender limbless undulating microswimmers. To achieve this, we developed a biomechanical microswimmer model based on Cosserat rod theory. Through numerical simulations of our model, we predict that gait modulation enables a microswimmer to prioritize between speed and energy efficiency. Based on the model swimmer's biomechanical properties and Basal Metabolic Rate, we derive a plausible range of undulation frequencies, swimming speed, and waveforms. Within this range, the lower limit represents the most efficient undulation gait, whereas the upper limit achieves maximum swimming speed, highlighting a continuous trade-off between speed and efficiency. Consequently, by comparing the model and experiment, we can infer whether a microswimmer selects an undulation gait that favors efficiency, speed, or a balance between the two. Leveraging this insight, we conducted a quantitative comparison between our model and available experimental data on *C. elegans*, leading to the following hypotheses:

1. *C. elegans* swimming gait optimizes for energy efficiency and not for swimming speed.
2. *C. elegans* continuous gait transition from low to high fluid viscosities optimizes for energy efficiency.
    (a) In low viscosities, internal friction dominates the worm's energy cost, which makes a long wavelength and small curvature amplitude more efficient.

(b) In high viscosities, external friction dominates the worm's energy cost, which makes a short wavelength and larger curvature amplitude more efficient.

From a modeling perspective, two notable observations can be made: Firstly, to bound the undulation parameters from below, the Basal Metabolic Rate must be included as an additional energy cost to the model, as it punishes excessively slow swimming speeds. Secondly, the ratio between internal viscosity and fluid viscosity determines whether the swimmer's energy cost is dominated by internal friction or external friction. Consequently, the value of the internal viscosity determines the transition region of the gait parameters. Using this insight, we predict a value of $\tilde{B} = 2.00 \times 10^{-15}\,\mathrm{N}^2\,\mathrm{m\,s}$ for the internal damping coefficient of *C. elegans*' body material.

While this study primarily focused on the undulatory locomotion of slender microswimmers, the concepts discussed could apply more broadly to other swimming organisms. Regardless of the organism of interest, the study of gait optimality requires the definition of objectives and performance metrics. In this thesis, we defined performance based on two primary objectives: speed and energy efficiency. In many instances, determining an organism's locomotion speed is easier than its energy expenditure. In the special case of swimming gaits, the locomotion speed can be determined without explicitly modeling the biomechanics of the swimmer's body, as we outlined in Section 2.1. Moreover, if the swimmer's shape sequence is known, then its swimming speed can, in principle, be predicted with very high accuracy by solving the Navier-Stokes equation. In contrast, estimating the swimmer's energy expenditure requires a biomechanical representation of its body, which can include arbitrary levels of complexity, ranging from basic to highly detailed models. Hence, modeling the microswimmer biomechanics and estimating its energy expenditure during locomotion emerged as one of the primary challenges in this work. It was not only challenging from a modeling standpoint but also conceptually. Thus, to convey the conceptual insights gained from this research, we revisit our car analogy one last time.

Imagine Jon and Jen who are driving from Leeds to the Yorkshire Dales to go for a long walk in the countryside. They make a short stop on top of the Buttertubs Pass, offering a breathtaking view of the surrounding dales and valleys. Jen breaks the silence, turning to Jon, who is at the wheel. "Jon, can you tell me how much energy we spent driving this far"? After thinking for a while, Jon responds, "Certainly. I can check the fuel gauge. We filled the tank before leaving, and now it's half empty; this means we've used 25 liters so far. The energy we spend must be equal to the chemical energy stored in this amount of fuel," and he starts his calculation. Jen, who is an expert on animal locomotion, replies. "That's a great idea, Jon, but I think there is another way, which involves the friction forces at play here. Let's say I account for the friction between the car's exterior and the air, the friction at the contact between wheels and road, the internal friction between all the moving parts in the engine, and the friction created by the brakes — what if I add up all the energy the car lost due to these friction forces since we left the petrol station in Leeds?" After a moment of contemplation, Jon says: "Aha, then you must get the same figure as me because energy must be conserved. "Exactly!" affirms Jen, and she starts her own calculation.

Now, do Jon and Jen's calculations genuinely yield the same figure for the car's energy expenditure? Unfortunately, the answer is no. This is because friction is everywhere, and in most practical cases, it is impossible to account for all sources of friction within a system. This is especially true for biological systems due to the inherent complexity of their structural components. So, a better question to ask is: How close will Jen's figure be to that of Jon? The answer to this question depends on two factors. Firstly, has Jen identified all relevant sources of friction within the system? Relevant sources are those responsible for the bulk of the energy loss. Secondly, how accurate is her model to estimate the energy loss associated with these sources?

Unfortunately, biological organisms do not have a fuel gauge, making it more challenging to assess their energy budget. In this thesis, we adopted Jen's approach to estimate the energy expenditure of a slender undulating microswimmer immersed in a Newtonian fluid during undulatory locomotion, specifically focusing on the model organism *C. elegans*. Like Jen, we should ask ourselves two questions. Did we identify the most relevant sources of friction contributing to the swimmer's energy cost, and how accurately does our model describe them? In our model, we included two sources of friction that contribute to the swimmer's energy expenditure: external friction with the surrounding fluid and internal friction caused by the deformations of the swimmer's passive body. To estimate the external friction, we used resistive-force theory (RFT) to describe the fluid-body interaction. To estimate the internal friction, we modeled the swimmer's body as a homogeneous linear viscoelastic rod. These are, of course, both simplifying assumptions.

Nevertheless, despite its simplicity, our model was able to produce realistic undulatory swimming across a wide range of scenarios, providing insights into the underlying reasons for gait selection and modulation of undulating microswimmers. Importantly, it demonstrates how the balance between internal body friction and external friction with the surrounding fluid shapes gait optimality. However, there is still a need for refinements and extensions to our model, which will be discussed in the next section.

7.2 Outlook

There are many possible directions to apply and refine the microswimmer model presented and characterized in this thesis. First, we are going to discuss possible applications that do not require modifications to the current version of the model. Subsequently, we motivate and detail possible model refinements and extensions.

During our exploration of gait modulation in Chapter 5, we showed that a swimmer can prioritize between speed and energy efficiency by modulating its frequency and waveform. However, we did not explore which modulation, either frequency or waveform, enables a more efficient trade-off. To explore this question, we can determine the paths in the three-dimensional parameter space spanned by the undulation frequency, wavelength, and curvature amplitude that yield the most efficient trade-off between speed and energy efficiency. Subsequently, we can examine whether microswimmers modulate their undulation gait along this optimal path in static environments. Unfortunately, the experimental data on *C. elegans* gait modulation in a given context is very limited [40, 70]. It would be worthwhile to investigate whether *C. elegans* have distinct undulation gears that either prioritize speed or efficiency.

So far, we have assumed that curvature body waves can be described as sinusoidal waves traveling with constant amplitude and wavelength. However, multiple studies have shown that a swimmer's body curvature during undulatory locomotion cannot always be accurately described by a sinusoidal wave [70, 106, 124]. For instance, studies have demonstrated that the amplitude of *C. elegans*' curvature wave decreases from head to tail [18, 22, 45, 126]. It is unclear whether this asymmetry solely results from its body anatomy, considering that *C. elegans* has stronger head-neck muscles [6] compared to the posterior part of their body, or if it has a functional purpose. Using our model, we compare the performance between gaits with and without decreasing curvature amplitude. Alternatively, a more general approach involves parameterizing the spatial profile of the actuation torque using a finite set of parameters, allowing for a diversity of waveforms [52, 53]. Optimizing those parameters with respect to a loss function that is defined in terms of the swimmer's speed, energy efficiency, and other objectives would allow for a more rigorous exploration of gait optimality, moving beyond the constraints of a specific waveform model. Such an approach would allow us to predict whether the optimal waveform demonstrates a smooth transition when the weights of the competing objectives in the loss function are varied.

Furthermore, in this thesis, we exclusively focused on planar undulatory locomotion. However, as we discussed in Section 2.4, *C. elegans* display a broad range of locomotion patterns such as reversals [39, 56], turning for steering [27, 106, 134], rolling maneuvers to 3D reorientation, [20], coiling behavior [70, 105]. Given that our model formulation allows for deformation in a three-dimensional, it is well suited to explore these locomotion patterns from the viewpoint of optimality. A promising starting point would be the turn maneuvers, as their objective can be clearly defined in terms of turning angle. We have already demonstrated that our model is capable of generating turns when actuated according to the piecewise sinusoidal linear curvature model proposed by Padmanabhan *et al*. [106]. However, more work is required to compare the performance of different turn maneuvers based on their energy efficiency. For a more comprehensive approach, we could drive our model with an actuation torque that represents body curvatures constructed through superpositions of eigenworms. Eigenworms refer to the principle components of the worm's shape space, typically calculated from large datasets. The eigenworms hold particular significance as different locomotion maneuvers can be associated with changes in the principle eigenworms, which make up the worm's current posture [70, 124]. Such an approach could enable us to infer the actuation patterns associated with distinct locomotion patterns, providing insights that could be valuable for neuromuscular modeling.

Having outlined potential future applications of our model, we conclude by discussing some of its limitations and propose possible refinements and extensions. One such limitation lies in our use of resistive-force theory (RFT) to describe the fluid-body interaction. While RFT provides a useful framework for approximating hydrodynamic forces and torques that act on the swimmer's body, it assumes that each body segment can be treated independently. However, whenever a body segment moves or rotates, then it sets off a fluid flow that imparts hydrodynamic stresses on all other segments and vice versa. This non-local coupling leads to corrections in the fluid drag force experienced by each segment and can be accounted for by more sophisticated theories such as slender-body theory (SBT) and regularized Stokes flow (RSF) [35, 36, 104].

SBT was initially developed by Lighthill [86] and Johnson [72] in the 1970s to describe the Stokes flow around an active, curved, slender body. Almost four decades later, Koens & Lauga [78] revisited this problem. They expanded the exact but implicit flow solution provided by the boundary integral method [142] in orders of the rod's slenderness parameter ε and showed that it contains Johnson's SBT. Following the same approach, Garg & Kumar [51] extended Koens & Lauga's results to the more general case of a Cosserat rod. In SBT, the fluid drag force that acts on a particular body segment is defined in terms of a convolution integral of the body's centreline velocity along its length. For each body segment, the convolution kernel is contingent on the swimmer's relative body shape. Consequently, the kernel must be recalculated for each segment anew. Nonetheless, because the relationship between fluid drag line distribution and centreline velocity is linear, it can be expressed as a matrix-vector multiplication in discretized space. Thus, in principle, it can be directly incorporated into the discretized weak form of our model equations, yielding a monolithic scheme that includes SBT. We have already demonstrated the viability of this approach. However, as the SBT matrix is contingent on the swimmer's body shape, it needs to be recalculated at every time step, which is computationally very demanding. This makes large parameter sweeps unfeasible, necessitating further refinement. However, for precise quantitative predictions of swimming speed and energy expenditure, an accurate fluid dynamics model is essential. This is especially true in the regime where the swimmer's energy cost is dominated by external friction.

Beyond the fluid dynamics model, there is a lot of opportunity for improving the biomechanical model used to describe the swimmer's body. So far, our model only considers the internal losses due to the viscoelastic properties of the swimmer's passive body material. However, in microswimmers, local bending is achieved through the contractile forces generated by molecular motors or muscles, respectively. These continuous contraction-relaxation processes generate friction, which contributes to the organism's internal energy loss. Muscles are often represented as spring-damper systems [23, 42, 59, 131], which exhibit dissipative behavior. Hence, the dissipative energy within the muscles can be calculated from the muscle model's equations and subsequently incorporated into our model. This requires combining our Cosserat rod model with muscle units responsible for the generation of the actuation torque along the worm's body. A model of this nature has already been introduced in Denham *et al.* [41, 42], providing a solid foundation for further research. However, for a consistent description, it is crucial to understand the relationship between the contractile muscle forces and resulting effective actuation. This relationship must be grounded in the mechanical properties of the worm's body to ensure accurate scaling of the contractile muscle and friction forces. This highlights a disadvantage of rod models as they do not allow for the direct integration of contractile muscle forces. This is because rods are composed of rigid cross-sections, which can not be locally deformed by muscle forces. A direct integration of muscle forces would require a 3D continuum model of the swimmer's body, which would be computationally very expensive, as it does not take advantage of the worm's slender body geometry. However, it would allow us to explore how contractile muscles achieve local bending.

To conclude, we note that this thesis involved simulating tens of thousands of undulation experiments, made possible by the computational efficiency of our model. This efficiency is attributed to the simplicity (locality) of our hydrodynamic model (RFT) and the one-dimensional parameterization of the swimmer's body in terms of a Cosserat rod. Hence, we believe that rod models have their merit by being computationally efficient while capturing essential features of undulatory locomotion. Nonetheless, exploring the impact of the outlined refinements and extensions to our model presents an exciting outlook for future research.

References

[1] R. McNeill Alexander. *Optima for Animals*. 1996. DOI: `10.2307/j.ctv173f0gj`.

[2] R. McNeill Alexander. *Principles of animal locomotion*. 2013. DOI: `10.1644/1545-1542(2004)085<0584:br>2.0.co;2`.

[3] Márcio de Almeida Mendes, Inácio da Silva, Virgílio Ramires, Felipe Reichert, Rafaela Martins, Rodrigo Ferreira, and Elaine Tomasi. "Metabolic equivalent of task (METs) thresholds as an indicator of physical activity intensity". In: *PLoS ONE* 13.7 (July 2018). ISSN: 19326203. DOI: `10.1371/journal.pone.0200701`.

[4] Martin S. Alnaes, Jan Blechta, Johan Hake, August Johansson, Benjamin Kehlet, Anders Logg, Chris Richardson, Johannes Ring, Marie E. Rognes, and Garth N. Wells. "The FEniCS Project Version 1.5". In: *Archive of Numerical Software* 3.100 (2015), pp. 9–23. ISSN: 2197-8263.

[5] Zeynep F. Altun and David H. Hall. *Introduction. In WormAtlas*. 2009. DOI: `doi:10.3908/wormatlas.1.1`.

[6] Zeynep F. Altun and David H. Hall. *Muscle system, introduction*. 2009. DOI: `doi:10.3908/wormatlas.1.6`.

[7] Zeynep F. Altun and David H. Hall. *Nervous system, general description*. 2011. DOI: `doi:10.3908/wormatlas.1.18`.

[8] Alexandros Anastasiadis, Laura Paez, Kamilo Melo, Eric D. Tytell, Auke J. Ijspeert, and Karen Mulleners. "Identification of the trade-off between speed and efficiency in undulatory swimming using a bio-inspired robot". In: *Scientific Reports* 13.1 (2023). ISSN: 20452322. DOI: `10.1038/s41598-023-41074-9`.

[9] Stuart S. Antman. *Nonlinear problems of elasticity*. Vol. 107. 2005, pp. 1–835. ISBN: 0387208801. DOI: `10.1007/978-1-4757-4147-6{\_}1`.

[10] Abhishek Arora, Ajeet Kumar, and Paul Steinmann. “A computational approach to obtain nonlinearly elastic constitutive relations of special Cosserat rods”. In: *Computer Methods in Applied Mechanics and Engineering* 350 (2019), pp. 295–314. ISSN: 00457825. DOI: `10.1016/j.cma.2019.02.032`.

[11] Akira Azuma. *The Biokinetics of Flying and Swimming, Second Edition*. 2006. DOI: `10.2514/4.862502`.

[12] Matilda Backholm, Alexandra K. S. Kasper, Rafael D. Schulman, and William S. Ryu. “The effects of viscosity on the undulatory swimming dynamics of C. elegans”. In: 091901.September (2015). DOI: `10.1063/1.4931795`.

[13] Matilda Backholm, William S. Ryu, and Kari Dalnoki-Veress. “Viscoelastic properties of the nematode Caenorhabditis elegans, a self-similar, shear-thinning worm”. In: *Proceedings of the National Academy of Sciences of the United States of America* 110.12 (2013), pp. 4528–4533. ISSN: 00278424. DOI: `10.1073/pnas.1219965110`.

[14] Rahul Bale, Anup A. Shirgaonkar, Izaak D. Neveln, Amneet Pal Singh Bhalla, Malcolm A. Maciver, and Neelesh A. Patankar. “Separability of drag and thrust in undulatory animals and machines”. In: *Scientific Reports* 4 (2014). ISSN: 20452322. DOI: `10.1038/srep07329`.

[15] Cornelia I. Bargmann and H. Robert Horvitz. “Chemosensory neurons with overlapping functions direct chemotaxis to multiple chemicals in C. elegans”. In: *Neuron* 7.5 (1991), pp. 729–742. ISSN: 08966273. DOI: `10.1016/0896-6273(91)90276-6`.

[16] George K. Batchelor. “Introduction to fluid mechanics”. In: *Modeling and Simulation in Science, Engineering and Technology* 56 (2012), pp. 427–457. ISSN: 21643725. DOI: `10.1007/978-0-8176-8352-8{\_}23`.

[17] George K. Batchelor. “Slender-body theory for particles of arbitrary cross-section in Stokes flow”. In: *Journal of Fluid Mechanics* 44.3 (1970), pp. 419–440. ISSN: 14697645. DOI: `10.1017/S002211207000191X`.

[18] Stefano Berri, Jordan H. Boyle, Manlio Tassieri, Ian A. Hope, and Netta Cohen. “Forward locomotion of the nematode C. elegans is achieved through modulation of a single gait”. In: *HFSP Journal* 3.3 (2009), pp. 186–193. ISSN: 1955205X. DOI: `10.2976/1.3082260`.

[19] Andrew A. Biewener and Sheila N. Patek. *Animal locomotion*. 2018. DOI: `10.1093/camqtly/xiv.2.145`.

[20] Alejandro Bilbao, Amar K. Patel, Mizanur Rahman, Siva A. Vanapalli, and Jerzy Blawzdziewicz. "Roll maneuvers are essential for active reorientation of Caenorhabditis elegans in 3D media". In: *Proceedings of the National Academy of Sciences of the United States of America* 115.16 (2018), E3616–E3625. ISSN: 10916490. DOI: `10.1073/pnas.1706754115`.

[21] Alejandro Bilbao, Eligiusz Wajnryb, Siva A. Vanapalli, and Jerzy Blawzdziewicz. "Nematode locomotion in unconfined and confined fluids". In: *Physics of Fluids* 25.8 (2013). ISSN: 10706631. DOI: `10.1063/1.4816718`.

[22] Jordan H. Boyle. "C. elegans locomotion: an integrated approach". PhD thesis. University of Leeds, 2009.

[23] Jordan H. Boyle, Stefano Berri, and Netta Cohen. "Gait modulation in C. elegans: An integrated neuromechanical model". In: *Frontiers in Computational Neuroscience* 6.FEBRUARY 2012 (2012), pp. 1–15. ISSN: 16625188. DOI: `10.3389/fncom.2012.00010`.

[24] John Brackenbury. "Fast locomotion in caterpillars". In: *Journal of Insect Physiology* 45.6 (1999), pp. 525–533. ISSN: 00221910. DOI: `10.1016/S0022-1910(98)00157-7`.

[25] John Brackenbury. "Locomotory modes in the larva and pupa of Chironomus plumosus (Diptera, Chironomidae)". In: *Journal of Insect Physiology* 46.12 (2000), pp. 1517–1527. ISSN: 00221910. DOI: `10.1016/S0022-1910(00)00079-2`.

[26] Sydney Brenner. "The genetics of Caenorhabditis elegans." In: *Genetics* 77.1 (1974), pp. 71–94. ISSN: 00166731. DOI: `10.1093/genetics/77.1.71`.

[27] Onno D. Broekmans, Jarlath B. Rodgers, William S. Ryu, and Greg J. Stephens. "Resolving coiled shapes reveals new reorientation behaviors in C. elegans". In: *eLife* 5.September (2016). ISSN: 2050084X. DOI: `10.7554/eLife.17227`.

[28] Charles J. Brokaw. "Effects of viscosity and ATP concentration on the movement of reactivated sea urchin sperm flagella". In: *Journal of Experimental Biology* 62.3 (1975), pp. 701–719. ISSN: 00220949. DOI: `10.1242/jeb.62.3.701`.

[29] Mayank Chadha and Michael D. Todd. "An introductory treatise on reduced balance laws of Cosserat beams". In: *International Journal of Solids and Structures* 126-127.August (2017), pp. 54–73. ISSN: 00207683. DOI: `10.1016/j.ijsolstr.2017.07.028`.

[30] Martin Chalfie, John E. Sulston, John G White, Eileen Southgate, J. Nichol Thomson, and Sydney Brenner. "The neural circuit for touch sensitivity in Caenorhabditis

elegans". In: *Journal of Neuroscience* 5.4 (1985), pp. 956–964. ISSN: 02706474. DOI: `10.1523/jneurosci.05-04-00956.1985`.

[31] Andy J. Chang, Nikolas Chronis, David S. Karow, Michael A. Marletta, and Cornelia I. Bargmann. "A distributed chemosensory circuit for oxygen preference in C. elegans". In: *PLoS Biology* 4.9 (2006), pp. 1588–1602. ISSN: 15457885. DOI: `10.1371/journal.pbio.0040274`.

[32] Beth L. Chen, David H. Hall, and Dmitri B. Chklovskii. "Wiring optimization can relate neuronal structure and function". In: *Proceedings of the National Academy of Sciences of the United States of America* 103.12 (Mar. 2006), pp. 4723–4728. ISSN: 00278424. DOI: `10.1073/pnas.0506806103`.

[33] Netta Cohen and Thomas Ranner. "A New Computational Method A Model of C. elegans Biomechanics: Insights into Elasticity and Locomotion Performance". In: *Angewandte Chemie International Edition, 6(11), 951–952.* 465 (2017), pp. 106–111. ISSN: 15281132.

[34] Kevin M. Collins, Addys Bode, Robert W. Fernandez, Jessica E. Tanis, Jacob C. Brewer, Matthew S. Creamer, and Michael R. Koelle. "Activity of the C. elegans egg-laying behavior circuit is controlled by competing activation and feedback inhibition". In: *eLife* 5.NOVEMBER2016 (2016). ISSN: 2050084X. DOI: `10.7554/eLife.21126`.

[35] Ricardo Cortez. "Regularized Stokeslet segments". In: *Journal of Computational Physics* 375 (2018), pp. 783–796. ISSN: 10902716. DOI: `10.1016/j.jcp.2018.08.055`.

[36] Ricardo Cortez, Lisa Fauci, and Alexei Medovikov. "The method of regularized Stokeslets in three dimensions: Analysis, validation, and application to helical swimming". In: *Physics of Fluids* 17.3 (2005). ISSN: 10706631. DOI: `10.1063/1.1830486`.

[37] Richard Courant and David Hilbert. *Methods of mathematical physics: partial differential equations*. John Wiley & Sons, 2008.

[38] Raymond G. Cox. "The motion of long slender bodies in a viscous fluid. Part 1. General theory". In: *Journal of Fluid Mechanics* 44.04 (1970), p. 791.

[39] Neil A. Croll. "Components and patterns in the behaviour of the nematode Caenorhabditis elegans". In: *Journal of Zoology* 176.2 (1975), pp. 159–176. ISSN: 14697998. DOI: `10.1111/j.1469-7998.1975.tb03191.x`.

[40] Lan Deng, Jack E. Denham, Charu Arya, Omer Yuval, Netta Cohen, and Gal Haspel. "Inhibition underlies fast undulatory locomotion in caenorhabditis elegans". In: *eNeuro* 8.2 (2021), pp. 1–23. ISSN: 23732822. DOI: `10.1523/ENEURO.0241-20.2020`.

[41] Jack Denham. "Neuromechanical modelling of C. elegans locomotion: proprioceptive feedback in the ventral nerve cord". PhD thesis. University of Leeds, 2021.

[42] Jack E. Denham, Thomas Ranner, and Netta Cohen. "Signatures of proprioceptive control in Caenorhabditis elegans locomotion". In: *Philosophical Transactions of the Royal Society B: Biological Sciences* 373.1758 (2018), pp. 26–28. ISSN: 14712970. DOI: `10.1098/rstb.2018.0208`.

[43] Rémi Dreyfus, Jean Baudry, Marcus L. Roper, Marc Fermigier, Howard A. Stone, and Jérôme Bibette. "Microscopic artificial swimmers". In: *Nature* 437.7060 (2005), pp. 862–865. ISSN: 14764687. DOI: `10.1038/nature04090`.

[44] Olivia Du Roure, Anke Lindner, Ehssan N. Nazockdast, and Michael J. Shelley. *Dynamics of flexible fibers in viscous flows and fluids*. 2019. DOI: `10.1146/annurev-fluid-122316-045153`.

[45] Christopher Fang-Yen, Matthieu Wyart, Julie Xie, Risa Kawai, Tom Kodger, Sway Chen, Quan Wen, and Aravinthan D.T. Samuel. "Biomechanical analysis of gait adaptation in the nematode Caenorhabditis elegans". In: *Proceedings of the National Academy of Sciences of the United States of America* 107.47 (2010), pp. 20323–20328. ISSN: 10916490. DOI: `10.1073/pnas.1003016107`.

[46] B. M. Friedrich, I. H. Riedel-Kruse, J. Howard, and F. Jülicher. "High-precision tracking of sperm swimming fine structure provides strong test of resistive force theory". In: *Journal of Experimental Biology* 213.8 (2010), pp. 1226–1234. ISSN: 00220949. DOI: `10.1242/jeb.039800`.

[47] Henry C. Fu, Thomas R. Powers, and Charles W. Wolgemuth. "Theory of swimming filaments in viscoelastic media". In: *Physical Review Letters* 99.25 (2007). ISSN: 00319007. DOI: `10.1103/PhysRevLett.99.258101`.

[48] Yuan-cheng Fung. *Biomechanics. Mechanical Properties of Living Tissues.* 2013. DOI: `10.1115/1.3162171`.

[49] Eamonn A. Gaffney, Hermes Gadêlha, David J. Smith, John R. Blake, and Jackson C. Kirkman-Brown. "Mammalian sperm motility: Observation and theory". In: *Annual Review of Fluid Mechanics* 43 (2011), pp. 501–528. ISSN: 00664189. DOI: `10.1146/annurev-fluid-121108-145442`.

[50] David A. Gagnon, Nathan C. Keim, and Paulo E. Arratia. “Undulatory swimming in shear-thinning fluids: Experiments with Caenorhabditis elegans”. In: *Journal of Fluid Mechanics* 758 (2014), R3. ISSN: 14697645. DOI: 10.1017/jfm.2014.539.

[51] Mohit Garg and Ajeet Kumar. “A slender body theory for the motion of special Cosserat filaments in Stokes flow”. In: February (2022), pp. 1–34. DOI: 10.1177/10812865221083323.

[52] Mattia Gazzola, Levi H. Dudte, Andrew G. McCormick, and Lakshminarayanan Mahadevan. “Forward and inverse problems in the mechanics of soft filaments”. In: *Royal Society Open Science* 5.6 (2018). ISSN: 20545703. DOI: 10.1098/rsos.171628.

[53] Mattia Gazzola, Wim M. Van Rees, and Petros Koumoutsakos. “C-start: Optimal start of larval fish”. In: *Journal of Fluid Mechanics* 698 (May 2012), pp. 5–18. ISSN: 14697645. DOI: 10.1017/jfm.2011.558.

[54] Herbert Goldstein, Charles Poole, John Safko, and Stephen R. Addison. “Classical Mechanics, 3rd ed.” In: *American Journal of Physics* 70.7 (July 2002), pp. 782–783. ISSN: 0002-9505. DOI: 10.1119/1.1484149.

[55] James Gray and Gregory J. Hancock. “The Propulsion of Sea-Urchin Spermatozoa”. In: *Journal of Experimental Biology* 32.4 (1955), pp. 802–814. ISSN: 0022-0949. DOI: 10.1242/jeb.32.4.802.

[56] James Gray and Hans-Werner Lissmann. “The Locomotion of nematodes.” In: *The Journal of experimental biology* 41 (1964), pp. 135–154. ISSN: 00220949. DOI: 10.1242/jeb.41.1.135.

[57] Carlos F. Guimarães, Luca Gasperini, Alexandra P. Marques, and Rui L. Reis. “The stiffness of living tissues and its implications for tissue engineering”. In: *Nature Reviews Materials* 5.5 (2020), pp. 351–370. ISSN: 20588437. DOI: 10.1038/s41578-019-0169-1.

[58] Zengcai V. Guo and Lakshminarayanan Mahadevan. “Limbless undulatory propulsion on land”. In: *Proceedings of the National Academy of Sciences of the United States of America* 105.9 (2008), pp. 3179–3184. ISSN: 00278424. DOI: 10.1073/pnas.0705442105.

[59] Christina Hamlet, Lisa J. Fauci, and Eric D. Tytell. “The effect of intrinsic muscular nonlinearities on the energetics of locomotion in a computational model of an anguilliform swimmer”. In: *Journal of Theoretical Biology* 385 (2015), pp. 119–129. ISSN: 10958541. DOI: 10.1016/j.jtbi.2015.08.023.

[60] Gregory J. Hancock. "The self-propulsion of microscopic organisms through liquids". In: *The Royal Society* 217.1128 (1953), pp. 96–121. ISSN: 0080-4630. DOI: 10.1098/rspa.1953.0048.

[61] Nikolaus Hansen, Sibylle D. Müller, and Petros Koumoutsakos. "Reducing the time complexity of the derandomized evolution strategy with covariance matrix adaptation (CMA-ES)". In: *Evolutionary Computation* 11.1 (Mar. 2003), pp. 1–18. ISSN: 10636560. DOI: 10.1162/106365603321828970.

[62] Nikolaus Hansen and Andreas Ostermeier. *Completely derandomized self-adaptation in evolution strategies.* June 2001. DOI: 10.1162/106365601750190398.

[63] John Happel and Howard Brenner. *Low Reynolds number hydrodynamics - with special applications to particulate media.* 1983. ISBN: 9024728770. DOI: 10.1016/0021-8502(75)90096-8.

[64] Gal Haspel and Michael J. O'Donovan. "A perimotor framework reveals functional segmentation in the motoneuronal network controlling locomotion in Caenorhabditis elegans". In: *Journal of Neuroscience* 31.41 (2011), pp. 14611–14623. ISSN: 02706474. DOI: 10.1523/JNEUROSCI.2186-11.2011.

[65] Edward M. Hedgecock and Richard L. Russell. "Normal and mutant thermotaxis in the nematode Caenorhabditis elegans". In: *Proceedings of the National Academy of Sciences of the United States of America* 72.10 (1975), pp. 4061–4065. ISSN: 00278424. DOI: 10.1073/pnas.72.10.4061.

[66] Archibald V. Hill. "The heat of shortening and the dynamic constants of muscle". In: *Proceedings of the Royal Society of London. Series B - Biological Sciences* 126.843 (Oct. 1938), pp. 136–195. ISSN: 2053-9193. DOI: 10.1098/rspb.1938.0050.

[67] S Howard. *Materials Data Book.* 2003.

[68] Anthony J. Hulbert and Paul L. Else. "Basal metabolic rate: History, composition, regulation, and usefulness". In: *Physiological and Biochemical Zoology.* Vol. 77. 6. Nov. 2004, pp. 869–876. DOI: 10.1086/422768.

[69] Sunghoon Hur, Rohith Mittapally, Swathi Yadlapalli, Pramod Reddy, and Edgar Meyhofer. "Sub-nanowatt resolution direct calorimetry for probing real-time metabolic activity of individual C. elegans worms". In: *Nature Communications* 11.1 (2020). ISSN: 20411723. DOI: 10.1038/s41467-020-16690-y.

[70] Thomas P. Ilett. "How worms move in 3D". PhD thesis. University of Leeds, 2023. URL: https://etheses.whiterose.ac.uk/32946/.

[71] Carter L. Johnson, Timothy J. Lewis, and Robert Guy. "Neuromechanical mechanisms of gait adaptation in C. elegans: Relative roles of neural and mechanical coupling". In: *SIAM Journal on Applied Dynamical Systems* 20.2 (2021), pp. 1022–1052. ISSN: 15360040. DOI: 10.1137/20M1346122.

[72] Robert E. Johnson. "An improved slender-body theory for Stokes flow". In: (1980).

[73] Sunghwan Jung, Kathleen Mareck, Lisa Fauci, and Michael J. Shelley. "Rotational dynamics of a superhelix towed in a Stokes fluid". In: *Physics of Fluids* 19.10 (2007). ISSN: 10706631. DOI: 10.1063/1.2800287.

[74] Yuko Kagawa-Nagamura, Keiko Gengyo-Ando, Masamichi Ohkura, and Junichi Nakai. "Role of tyramine in calcium dynamics of GABAergic neurons and escape behavior in Caenorhabditis elegans". In: *Zoological Letters* 4.1 (July 2018). ISSN: 2056306X. DOI: 10.1186/s40851-018-0103-1.

[75] Akhil Kandhari, Yifan Wang, Hillel J. Chiel, Roger D. Quinn, and Kathryn A. Daltorio. *An Analysis of Peristaltic Locomotion for Maximizing Velocity or Minimizing Cost of Transport of Earthworm-Like Robots*. Aug. 2021. DOI: 10.1089/soro.2020.0021.

[76] Richard D Keynes, David J Aidley, and Christopher L H Huang. *Nerve and muscle*. 2001. DOI: 10.1017/s0952523811000046.

[77] Sangtae Kim and Seppo J. Karrila. *Microhydrodynamics: principles and selected applications*. 2013.

[78] Lyndon Koens and Eric Lauga. "The boundary integral formulation of Stokes flows includes slender-body theory". In: *Journal of Fluid Mechanics* 850 (2018), R11–R112. ISSN: 14697645. DOI: 10.1017/jfm.2018.483.

[79] Jeremie Korta, Damon A. Clark, Christopher V. Gabel, Lakshminarayanan Mahadevan, and Aravinthan D.T. Samuel. "Mechanosensation and mechanical load modulate the locomotory gait of swimming C. elegans". In: *Journal of Experimental Biology* 210.13 (2007), pp. 2383–2389. ISSN: 00220949. DOI: 10.1242/jeb.004572.

[80] Holger Lang, Sigrid Leyendecker, and Joachim Linn. "Numerical experiments for viscoelastic Cosserat rods with Kelvin-Voigt damping". In: *Proceedings of the ECCOMAS Thematic Conference on Multibody Dynamics 2013* January (2013), pp. 453–462.

[81] Holger Lang, Joachim Linn, and Martin Arnold. "Multi-body dynamics simulation of geometrically exact Cosserat rods". In: *Multibody System Dynamics* 25.3 (Mar. 2011), pp. 285–312. ISSN: 13845640. DOI: `10.1007/S11044-010-9223-X`.

[82] Ricardo Laranjeiro, Girish Harinath, Daniel Burke, Bart P. Braeckman, and Monica Driscoll. "Single swim sessions in C. elegans induce key features of mammalian exercise". In: *BMC Biology* 15.1 (Apr. 2017). ISSN: 17417007. DOI: `10.1186/s12915-017-0368-4`.

[83] Eric Lauga. *The Fluid Dynamics of Cell Motility*. 2020. DOI: `10.1017/9781316796047`.

[84] Félix Lebois, Pascal Sauvage, Charlotte Py, Olivier Cardoso, Benoît Ladoux, Pascal Hersen, and Jean-Marc Di Meglio. "Locomotion control of Caenorhabditis elegans through confinement". In: *Biophysical Journal* 102.12 (2012), pp. 2791–2798. ISSN: 00063495. DOI: `10.1016/j.bpj.2012.04.051`.

[85] Zhilin Li, Zhonghua Qiao, and Tao Tang. *Numerical solution of differential equations: introduction to finite difference and finite element methods*. 2017.

[86] James Lighthill. "Flagellar Hydrodynamics". In: *SIAM Review* (1976).

[87] James Lighthill. *Mathematical biofluiddynamics*. Vol. 24. Society for Industrial and Applied Mathematics, Jan. 1975, pp. i–ix. DOI: `10.1137/1.9781611970517.fm`.

[88] Joachim Linn, Holger Lang, and Andrey Tuganov. "Geometrically exact Cosserat rods with Kelvin–Voigt type viscous damping". In: *ms.copernicus.org* 4 (2013), pp. 79–96. DOI: `10.5194/ms-4-79-2013`.

[89] Robyn Lints and David H. Hall. *The cuticle*. 2009. DOI: `doi:10.3908/wormatlas.1.12`.

[90] Anders Logg, Kent A. Mardal, and Garth N. Wells. "Automated solution of differential equations by the finite element method". In: *Lecture Notes in Computational Science and Engineering* 84 LNCSE (2012), pp. 1–736. ISSN: 14397358. DOI: `10.1007/978-3-642-23099-8{\_}1`.

[91] Alberto Lolli, Giovanni Corsi, and Antonio DeSimone. "Control and navigation problems for model bio-inspired microswimmers". In: *Meccanica* 57.10 (Oct. 2022), pp. 2431–2445. ISSN: 15729648. DOI: `10.1007/s11012-022-01567-9`.

[92] Thomas D. Loreng and Elizabeth F. Smith. "The central apparatus of cilia and eukaryotic flagella". In: *Cold Spring Harbor Perspectives in Biology* 9.2 (2017). ISSN: 19430264. DOI: `10.1101/cshperspect.a028118`.

[93] Christopher P. Lowe. “Dynamics of filaments: Modelling the dynamics of driven microfilaments”. In: *Philosophical Transactions of the Royal Society B: Biological Sciences*. Vol. 358. 1437. Royal Society, Sept. 2003, pp. 1543–1550. DOI: 10.1098/rstb.2003.1340.

[94] Jin-Chun Lu, Yu-Fen Huang, and Nian-Qing Lü. “Computer-aided sperm analysis: Past, present and future”. In: *Andrologia* 46.4 (2014), pp. 329–338. ISSN: 14390272. DOI: 10.1111/and.12093.

[95] Christopher W. Macosko. *Rheology Principles. Measurements and Applications*. 1994.

[96] Dimitris G. Manolakis and Vinay K. Ingle. *Applied Digital Signal Processing*. 2011. DOI: 10.1017/cbo9780511835261.

[97] J. D. Martindale, M Jabbarzadeh, and H. C. Fu. “Choice of computational method for swimming and pumping with nonslender helical filaments at low Reynolds number”. In: *Physics of Fluids* 28.2 (2016). ISSN: 10897666. DOI: 10.1063/1.4940904.

[98] Albert G. Moat, John W. Foster, and Michael P. Spector. *Microbial physiology*. 2002.

[99] Ikue Mori. *Genetics of chemotaxis and thermotaxis in the nematode Caenorhabditis elegans*. 1999. DOI: 10.1146/annurev.genet.33.1.399.

[100] Hoa Nguyen and Lisa Fauci. “Hydrodynamics of diatom chains and semiflexible fibres”. In: *Journal of the Royal Society Interface* 11.96 (July 2014). ISSN: 17425662. DOI: 10.1098/rsif.2014.0314.

[101] Ernst Niebur and Paul Erdös. “Theory of the locomotion of nematodes: Dynamics of undulatory progression on a surface”. In: *Biophysical Journal* 60.5 (1991), pp. 1132–1146. ISSN: 00063495. DOI: 10.1016/S0006-3495(91)82149-X.

[102] Ernst Niebur and Paul Erdos. “Theory of the locomotion of nematodes: Control of the somatic motor neurons by interneurons”. In: *Mathematical Biosciences* 118.1 (1993), pp. 51–82. ISSN: 00255564. DOI: 10.1016/0025-5564(93)90033-7.

[103] Makoto Okuno. “Inhibition and relaxation of sea urchin sperm flagella by vandate”. In: *The Journal of Cell Biology* 85.June (1980).

[104] Sarah D. Olson, Sookkyung Lim, and Ricardo Cortez. “Modeling the dynamics of an elastic rod with intrinsic curvature and twist using a regularized Stokes formulation”. In: *Journal of Computational Physics* 238 (2013), pp. 169–187. ISSN: 10902716. DOI: 10.1016/j.jcp.2012.12.026.

[105] Yuval Omer. “The neuromechanical control of Caenorhabditis elegans head motor behaviour in 3D environments”. PhD thesis. University of Leeds, 2022.

[106] Venkat Padmanabhan. *Locomotion of C. elegans: A Piecewise-HarmonicCurvature Representation of Nematode Behavior*. 2012.

[107] Lipika Parida. “The locomotory characteristics of Caenorhabditis elegans in various external environments: A review”. In: *Applied Animal Behaviour Science* 255 (2022). ISSN: 01681591. DOI: 10.1016/j.applanim.2022.105741.

[108] Sung J. Park, Miriam B. Goodman, and Beth L. Pruitt. “Analysis of nematode mechanics by piezoresistive displacement clamp”. In: *Proceedings of the National Academy of Sciences of the United States of America* 104.44 (Oct. 2007), pp. 17376–17381. ISSN: 00278424. DOI: 10.1073/pnas.0702138104.

[109] Dominic W. Pelle, Charles J. Brokaw, Kathleen A. Lesich, and Charles B. Lindemann. “Mechanical properties of the passive sea urchin sperm flagellum”. In: *Cell Motility and the Cytoskeleton* 66.9 (2009), pp. 721–735. ISSN: 08861544. DOI: 10.1002/cm.20401.

[110] Marko Popovic. *Biomechanics and robotics*. 2013, pp. 1–351. ISBN: 9789814411387. DOI: 10.4032/9789814411387.

[111] Thomas Ranner. “A stable finite element method for low inertia undulatory locomotion in three dimensions”. In: *Applied Numerical Mathematics* 156 (2020), pp. 422–445. ISSN: 01689274. DOI: 10.1016/j.apnum.2020.05.009.

[112] Robert Rikmenspoel. “Elastic Properties of the Sea Urchin Sperm Flagellum”. In: *Biophysical Journal* 6.4 (1966), pp. 471–479. ISSN: 00063495. DOI: 10.1016/S0006-3495(66)86670-5.

[113] Robert Rikmenspoel. “Movement of sea urchin sperm flagella”. In: *Journal of Cell Biology* 76.2 (1978), pp. 310–322. ISSN: 00219525. DOI: 10.1083/jcb.76.2.310.

[114] Robert Rikmenspoel. “Movements and active moments of bull sperm flagella as a function of temperature and viscosity.” In: *Journal of Experimental Biology* 108 (1984), pp. 205–230. ISSN: 00220949. DOI: 10.1242/jeb.108.1.205.

[115] Bruce Rodenborn, Chih Hung Chen, Harry L Swinney, Bin Liu, and H P Zhang. “Propulsion of microorganisms by a helical flagellum”. In: *Proceedings of the National Academy of Sciences of the United States of America* 110.5 (Jan. 2013). ISSN: 00278424. DOI: 10.1073/pnas.1219831110.

[116] C Rorai, M. Zaitsev, and S. Karabasov. “On the limitations of some popular numerical models of flagellated microswimmers: Importance of long-range forces and flagellum waveform”. In: *Royal Society Open Science* 6.1 (2019). ISSN: 20545703. DOI: 10.1098/rsos.180745.

[117] David Rubin and Erhard Krempl. *Introduction to Continuum Mechanics.* 2010. ISBN: 9780750685603. DOI: 10.1016/B978-0-7506-8560-3.X0001-1.

[118] Pascal Sauvage. “Etude de la locomotion chez C. elegans et perturbations mecaniques du mouvement”. PhD thesis. Laboratoire Matiere et Systemes Compiexes, 2007, pp. 1–152.

[119] William W. Schultz and Paul W. Webb. “Power requirements of swimming: Do new methods resolve old questions?” In: *Integrative and Comparative Biology.* Vol. 42. 5. 2002, pp. 1018–1025. DOI: 10.1093/icb/42.5.1018.

[120] Xiao N. Shen, Josué Sznitman, Predrag Krajacic, Todd Lamitina, and Paulo E. Arratia. “Undulatory locomotion of Caenorhabditis elegans on wet surfaces”. In: *Biophysical Journal* 102.12 (2012), pp. 2772–2781. ISSN: 00063495. DOI: 10.1016/j.bpj.2012.05.012.

[121] Juan C. Simo and Loc Vu-Quoc. “A finite strain beam formulation. The three-dimensional dynamic problem. Part I”. In: *Computer methods in applied mechanics* (1985).

[122] Saverio E. Spagnolie and Eric Lauga. “The optimal elastic flagellum”. In: *Physics of Fluids* 22.3 (2010), pp. 1–15. ISSN: 10706631. DOI: 10.1063/1.3318497.

[123] Karl E. Spear and John P. Dismukes. *Synthetic diamond: emerging CVD science and technology.* John Wiley etJ Sons, 1994.

[124] Greg J. Stephens, Bethany Johnson-Kerner, William Bialek, and William S. Ryu. “Dimensionality and dynamics in the behavior of C. elegans”. In: *PLoS Computational Biology* 4.4 (2008). ISSN: 15537358. DOI: 10.1371/journal.pcbi.1000028.

[125] Josué Sznitman, Prashant K. Purohit, Predrag Krajacic, Todd Lamitina, and Paulo E. Arratia. “Material properties of Caenorhabditis elegans swimming at low reynolds number”. In: *Biophysical Journal* 98.4 (2010), pp. 617–626. ISSN: 15420086. DOI: 10.1016/j.bpj.2009.11.010.

[126] Josué Sznitman, Xiao N. Shen, Prashant K. Purohit, and Paulo E. Arratia. “The effects of fluid viscosity on the kinematics and material properties of C. elegans swimming at low reynolds number”. In: *Proceedings of the Society for Experimental*

Mechanics, Inc. 67 (2010), pp. 1303–1311. ISSN: 10466789. DOI: 10.1007/S11340-010-9339-1.

[127] Geoffrey I. Taylor. "Analysis of the swimming of microscopic organisms". In: *The Royal Society* (1951). ISSN: 1816448X. DOI: 10.20537/nd1102011.

[128] Geoffrey Taylor Taylor. "The action of waving cylindrical tails in propelling microscopic organisms". In: *Proceedings of the Royal Society of London. Series A. Mathematical and Physical Sciences* 211.1105 (Feb. 1952), pp. 225–239. ISSN: 0080-4630. DOI: 10.1098/rspa.1952.0035.

[129] Anna Karin Tornberg and Michael J. Shelley. "Simulating the dynamics and interactions of flexible fibers in Stokes flows". In: *Journal of Computational Physics* 196.1 (2004), pp. 8–40. ISSN: 00219991. DOI: 10.1016/j.jcp.2003.10.017.

[130] Eric D. Tytell. "Do trout swim better than eels? Challenges for estimating performance based on the wake of self-propelled bodies". In: *Experiments in Fluids* 43.5 (Nov. 2007), pp. 701–712. ISSN: 07234864. DOI: 10.1007/s00348-007-0343-x.

[131] Eric D. Tytell, Jennifer A. Carr, Nicole Danos, Christopher Wagenbach, Caitlin M. Sullivan, Tim Kiemel, Noah J. Cowan, and M. Mert Ankarali. "Body stiffness and damping depend sensitively on the timing of muscle activation in lampreys". In: *Integrative and comparative biology* 58.5 (2018), pp. 860–873. ISSN: 15577023. DOI: 10.1093/icb/icy042.

[132] Wim M. Van Rees, Mattia Gazzola, and Petros Koumoutsakos. "Optimal shapes for anguilliform swimmers at intermediate Reynolds numbers". In: *Journal of Fluid Mechanics* 722 (2013). ISSN: 14697645. DOI: 10.1017/jfm.2013.157.

[133] Steven Vogel. *Comparative biomechanics: life's physical world*. Princeton University Press, 2013.

[134] Harry R. Wallace. "The Dynamics of Nematode Movement". In: *Annual Review of Phytopathology* 6.1 (Sept. 1968), pp. 91–114. ISSN: 0066-4286. DOI: 10.1146/annurev.py.06.090168.000515.

[135] Wei Wang, Aihong Ji, Poramate Manoonpong, Huan Shen, Jie Hu, Zhendong Dai, and Zhiwei Yu. *Lateral undulation of the flexible spine of sprawling posture vertebrates*. Aug. 2018. DOI: 10.1007/s00359-018-1275-z.

[136] Yongxing Wang, Thomas Ranner, Thomas P. Ilett, Yan Xia, and Netta Cohen. "A monolithic optimal control method for displacement tracking of Cosserat rod with ap-

plication to reconstruction of C. elegans locomotion". In: *Computational Mechanics* 71.3 (Mar. 2023), pp. 409–432. ISSN: 14320924. DOI: 10.1007/S00466-022-02247-X.

[137] Jamie Q. White, Thomas J. Nicholas, Jeff Gritton, Long Truong, Eliott R. Davidson, and Erik M. Jorgensen. "The Sensory Circuitry for Sexual Attraction in C. elegans Males". In: *Current Biology* 17.21 (2007), pp. 1847–1857. ISSN: 09609822. DOI: 10.1016/j.cub.2007.09.011.

[138] John G. White, Eileen Southgate, J. Nichol Thomson, and Syndey Brenner. "The structure of the nervous system of the nematode Caenorhabditis elegans". In: *Philosophical Transactions of the Royal Society of London. B, Biological Sciences* 314.1165 (1986), pp. 1–340. ISSN: 0080-4622. DOI: 10.1098/rstb.1986.0056.

[139] John G. White, Eileen Southgate, J. Nichol Thomson, and Syndey Brenner. "The structure of the ventral nerve cord of Caenorhabditis elegans." In: *Philosophical transactions of the Royal Society of London. Series B, Biological sciences* 275.938 (1976), pp. 327–348. ISSN: 09628436. DOI: 10.1098/rstb.1976.0086.

[140] Steven J. Wickler, Donald F. Hoyt, Edward A. Cogger, and Misty H. Hirschbein. "Preferred, speed and cost of transport: The effect of incline". In: *Journal of Experimental Biology* 203.14 (2000), pp. 2195–2200. ISSN: 00220949. DOI: 10.1242/jeb.203.14.2195.

[141] Basit Yaqoob, Andrea Rodella, Emanuela del Dottore, Alessio Mondini, Barbara Mazzolai, and Nicola M. Pugno. "Mechanics and optimization of undulatory locomotion in different environments, tuning geometry, stiffness, damping and frictional anisotropy". In: (2023).

[142] Gary K. Youngren and Andrias Acrivos. "Stokes flow past a particle of arbitrary shape: A numerical method of solution". In: *Journal of Fluid Mechanics* 69.2 (1975), pp. 377–403. DOI: 10.1017/S0022112075001486.

[143] M A Zaitsev and S A Karabasov. "Mathematical Modelling of Flagellated Microswimmers". In: *Computational Mathematics and Mathematical Physics* 58.11 (Nov. 2018), pp. 1804–1816. DOI: 10.1134/S0965542518110167.

[144] Xiaotian Zhang, Noel Naughton, Tejaswin Parthasarathy, and Mattia Gazzola. "Friction modulation in limbless, three-dimensional gaits and heterogeneous terrains". In: *Nature Communications* 12.1 (2021). ISSN: 20411723. DOI: 10.1038/s41467-021-26276-x.

Appendix A

Appendix

A.1 Background

A.1.1 Response Time to Hydrodynamic Stress

From the swimmer's linear equation of motion Eq. (2.8), we derive the scaling relation

$$\frac{MU}{\tau} \sim \mu U L_0, \tag{A.1}$$

where M is the swimmer's mass, U its swimming speed, tau is characteristic response time to actuation, μ the fluid viscosity and L_0 the swimmer's body length. The magnitude of the hydrodynamic force on the right-hand side of Eq. (A.1) can be estimated as $F \sim \sigma L_0^2$. Here, σ represents the fluid stress tensor, which is of the magnitude of $\sigma \sim \mu U/L_0$ since U/L_0 is the relevant shear rate in the fluid. Solving Eq. (A.1) for τ yields $\tau \sim M\mu L_0$. Thus, the time scale ratios between the swimmer's response τ and swimming time scale $\tau_\mathrm{S} \sim L_0/U$ is given by

$$\frac{\tau}{\tau_\mathrm{S}} \sim \frac{MU}{\mu L_0^2} = \frac{\rho_\mathrm{S}}{\rho}\mathrm{Re}, \tag{A.2}$$

where we used that $M \sim \rho_\mathrm{S} L_0^3$ and $\mathrm{Re} = \rho L_0 U/\mu$. The scale ratio between τ and the gait (deformation) time scale $T = 1/f$ is given by

$$\frac{\tau}{T} \sim \frac{M}{\mu L_0 T} = \frac{\rho_\mathrm{S}}{\rho}\mathrm{Re}_f, \tag{A.3}$$

where we again used that $M \sim \rho_\mathrm{S} L_0^3$ and that $\mathrm{Re}_f = \rho L_0^2 f/\mu$. Similar equations for the swimmer's response time to hydrodynamic torques can be derived from the swimmer's angular momentum equation.

A.2 Model formulation

A.2.1 Derivation of Energetic Terms

Here, we present a derivation of the relevant energetic terms in our model directly from the equations of motion introduced in Chapter 3 given by

$$\mathbf{0} = \boldsymbol{f}_{\mathrm{F}} + \partial_s \boldsymbol{N} + \partial_s \boldsymbol{F}_A, \tag{A.4}$$

$$\mathbf{0} = \boldsymbol{l}_{\mathrm{F}} + \partial_s \boldsymbol{r} \times \boldsymbol{N} + \partial_s \boldsymbol{M} + \partial_s \boldsymbol{L}_A. \tag{A.5}$$

Multiplying the linear balance equation (A.4) by the centreline velocity $\boldsymbol{u}$ and integrating over domain of the body coordinate s yields

$$\int_0^{L_0} \boldsymbol{f}_{\mathrm{F}} \cdot \boldsymbol{u}\, ds + \int_0^{L_0} (\partial_s \boldsymbol{N}) \cdot \boldsymbol{u}\, ds + \int_0^{L_0} \boldsymbol{f}_{\mathrm{A}} \cdot \boldsymbol{u}\, ds = 0, \tag{A.6}$$

where we used that $\boldsymbol{f}_{\mathrm{A}} = \partial_s \boldsymbol{F}_{\mathrm{A}}$. For the remainder, we will suppress the integral boundaries 0 and L_0 for brevity. The first and last integrals contribute to the fluid dissipation rate and the mechanical work done by the actuation force, respectively. Using partial integration on the second integral, the above equation can be written as

$$\int \boldsymbol{f}_{\mathrm{F}} \cdot \boldsymbol{u}\, ds - \int \boldsymbol{N} \cdot \partial_s \boldsymbol{u}\, ds + \int \boldsymbol{f}_{\mathrm{M}} \cdot \boldsymbol{u} = 0\, ds, \tag{A.7}$$

where we used that the internal force resultant $\boldsymbol{N}$ is zero at the boundaries as discussed in Section 3.4.1.

The arc-length derivative of the centreline velocity $\boldsymbol{u}$ can be expressed in terms of the shear vector $\bar{\boldsymbol{\sigma}}$ as follows

$$\begin{aligned}
\partial_s \boldsymbol{u} &= \partial_s \partial_t \boldsymbol{r} && \text{(A.8)}\\
&= \partial_t \boldsymbol{Q}^T \boldsymbol{Q} \partial_s \boldsymbol{r} && \text{(A.9)}\\
&= \left(\partial_t \boldsymbol{Q}^T\right) \boldsymbol{Q} \partial_s \boldsymbol{r} + \boldsymbol{Q}^T \partial_t \boldsymbol{Q} \partial_s \boldsymbol{r} && \text{(A.10)}\\
&= \boldsymbol{\omega} \times \partial_s \boldsymbol{r} + \boldsymbol{Q}^T \partial_t \bar{\boldsymbol{\sigma}} && \text{(A.11)}
\end{aligned}$$

where we used that $\boldsymbol{Q}^T \boldsymbol{Q} = \mathbf{1}$, $[\boldsymbol{\omega}]_\times = \left(\partial_t \boldsymbol{Q}^T\right) \boldsymbol{Q}$ and that $\partial_t \bar{\boldsymbol{\sigma}} = \partial_t \boldsymbol{Q} \partial_s \boldsymbol{r}$. Substituting into the second term in Eq. (A.7) yields

$$\begin{aligned}\int \boldsymbol{N}\cdot\partial_s\boldsymbol{u} &= \int \boldsymbol{N}\cdot\left(\boldsymbol{\omega}\times\partial_s\boldsymbol{r}+\boldsymbol{Q}^T\partial_t\bar{\boldsymbol{\sigma}}\right)\,ds,\\ &= \int \boldsymbol{N}\cdot\left(\boldsymbol{\omega}\times\partial_s\boldsymbol{r}\right)\,ds+\int \boldsymbol{N}\cdot\boldsymbol{Q}^T\partial_t\bar{\boldsymbol{\sigma}}\,ds,\\ &= \int \boldsymbol{N}\cdot\left(\boldsymbol{\omega}\times\partial_s\boldsymbol{r}\right)\,ds+\int \bar{\boldsymbol{N}}\cdot\partial_t\bar{\boldsymbol{\sigma}}\,ds,\\ &= \int \boldsymbol{N}\cdot\left(\boldsymbol{\omega}\times\partial_s\boldsymbol{r}\right)\,ds+\int \partial_t\bar{\boldsymbol{\sigma}}\cdot\boldsymbol{S}\,\bar{\boldsymbol{\sigma}}\,ds+\int \partial_t\bar{\boldsymbol{\sigma}}\cdot\tilde{\boldsymbol{S}}\,\partial_t\bar{\boldsymbol{\sigma}}\,ds.\end{aligned}$$

Substituting back into Eq. (A.7) yields

$$\int \boldsymbol{f}_{\mathrm{F}}\cdot\boldsymbol{u}\,ds-\int \boldsymbol{N}\cdot\left(\boldsymbol{\omega}\times\partial_s\boldsymbol{r}\right)\,ds-\int \partial_t\bar{\boldsymbol{\sigma}}\cdot\boldsymbol{S}\,\bar{\boldsymbol{\sigma}}\,ds-\int \partial_t\bar{\boldsymbol{\sigma}}\cdot\tilde{\boldsymbol{S}}\,\partial_t\bar{\boldsymbol{\sigma}}\,ds+\int \boldsymbol{f}_{\mathrm{A}}\cdot\boldsymbol{u}\,ds=0. \tag{A.12}$$

Taking the scalar product of the angular balance equation (A.5) with the angular velocity $\boldsymbol{w}$ and integrating over the domain of s yields

$$\int \boldsymbol{l}_{\mathrm{F}}\cdot\boldsymbol{\omega}\,ds+\int \left(\partial_s\boldsymbol{r}\times\boldsymbol{N}\right)\cdot\boldsymbol{\omega}\,ds-\int \boldsymbol{M}\cdot\partial_s\boldsymbol{\omega}\,ds+\int \boldsymbol{l}_{\mathrm{A}}\cdot\boldsymbol{\omega}\,ds=0, \tag{A.13}$$

we used that $\boldsymbol{l}_{\mathrm{A}}=\partial_s\boldsymbol{L}_{\mathrm{A}}$ and that the internal torque resultant $\boldsymbol{M}$ is zero at the boundaries to move the derivative onto the angular velocity in the third integral. Using that $\partial_s\boldsymbol{\omega}=(\partial_t\boldsymbol{\kappa}+\boldsymbol{\kappa}\times\boldsymbol{\omega})$, the third integral in the above equation can be written as

$$\begin{aligned}\int \boldsymbol{M}\cdot\partial_s\boldsymbol{\omega}\,ds &= \int \boldsymbol{M}\cdot\left(\partial_t\boldsymbol{\kappa}+\boldsymbol{\kappa}\times\boldsymbol{\omega}\right)\,ds,\\ &= \int \boldsymbol{M}\cdot\partial_t\boldsymbol{\kappa}\,ds+\int \boldsymbol{M}\cdot\left(\boldsymbol{\kappa}\times\boldsymbol{\omega}\right)\,ds,\\ &= \int \boldsymbol{M}\cdot\partial_t\boldsymbol{Q}^T\bar{\boldsymbol{\kappa}}\,ds+\int \boldsymbol{M}\cdot\left(\boldsymbol{\kappa}\times\boldsymbol{\omega}\right)\,ds,\\ &= \int \boldsymbol{M}\cdot\left(\partial_t\boldsymbol{Q}^T\right)\bar{\boldsymbol{\kappa}}\,ds+\int \boldsymbol{M}\cdot\boldsymbol{Q}^T\partial_t\bar{\boldsymbol{\kappa}}\,ds+\int \boldsymbol{M}\cdot\left(\boldsymbol{\kappa}\times\boldsymbol{\omega}\right)\,ds\\ &= \int \boldsymbol{M}\cdot\left(\boldsymbol{\omega}\times\boldsymbol{\kappa}\right)\,ds+\int \bar{\boldsymbol{M}}\cdot\partial_t\bar{\boldsymbol{\kappa}}\,ds+\int \boldsymbol{M}\cdot\left(\boldsymbol{\kappa}\times\boldsymbol{\omega}\right)\,ds,\\ &= \int \bar{\boldsymbol{M}}\cdot\partial_t\bar{\boldsymbol{\kappa}}\,ds,\\ &= \int \partial_t\bar{\boldsymbol{\kappa}}\cdot\boldsymbol{B}\,\bar{\boldsymbol{\kappa}}\,ds+\int \partial_t\bar{\boldsymbol{\kappa}}\cdot\tilde{\boldsymbol{B}}\,\partial_t\bar{\boldsymbol{\kappa}}\,ds.\end{aligned}$$

Substituting back into Eq. (A.13) yields

$$\int \boldsymbol{l}_{\mathrm{F}}\cdot\boldsymbol{\omega}\,ds+\int \left(\partial_s\boldsymbol{r}\times\boldsymbol{N}\right)\cdot\boldsymbol{\omega}\,ds-\int \partial_t\bar{\boldsymbol{\kappa}}\cdot\boldsymbol{B}\,\bar{\boldsymbol{\kappa}}\,ds-\int \partial_t\bar{\boldsymbol{\kappa}}\cdot\tilde{\boldsymbol{B}}\,\partial_t\bar{\boldsymbol{\kappa}}\,ds+\int \boldsymbol{l}_{\mathrm{A}}\cdot\boldsymbol{\omega}\,ds=0 \tag{A.14}$$

Finally, adding the linear and angular equations A.12 and A.14 yields

$$\begin{aligned}\int \{\partial_t\bar{\boldsymbol{\sigma}}\cdot\boldsymbol{S}\,\bar{\boldsymbol{\sigma}}+\partial_t\bar{\boldsymbol{\kappa}}\cdot\boldsymbol{B}\,\boldsymbol{\kappa}\}\,ds &= \int \{\boldsymbol{f}_{\mathrm{F}}\cdot\boldsymbol{u}+\boldsymbol{l}_{\mathrm{F}}\cdot\boldsymbol{\omega}\}\,ds\\ &\quad -\int \left\{\partial_t\bar{\boldsymbol{\sigma}}\cdot\tilde{\boldsymbol{S}}\,\partial_t\bar{\boldsymbol{\sigma}}+\partial_t\bar{\boldsymbol{\kappa}}\cdot\tilde{\boldsymbol{B}}\,\partial_t\bar{\boldsymbol{\kappa}}\right\}ds\\ &\quad +\int \{\boldsymbol{f}_{\mathrm{A}}\cdot\boldsymbol{u}+\boldsymbol{l}_{\mathrm{A}}\cdot\boldsymbol{\omega}\}\,ds. \end{aligned}\tag{A.15}$$

Substituting the definitions for the elastic potential energy V, fluid dissipation rate $\dot{D}_{\mathrm{F}}$, the internal dissipation rate $\dot{D}_{\mathrm{I}}$ and the actuation power $\dot{W}$ given by

$$V(t) = \frac{1}{2}\int_0^{L_0}(\bar{\boldsymbol{\kappa}}\cdot\boldsymbol{B}\bar{\boldsymbol{\kappa}}+\bar{\boldsymbol{\sigma}}\cdot\boldsymbol{S}\bar{\boldsymbol{\sigma}})\,ds, \tag{A.16}$$

$$\dot{D}_{\mathrm{I}}(t) = -\int_0^{L_0}\left(\partial_t\bar{\boldsymbol{\kappa}}\cdot\tilde{\boldsymbol{B}}\,\partial_t\bar{\boldsymbol{\kappa}}+\partial_t\bar{\boldsymbol{\sigma}}\cdot\tilde{\boldsymbol{S}}\,\partial_t\bar{\boldsymbol{\sigma}}\right)ds, \tag{A.17}$$

$$\dot{D}_{\mathrm{F}}(t) = \int_0^{L_0}(\boldsymbol{f}_F\cdot\boldsymbol{u}+\boldsymbol{l}_F\cdot\boldsymbol{\omega})\,ds, \tag{A.18}$$

$$\dot{W}(t) = \int_0^{L_0}(\boldsymbol{f}_{\mathrm{A}}\cdot\boldsymbol{u}+\boldsymbol{l}_{\mathrm{A}}\cdot\boldsymbol{\omega})\,ds, \tag{A.19}$$

into Eq. (A.15), we derive the instantaneous power balance

$$\dot{V} = \dot{D}_{\mathrm{F}}+\dot{D}_I+\dot{W}. \tag{A.20}$$

A.2.2 Derivation of Dimensionless Equations of Motion

In Chapter 3, we introduced the following linear and angular balance equations for an inertia-less viscoelastic Cosserat rod immersed in a Newtonian fluid

$$\boldsymbol{0} = \boldsymbol{f}_{\mathrm{F}}+\partial_s\boldsymbol{N}+\partial_s\boldsymbol{F}_A, \tag{A.21}$$

$$\boldsymbol{0} = \boldsymbol{l}_{\mathrm{F}}+\partial_s\boldsymbol{r}\times\boldsymbol{N}+\partial_s\boldsymbol{M}+\partial_s\boldsymbol{L}_A. \tag{A.22}$$

Internal force and torque resultants are defined as

$$\bar{\boldsymbol{N}} = \boldsymbol{S}\bar{\boldsymbol{\sigma}}+\boldsymbol{S}\partial_t\bar{\boldsymbol{\sigma}}, \tag{A.23}$$

$$\bar{\boldsymbol{M}} = \boldsymbol{B}\bar{\boldsymbol{\kappa}}+\tilde{\boldsymbol{B}}\partial_t\bar{\boldsymbol{\kappa}}. \tag{A.24}$$

The fluid drag force and torque are defined as

$$\boldsymbol{f}_{\mathrm{F}} = -\mu\left[c_{\|}\,(\boldsymbol{d}_3\otimes\boldsymbol{d}_3)+c_{\perp}\,(\boldsymbol{1}-\boldsymbol{d}_3\otimes\boldsymbol{d}_3)\right]\boldsymbol{u}, \tag{A.25}$$

$$\boldsymbol{l}_{\mathrm{F}} = -\mu\left[\gamma_{\|}\,(\boldsymbol{d}_3\otimes\boldsymbol{d}_3)+\gamma_{\perp}\,(\boldsymbol{1}-\boldsymbol{d}_3\otimes\boldsymbol{d}_3)\right]\boldsymbol{\omega}. \tag{A.26}$$

We choose the gait period T as the characteristic time scale of the system and L_0 as the characteristic length scale. Thus, the dimensionless $t*$ and reference arc-length parameter s^* as

$$s^* = \frac{s}{L_0}, \quad t^* = \frac{t}{T}.. \tag{A.27}$$

Similarly, we define the dimensionless centreline $\boldsymbol{r}^*$, Euler angle $\boldsymbol{\theta}^*$, strain vector $\bar{\boldsymbol{\sigma}}^*$, curvature vector, and longitudinal body frame vector $\boldsymbol{d}_3^*$ $\bar{\boldsymbol{\kappa}}^*$ as

$$\boldsymbol{r}^* = \frac{\boldsymbol{r}}{L_0}, \quad \boldsymbol{\theta}^* = \boldsymbol{\theta}, \quad \boldsymbol{\sigma}^* = \boldsymbol{\sigma}, \quad \boldsymbol{\kappa}^* = L_0\boldsymbol{\kappa}, \quad \boldsymbol{d}_3^* = \boldsymbol{d}_3. \tag{A.28}$$

Relevant derivatives are the dimensionless centreline velocity $\boldsymbol{u}^*$, the angular velocity $\boldsymbol{\omega}^*$, the unit tangent $\boldsymbol{t}^*$, and the two strain rates $\dot{\boldsymbol{\kappa}}^*$ and $\dot{\boldsymbol{\sigma}}^*$ which are given by the equations

$$\begin{aligned}
\boldsymbol{u}^* &= \frac{\partial \boldsymbol{r}^*}{\partial t^*} = \frac{T}{L_0}\frac{\partial \boldsymbol{r}}{\partial t} = \frac{T}{L_0}\boldsymbol{u}, \\
\boldsymbol{\omega}^* &= \boldsymbol{A}^*\frac{\partial \boldsymbol{\theta}^*}{\partial t^*} = T\boldsymbol{A}\frac{\partial \boldsymbol{\theta}}{\partial t} = T\boldsymbol{\omega}, \\
\boldsymbol{t}^* &= \frac{\partial \boldsymbol{r}^*}{\partial s^*} = \frac{\partial \boldsymbol{r}}{\partial s} = \boldsymbol{t}, \\
\dot{\boldsymbol{\kappa}}^* &= \frac{\partial \boldsymbol{\kappa}^*}{\partial t^*} = L_0 T\frac{\partial \boldsymbol{\kappa}}{\partial t} = L_0 T\dot{\boldsymbol{\kappa}}, \\
\dot{\boldsymbol{\sigma}}^* &= \frac{\partial \boldsymbol{\sigma}^*}{\partial t^*} = T\frac{\partial \boldsymbol{\sigma}}{\partial t} = T\dot{\boldsymbol{\sigma}}.
\end{aligned} \tag{A.29}$$

Substituting Eqs. (A.25) and (A.23) into the linear balance equation Eq. (A.21), and Eqs. (3.28) and (3.23) into the angular balance equation Eq. (A.22) yields

$$-\mu\left[c_{\|}\boldsymbol{d}_3 \otimes \boldsymbol{d}_3 + c_{\perp}\left(\boldsymbol{1} - \boldsymbol{d}_3 \otimes \boldsymbol{d}_3\right)\right]\boldsymbol{u} + \partial_s \boldsymbol{Q}\left(\boldsymbol{S}\bar{\boldsymbol{\sigma}} + \tilde{\boldsymbol{S}}\dot{\bar{\boldsymbol{\sigma}}}\right) = 0, \tag{A.30}$$

$$-\mu\left[\gamma_{\|}\boldsymbol{d}_3 \otimes \boldsymbol{d}_3 + \gamma_{\perp}\left(\boldsymbol{1} - \boldsymbol{d}_3 \otimes \boldsymbol{d}_3\right)\right]\boldsymbol{\omega} + \boldsymbol{t} \times \boldsymbol{N} + \partial_s \boldsymbol{Q}\left(\boldsymbol{B}\bar{\boldsymbol{\kappa}} + \tilde{\boldsymbol{B}}\dot{\bar{\boldsymbol{\kappa}}}\right) + \partial_s \boldsymbol{L}_{\mathrm{A}} = 0. \tag{A.31}$$

In the linear balance equation Eq. (A.30), we substitute all equation variables and derivatives by their dimensionless in and multiply with $T/\mu c_{\|} L_0$ which yields

$$-\left[\boldsymbol{d}_3^* \otimes \boldsymbol{d}_3^* + K_c\left(\boldsymbol{1} - \boldsymbol{d}_3^* \otimes \boldsymbol{d}_3^*\right)\right]\boldsymbol{u}^* + \partial_{s^*}\boldsymbol{Q}\left(\boldsymbol{S}^*\bar{\boldsymbol{\sigma}}^* + \tilde{\boldsymbol{S}}^*\dot{\bar{\boldsymbol{\sigma}}}^*\right) + \frac{T}{\mu c_{\|} L_0^2}\partial_{s^*}\boldsymbol{F}_{\mathrm{A}} = 0, \tag{A.32}$$

where we defined the dimensionless drag coefficient ratios $K_c = c_{\perp}/c_{\|}$ and the dimensionless shear-stretch rigidity matrix $\boldsymbol{S}^*$ and viscosity matrix $\tilde{\boldsymbol{S}}^*$ as

$$\boldsymbol{S}^* = \frac{T}{\mu c_{\|} L_0^2}\boldsymbol{S}, \quad \tilde{\boldsymbol{S}}^* = \frac{1}{\mu c_{\|} L_0^2}\tilde{\boldsymbol{S}}. \tag{A.33}$$

Eq. (A.32) can be written as

$$\boldsymbol{f}_{\mathrm{F}}^* + \partial_{s^*}\boldsymbol{N}^* + \partial_{s^*}\boldsymbol{F}_{\mathrm{A}}^* = 0, \tag{A.34}$$

where we defined the dimensionless fluid drag line density $\boldsymbol{f}_{\mathrm{F}}^*$ as

$$\boldsymbol{f}_{\mathrm{F}}^* = -\left[\boldsymbol{d}_3^* \otimes \boldsymbol{d}_3^* + K_c \left(\mathbf{1} - \boldsymbol{d}_3^* \otimes \boldsymbol{d}_3^*\right)\right] \boldsymbol{u}^*, \tag{A.35}$$

the dimensionless internal force resultant $\boldsymbol{N}^*$ as

$$\boldsymbol{N}^* = \partial_{s^*} \boldsymbol{Q}^* \bar{\boldsymbol{N}}^*, \quad \bar{\boldsymbol{N}}^* = \boldsymbol{S}^* \bar{\boldsymbol{\sigma}}^* + \tilde{\boldsymbol{S}}^* \dot{\bar{\boldsymbol{\sigma}}}^* \tag{A.36}$$

and the dimensionless actuation force $\boldsymbol{F}_{\mathrm{A}}^*$ as

$$\boldsymbol{F}_{\mathrm{A}}^* = \frac{T}{\mu c_{\parallel} L_0^2} \boldsymbol{F}_{\mathrm{A}}. \tag{A.37}$$

Next, in the angular balance equation Eq. (A.31), we substitute all variables and derivatives by their dimensionless counterparts and multiply with $T/\mu c_{\parallel} L_0^2$ which yields

$$\begin{aligned} 0 = &- K_{\parallel} \left[\boldsymbol{d}_3^* \otimes \boldsymbol{d}_3^* + K_{\gamma} \left(\mathbf{1} - \boldsymbol{d}_3^* \otimes \boldsymbol{d}_3^*\right)\right] \boldsymbol{\omega}^* \\ &+ \partial_{s^*} \boldsymbol{r}^* \times \boldsymbol{N}^* + \partial_{s^*} \boldsymbol{Q}^* \left(\boldsymbol{B}^* \bar{\boldsymbol{\kappa}}^* + \tilde{\boldsymbol{B}}^* \dot{\bar{\boldsymbol{\kappa}}}^*\right) + \partial_{s^*} \frac{T}{\mu c_{\parallel} L_0^3} \boldsymbol{L}_{\mathrm{A}}, \end{aligned} \tag{A.38}$$

where we defined the drag coefficient ratios $K_{\parallel} = \gamma_{\parallel}/c_{\parallel} L_0^2$ and $K_{\gamma} = \gamma_{\perp}/\gamma_{\parallel}$ and the dimensionless bend-twist rigidity matrix $\boldsymbol{B}^*$ and viscosity matrix $\tilde{\boldsymbol{B}}^*$ as

$$\boldsymbol{B}^* = \frac{T}{\mu c_{\parallel} L_0^4} \boldsymbol{B}, \quad \tilde{\boldsymbol{B}}^* = \frac{1}{\mu c_{\parallel} L_0^4} \tilde{\boldsymbol{B}}. \tag{A.39}$$

Eq. (A.38) can be written as

$$0 = \boldsymbol{l}_{\mathrm{F}}^* + \partial_{s^*} \boldsymbol{r}^* \times \boldsymbol{N}^* + \partial_{s^*} \boldsymbol{M}^* + \partial_{s^*} \boldsymbol{L}_{\mathrm{A}}^*, \tag{A.40}$$

where we defined the dimensionless fluid drag torque density $\boldsymbol{l}_{\mathrm{F}}^*$ as

$$\boldsymbol{l}_{\mathrm{F}}^* = -K_{\parallel} \left[\boldsymbol{d}_3^* \otimes \boldsymbol{d}_3^* + K_{\gamma} \left(\mathbf{1} - \boldsymbol{d}_3^* \otimes \boldsymbol{d}_3^*\right)\right] \boldsymbol{\omega}^*, \tag{A.41}$$

the dimensionless internal torque resultant $\boldsymbol{M}^*$ as

$$\boldsymbol{M}^* = \partial_{s^*} \boldsymbol{Q}^* \bar{\boldsymbol{M}}^*, \quad \bar{\boldsymbol{M}}^* = \left(\boldsymbol{B}^* \bar{\boldsymbol{\kappa}}^* + \tilde{\boldsymbol{B}}^* \dot{\bar{\boldsymbol{\kappa}}}^*, \right) \tag{A.42}$$

and the dimensionless actuation torque $\boldsymbol{L}_{\mathrm{A}}^*$ as

$$\boldsymbol{L}_{\mathrm{A}}^* = \frac{T}{\mu c_{\parallel} L_0^3} \boldsymbol{L}_{\mathrm{A}}. \tag{A.43}$$

To conclude, the dimensionless form of the equations of motion takes the following form

$$0 = \boldsymbol{f}_{\mathrm{F}}^{*} + \partial_{s^*}\boldsymbol{N}^{*} + \partial_{s^*}\boldsymbol{F}_{\mathrm{A}}^{*} \tag{A.44}$$

$$,0 = \boldsymbol{l}_{\mathrm{F}}^{*} + \partial_{s^*}\boldsymbol{r}^{*} \times \boldsymbol{N}^{*} + \partial_{s^*}\boldsymbol{M}^{*} + \partial_{s^*}\boldsymbol{L}_{\mathrm{A}}^{*} \tag{A.45}$$

In physical units, the rigidity and viscosity matrices are given by

$$\boldsymbol{S} = EA\varphi^2 \begin{bmatrix} p & 0 & 0 \\ 0 & p & 0 \\ 0 & 0 & 1 \end{bmatrix}, \quad \tilde{\boldsymbol{S}} = \varphi^2 \eta A \begin{bmatrix} p & 0 & 0 \\ 0 & p & 0 \\ 0 & 0 & 1 \end{bmatrix}, \tag{A.46}$$

$$\boldsymbol{B} = EI\varphi^4 \begin{bmatrix} 1 & 0 & 0 \\ 0 & 1 & 0 \\ 0 & 0 & p \end{bmatrix}, \quad \tilde{\boldsymbol{B}} = \eta I \varphi^4 \begin{bmatrix} 1 & 0 & 0 \\ 0 & 1 & 0 \\ 0 & 0 & p \end{bmatrix}, \tag{A.47}$$

where we defined the dimensionless material parameter $p = G/E = \nu/\eta$ (see Section 3.1.3). Thus, according to Eq. (A.39), the dimensionless bend-twist rigidity matrix $\boldsymbol{B}^*$ is given by

$$\boldsymbol{B}^* = \varphi^4 \frac{TEI}{\mu c_{\|} L_0^4} \begin{bmatrix} p & 0 & 0 \\ 0 & p & 0 \\ 0 & 0 & 1 \end{bmatrix} = \varphi^4 \frac{T}{\tau} \begin{bmatrix} p & 0 & 0 \\ 0 & p & 0 \\ 0 & 0 & 1 \end{bmatrix} = \frac{\varphi^4}{a} \begin{bmatrix} p & 0 & 0 \\ 0 & p & 0 \\ 0 & 0 & 1 \end{bmatrix}, \tag{A.48}$$

where we define the time scale $\tau = \mu c_{\|} L_0^4 / EI$ and the time scale ratio $a = \tau/T$. Furthermore, according to Eq. (A.39), the dimensionless bend-twist viscosity matrix $\tilde{\boldsymbol{B}}^*$ can be expressed as

$$\tilde{\boldsymbol{B}} = \varphi^4 \frac{\eta I}{\mu c_{\|} L_0^4} \begin{bmatrix} p & 0 & 0 \\ 0 & p & 0 \\ 0 & 0 & 1 \end{bmatrix} = \varphi^4 \frac{\xi}{T} \frac{T}{\tau} \begin{bmatrix} p & 0 & 0 \\ 0 & p & 0 \\ 0 & 0 & 1 \end{bmatrix} = \varphi^4 \frac{b}{a} \begin{bmatrix} p & 0 & 0 \\ 0 & p & 0 \\ 0 & 0 & 1 \end{bmatrix} \tag{A.49}$$

where we define the time scale $\xi = \eta/E$ and the time scale ratio $b = \xi/T$. According to Eq. (A.46), the dimensionless shear-stretch rigidity matrix $\boldsymbol{S}$ is given by

$$\boldsymbol{S}^* = \frac{TEA}{\mu c_{\|} L_0^2} \varphi^2 \begin{bmatrix} p & 0 & 0 \\ 0 & p & 0 \\ 0 & 0 & 1 \end{bmatrix} = \frac{TAL_0^2}{\tau I} \varphi^2 \begin{bmatrix} p & 0 & 0 \\ 0 & p & 0 \\ 0 & 0 & 1 \end{bmatrix} = \frac{1}{ag} \varphi^2 \begin{bmatrix} p & 0 & 0 \\ 0 & p & 0 \\ 0 & 0 & 1 \end{bmatrix}, \tag{A.50}$$

where we defined the dimensionless geometric ratio $g = I/AL_0^2$ which is proportional to squared slenderness parameter $\varepsilon = 2R_{\max}/L_0$. Lastly, according to Eq. (A.46), the dimensionless shear-stretch viscosity matrix $\tilde{\boldsymbol{S}}^*$ can be expressed as

$$\tilde{\boldsymbol{S}}^* = \frac{\eta A}{\mu c_\parallel L_0^2}\varphi^2 \begin{bmatrix} p & 0 & 0 \\ 0 & p & 0 \\ 0 & 0 & 1 \end{bmatrix} = \frac{\xi A L_0^2}{\tau E I}\varphi^2 \begin{bmatrix} p & 0 & 0 \\ 0 & p & 0 \\ 0 & 0 & 1 \end{bmatrix} = \frac{b}{ag}\varphi^2 \begin{bmatrix} p & 0 & 0 \\ 0 & p & 0 \\ 0 & 0 & 1 \end{bmatrix} \tag{A.51}$$

To conclude, the key parameters are

$$\tau = \frac{\mu c_\parallel L_0^4}{EI}, \quad \xi = \frac{\eta}{E}, \quad a = \frac{\tau}{T}, \quad b = \frac{\xi}{/}T, \quad g = \frac{I}{A L_0^2}, \quad p = \frac{G}{E} = \frac{\nu}{\eta}, \tag{A.52}$$

They can be understood as:

1. τ: intrinsic time scale that measures the relative importance between viscous and elastic stresses
2. ξ: intrinsic time scale which measures the relative importance between internal viscous elastic stresses
3. a: time scale ratio between τ and gait timescale T
4. b: time scale ratio between ξ and the gait timescale T
5. g: geometric ratio that measures the slenderness of the body
6. p: Ratio between shear and Young's modulus

A.2.3 Derivation of Discretized Weak Form

The discretized weak form of the rod's dimensionless equations of motions is given by (see Section 3.4.2)

$$0 = \int_0^1 \boldsymbol{f}_{\mathrm{F},n} \cdot \boldsymbol{\phi}\, ds - \int_0^1 (\boldsymbol{N}_n + \boldsymbol{F}_{\mathrm{A},n}) \cdot \partial_s \boldsymbol{\phi}\, ds, \tag{A.53}$$

$$0 = \int_0^1 \boldsymbol{l}_{\mathrm{F},n} \cdot \boldsymbol{\phi}\, ds + \int_0^1 (\partial_s \boldsymbol{r}_n \times \boldsymbol{N}_n) \cdot \boldsymbol{\phi}\, ds - \int_0^1 (\boldsymbol{M}_n + \boldsymbol{L}_{\mathrm{A},n}) \cdot \partial_s \boldsymbol{\phi}\, ds, \tag{A.54}$$

According to Section A.2.2, the discrete fluid drag force line density $\boldsymbol{f}_{\mathrm{F},n}$, fluid drag torque line density $\boldsymbol{l}_{\mathrm{F},n}$, internal force resultant $\boldsymbol{N}_n$ and internal torque resultant $\boldsymbol{M}_n$ are given by:

$$\begin{aligned}
\boldsymbol{f}_{\mathrm{F},n} &= -\left[\boldsymbol{d}_{3,n}\otimes\boldsymbol{d}_{3,n} + K_c\left(\boldsymbol{1}-\boldsymbol{d}_{3,n}\otimes\boldsymbol{d}_{3,n}\right)\right]\boldsymbol{u}_n\\
\boldsymbol{l}_{\mathrm{F},n} &= -K_{\|}\boldsymbol{Q}_n^T\left[\boldsymbol{e}_3\otimes\boldsymbol{e}_3 + K_\gamma\left(\boldsymbol{1}-\boldsymbol{e}_3\otimes\boldsymbol{e}_3\right)\right]\bar{\boldsymbol{\omega}}_n\\
\boldsymbol{N}_n &= \boldsymbol{Q}_n^T\left(\boldsymbol{S}\bar{\boldsymbol{\sigma}}_n + \tilde{\boldsymbol{S}}\partial_t\bar{\boldsymbol{\sigma}}_n\right)\\
\boldsymbol{M}_n &= \boldsymbol{Q}_n^T\left(\boldsymbol{B}\bar{\boldsymbol{\kappa}}_n + \tilde{\boldsymbol{B}}\partial_t\bar{\boldsymbol{\kappa}}_n\right)
\end{aligned}\tag{A.55}$$

Here, we used Eq. (3.8) to transform the drag torque line density, internal force, and torque resultants from the body to the lab frame. The discrete body frame vectors $\boldsymbol{d}_{k,n}$, centreline velocity $\boldsymbol{u}_n$ and angular velocity $\bar{\boldsymbol{\omega}}_n$ are defined as:

$$\boldsymbol{d}_{i,n} = \boldsymbol{Q}_n\boldsymbol{e}_i, \quad \boldsymbol{u}_n = \partial_t\boldsymbol{r}_n, \quad \bar{\boldsymbol{\omega}}_n = \boldsymbol{A}_n\partial_t\boldsymbol{\theta}_n. \tag{A.56}$$

The discrete strain vector $\bar{\boldsymbol{\sigma}}_n$ and curvature vector $\bar{\boldsymbol{\kappa}}_n$ are defined as:

$$\bar{\boldsymbol{\sigma}}_n = \boldsymbol{Q}_n\partial_s\boldsymbol{r}_n - \boldsymbol{e}_3, \quad \bar{\boldsymbol{\kappa}}_n = \boldsymbol{A}_n\partial_s\boldsymbol{\theta}_n \tag{A.57}$$

Taking the time derivative of the above equations yields the following discrete strain and curvature rates:

$$\partial_t\bar{\boldsymbol{\sigma}} = \boldsymbol{Q}_n\partial_s\partial_t\boldsymbol{r}_n - \boldsymbol{A}_n\partial_t\boldsymbol{\theta}_n\times\boldsymbol{Q}_n\partial_s\partial_t\boldsymbol{r}_n, \quad \partial_t\bar{\boldsymbol{\kappa}}_n = \boldsymbol{A}_n\partial_s\partial_t\boldsymbol{\theta}_n + \left(\partial_t\boldsymbol{A}_n\right)\partial_s\boldsymbol{\theta}_n \tag{A.58}$$

The first-order time derivatives in the weak form are approximated by finite backward differences of order k, as follows:

$$\tilde{\partial}_t^{(k)}\boldsymbol{x}_n \approx \frac{1}{\Delta t}\sum_{i=0}^{k} c_{n-i}\boldsymbol{x}_{n-i} + \mathcal{O}(\Delta t^k), \tag{A.59}$$

Substituting Eqs. (A.56) and Eqs. (A.58) into Eq. (A.55) yields

$$\begin{aligned}
\boldsymbol{f}_{\mathrm{F},n} &= -\left[\boldsymbol{d}_{3,n}\otimes\boldsymbol{d}_{3,n} + K_c\left(\boldsymbol{1}-\boldsymbol{d}_{3,n}\otimes\boldsymbol{d}_{3,n}\right)\right]\tilde{\partial}_t^{(k)}\boldsymbol{r}_n\\
\boldsymbol{l}_{\mathrm{F},n} &= -K_{\|}\boldsymbol{Q}_n^T\left[\boldsymbol{e}_3\otimes\boldsymbol{e}_3 + K_\gamma\left(\boldsymbol{1}-\boldsymbol{e}_3\otimes\boldsymbol{e}_3\right)\right]\boldsymbol{A}_n\tilde{\partial}_t^{(k)}\boldsymbol{\theta}_n\\
\boldsymbol{N}_n &= \boldsymbol{Q}_n^T\left[\boldsymbol{S}\left(\boldsymbol{Q}_n\partial_s\boldsymbol{r}_n - \boldsymbol{e}_3\right) + \tilde{\boldsymbol{S}}\left(\boldsymbol{Q}_n\partial_s\tilde{\partial}_t^{(k)}\boldsymbol{r}_n - \boldsymbol{Q}_n\boldsymbol{A}_n\tilde{\partial}_t^{(k)}\boldsymbol{\theta}_n\times\boldsymbol{Q}_n\partial_s\boldsymbol{r}_n\right)\right]\\
\boldsymbol{M}_n &= \boldsymbol{Q}_n^T\left[\boldsymbol{B}\boldsymbol{A}_n\partial_s\boldsymbol{\theta}_n + \tilde{\boldsymbol{B}}\left(\boldsymbol{A}_n\partial_s\tilde{\partial}_t^{(k)}\boldsymbol{\theta}_n + \left(\tilde{\partial}_t^{(k)}\boldsymbol{A}_n\right)\partial_s\boldsymbol{\theta}_n\right)\right]
\end{aligned}\tag{A.60}$$

To solve the weak form, we use the Picard iteration. The solution at the i-th Picard iteration step is denoted by a $i+1$ superscript. Annotating all variables in Eq. (A.60) yields

$$
\begin{aligned}
\boldsymbol{f}_{\mathrm{F},n}^{i+1} &= -\left[\boldsymbol{d}_{3,n}^{i+1} \otimes \boldsymbol{d}_{3,n} + K_c \left(\mathbf{1} - \boldsymbol{d}_{3,n}^{i+1} \otimes \boldsymbol{d}_{3,n}^{i+1}\right)\right] \tilde{\partial}_t^{(k)} \boldsymbol{r}_n^{i+1} \\
\boldsymbol{l}_{\mathrm{F},n}^{i+1} &= -K_{\|} \boldsymbol{Q}_n^{i+1,T} \left[\boldsymbol{e}_3 \otimes \boldsymbol{e}_3 + K_\gamma \left(\mathbf{1} - \boldsymbol{e}_3 \otimes \boldsymbol{e}_3\right)\right] \boldsymbol{A}_n^{i+1} \tilde{\partial}_t^{(k)} \boldsymbol{\theta}_n^{i+1} \\
\boldsymbol{N}_n^{i+1} &= \boldsymbol{Q}_n^{i+1,T} \left[\boldsymbol{S} \left(\boldsymbol{Q}_n^{i+1} \partial_s \boldsymbol{r}_n^{i+1} - \boldsymbol{e}_3\right) + \tilde{\boldsymbol{S}} \left(\boldsymbol{Q}_n^{i+1} \partial_s \tilde{\partial}_t^{(k)} \boldsymbol{r}_n^{i+1} - \boldsymbol{A}_n^{i+1} \left(\tilde{\partial}_t^{(k)} \boldsymbol{\theta}_n^{i+1}\right) \times \boldsymbol{Q}_n^{i+1} \partial_s \boldsymbol{r}_n^{i+1}\right)\right] \\
\boldsymbol{M}_n^{i} &= \boldsymbol{Q}_n^{i+1,T} \left[\boldsymbol{B} \boldsymbol{A}_n^{i+1} \partial_s \boldsymbol{\theta}_n^{i+1} + \tilde{\boldsymbol{B}} \left(\boldsymbol{A}_n^{i+1} \partial_s \tilde{\partial}_t^{(k)} \boldsymbol{\theta}_n^{i+1} + \left(\tilde{\partial}_t^{(k)} \boldsymbol{A}_n^{i+1}\right) \partial_s \boldsymbol{\theta}_n^{i+1}\right)\right]
\end{aligned}
\tag{A.61}
$$

To linearize the nonlinear terms in the above expressions, we approximate the current solution $i+1$ by the solution from the previous Picard iteration step i which yields

$$
\begin{aligned}
\boldsymbol{f}_{\mathrm{F},n}^{i+1} &\approx -\left[\boldsymbol{d}_{3,n}^{i} \otimes \boldsymbol{d}_{3,n}^{i} + K_c \left(\mathbf{1} - \boldsymbol{d}_{3,n}^{i} \otimes \boldsymbol{d}_{3,n}^{i}\right)\right] \tilde{\partial}_t^{(k)} \boldsymbol{r}_n^{i+1} \\
\boldsymbol{l}_{\mathrm{F},n}^{i+1} &\approx -K_{\|} \boldsymbol{Q}_n^{i,T} \left[\boldsymbol{e}_3 \otimes \boldsymbol{e}_3 + K_\gamma \left(\mathbf{1} - \boldsymbol{e}_3 \otimes \boldsymbol{e}_3\right)\right] \boldsymbol{A}_n^{i} \tilde{\partial}_t^{(k)} \boldsymbol{\theta}_n^{i+1} \\
\boldsymbol{N}_n^{i+1} &\approx \boldsymbol{Q}_n^{i,T} \left[\boldsymbol{S} \left(\boldsymbol{Q}_n^{i} \partial_s \boldsymbol{r}_n^{i+1} - \boldsymbol{e}_3\right) + \tilde{\boldsymbol{S}} \left(\boldsymbol{Q}_n^{i} \partial_s \tilde{\partial}_t^{(k)} \boldsymbol{r}_n^{i+1} - \boldsymbol{A}_n^{i} \left(\tilde{\partial}_t^{(k)} \boldsymbol{\theta}_n^{i+1}\right) \times \boldsymbol{Q}_n^{i} \partial_s \boldsymbol{r}_n^{i}\right)\right] \\
\boldsymbol{M}_n^{i+1} &\approx \boldsymbol{Q}_n^{i,T} \left[\boldsymbol{B} \boldsymbol{A}_n^{i} \partial_s \boldsymbol{\theta}_n^{i+1} + \tilde{\boldsymbol{B}} \left(\boldsymbol{A}_n^{i} \partial_s \tilde{\partial}_t^{(k)} \boldsymbol{\theta}_n^{i+1} + \left(\tilde{\partial}_t^{(k)} \boldsymbol{A}_n^{i+1}\right) \partial_s \boldsymbol{\theta}_n^{i}\right)\right]
\end{aligned}
\tag{A.62}
$$

Substituting Eq. (A.62) into Eqs. (A.53) and (A.54) yields the linearized weak form of the equations of motion at i-th Picard iteration step:

$$
\begin{aligned}
0 = &-\int_0^1 \left[\boldsymbol{d}_{3,n}^{i} \otimes \boldsymbol{d}_{3,n}^{i} + K_c \left(\mathbf{1} - \boldsymbol{d}_{3,n}^{i} \otimes \boldsymbol{d}_{3,n}^{i}\right)\right] \tilde{\partial}_t^{(k)} \boldsymbol{r}_n^{i+1} \cdot \boldsymbol{\phi}\, ds \\
&- \int_0^1 \left\{\boldsymbol{Q}_n^{i,T} \left[\boldsymbol{S} \left(\boldsymbol{Q}_n^{i} \partial_s \boldsymbol{r}_n^{i+1} - \boldsymbol{e}_3\right) + \tilde{\boldsymbol{S}} \left(\boldsymbol{Q}_n^{i} \partial_s \tilde{\partial}_t^{(k)} \boldsymbol{r}_n^{i+1} - \boldsymbol{A}_n^{i} \left(\tilde{\partial}_t^{(k)} \boldsymbol{\theta}_n^{i+1}\right) \times \boldsymbol{Q}_n^{i} \partial_s \boldsymbol{r}_n^{i}\right)\right] + \boldsymbol{F}_{\mathrm{A},n}^{i+1}\right\} \cdot \partial_s \boldsymbol{\phi}\, ds, \\
0 = &-\int_0^1 K_{\|} \boldsymbol{Q}_n^{i,T} \left[\boldsymbol{e}_3 \otimes \boldsymbol{e}_3 + K_\gamma \left(\mathbf{1} - \boldsymbol{e}_3 \otimes \boldsymbol{e}_3\right)\right] \boldsymbol{A}_n^{i} \tilde{\partial}_t^{(k)} \boldsymbol{\theta}_n^{i+1} \cdot \boldsymbol{\phi}\, ds \\
&+ \int_0^1 \left\{\partial_s \boldsymbol{r}_n^{i} \times \boldsymbol{Q}_n^{i,T} \left[\boldsymbol{S} \left(\boldsymbol{Q}_n^{i} \partial_s \boldsymbol{r}_n^{i+1} - \boldsymbol{e}_3\right) + \tilde{\boldsymbol{S}} \left(\boldsymbol{Q}_n^{i} \partial_s \tilde{\partial}_t^{(k)} \boldsymbol{r}_n^{i+1} - \boldsymbol{A}_n^{i} \left(\tilde{\partial}_t^{(k)} \boldsymbol{\theta}_n^{i+1}\right) \times \boldsymbol{Q}_n^{i} \partial_s \boldsymbol{r}_n^{i}\right)\right]\right\} \cdot \boldsymbol{\phi}\, ds \\
&- \int_0^1 \left\{\boldsymbol{Q}_n^{i,T} \left[\boldsymbol{B} \boldsymbol{A}_n^{i} \partial_s \boldsymbol{\theta}_n^{i+1} + \tilde{\boldsymbol{B}} \left(\boldsymbol{A}_n^{i} \partial_s \tilde{\partial}_t^{(k)} \boldsymbol{\theta}_n^{i+1} + \left(\tilde{\partial}_t^{(k)} \boldsymbol{A}_n^{i+1}\right) \partial_s \boldsymbol{\theta}_n^{i}\right)\right] + \boldsymbol{L}_{\mathrm{A},n}^{i+1}\right\} \cdot \partial_s \boldsymbol{\phi}\, ds,
\end{aligned}
\tag{A.63}
$$

where we omitted the integral boundaries and ds.

A.3 Gait Modulation

A.3.1 Geometric model

This section formulates a purely geometric model of a slender microswimmer. This model with help us the swimmer's swimming speed modulates with its undulation parameters, namely the curvature amplitude A and the wavelength λ. Consider a slender microswimmer whose centreline is represented by the curve $\boldsymbol{r}(s,t)$, where s is the curve's arc-length parameter $s=[0,1]$ in dimensionless coordinates. Using the Frenet-Serret frame, the curve $\boldsymbol{r}$ can alternatively be described in terms of its curvature $\kappa(s,t)$ and torsion $\tau(s,t)$. Using standard notation, the Frenet-Serret frame is defined in terms of a local orthonormal coordinate system given by the curve's tangent, $\boldsymbol{T}(s,t)$, normal $\boldsymbol{N}(s,t)$ and binormal $\boldsymbol{B}(s,t)$ frame vectors.

Given a curve's curvature $\kappa(s,t)$ and torsion $\tau(s,t)$, the Frenet-Serret frame can be obtained by solving the famous Frenet-Serret equations:

$$\frac{d}{ds}\begin{pmatrix}\boldsymbol{T}\\ \boldsymbol{N}\\ \boldsymbol{B}\end{pmatrix}=\begin{bmatrix}0 & \kappa & 0\\ -\kappa & 0 & \tau\\ 0 & -\tau & 0\end{bmatrix}\begin{pmatrix}\boldsymbol{T}\\ \boldsymbol{N}\\ \boldsymbol{B}\end{pmatrix}, \tag{A.64}$$

which are a coupled set of ordinary differential equations. To solve the Frenet-Serret equations at a given time t, we need to specify the initial frame orientation at the swimmer's head $s=0$,

$$\boldsymbol{T}_0(t)=\boldsymbol{T}(0,t), \quad \boldsymbol{N}_0(t)=\boldsymbol{N}(0,t), \quad \boldsymbol{B}_0(t)=\boldsymbol{B}(0,t), \tag{A.65}$$

If the curve's tangent vector $\boldsymbol{T}(s,t)$ is known then its centreline $\boldsymbol{r}(s,t)$ can be calculated via the equation:

$$\boldsymbol{r}(s,t)=\boldsymbol{r}_0(t)+\int_0^s \boldsymbol{T}(s')ds', \tag{A.66}$$

where $\boldsymbol{r}_0(t)$ is the swimmer's head position at time t. For the remainder, we make the simplifying assumption that the swimmer's head is fixed at the origin $\boldsymbol{r}_0(t)=0$ reminiscent of the experiments in [12]. It follows than that the centreline velocity $\boldsymbol{u}=\partial_t\boldsymbol{r}$ can be expressed as:

$$\boldsymbol{u}(s,t)=+\partial t\int_0^s \boldsymbol{T}(s',t)ds'. \tag{A.67}$$

For the special case of a planar curve, the torsion $\tau(s,t)=0$, i.e. the Frenet-Serret Eqs. (A.64) simplify to

$$\frac{d}{ds}\begin{pmatrix}\boldsymbol{T}\\ \boldsymbol{N}\end{pmatrix}=\kappa\begin{bmatrix}0 & 1\\ -1 & 0\end{bmatrix}\begin{pmatrix}\boldsymbol{T}\\ \boldsymbol{N}\end{pmatrix}, \quad \frac{d\boldsymbol{B}}{ds}=0. \tag{A.68}$$

Here, we choose $\boldsymbol{B}(0)=(0,0,1)$ so that $\boldsymbol{r}(s)$ is located in the $\boldsymbol{e}_1\boldsymbol{e}_2$-plane. Writing Eq.

(A.69) component-wise yields two decoupled equations for the $\boldsymbol{e}_1$ and $\boldsymbol{e}_2$ component of $\boldsymbol{T}$ and $\boldsymbol{N}$

$$\frac{d}{ds}\begin{pmatrix} T_i \\ N_i \end{pmatrix} = \kappa \begin{bmatrix} 0 & 1 \\ -1 & 0 \end{bmatrix} \begin{pmatrix} T_i \\ N_i \end{pmatrix}, \quad i = [1, 2] \tag{A.69}$$

The solution to Eq. (A.69) can be expressed in terms of the matrix exponential

$$\begin{pmatrix} T_i \\ N_i \end{pmatrix} = \exp\left(\int_0^s \kappa(s')ds'\boldsymbol{A}\right)\begin{pmatrix} T_{i,0} \\ N_{i,0}, \end{pmatrix} \tag{A.70}$$

where and defined the matrix $\boldsymbol{A}$ as

$$\boldsymbol{A} = \begin{bmatrix} 0 & 1 \\ -1 & 0 \end{bmatrix}, \tag{A.71}$$

and suppressed the time argument for brevity. Note that matrix $\boldsymbol{A}$ does not depend on the arc-length parameter s, i.e. the matrix exponential in Eq. (A.70) can be written as:

$$\exp\left(\int_0^s \kappa(s)ds'\boldsymbol{A}\right) = \exp\left(\alpha\boldsymbol{A}\right) = \begin{bmatrix} \cos(\alpha) & \sin(\alpha) \\ -\sin(\alpha) & \cos(\alpha) \end{bmatrix}, \tag{A.72}$$

where we defined

$$\alpha(s,t) = \int_0^s \kappa(s',t)ds'. \tag{A.73}$$

Substituting into Eq. (A.70) yields.

$$\begin{pmatrix} T_i \\ N_i \end{pmatrix} = \begin{bmatrix} \cos(\alpha) & \sin(\alpha) \\ -\sin(\alpha) & \cos(\alpha) \end{bmatrix}\begin{pmatrix} T_{i,0} \\ N_{i,0} \end{pmatrix}, \tag{A.74}$$

If we choose the initial orientation $\boldsymbol{T}_0 = (1, 0)$ and $\boldsymbol{N}_0 = (0, 1)$ for the frame vectors at the swimmer's head, then Eq. (A.74) simplifies to

$$\boldsymbol{T} = \begin{pmatrix} \cos(\alpha) \\ \sin(\alpha) \end{pmatrix}, \quad \boldsymbol{N} = \begin{pmatrix} -\sin(\alpha) \\ \cos(\alpha) \end{pmatrix}. \tag{A.75}$$

Substituting the above expression for $\boldsymbol{T}$ into Eq. (A.64) yields the following equation for the centreline velocity

$$\boldsymbol{u}(s,t) = \int_0^s \partial_t(\alpha(s',t))\boldsymbol{N}(s',t)ds'. \tag{A.76}$$

The curve's tangent vector $\boldsymbol{T}$ can be defined in terms of its tangent angle ψ as follows:

$$\boldsymbol{T} = \cos\psi\boldsymbol{e}_1 + \sin\psi\boldsymbol{e}_2 \tag{A.77}$$

In the context of undulatory locomotion, ψ is commonly referred to as the angle of attack.

By comparing the above equation to Eq. (A.75), it follows $\psi = \alpha$. Note that this relationship results from our specific choice for the initial frame orientation $\boldsymbol{T}_0$ and $\boldsymbol{N}_0$.

To approximate the fluid drag-force line density $\boldsymbol{f}_{\mathrm{F}}$, we use resistive-force theory:

$$\boldsymbol{f}_{\mathrm{F}} = -\left[\boldsymbol{T} \otimes \boldsymbol{T} + K_c\left(\mathbf{1} - \boldsymbol{T} \otimes \boldsymbol{T}\right)\right]\boldsymbol{u} = \left(K_c - 1\right)\boldsymbol{T} \otimes \boldsymbol{T}\boldsymbol{u} - K_c\boldsymbol{u}, \tag{A.78}$$

where K_c is linear drag coefficient ratio. The outer vector-product $\boldsymbol{T} \otimes \boldsymbol{T}$ is given by

$$\boldsymbol{T} \otimes \boldsymbol{T} = \begin{bmatrix} \cos^2\theta & \sin\theta\cos\theta \\ \sin\theta\cos\theta & \sin^2\theta. \end{bmatrix} \tag{A.79}$$

Substituting into Eq. (A.78) yields

$$\boldsymbol{f}_{\mathrm{F}} = \left(K_c - 1\right)\begin{pmatrix} \cos^2\psi u_1 + \sin\psi\cos\psi u_2 \\ \sin\psi\cos\psi u_1 + \sin^2\psi\, u_2 \end{pmatrix} - K_c\begin{pmatrix} u_1 \\ u_2 \end{pmatrix} \tag{A.80}$$

To calculate the propulsion f_{p}, we need to know the swimming direction $\boldsymbol{e}_S$. For the chosen initial values $\boldsymbol{r}_0 = 0$ and $\boldsymbol{T}_0$ and $\boldsymbol{N}_0$, the swimmer's body is orientated such that the swimming direction coincides with the negative $\boldsymbol{e}_1$-axis. Hence, projecting the fluid-drag force onto $\boldsymbol{e}_{\mathrm{S}}$ yields the propulsion force

$$f_{\mathrm{p}} = -\frac{1}{2}\left(K_c - 1\right)\sin(2\psi)u_2 + \left[K_c\sin^2\psi + \cos^2\psi\right]u_1 \tag{A.81}$$

Hence, the transversal movement u_2 of the swimmer's body segments generates the propulsive force

$$f_{\mathrm{p}} = -\frac{1}{2}\left(K_c - 1\right)\sin(2\psi)u_2, \tag{A.82}$$

which implies that:

1. If $K_c > 1$, then the swimmer moves in the opposite direction to the curvature wave's propagation. If $K_c = 1$, there is no propulsion. If $K_c < 1$, the swimmer moves in the same direction as the curvature wave's propagation.
2. To maximize f_{p}, the optimal angle of attack is $\psi = 45°$
3. The propulsive force f_{p} scales linearly with u_2

To model undulatory locomotion, we choose the curvature $\kappa(s,t)$ to be a sinusoidal travelling wave

$$\kappa(s,t) = A\sin(qs - 2\pi t), \tag{A.83}$$

where A is the dimensionless curvature amplitude and q the undulation wavenumber. Note that we used that $f = 1$ in dimensionless coordinates. Substituting into Eq. (A.73) yields

$$\alpha(s,t) = \psi(s,t) = -c\cos(qs - 2\pi t), \tag{A.84}$$

where we defined the wave's shape factor $c = A/q$. The above equation tells us that the maximum absolute angle of attack scales with c. To obtain the average angle of attack $\bar{\psi}$ across the swimmer's body, we calculate the integral of the absolute angle of attack

$$\bar{\psi}(t) = c\int_0^1 |\cos(qs - 2\pi t)|\, ds, \tag{A.85}$$

which can only be solved numerically for arbitrary values of q. The centreline coordinates $\boldsymbol{r}(s)$ and angle of attack ψ, calculated from Eqs. (A.66) and (A.84) for some exemplary values for c and λ and displayed in Fig. A.1A,B. The contour plot of the average angle of attack $\bar{\psi}$ as a function of the c and λ are displayed in Fig. A.1C. The parallel horizontal contour bands are explained by the scaling of $\bar{\psi}$ with the shape factor c. Interestingly, the bands are modulated by the wavelength λ due to the q dependence of the integral in Eq. (A.85).

To compute the centreline velocity $\boldsymbol{u}$ across the swimmer's body, we substitute the time derivative of $\alpha(s,t)$ into Eq. (A.76), which yields:

$$\boldsymbol{u} = -2\pi c\int_0^s \cos(qs' - 2\pi t)\begin{pmatrix}\cos(\alpha)\\ -\sin(\alpha)\end{pmatrix} ds', \tag{A.86}$$

which needs to be solved numerically. However, we can infer from the above equation that $\boldsymbol{u} \propto c\lambda$, as $q = 2\pi/\lambda$. As the discussed earlier, the propulsion force f_p generated by the body segments transversal motion, perpendicular to the swimming direction $\boldsymbol{e}_\mathrm{S}$, scales linearly with u_2. The maximum velocity $u_{2,\mathrm{max}}$ across the length of the swimmer's body is displayed in Fig. A.1D. The bow-like pattern of the contour bands is explained by the scaling $u_{2,\mathrm{max}} \propto c\lambda$.

From the first term in Eq. (A.81) it follows that $f_\mathrm{p} \propto \sin(2\theta)u_2$. Consequently, to maximize the propulsion force generated by body segments transversal motion, an average angle of attack of $\bar{\theta} = 45°$ and large maximum speed $u_{2,\mathrm{max}}$ are favorable.

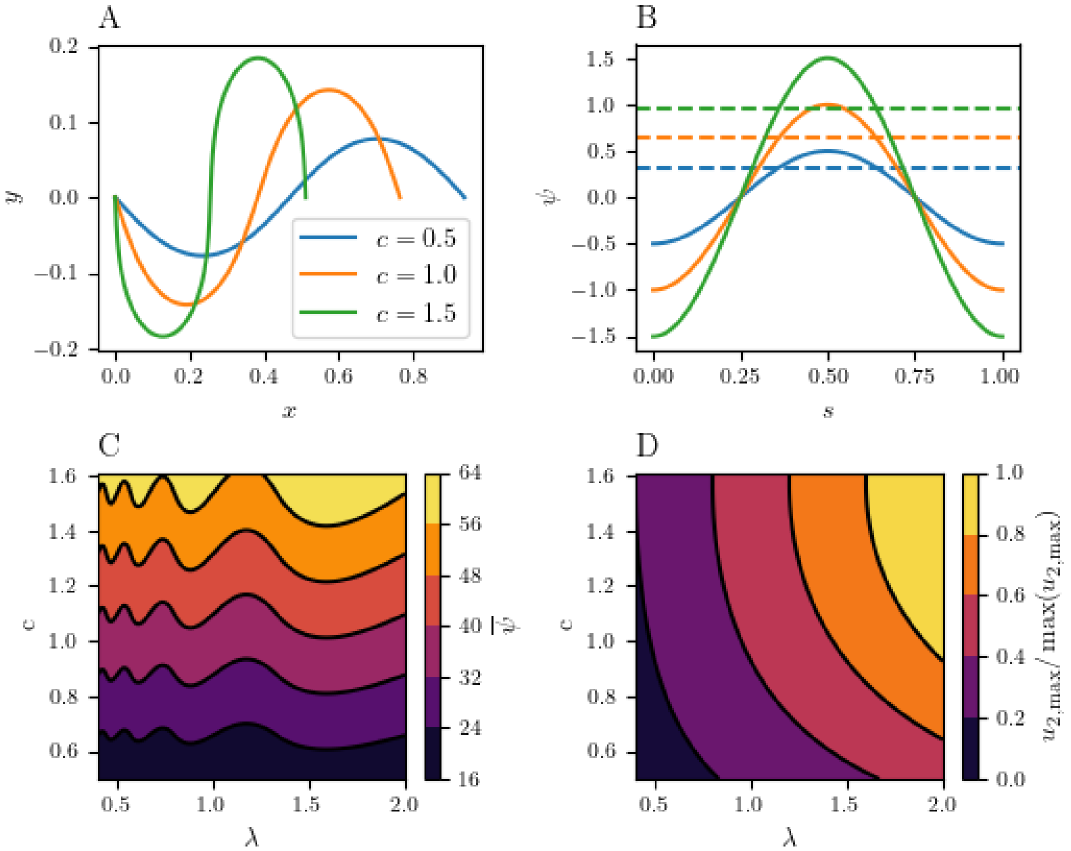

Figure A.1: Geometric prediction of swimmer's angle of attack and transversal centreline velocity during undulatory locomotion. (**A**): Centre line coordinates for different shape factors c and fixed wavelength $\lambda = 1$. (**B**): Angle of attack ψ as a function of the body coordinate s for the values of shape factors c presented in A. Dashed lines represent the average $\bar{\psi}$ of the absolute angle of attack across the length of the swimmer's body. (**C**): Average angle of attack $\bar{\psi}$ (degrees) as a function of λ and c. (**D**): Maximum transversal centreline velocity $u_{2,\max}$ across the length of the swimmer's body. $\boldsymbol{e}_2$. The velocity is normalized by its maximum value within the specified range of λ and c.

A.4 Application

A.4.1 *C. elegans* Optimal Waveform in Water

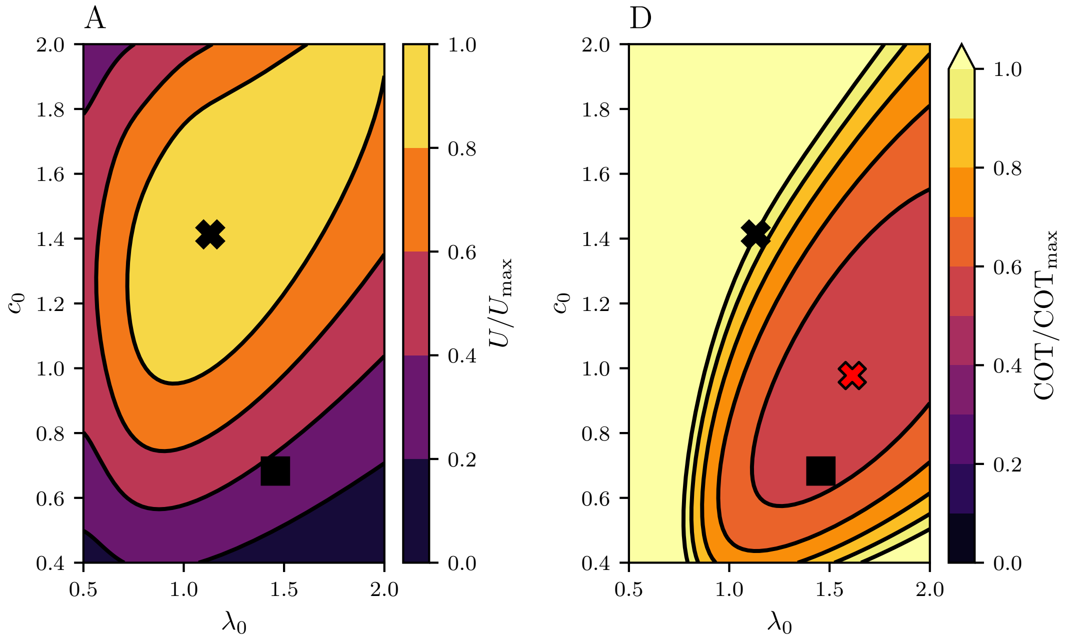

Figure A.2: *C. elegans*' optimal waveform in water. (**A**): Normalized swimming speed U/U_{max} as a function of preferred wavelength λ_0 and shape factor c_0, where U_{max} is the maximum swimming speed over the specified range. (**B**): Normalized Cost of Transport $\mathrm{COT}/\mathrm{COT}_{\mathrm{max}}$, where $\mathrm{COT}_{\mathrm{max}}$ is the COT associated with the fastest waveform (black cross) shown in panel A. The normalized Basal Metabolic Rate is set to $BMR/W_{\mathrm{c}} = 0.5$ [82]. Markers include: Fastest waveform ($\lambda_{0,\mathrm{max}}$=1.13, $A_{0,\mathrm{max}} = 7.84$) (black cross), most efficient waveform ($\lambda_{0,\mathrm{min}} = 1.61$, $A_{0,\mathrm{min}} = 3.8$) (red cross) and *C. elegans* characteristic waveform ($\lambda = 1.46$, $A = 2.94$) (rectangle) obtained from experimental fits in Fig. 6.1. Here, we used the expression $A = 2\pi c/\lambda$ to convert the shape factor c into curvature amplitude A. Effective response times are set at $a = 0.057$ and $b = 0.017$. All other dimensionless parameters are taken from Tab. 6.2.

A.4.2 Swimming Speed of *C. elegans*

Sznitman *et al.* [126] and Gagnon *et al.* [50] measured the swimming speed in the low and intermediate viscosities under comparable experimental conditions used by Fang Yen *et al.* [45]. To compare our model to these studies, Fig. A.3E plots the worm's swimming speed as a function of viscosity μ. For each value of μ, the undulation frequency f, preferred wavelength λ_0, and preferred curvature amplitude A_0 are determined from the experimental fits presented in Fig. 6.1A. The colored curves represent the swimming speed for different values of the linear drag coefficient ratio K_c. The black dots and rectangles represent the experimental data from both studies. Comparing our model to these data points, we predict a drag coefficient ratio within the range $K_\mathrm{c} \in [3.25, 4.0]$. Note that this range is significantly larger than the theoretically predicted value of $K_\mathrm{c} = 1.40$ derived from resistive-force theory for an unconfined fluid.

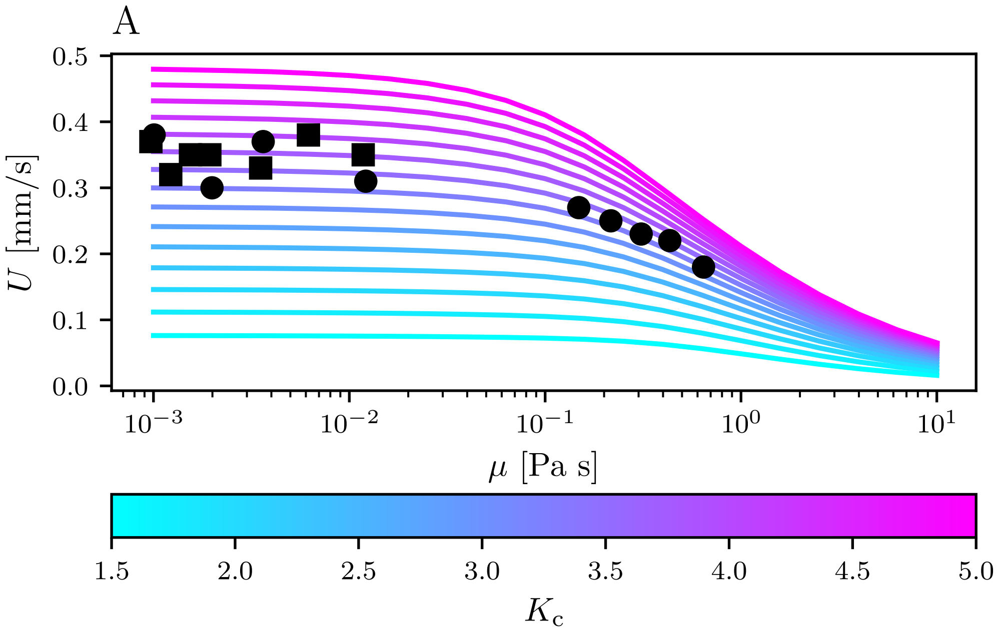

Figure A.3: *C. elegans*' swimming speed across varying fluid viscosities. Physical swimming speed U plotted against fluid viscosity μ. Colored lines correspond to different values of linear drag coefficient ratio K_c. For each value of μ, the undulation frequency f, preferred wavelength λ_0, and preferred curvature amplitude A_0 are determined from the experimental fits to the data reported by Fang Yen *et al.* [45] (see Fig. 6.1A). As model parameters, choose the optimal values. Other dimensionless parameter are taken from Tab. 6.2.

As previously mentioned, during the experiments, the worms are placed in a wall chamber, constituting a confined fluid environment. The presence of the boundary walls makes it more difficult for the fluid to flow past the worm's actively deforming body. To illustrate this, imagine that the gap between both chamber walls is as wide as the diameter of the worm's cross-section. In this extreme scenario, no fluid can flow above or below the worm's body. Hence, it needs to flow either along the in-plane transversal body axis or the longitudinal body axis. This significantly increases the resistance to transversal motion. This larger resistance stems from the pressure distribution needed to drive the fluid passed the longitudinal body axis, which is much longer compared to the cross-sectional diameter of the worm [21]. Consequently, the ratio K_c between the transversal and longitudinal linear drag coefficient is expected to be larger in a confined fluid environment. In fact, Bilbao *et al.* [21] showed that the drag coefficient increases with the length of the swimmer's body and decreases with the relative height of the wall chamber. A thorough comparison between the fluid dynamics of an unconfined vs an unconfined environment would require a Stokes equation with appropriate boundary conditions that are beyond the scope of this thesis. We conclude this chapter with a summary and interpretation of the obtained results.